A Numerical Investigation of the Interactions Between Adjacent Cooling Tower Plumes

A Thesis Submitted for the Degree of Doctor of Philosophy

by

Robin B. Bornoff
B.Sc.

Department of Mechanical Engineering, Brunel University

May 1997

Acknowledgements

In presenting this thesis, I would like to acknowledge the contributions of the following.

Dr. M. R. Mokhtarzadeh-Deghan my supervisor for his continuing support, guidance and encouragement. National Power PLC for part funding this work in particular Dr. G. Hunter and Dr. A. Robins (now at the Department of Mechanical Engineering of Surrey University) for their invaluable discussions throughout the project. The Science and Engineering Council for providing computing resources under grant number GR/K05016. The Department of Mechanical Engineering of Brunel University for the scholarship providing support for three years. My thanks also go to the Computer Centres of Brunel University and the University of London for their tireless support and to Dr. A. Manning for his useful comments and advice.

Finally, I am indebted to my wife Jackie and my son Joseph for their love, support and patience when it most mattered.

Abstract

Cooling tower plume rise, dilution and dispersion is investigated using a numerical model. Both single and double sources are considered. The main aim of the investigation is concerned with comparison of the computational results to existing wind tunnel experimental data as well as simple empirical rise height formula. Analysis of the interaction of adjacent sources, and subsequent rise augmentation compared to that of a single source, is a central theme of the work.

A full-scale hybrid mechanical cooling tower is modelled as a surface mounted cuboid block 20 m high with an internal development duct of 10 m diameter. Both jet and moderately buoyant plume type sources are studied. Two exit velocity ratios are also considered. An oncoming atmospheric boundary is modelled with an associated logarithmic velocity profile and profiles of turbulence kinetic energy and length scale. Two double source orientations, tandem and side-by-side with respect to the oncoming cross wind, are studied. Physical symmetry is utilised and so only half of the domain is modelled.

Both the small-scale (wind tunnel) and full-scale were modelled. The small-scale work used combinations of a low Reynolds number k–ε turbulence model and both hybrid and QUICK discretisation schemes. The high Reynolds numbers encountered in the full-scale allowed the use of a number of different turbulence models, namely the standard k–ε model, the RNG k–ε model and a differential flux model, combined again with the hybrid and QUICK discretisation schemes.

The results of a number of sensitivity tests showed that plume rise in this case was not sensitive to the turbulence model constant C_3 or to source turbulence levels. A decrease in the turbulent Prandtl number led to a marked increase in the turbulent diffusion of the thermal plume.

Horizontal plume spreading was underpredicted in both small and full-scales compared to the experimental data. Plume rise and dilution was, in the majority of cases, predicted accurately compared to both the experimental data and also to rise heights given by simple empirical relationships. Generally, the choice of discretisation scheme was a more important factor than choice of turbulence model.

Interaction of side-by-side plumes was dominated by the interaction of the rotating vortex pairs within the plumes. A tandem source arrangement led to early merging and efficient rise enhancement. Merging into a single type plume occurred sooner with an decrease in exit velocity ratio, *R*.

Nomenclature

$\bar{\phi}$	Average value of variable ϕ
Δx	Cell length in the x direction
ϕ'	Instantaneous value of variable ϕ
ϕ	'Wild-card' variable
ς	Bulk viscosity
β	Coefficient of thermal expansion
ρ	Density
μ	Dynamic laminar viscosity
Γ_ϕ	Effective diffusivity
τ	Laminar shear stress
π	Pressure-scalar gradient term
ε	Rate of dissipation of kinetic energy
λ	Thermal conductivity
η	Value in RNG k-ε turbulence model
σ_ε	Constant in ε transport equation
σ_{DF}	Constant in differential flux transport equation
μ_{eff}	Effective viscosity ($\mu + \mu_T$)
σ_{HF}	Constant in differential flux transport equation
δ	Boundary layer thickness
δ_{ij}	Kronecker delta
σ_k	Constant in k transport equation
Γ_T	Turbulent (eddy) diffusivity
μ_T	Turbulent (eddy) viscosity
σ_T	Turbulent Prandtl number
a	Matrix coefficient
C	Convection coefficient
C_μ	Turbulence model constant
C_1	Turbulence model constant
C_{1F}	Turbulence model constant

$\mathrm{C}_{1\mathrm{RNG}}$	Turbulence model constant
C_2	Turbulence model constant
$\mathrm{C}_{2\mathrm{F}}$	Turbulence model constant
C_3	Turbulence model constant
$\mathrm{C}_{3\mathrm{F}}$	Turbulence model constant
C_P	Specific heat
D	Diffusion coefficient
D	Source diameter
E	Additional function in low Reynolds number turbulence model
E	Constant in log-law equation
f_μ, f_2	Additional function in low Reynolds number turbulence model
F_b	Source buoyancy flux
F_m	Source momentum flux
Fr	Froude number
G	Production of k term due to buoyancy in k-ε model
G	Production of Reynolds stress due to buoyancy
G_F	Production of Reynolds flux due to buoyancy
g_i	Gravitational acceleration
h	Static enthalpy
H	Total enthalpy
$\mathbf{I}$	Identity tensor
k	Turbulent kinetic energy
L_x	Cross wind length scale
P	Pressure
$\mathbf{P}$	Shear production of k in k-ε model
P	Shear production of Reynolds stress in stress transport equation
Pe	Cell Peclet number
P_F	Shear production of Reynolds flux in flux transport equation
P_h	Production term in transport equation for $\overline{h'^2}$
R	Exit velocity ratio
R_F	Turbulence model constant
R_T	Turbulent Reynolds number

S	Non-dimensional source spacing factor
S	Source term
s	spacing between virtual sources
T	Temperature
t	Time
$TI_{x,y,z}$	Turbulence intensity in the x, y or z direction
U_∞	Freestream velocity above boundary layer
u^+	Non-dimensionalised velocity $= -U\sqrt{\rho\tau_k}/\tau$ where $\tau_k = \rho\sqrt{C_\mu}k$
U_i	Velocity tensor
W	Molecular weight
x_i	Distance tensor
y^+	Non-dimensionalised distance $= y\sqrt{\rho\tau_k}/\mu$
y_0^+	Near wall starting point for the boundary layer logarithmic region
z_0	Surface roughness length

Subscripts:

0	Source conditions
a	Ambient conditions
f	Full-scale
nn	Nearest neighbour
P	Current cell or point
s	Small-scale
W	Adjacent cell to the west (E for east etc.)
w	West face of cell (e for eastern face etc.)

Contents

Chapter 2. Previous Work

Chapter 3. Mathematical Model

Chapter 4. Problem Under Consideration

Chapter 5. Results and Discussion

Chapter 6.Conclusions

Chapter 1. Introduction

Plumes and jets issuing into a cross-flow have been widely researched in the last 40 years. The importance of this flow geometry can be seen in the number of applications in which it occurs. These range from film cooling of turbine blade surfaces, vertical takeoff and landing (VTOL) aircraft, dispersion of contaminants in a cross-flowing ambient and cooling tower plume rise. With a growing public awareness of environmental issues including pollution, the need for a full understanding of the plume dispersion problem is required now more than ever. To date, much emphasis has been placed on empirical prediction of plume bending, trajectory and spreading. This, however, restricts prediction to a limited number of atmospheric and plume source conditions. By taking a more analytical approach it is hoped that an insight into the mechanisms that govern adjacent plume interaction and plume dispersion will be obtained. This is expected to lead to more accurate predictive models that have a greater range of applicability.

The largest single need for water cooling comes from the power generation industry. Water used in the steam turbine power cycle cannot be siphoned continuously from a natural supply. This water is, therefore, confined to a closed system where it is alternately heated to a steam state, introduced into the steam turbine and then cooled before being reintroduced into the cycle again. It is during this cooling process that steam plumes can be introduced into the atmospheric boundary layer. Even though there are no contaminants within the plume there is a common psychological reaction in the public equating the visible plume with smokestack emissions. In a more real sense there is the risk of plumes returning to ground level causing effects such as localised ground fogging, possible ice formation on nearby structures, blocking of sunlight and even reingestion of saturated air into other nearby cooling towers.

The most common form of water cooling at industrial power generation sites has been by large natural draught cooling towers (NDCT). Here, the hot water is brought into direct contact with colder air, whereupon evaporation leads to a decrease in the temperature of the hot water. These concrete hyperbolic towers can be as high as 150m. Any plume being introduced into the cross-wind at this height runs little chance of ever spreading back down to ground level. However, towers such as these tend to be considered as eyesores, especially in built-up or urban areas. Because of this public attitude towards the visual impact of NDCTs, a need has arisen for much smaller water cooling towers even though the environmental impact of plumes issued closer to ground level is generally much greater. The introduction of smaller mechanical draught and hybrid draught towers is becoming more frequent at UK power stations. With these towers a fan is used to induce air up through the tower and does not rely upon vertical air density gradients, as happens with the NDCTs. The hybrid and mechanical type towers are, on average, approximately 20m high. The flux to be cooled in a single NDTC has to be split into smaller amounts and passed through an array of mechanical draught towers to achieve the same cooling rate. It is due to this that adjacent sources issue plumes, in close proximity to each other, into the oncoming cross-wind. It is study of the interaction of these adjacent plumes, the efficiency of mixing and subsequent plume rise augmentation over and above the rise for a single plume that is the central part of this thesis. It is hoped that an understanding of the interaction process and its dependence on source configuration and cross-wind condition will lead to better design and siting of these smaller cooling towers at sites where water cooling is required.

Empirical predictions of plume rise rely on fundamental parameters for source and cross-flow conditions. Assuming a top-hat profile for the plume source the following fluxes can be written as:

$$Q = \pi r_0^2 w_0 \tag{1.1}$$

$$F_m = Q w_0 \frac{\rho_0}{\rho_a} \tag{1.2}$$

$$F_b = Qg\frac{(\rho_a - \rho_0)}{\rho_a} \tag{1.3}$$

where Q is the initial volume flux, F_m is the source momentum flux and F_b is the source buoyancy flux. The Froude number is often used to give an indication of the ratio between source momentum and buoyancy:

$$\mathrm{Fr}_0 = \frac{F_m / w_0^2 D^2}{\mathrm{F_b} / w_0^3 D} = \frac{w_0^2}{gD(\rho_a - \rho_0)/\rho_0} \tag{1.4}$$

A source Froude number of zero would indicate a purely buoyant source (i.e. a plume), whilst an infinite source Froude number would result in a jet. The relationship between plume source speed, w_0, and cross-wind speed, U, known as the exit velocity ratio, is written as:

$$R = \frac{w_0}{U} \tag{1.5}$$

This parameter gives an indication of how far the plume or jet will penetrate into the oncoming cross-wind. Atmospheric stability can play a vital role in the rise of cooling tower plumes and is characterised by the Brunt-Vaisala frequency. As this study is primarily concerned with plume conditions near the source and the ground, stably stratified conditions, where this frequency is zero, are assumed.

Chapter 2 of this study starts by covering existing work on simple empirical relationships, involving the above parameters, for prediction of plume rise. More advanced integral models are also introduced as well as state-of-the-art computational fluid dynamic (CFD) studies. The mathematical model used to predict the flow geometry is defined in Chapter 3. The problem of turbulence modelling will be introduced at this stage. In Chapter 4 the problem under consideration in this thesis will be defined and more will be said on the operation of the differing types of cooling tower. The various cooling tower configurations to be investigated as well as choice of source and ambient conditions will be explained. The results generated by the mathematical model will be detailed and discussed in Chapter 5. Final conclusions and recommendations for further work are presented in Chapter 6.

Chapter 2. Previous Work

This review of previous studies falls into two areas. Firstly, analytical, experimental and computational work on a single plume in a cross-wind is covered in Section 2.1. Definitions of standard rise laws and more complex integral models are given, followed by experimental studies and CFD modelling. Secondly, a similar approach is taken for work on two or more adjacent plumes issued into a cross-wind, which is addressed in Section 2.2.

2.1 SINGLE PLUMES

2.1.1 Theoretical work

The simplest one-dimensional plume rise laws are derived from the basic conservation equations governing the rise, bending over and dispersion of a plume or jet in a neutrally stable cross-flow. The five basic equations are the conservation of mass, the conservation of horizontal and vertical momentum, the energy equation and the equation of state. An entrainment hypothesis is also used to calculate by how much the plume grows due to mixing with the ambient. There is no general self-similar solution to these equations for a plume or jet in a cross-flow because there is no single characteristic length scale applicable to all regimes of this flow. Figure 2.1 shows the basic co-ordinate system for a plume in a cross-wind.

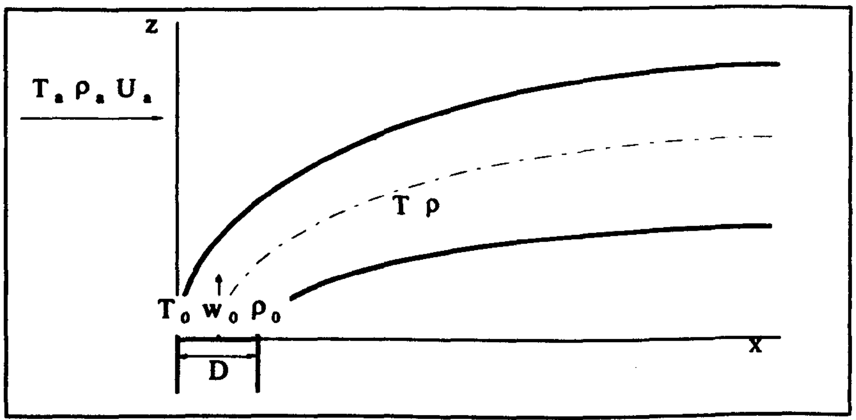

Figure 2.1 Bent-over plume schematic.

Two length scales for buoyancy and momentum are defined, respectively, by:

$$l_b = \frac{F_b}{U_a^3} \tag{2.1}$$

$$l_m = \frac{\sqrt{F_m}}{U_a} \tag{2.2}$$

In buoyancy dominated flows l_b gives a measure of the scale over which the plume bends in the cross-wind. For momentum dominated flows l_m gives this measure.

An assumption has to be made about how the plume radius grows due to the turbulent entrainment of ambient air into the plume, thus closing the set of governing equations. Many such closure methods have been advocated, a summary of which is given by Briggs (1975). Entrainment coefficients, α and β, are used in the calculation of the entrainment rate, E, such that $E = 2r\beta u$ or $E = 2r\alpha v$. Where u is the speed of the plume when it is bent-over and v is the speed of the plume when it is vertical. The parameter α corresponds to vertical plume rise, whilst β is used for the bent-over plume rise. This is the most common assumption and is called the Taylor entrainment hypothesis. Usually, the two parameters, α and β, are both assumed to be constant for a given flow geometry. Bosanquet (1957) originally assumed that α = β, although it was later shown by Briggs (1975) and Hoult and Weil (1972) that for a bent-over plume β was about five times greater than α; the buoyancy dominated section being much more efficient at entrainment than the initial momentum dominated phase. Hoult and Weil (1972) calculated that $\alpha = 0.1$ and $\beta = 0.6$. Hoult *et al.* (1969) considered two entrainment mechanisms. The first mechanism is due to velocity differences parallel to the plume axis. The second mechanism is due to differences normal to the plume axis. The two, treated separately, are then summed for the entrainment rate calculation.

Hirst (1971) assumed the two coefficients to be functions of the local Froude number and so not constant for a given geometry. This is also supported by Briggs (1975). The importance of understanding the entrainment mechanism is apparent here. The simplicities of these models, although giving quick trajectory solutions, do suffer from the assumptions necessary for economic closure.

Very close to the source (the near-field), the plume centre line departs slightly from the vertical due to the cross-wind, and the flow is dominated by source mass and momentum fluxes. Rise in this region is shown to follow the proportionality:

$$\frac{z}{l_m} \propto \left(\frac{x}{l_m}\right)^{1/2} \text{ if } \frac{z}{l_m} << 1 \qquad (2.3)$$

The proportionality factor is dependent upon the entrainment assumption. Using an entrainment assumption of Hoult *et al.* (1969) the exact relationship then becomes:

$$\frac{z}{l_m} = \left(\frac{R}{\alpha R + \beta}\right)^{1/2} \left(\frac{x}{l_m}\right)^{1/2} \text{ if } \frac{z}{l_m} << 1 \qquad (2.4)$$

Two relationships exist for rise far from the source (the far-field): one for momentum dominated sources the other for buoyancy dominated sources. For the former case, trajectory in this region is dominated by initial momentum flux and entrainment rate. The most common relationship for jet-like sources, including the entrainment assumption (Csanady, 1961; Briggs, 1965), is:

$$\frac{z}{l_m} = \left(\frac{3}{\beta^2}\right)^{1/3} \left(\frac{x}{l_m}\right)^{1/3} \text{ if } \frac{x}{l_m} >> 1 \qquad (2.5)$$

Where β is equal to 0.6 (Hoult & Weil, 1972), although Briggs (1975, 1984) empirically found that $\beta = 0.4 + 1.2/R$. Equation (2.5) is often referred to as the 'one-third' law.

For a buoyant plume in the far-field region, rise is dominated by the initial buoyancy flux and entrainment rate. Again, the commonly accepted relationship is:

$$\frac{z}{l_b}=\left(\frac{3}{2\beta^2}\right)^{1/3}\left(\frac{x}{l_b}\right)^{2/3} \text{ if } \frac{x}{l_b}\gg 1 \tag{2.6}$$

This relationship that is commonly called the 'two-thirds' law. The dependence of momentum and buoyancy fluxes in both cases is shown by the effect of the two length scales. For sources with significant source momentum and buoyancy fluxes the following equation for rise far from the source is used:

$$\frac{z}{l_b}=\left[\frac{3}{\beta^2}\left(\frac{l_m}{l_b}\right)^2\frac{x}{l_b}+\frac{3}{2\beta^2}\left(\frac{x}{l_b}\right)^2\right]^{1/3} \tag{2.7}$$

Regions of applicability of Equations (2.4–2.7) downstream of the source are defined by Hoult and Weil (1972).

The length of the region very near to the source is found to be so small that it has a limited range of applications. Overcamp and Ku (1986) have found good agreement with experimental data for $\beta=0.6$ with little or no dependence on R in a range of $3<R<20$.

The two-thirds law predicts continuing plume rise downwind of the source after the near-field. In reality, many unstable plumes are seen to deviate from the two-thirds law. This can either be due to stable stratification conditions or due to the effect of the far-field ambient turbulence. In the latter case, depending upon meteorological conditions, atmospheric turbulence can either be greater or less than the plume turbulence. High atmospheric turbulence limits unsteady plume rise whilst low turbulence can enhance it beyond the two-thirds trajectory. Slawson and Csanady (1966, 1971) described three phases of the plume trajectory with regards to both internal and external turbulence:

1 *Initial phase* of self-generating turbulence in the plume dominates mixing.

2 *Intermediate phase* where environmental turbulence in the inertial subrange dominates mixing.

3 *Final phase* where the energy-containing eddies of the environmental turbulence dominates mixing.

The initial phase ends in the two-thirds law for buoyancy dominated plumes (or the one-third law for momentum dominated plumes). The intermediate or transitional phase may be small if the initial plume diameter is large enough. Batchelor (1950, 1952) described an entrainment relationship for this intermediate inertial subrange dominated flow which involves the rate of dissipation of turbulence energy, ε, of the atmospheric turbulence. Here we find the Taylor entrainment assumption giving way to an influx velocity proportional to the velocity scale of the atmospheric eddies.

Slawson and Csanady (1967) found that in the final stage the plume is mixed primarily by large-scale atmospheric eddies. Due to the lack of observed data for plumes after the intermediate phase most of the work by Slawson and Csanady is qualitatively based. It does, however, give an indication of the effect of ambient turbulence on plume rise in general.

2.1.1.1 Downwash

If the turbulent mixing in the wake of a cooling tower is sufficiently strong, the plume's rise in the near-field may be inhibited or, at worst, plume material will be drawn into the wake and reingested back into the cooling tower. The possibility of ground fogging also exists and is undesirable, especially at power stations. Because of the dependence of the geometry of the stack or tower it is difficult to formulate a generalised downwash predictor model. A common rule of thumb is that if $R > 1.5$ then downwash should not occur. The plume's initial momentum pushes it high enough to escape the effects of the wake.

A technical note by Tatom (1986) provides a simple model for the occurrence of downwash. The drag coefficient of the stack is included to encompass the relationship between stack geometry, stack wake and plume/wake interaction. A more comprehensive study was done by Snyder and Lawson (1990). Wind tunnel tests were carried out and super-critical and sub-critical flow regimes were identified which related to lower and higher base pressure coefficients of a cylindrical stack. Downwash distance was shorter in the sub-critical regime. The importance of the wake of the stack and its interaction with the plume means that an understanding of flow around simple bluff bodies is needed. The extensive work by Castro and Robins (1977) and Sakamoto *et al.* (1982) covers this area.

2.1.1.2 Non-neutral conditions

Theoretical accommodation of more complex atmospheric conditions is in itself much more difficult to perform. A common non-neutral atmospheric condition is the inversion. An elevated inversion layer and then a layer of stably stratified air often exist above a daytime convective boundary layer (CBL). A thin inversion layer is characterised by a potential temperature jump, and thick inversion layers by a potential temperature gradient. If the plume cannot penetrate the inversion it will get trapped and could eventually mix down to the surface and drastically increase ground-level concentrations.

There are two main models for predicting penetration of thin inversions by bent-over plumes. The first, by Briggs (1975), was derived by modifying the buoyancy flux equation (Equation 1.3) to account for the change in F_b in the portion of the plume within the inverted layer. Adding a few simplifications he derived three inequalities to predict whether the plume would not, partially or completely penetrate the inversion layer.

The second model, by Manins (1979), adopts a Gaussian distribution as a reasonable approximation of temperature profiles in a bent-over plume. The assumption that penetration would occur when the maximum excess temperature equals that of the local temperature difference was used. With a few simplifications and modifications a 'fraction of plume-trapped' relationship was derived to predict how fraction of the plume was trapped by the inversion. Penetration of thick inversion layers is covered by Briggs (1984) and Berkowicz *et al.* (1986).

With these models (and any other simple inversion penetration models) the errors incurred in the standard single plume trajectory equations are compounded. Relatively complex atmospheric conditions are accounted for by modifications to already simplified relationships. A more generic approach is called for to take into account more complex source and atmospheric conditions. The next level in predictive accuracy is the integral model.

2.1.2 Integral models

With the increase in computer applicability in the last decade the need to close the governing equations for ease of solution is not as strong as it once was. Increased complexity in models is now achievable by solving a group of integral equations. The comparative survey by Carhart *et al.* (1982) gives a very good indication as to the type and success of various existing models. In all, 16 models were compared. The greater complexity of these models allows prediction of visible plume length, ground-level concentration and other more specific aspects of plume dispersion. Five areas were identified where the solutions of unresolved issues would greatly improve model accuracy:

1 The loss of plume momentum due to dilutive entrainment mechanisms is the primary modelling issue. Simpler models use very simple entrainment hypotheses to account for dilution. The models compared by Carhart *et al.* (1982) all assume entrained air adds all of its horizontal momentum to the plume. An Archemedes-type buoyancy force acting on the plume is also assumed even though the plume is not static. The correct balance of momentum transfer by drag forces, entrainment and the action of

buoyancy needs to be specified for accurate prediction of trajectory and dilution of the plume. Use of the bent-over plume assumption, i.e. that the horizontal velocity of the plume is equal to the ambient velocity at all heights after the plume has been bent-over, does help to resolve the dilution/momentum transfer more realistically. Using a larger spread of momentum than of temperature across the plume cross-section decreases buoyancy and leads to more rapid plume bend over.

2 The two-phase nature of the wet plume is covered by all but three of the models compared. The immediate supersaturation or subsaturation of the plume by the entrained air affects plume cooling rates and thermal profiles. Obviously, the importance of thermodynamic effects, augmented by a large temperature difference at the source, are case-dependent and should be considered in conjunction with thermodynamics when necessary. Use of different spreading rates for moisture and temperature can help solve this problem.

3 Downwash of the plume due to the interaction of plume and tower wake is only accommodated by two of the models. Unless the tower geometry is known it is very difficult to predict the effective increase in bending over of the plume and accompanying increased radial growth. Inclusion of an increased entrainment parameter in the downwash region or a downwash constant in the trajectory equation compensates for the phenomena.

4 In the far-field, where buoyancy and relative velocity of the plume approach zero, the plume is diluted primarily due to atmospheric turbulence. Seven of the 16 models included a separate means for calculating atmospheric diffusion of the plume. Whilst some models assumed ambient diffusion throughout the rise others chose to initiate it either when vertical plume velocity approached zero or when the plume levelled off.

5 The problem of multiple plume interaction, and how the six of the 16 models are capable of tackling this, is covered in Section 2.2.2.

No model performed well for all comparative data sets. A strong dependence on accuracy with the data used for calibration was apparent. Calibration of the models with the experimental and observational data used for comparison would result in better predictions.

Other integral models not included in the review by Carhart *et al.* (1982) include that of Ooms and Mahieu (1981). This model is capable of predicting ground-level concentrations as well as trajectory. Gaussian similarity profiles and an elliptical cross-section are assumed. Concentration distributions very close to the stack and heavier than air plumes were predicted well.

Schatzmann and Policastro (1984) focused on the theoretically deficient areas identified by Carhart *et al.* (1982) to produce a more advanced integral model. They used radial profiles of temperature, velocity and total water, which were of a Gaussian distribution. Downwash effects and plume thermodynamics were also treated. Although calibrated with the same data as in Carhart *et al.* (1982), the performance was more accurate than the better models in Carhart *et al.* (1982).

Carhart and Policastro (1991) presented one of the more recent models. This Argonne National Laboratory and the University of Illinois (ANL/UI) model uses a greater amount of physics than previous models, including tower-wake effects as well as more thermodynamics and the inclusion of an atmospheric turbulence regime. The results for plume rise are accurate within a factor of two for 70% of cases. Gangoiti *et al.* (1995) presented an integral plume rise model for emissions from tall stacks capable of handling realistic atmospheric conditions. These include wind shear and stability variations with height as well as water phase changes along the plume trajectory. Agreement with observations from two tall stacks in complex meteorological conditions was good.

2.1.3 Experimental work

Experiments have been conducted using flow visualisation techniques, as well as hot wire and laser anenometry to define the physical structure of the plume. Its development and the actual process by which surrounding fluid is entrained and the plume diluted, within a neutrally stable boundary layer-type cross-wind, have been investigated. Wind tunnel tests, amongst the many that have been published, include those by Andrepoulus (1989a) and Kuhlman and Chu (1983) as well as the comprehensive study of Andrepoulus and Rodi (1984). Flow features such as the formation of a wake behind the plume in the immediate vicinity of the source as well as subsequent evolution of two counter-rotating vortices within the plume were noted. Figure 2.2 shows a schematic of a plume in a cross-wind with the associated flow features.

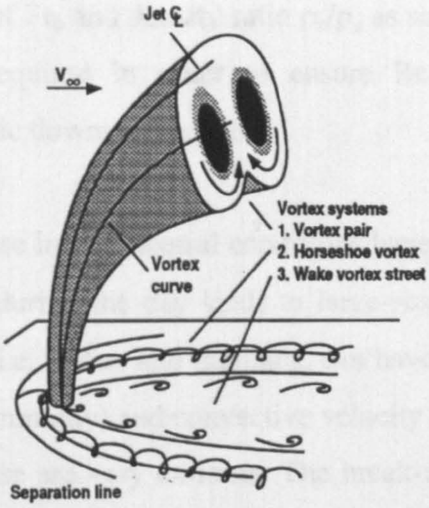

Figure 2.2 Plume in a cross-wind development (Margason, 1993).

All investigators identified the effect of Reynolds number, exit velocity ratio, *R*, and Froude number on plume trajectory in a cross-flow. Andrepoulos (1989b) found the plume structures to be dependent on *R*; the appearance of coherent vortex structures within the plume being qualitatively related to *R*. An important point, made by Andrepoulus and Rodi (1984), was that the near-field, especially at high-velocity ratios, was controlled largely by complex inviscid dynamics, although further downstream, mixing is always influenced by turbulent diffusion. Ramparin and Haniu (1989) took detailed experimental measurements of a two-dimensional plume in a cross-flowing ambient. They noted that there was a higher level of turbulent heat flux at the upper section of a bent-over plume compared to the under side. This is due to the stabilising and destabilising temperature gradients within the inclined plume. Variations in eddy viscosity, as well as thermal eddy diffusivity, were also noted and attributed to the shift in the position of zero shear stress and zero heat flux points compared to the vertical case. In a wind tunnel study by Schatzmann *et al.* (1987), modelling the Niederaussem power plant in Germany, it was shown that flue gas, mixed with the plume from a cooling tower, resulted in better (lower) ground-level concentrations than the emissions from a stack. This work is an example of the need for more detailed dispersion studies to meet ever more stringent EC emissions standards. A study of scaling criteria for physical modelling of buoyant plume rise in a neutral windy atmosphere was conducted by Arya and Lape (1990). It was found that correct scaling of l_b/D was more critical than the use of Fr_0 and density ratio ρ_0/ρ_a as scaling criteria. Large enough values of Re_0 and R are required in order to ensure Reynolds number independence and to avoid unrealistic downwash effects.

Plume rise in non-neutral conditions have also been studied. Heating of land masses by the sun during the day leads to large-scale convective mixing. Large-scale convective motion, i.e. eddies and thermals, can have length scales the size of the mixing layer (1–2 km commonly) and convective velocity scales of about $2ms^{-1}$. The effects of a CBL on plume rise are very extreme. The break-up of the plume by plume scale eddies in the CBL is covered by Hoult and Weil (1972), Weil (1974) and Briggs (1975). Willis and Deardorff (1983) studied plume rise within a CBL. Simple power laws for plume rise were found to overpredict rise, except close to the source, due to plume dilution, which was primarily caused by ambient turbulence. Values for the downstream location of plume break-up, as well as a minimum source buoyancy parameter for buoyant effects to become appreciable, were defined.

Hunter (1992) investigated buoyant jet rise in two types of stability situations using a stratified flow towing tank. A stable layer above a neutral region and also a stable layer above a neutral region and an inversion were studied. It was found that although an integral model gave good prediction of rise in neutral conditions, the oscillation of the plume at the equilibrium height was overpredicted. The experimental work showed that in practice these oscillations were quickly damped out. The work on rise through an elevated inversion layer into a stable region indicated that a range of behaviour could occur, from a partial penetration into the inversion and stable layers, to bifurcation occurring at the density interface of the inversion layer. These results agree very well with the Lagrangian computational work of Zhang and Ghoniem (1994a, b). Surprisingly little work has been conducted in these non-neutral conditions considering that in reality they occur far more often than a neutrally stable atmospheric boundary layer.

Full-scale measurements have been conducted by Thorp and Orgill (1984) who used time-integrated photo-analysis to infer plume rise values. Haman and Malinowski (1989) used aircraft observations to measure cooling tower plume dispersion, and observed dynamic influences of the plume on the ambient atmosphere in the form of temperature and humidity disturbances around the plume. Uthe (1984) analysed plume rise by air-borne lidar measurements over complex terrain. It was found that this lidar technique showed substantially higher plume rise than by photographic methods, as sensitivity of the lidar is well above the visual threshold.

Pollutant dispersion above the atmospheric boundary layer was experimentally modelled in a wind tunnel study by Sideridis *et al.* (1995). Hot wire measurements of the simulated anisotropic, quasi two-dimensional turbulent diffusion of an elevated source were taken. Papaspyros *et al.* (1995) took detailed hot-wire measurements of a plume in cross-flow. Turbulent transport terms of the flow field were directly measured, including both Reynolds fluxes and stresses. Good agreement with simple entrainment models was found when plume trajectory and dilution results were combined in a non-dimensional form with Richardson number and exit velocity ratio.

2.1.4 Computational modelling

The closed and integral models already presented are specific solutions of the governing differential equations. Any complication, such as the interaction of a wall or a complex geometry, tends to invalidate one if not all the assumptions used when deriving the simple model. The amount of empirical input required for these models also makes their accuracy sensitive to the data used for calibration. The rise in computing power and drop in relative cost over the last decade has enabled an ever-growing number of solutions of the equations describing turbulent flows; the Navier–Stokes equations. With the continuing increase in computer viability, the reasons for the need for specific solutions of the governing equations have been eroded. In general, therefore, a marked increase in the use of CFD in this area should be expected.

Previous computational work on plumes and buoyant jets has been conducted for two distinct purposes. The first is the verification of new turbulence models or numerical methods by solving the flow field of a buoyant jet and comparing results with experimental data. The effect of buoyancy and streamline curvature on turbulence isotropy makes the plume a good bench test for models and methods that try to compensate for this added complexity. The second purpose is that of modelling plume trajectory and dispersion characteristics with specific applications in mind. In this study, the case of primary concern is of cooling tower plume dispersion.

Ideriah (1979) proposed a new finite difference technique called EMIT for flows that are parabolic in some regions and elliptic in others. Plume rise in calm stably stratified surroundings is a good example of a combined elliptic and parabolic flow. Results were compared with those of Patankar and Spalding (1972) who used the now commonly employed SIMPLE procedure.

Chien and Schetz (1975) solved the three-dimensional Navier–Stokes equations using a constant eddy viscosity model. The governing equations were written in terms of velocity, vorticity and temperature and solved using upwind differencing. Using the thermal energy equation with the Boussinesq approximation and the Prandtl number set to 0.8, the results underestimated the penetration of the buoyant jet into the cross-flow. It was noted that a finer grid would yield more accurate results.

Using the three-dimensional Navier–Stokes equations with the k–ε model and an elliptic finite difference scheme, Patankar *et al.* (1977) modelled the flow field generated by a round turbulent jet in a cross-stream. Velocity ratios, R, from 2 to 10 were used. Comparison with experimental data of Keffer and Baines (1963) and others showed good agreement. Although buoyancy was not included, it was noted that fundamental modifications of the k–ε model would be needed if body forces due to buoyancy were present.

Malin and Younis (1990) used a Reynolds stress and heat flux closure model to calculate the flow field of a turbulent buoyant plume. Equations were solved for both Reynolds stresses, heat fluxes, energy dissipation and also the turbulent temperature correlation, $\overline{T'^2}$. It was reported that closure at this level results in a more accurate prediction than the much simpler two-equation models. Solution of the thermal dissipation rate transport equation was also investigated and the subsequent avoidance of empirically prescribed ratio of thermal to mechanical time scales were noted. Again, comparison with existing experimental data was found to be in reasonable agreement.

Bergstrom *et al.* (1990) used non-equilibrium algebraic turbulence models for the Reynolds stress and heat flux, solved in an elliptic framework, for a plane vertical plume. The deviation from equilibrium models was based on the observation that the ratio of production to dissipation varies significantly across the flow.

There have been relatively few computational studies specifically for the purpose of calculating cooling tower plume dispersion. Nieuwstadt and Valk (1987) performed a large eddy simulation of non-buoyant and buoyant plume dispersion in a CBL. The filtered momentum and temperature equations together with an extra equation for subgrid energy were used. The flow domain (5km × 5km) was capped by a stable layer to give realistic results. The large eddy simulation for the dispersion of non-buoyant plumes agreed very well with the work of Willis and Deardorff (1981). For the case of a buoyant point source, however, the agreement was less accurate. The effect of buoyancy seemed to increase the height of the plume centre line only slightly in comparison to the non-buoyant case. Good agreement was found between the buoyant plume (surface source) and the well-known two-thirds law. The use of large eddy simulation works very well when modelling the CBL, due to the eddy structure of the latter. It was noted by Nieuwstadt and Valk (1987) that the simulation of buoyant plumes in their study was only of a preliminary nature.

Demuren and Rodi (1987) used three-dimensional numerical calculations to simulate plume spreading past cooling towers. The locally elliptic procedure of Rodi and Srivatsa (1980) was used in this near-field investigation. A rectangular grid was used, so the cylindrical tower had to be approximated by steps. Comparison was made to several idealised cooling tower experiments to test whether the calculation method captured the most essential characteristics of the flow. An additional production term added to the ε transport equation, associated with turbulence production due to buoyancy, was included for the vertical jet case but may not be entirely satisfactory for this bent-over plume case (Rodi, 1982). Comparison of the results with the experimental work by Viollet (1977) were made. The numerical method captured the major flow characteristics such as downwash, longitudinal vortices causing the kidney-shaped plume cross-sections, temperature profiles and concentration decay along the plume centre line. In general, the numerical calculations underpredicted the lifting effect of buoyancy within the plume in the initial region of rise. This was due, in part, to numerical diffusion and also due to the turbulence model. It was proposed that a greater degree of accuracy would be achieved if a higher order discretisation method and a modified turbulence model was used.

Majumdar and Rodi (1989), using the same k–ε turbulence model as Demuren and Rodi (1987), performed a three-dimensional numerical study of flow and plume spreading past a cooling tower. Instead of a rectangular grid, a body-fitted curvilinear grid was used. Two test cases were modelled. The first, by Hölscher and Niemann (1987), was flow around a surface-mounted cylinder immersed in a simulated atmospheric boundary layer in a wind tunnel. The second test case, by Viollet (1977), was a non-buoyant tracer-marked jet issued from a cylindrical cooling tower into an oncoming boundary layer in a water tunnel. The SIMPLEC algorithm by Vandoormal and Raithby (1984) was implemented to calculate the pressure field. Further comparison to the first test case shows the effect of the plume on the flow field. The entrainment of the flow around the cylinder into the plume causes an upward motion over a fairly large region. The horseshoe vortex seen behind the tower in the first test case was not predicted due to this upward motion. As in Demuren and Rodi (1987), excessive deformation of the calculated iso-concentration cross-sections into exaggerated 'kidney shapes' occurs due to the longitudinal vortices created by the plume. This is blamed upon the coarse polar grid further downstream as well as large numerical diffusion due to the upwind discretisation scheme.

Alvarez *et al.* (1993) compared results from first- and second-order turbulence closure models applied to a single jet in a cross-flow. At low-velocity ratios, results are very sensitive to jet inlet conditions as the strong cross-wind has greater influence on the weaker discharge. There was little difference in predictions from the two turbulence models, although the second-order closure gave a slightly more accurate comparison to experimental data. Pressure distribution around a jet discharge into a cross-flow was predicted by Kavsaoglu *et al.* (1993) using the Boldwin–Lomax turbulence model as well as the curved jet algebraic model. Methods such as the gradual introduction of boundary conditions throughout the convergence process were explored as well as the effects of differing boundary conditions around the domain. Chiu *et al.* (1993) investigated a subsonic jet in a cross-flow using an advanced chimera grid, i.e. a bent-over O-grid, to accommodate the jet, embedded in an H-grid for the cross-wind. A grid resolution of *D*/10000 at the jet discharge location was fine enough to capture the experimentally observed horseshoe vortex. A fine grid was also used to integrate directly to the walls, thus enabling highly accurate prediction of surface pressure distribution. Overall, very good agreement with the experimental pressure coefficients around the discharge area was obtained.

An integrated CFD and experimental approach was undertaken by Craig *et al.* (1995). A global positioning system was used for mapping of a complex real terrain which was then used to create both wind tunnel and computational geometries. Representative results between both wind tunnel and computational model compared well. A vortex type flow was predicted in the terrain valleys which would certainly have serious implications on plume rise and dispersion from a source on the valley floor.

An Eulerian approach is by far the most common one taken in CFD, although a Lagrangian method can be just as effective. Gaffen *et al.* (1987) used a three-dimensional Lagrangian dispersion model for moist buoyant plumes. Lagrangian markers representing water in both liquid and vapour phases were introduced into the flow field, where they were displaced by mean and turbulent winds, derived from the Langevin equation as well as by buoyant body forces. Good agreement was found, although limited due to the two-dimensional description of the atmospheric boundary layer used. It was noted that inclusion of non-neutral ambient conditions would have improved accuracy. Zhang and Ghoniem (1994a, b) also used a Lagrangian model, studying cases of a boundary layer under linear stability conditions as well as penetration of an elevated inversion layer by the plume. With linear stratification the two-thirds law was followed until the plume reached its equilibrium height. For cases with strong stratification, the plume exhibited weak, fast decaying oscillations around the equilibrium height. Interaction with an inversion layer produced effects such as accelerating plume bifurcation into two distinct lumps and the creation of internal gravity waves which absorb some of the plume energy thus reducing its penetration potential. The plume was found to either completely or partially penetrate the inversion or get trapped beneath it. These observations are in very good agreement to that found experimentally.

2.2 MULTIPLE PLUMES

The reason for the trend in use of natural draught cooling towers at nearly all major power stations in Britain has been to combine as much effluent as possible into one tower to assure maximum plume rise. Normally, these towers are either standing alone or are far enough apart so that plume interaction is minimal. The smaller hybrid mechanical/natural draught cooling towers, arranged in banks, have to ensure efficient plume interaction to assure as good a rise as that of a single large plume with the same 'total' buoyancy and momentum flux. As plume rise is proportional to $F_b^{1/3}$, the theoretical maximum rise enhancement due to plume interaction and merging would only be $N^{1/3}$, where N is the number of smaller towers.

2.2.1 Theoretical work

Previous work has led to only a few models for multiple plume rise. The two main reviews by Overcamp (1982) and Briggs (1984) centred on the models of Briggs (1974, 1975), Murphy (1975), Anfossi *et al.* (1978) and Scire and Schulman (1981). The models themselves all use single plume rise equations, so multiple plume rise models are commonly limited to three cases: (i) rise in neutral windy conditions; (ii) stably stratified rise in a cross-wind; and (iii) rise in calm (i.e. no cross-wind) stable conditions.

Briggs (1974) took a general approach to the problem. When considering plumes issued side-by-side with respect to the cross-wind, no interaction would occur when the plumes were far apart, and if they were close enough together they would combine. Diagrammatically, it can be seen how the plumes issued from side by side sources interact (Figure 2.3).

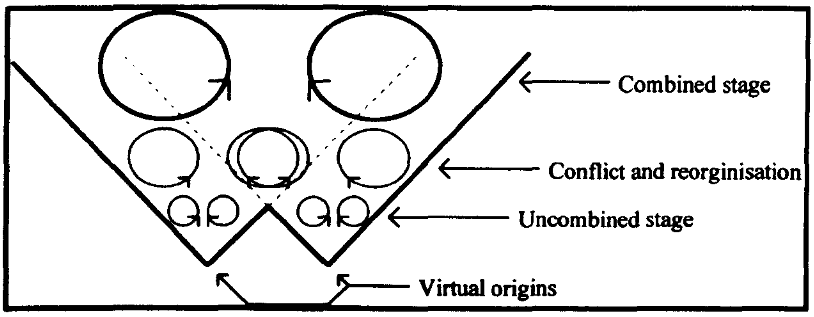

Figure 2.3 Schematic of Adjacent Plume Interaction (Briggs, 1974).

The combined plume rise can be seen as a function of a single plume rise, the number of plumes and the spacing of the virtual origin. Calculation of an enhancement factor defined as:

$$E_N = \frac{\Delta h_N}{\Delta h_1} \tag{2.8}$$

would give a theoretical value of the combined plume rise, Δh_N, when compared to the rise of just one plume, Δh_1. Theoretical work on multiple plume rise centres on the prediction of these enhancement factors. The simplest relationship that Briggs derived was carried out by fitting data from multiple sources to a simple monotonic function of the non-dimensionlised spacing factor, S, giving the relationship:

$$E_N = \left(\frac{N+S}{1+S}\right)^n \tag{2.9}$$

Other more complex relationships hinted at a possible jump in the enhancement factor for values of S below some critical value.

Using data from the Tennessee Valley Authority (TVA) study by Carpenter *et al.* (1968), together with the two-thirds law for buoyant plume rise, calibrated the following equations for S and E_N:

$$E_N = \left(\frac{N+S}{1+S} \right)^{1/3} \tag{2.10}$$

$$S = 6\left(\frac{(N-1)}{N^{1/3}} \frac{s}{\Delta h_1} \right)^{3/2} \tag{2.11}$$

By substituting Equation (2.11) into Equation (2.10), the enhancement factor over single plume rise can be calculated. Subsequently, Briggs (1975) modified this relationship to produce:

$$E_N = \left(\frac{N + \frac{1}{2}(N-1)\left(\Delta h_1 / s\right)^{-3}}{1 + \frac{3}{2}(N-1)\left(\Delta h_1 / d\right)^{-1}} \right)^{1/3} \tag{2.12}$$

Using the above relationship, Dennis *et al.* (1982) found reasonable agreement in analysis of field data. The multiple plume rise model of Anfossi *et al.* (1978) incorporated plumes issued from stacks of differing height by a virtual stack concept. The intersection height of the trajectories of two plumes issued from stacks of different heights (a virtual stack height) is set. A virtual buoyancy flux is then determined at that point that results in the same maximum rise height for the two separate sources. In the limit case for stacks of the same height and source strength the enhancement factor is defined as:

$$E_N = \frac{1 - N^{1/3}}{1 + (N-1)^{-1}\left(\Delta h_1 / s\right)} + N^{1/3} \tag{2.13}$$

Evaluation of this model was made by comparison with the data used by Briggs (1974) as well as Briggs's enhancement models, Equations (2.10 and 2.11) . Good comparison was found, especially at smaller source spacing. Further verification of the model was shown by Anfossi *et al.* (1982) with water-channel multiple plume dispersion experiments. In the models presented, calculation of Δh_1 is needed to obtain an enhancement factor, E_N. The range of applicability for all these enhancement models is therefore set by the range of applicability of the single source laws. The two-thirds law for rise of a buoyant source into a neutrally stable cross-wind has already been covered (see Equation 2.6). There are also maximum rise height formulae, and the downstream distance at which it occurs, for rise in both stable and calm as well as stable and windy conditions. For the latter two cases, only final rise height enhancement factors may be predicted. For neutral conditions, a rule of thumb for the downstream position of maximum plume rise (x_{max}) is 10H (Briggs, 1969, 1975; Perkins, 1974; Stern, 1976), where H is the tower height.

By having no wind direction term in the formulas covered so far, clusters of towers can be considered. Early work and observations gave no indication of, or did not report any, rise enhancement as a function of wind direction (Anfossi *et al.*, 1979; Sandroni *et al.*, 1981). However, it has since been recognised that maximum enhancement occurs when the cross-wind is flowing parallel to a line of towers, and little enhancement when flowing perpendicular (Anfossi *et al.*, 1982; Gregoric *et al.*, 1982; Overcamp & Ku, 1988). To confuse matters, Venter (1977) reported greater enhancement for a more perpendicular cross-wind approach to a line of towers. The assumption has been that if rise is enhanced due to a specific wind direction then enhancement will be maintained independent of the number of sources aligned in that direction. It may well be the case that an entirely different process, and successfully increased rise, of adjacent plume interaction occurs for a 1 × 2 arrangement when compared to a 1 × 10 array. Briggs (1984) proposed that the dimensionless spacing factor be changed to incorporate wind direction, i.e.:

$$S' = \left(\frac{S}{F_b^{1/3}}\right)\frac{u\sin\phi}{(\cos\phi)^{2/3}} \qquad (2.14)$$

Where ϕ is the wind direction angle relative to the axis of the line of sources and S is simply the spacing between sources and u is the wind speed. Tentative conclusions made by Briggs (1984) predicted that there would be little or no plume rise enhancement if $S' > 3.3$ and that rise would be enhanced if $S' < 2.3$ with a marked transition point between these two values. Therefore, rise enhancement formulas should only be used when the latter condition is satisfied

2.2.2 Integral models

Six of the 16 models compared by Carhart *et al.* (1982) were capable of handling multiple source configurations. Two methods of plume merging were used in these studies. The first method, used by Calabrese *et al.* (1974) and Orville *et al.* (1975), simply sums the fluxes of each source to form an effective source in the exit plane. Theoretically, this assumes totally effective interaction as soon as the plume leaves the towers. The second method, used by Hanna (1975), Slawson and Wigley (1975) and Lee (1977), is the more realistic of the two. The largest of the multiple plumes (that with the greatest source strength) is modelled. When its radius has grown to 50% of the separation distance to the next tower, all the plume fluxes are summed and the combined plume established at that point in the trajectory. The latter method allows for the bending over of the multiple plumes before merging, thus giving more accurate trajectory predictions. If the spacing between the towers were to increase, substantial differences would be seen in the plume dispersion calculations of the two models.

None of the models was sensitive to wind direction. A single line of towers, therefore, would be combined by the models to form a combined plume, independent of source configuration, either in the exit plane by the former method or at some point after the initial bending by the latter method. The latter method could be improved if the criteria for the merging of two adjacent plumes could first be quantified. Then, instead of the largest plume initiating an immediate merging of all plumes, adjacent plumes could merge (as a pair) to form a combined flux. In turn, the merged plume could combine with its neighbour, and so on. Increased model complexity would occur, but complex tower arrangement could be modelled with much greater accuracy. It is this reasoning that led Policastro *et al.* (1993) to create an advanced submodel for the ANL/UI integral model, capable of accurately handling multiple sources. Greater insight was used to account for factors such as wind direction, the tendency for elongated cross-sections to become more circular, a transitional region where plumes are in the process of merging and also the effect of tower wake and downwash. The merging methodology used is highly evolved. The first upstream plume is modelled first; further plumes are initiated when the original plume passes other source locations. At each time-step the model checks in three dimensions to see if plumes have overlapped sufficiently to qualify as merged. A single elongated plume is then defined in such a way as to preserve shape, orientation and conserve all fluxes. This method is by far the most generic of all integral models capable of handling multiple sources. The only area for advancement would be to modify the criteria for when overlapping plumes merge. The criteria may well be more than just a function of spatial overlapping; factors such as vorticity may play a very dominant role in how easily adjacent plumes combine.

2.2.3 Experimental work

Experimental work on merging plumes has been conducted, more often than not, for validation of the simple enhancement formulas covered in this section. Very little analysis of the interaction processes themselves have been published. Gregoric *et al.* (1982) used a unique visualisation technique to study merging of inverted salt water jets towed through stagnant water. Instantaneous cross-section photographs were taken of the plumes at many downstream locations. Kidney-shaped cross-sections were observed for a single plume and multiple plumes issued parallel to the towing direction, whilst no such shape was seen when the flow was perpendicular to the line of sources. The normalised areas of the cross-sections (normalised with respect to source diameter and number of sources) were much larger for high values of R; a plume penetrating further into the cross-stream entrains ambient more readily than one that is bent over quickly by the cross-flow. Surprisingly, little effect was seen on trajectory with increasing number of sources. In these experiments a jet Froude number of 6.0 was used so that increase in height due to added buoyancy flux would be minor. However, the rate of increase in normalised cross-sectional area decreased rapidly with increasing N. This shows that entrainment of ambient was reduced when two or more plumes competed for the same fluid. The vortex pair within the kidney-shaped cross-section was strongest for the parallel line of sources and, subsequently, normalised area was highest. This indicates that fast and efficient merging takes place for this source orientation, producing a large single plume which is capable of entraining more ambient.

Davis *et al.* (1978) used a similar type of towing tank to study merging of adjacent buoyant jets. Increasing the number of sources led to a lower rate of dilution as the ratio of plume surface area to plume cross-sectional area is reduced. Sources were positioned perpendicular to the cross-flow, and cross-sections at four downstream locations were recorded. The regimes of merging have been defined by Sforza *et al.* (1966) for rectangular slot jets of air. Firstly, there is a development zone where mixing has not yet reached into the potential core of the jet. Secondly, there is a decay region where spreading in the minor axis direction (i.e. vertically for this arrangement due to the cross-flow being parallel to the line of sources) is faster than that in the major axis direction. Finally, there is an axisymmetrical decay region where the plume behaves as one single plume. It may well be that this differing merging process between sources of varying orientation that explains enhancement as being a function of cross-flow direction.

Isaac and Schetz (1982) used drag coefficients around adjacent cylinders to try to explain the differences in initial rise of two sources positioned parallel and perpendicular to the cross-flow. The negative drag coefficient sensed by the upstream edge of the downstream cylinder (source) may well explain the ability for a jet issued there to rise higher, as the pressure gradient bending it over is less than that applied to the upstream source. The upstream source offers a protective shielding for the downstream source, although with a longer line of sources downstream plume rise may be inhibited by the already bent-over upstream plumes, especially if source buoyancy flux is low. In this initial region, where the trajectory is dominated by inviscid processes, this kind of approach may offer a more realistic explanation of overall merging as a function of source orientation.

Toy *et al.* (1993) used real-time quantitative video-image analysis to study adjacent jets issued into a cross-flow. Source spacing of five diameters was used with $R = 8$. The increased penetration of the in-line or tandem arrangement of sources was seen and attributed, again, to the downstream plume entering into the low-pressure wake region of the upstream source. For the side-by-side arrangement only two counter-rotating vortices were noted. This is probably due to the downstream measuring station (5D) and the fact that merging of the vortices at that location will have been completed.

2.2.4 Associated applications

There are other applications where similarity exists to the bent-over plume flow field. Indeed, the jet or plume in a cross-flow is found in many engineering applications. However, inspite of this similarity, it is rare that any direct comparison between these studies can be made. Two such applications are briefly discussed here.

Much work on multiple jets and plumes for VTOL aircraft applications has been conducted. These include the experimental work by Barata *et al.* (1992) and Saripalli (1987) for impinging jets without a cross-flow. Andrepoulus and Rodi (1984), Sugiyama and Usami (1979) and Shayesteh *et al.* (1985) have conducted experimental work on impinging jets with a cross-flow. Ince and Leschziner (1993) performed a computational study using a Reynolds stress transport closure turbulence model for a double side by side and triangular arrangement of sources with wall impingement in a cross-flow. It was found that the jet discharge conditions were important for accurate modelling, especially at high values of R. Comparison with experimental data supported the conclusion that the second moment closure models resulted in superior results when compared with the models based on the k–ε model. A free jet in a cross-flow was also modelled, and resolution of the turbulence field in the leeward side of the discharge was found to be influential to accuracy. This could be due to correct jet wake pressure prediction being a dominant factor in overall accuracy of the results.

However, the VTOL work has only slight relevance to this study, as any merging of the adjacent jets experience is affected by the flow field resulted from the jet's impingement on the floor. Buoyancy is not a critical factor in this impingement region, where momentum and turbulent entrainment in the fountain region dominates the flow.

Turbine blade film cooling is another area where similarity with the present study exists. However, where it is a goal to enable maximum penetration of cooling tower plumes into the atmospheric boundary layer, this is exactly what is *not* desired in the realm of film cooling. Heat transfer from the cross-flow to the turbine blade is minimised by injection of cooling air to the blade surface. The blowing ratio (equivalent to R) is an important factor in cooling effectiveness; an optimum blowing rate gives maximum cooling above which efficiency drops as the cooling air penetrates further into the boundary layer. A staggered hole pattern is more effective than an in-line pattern due to the interaction of up- and downstream sources, possibly due to the interaction mechanisms already highlighted in this section. Also, an inclined injection angle is found to be more efficient than a normal injection angle. The majority of work has centred on heat transfer characteristics at the blade surface and its dependency upon the wall jet-type flow established. Experiments have been conducted to measure velocity, concentration and turbulent profiles (Yavuzkurt *et al.*, 1980; Afejuku *et al.*, 1983; Jubran & Brown, 1985). Mathematical models have also been employed to predict film-cooling effectiveness. These include a comparative study of two turbulence models by Amer *et al.* (1992), a film-cooling model incorporated into a two-dimensional boundary layer procedure by Schönung and Rodi (1987) and three-dimensional detailed studies by Demuren *et al.* (1983) and Bergeles *et al.* (1981). Despite the apparent similarity between the present study and that of film cooling, very little information from the work on film cooling can be successfully incorporated into this study.

2.2.5 Computational modelling

Although a well-reasoned approach has been taken for treatment of the merging and interaction processes of adjacent plumes in the more advanced integral models, surprisingly little computational work has been performed in this area. Computational predictions of the flow field associated with adjacent plumes and jets issued into a cross-flow have centred on VTOL and film-cooling applications already covered in this section (2.2.4). The present author has conducted computational work of a preliminary nature into the interaction of adjacent plumes (Bornoff and Mokhtarzadeh, 1994). The differences in interaction mechanisms between adjacent side-by-side and tandem sources were identified. Also, the effect of decreasing source separation, and its effect on decreasing downstream dilution rates, was noted. Apart from this, it is apparent that little or no work has been carried out on the three-dimensional prediction of the interaction of adjacent cooling tower plumes in the atmospheric boundary layer. Up until this point, there has been little or no need as cooling tower plumes have been issued so far above ground level into the cross-wind that their subsequent trajectory is of little interest. Optimised placing of adjacent sources for maximum enhanced rise is one of the main goals of the present study. It is hoped that understanding of some of the fundamental processes of merging may enable more realistic hypotheses to be put forward and incorporated into less expensive predictive tools.

Chapter 3. Mathematical Model

The equations that govern fluid flow are solved by taking an Eulerian approach, using a finite volume method. Examples of this type of implementation can be found in various forms (Versteeg & Malalasekera, 1995). The form used in this thesis follow the description given by CFDS-FLOW3D (1994). The problem is treated as steady state as there are no time-dependent boundary conditions, and it is assumed that there are no dominant transient flow features such as vortex shedding. The problem is also said to be turbulent and the governing equations modified accordingly. Various combinations of the governing equations are used to model differing plume arrangements. All equations that will be used are given in the following subsections.

3.1 GOVERNING EQUATIONS

The governing equations are those that, taken together, completely describe the behaviour of the fluid to be modelled. The main equations are derived theoretically requiring no empirical constants (the part empirical, part theoretical turbulence modelling is dealt with in Section 3.2.1). These relationships have been known for over one century but it is only in the last few decades that they have been solvable using computers.

3.2 NAVIER–STOKES EQUATIONS

The basic set of governing equations are called the Navier–Stokes equations. These are the continuity equation:

$$\frac{\partial \rho}{\partial t}+\frac{\partial \rho U_i}{\partial x_i}=0 \qquad (3.1)$$

the momentum equation:

$$\frac{\partial \rho U_i}{\partial t} + \frac{\partial}{\partial x_j}\left(\rho U_i U_j\right) = -\frac{\partial P}{\partial x_i} + \frac{\partial}{\partial x_j}\left(\mu \frac{\partial U_i}{\partial x_j}\right) + g_i\left(\rho - \rho_0\right) \tag{3.2}$$

and the thermal energy equation:

$$\frac{\partial \rho H}{\partial t} + \frac{\partial}{\partial x_i}\left(\rho U_i H\right) = \frac{\partial}{\partial x_i}\left(\lambda \frac{\partial T}{\partial x_i}\right) + \frac{\partial P}{\partial t} \tag{3.3}$$

The above three equations are all in an instantaneous form, and they apply to all classes of flow including laminar and turbulent. In the laminar steady state case all temporal terms disappear. In turbulent flow these temporal terms take into account the rapid fluctuations associated with the high, non-periodic nature of the mixing fluid. To model all of these fluctuations individually one would need a transient calculation in the order of many thousand time steps per second as well as a grid fine enough to capture all turbulent microscales. To model these fluctuations more efficiently all variables are broken down, or decomposed, into a mean and instantaneous component, e.g.:

$$\begin{aligned} U &= \overline{U} + u' \\ H &= \overline{H} + h' \end{aligned} \tag{3.4}$$

When these relationships are substituted back into the instantaneous equations, extra terms are generated as a direct result of the turbulent nature of the flow. As the flow is assumed to be in steady state, any time averaged temporal terms are ignored. The equations can now be written as:

$$\frac{\partial \rho \overline{U}_i}{\partial x_i} = 0 \tag{3.5}$$

$$\frac{\partial}{\partial x_j}\left(\rho \overline{U}_i \overline{U}_j\right) = -\frac{\partial P}{\partial x_i} + \frac{\partial}{\partial x_j}\left(\mu \frac{\partial \overline{U}_i}{\partial x_j} - \rho \overline{u_i' u_j'}\right) + g_i\left(\rho - \rho_0\right) \tag{3.6}$$

$$\frac{\partial}{\partial x_i}\left(\rho \overline{U}_i \overline{H}\right) = \frac{\partial}{\partial x_i}\left(\lambda \frac{\partial \overline{T}}{\partial x_i} - \rho \overline{u_i' h'}\right) \qquad (3.7)$$

where the mean total enthalpy is given by:

$$\overline{H} = h + \tfrac{1}{2}U_i^2 + k \qquad (3.8)$$

The flow can be either incompressible or compressible. An incompressible flow can still take into account density differences that give rise to buoyancy using what is known as the Boussinesq assumption. Density is assumed constant and, thus, omitted in all terms except for the body force term in the momentum equation. Here, the density is calculated using the simple relationship:

$$\rho = \rho_a\left(1 - \beta\left(T - T_a\right)\right) \qquad (3.9)$$

This assumption is valid for small temperature differences, which only go to aid buoyancy. Large temperature differences effectively make density a variable and so has to be included in all terms.

If density does vary sufficiently to be classed as a variable, then the flow is said to be compressible. There are two classes of compressibility. The first is called weakly compressible. Here, although density varies, the associated overpressure, P, is very small compared with the reference pressure P_{REF}. This is valid at Mach numbers less than 0.3 (e.g. natural convection and combusting type flows). In this case density is calculated from a modified equation of state where it is a function of temperature and a reference pressure only:

$$\rho = \frac{P_{REF} W}{RT} \qquad (3.10)$$

Where here R is the universal gas constant and W the molecular weight of the fluid. This is analogous to saying that the speed of sound is infinite in a weakly compressible flow. It is this definition of density that is used in the buoyancy body force term. The other compressible option is fully compressible. This applies to flows where the speed of sound is important and shock waves and associated features are present. In this case the standard equation of state is used. However, this condition is not encountered in this study and so is not covered here.

The flows encountered in this study fall into the incompressible (with the Boussinesq assumption for buoyancy) and weakly compressible categories. Under these conditions contributions from mean and turbulent kinetic energies are ignored in Equation (3.8) and therefore the equation for static enthalpy is solved only.

In the time-averaged Equations (3.6, 3.7) the extra terms, arising from the non-linear convective terms in the laminar equations, reflect the diffusive transport by turbulent fluctuations leading to enhanced mixing over and above diffusion at the molecular level. These additional terms are:

- Reynolds stress = $\rho\overline{u'_i u'_j}$
- Reynolds flux = $\rho\overline{u'_i h'}$

It is the calculation of these stresses and fluxes that is the heart of turbulence modelling. In high-Reynolds number flows, mixing is due almost entirely to turbulent action and so the correct prediction of the turbulence field is essential for accurate modelling of full-scale plume dispersion in a cross-wind.

3.2.1 Turbulence modelling

The introduction of the Reynolds stresses and fluxes after decomposition of the turbulent fluctuating variables, means that the equation set is now not closed. Some form of closure is required to model these fluxes and stresses. There have been a wide range of methods used to do this, varying from the most simple zero-equation models to the much more complex Reynolds stress transport equations. Figure 3.1 shows how these turbulence models relate to each other. A more specific description of these models is now covered.

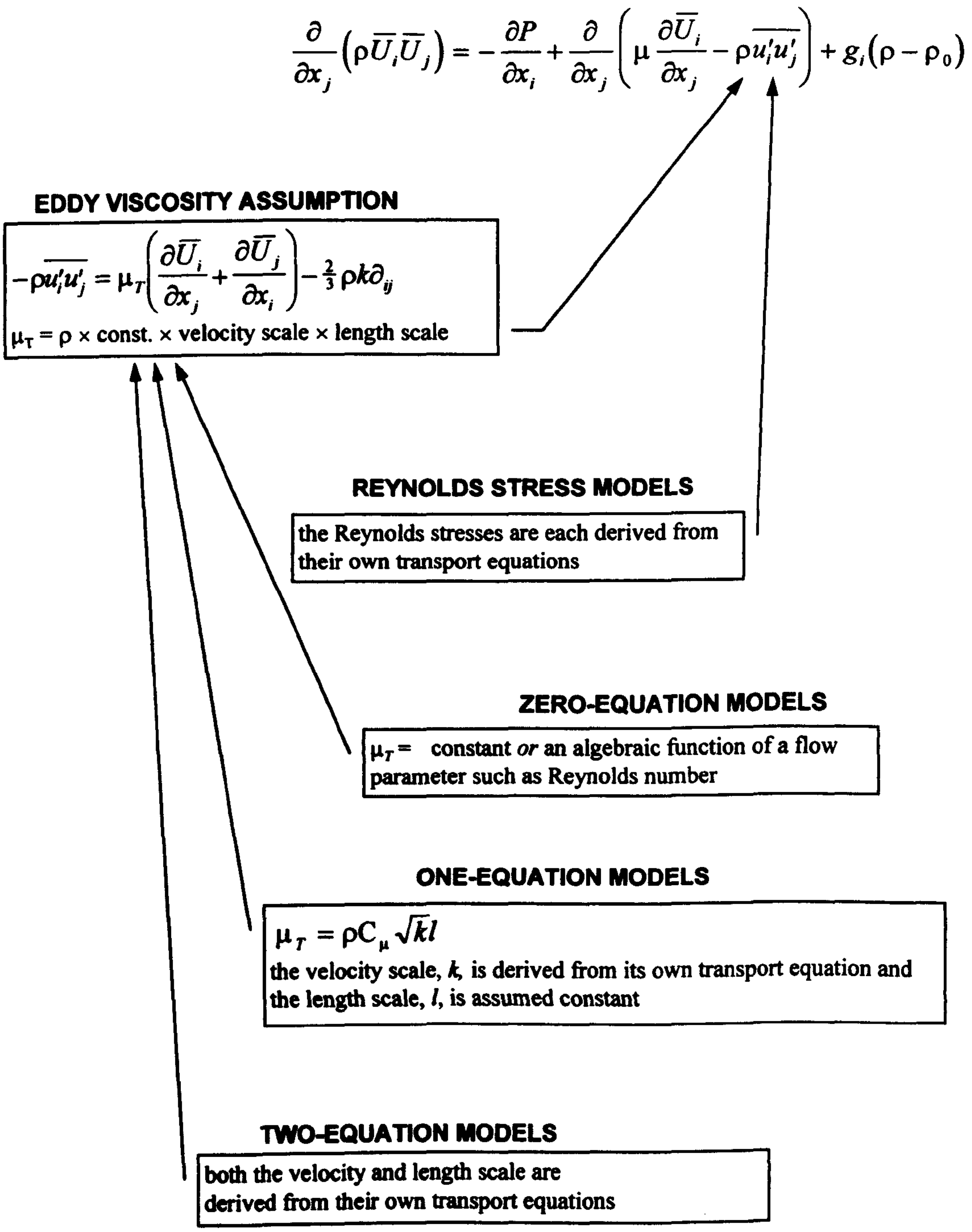

Figure 3.1 Tree of turbulence modelling.

At the centre of the zero-, one- and two-equation models lies the analogy that where a laminar stress exists, then so can an equivalent turbulent stress (i.e. Reynolds stress). A laminar shear stress is defined as:

$$\tau = \mu\left(\frac{\partial U_i}{\partial x_j} + \frac{\partial U_j}{\partial x_i}\right) \tag{3.11}$$

So if a fluid can have a laminar viscosity, μ, then a turbulent flow should have a turbulent or eddy viscosity, μ_T. So, by using this eddy viscosity hypothesis we can relate the Reynolds stress to the mean strain by:

$$-\rho\overline{u_i' u_j'} = \mu_T\left(\frac{\partial \overline{U}_i}{\partial x_j} + \frac{\partial \overline{U}_j}{\partial x_i}\right) - \tfrac{2}{3}\rho k \delta_{ij} \tag{3.12}$$

The main limitation imposed at this stage by Equation (3.12) is that the eddy viscosity is the same in all directions at any point. Now, where this may be true of laminar viscosity (being a property of the fluid) it may not be true of turbulent viscosity, which is effectively a property of the flow. Therefore, this eddy viscosity can have differing values in relation to differing Reynolds stresses. This occurs when the turbulence is said to be anisotropic. Conditions that cause anisotropy, and thus could invalidate the isotropic assumption of Equation (3.12), include streamline curvature, swirl, adverse pressure gradients, history effects and buoyancy. This fundamental limitation in the applicability of this model is discussed in Section 3.2.2.

The momentum equation, incorporating the new turbulent viscosity, can now be rewritten as:

$$\frac{\partial}{\partial x_j}\left(\rho\overline{U}_i\overline{U}_j\right) = -\frac{\partial P'}{\partial x_i} + \frac{\partial}{\partial x_j}\left(\mu_{eff}\frac{\partial \overline{U}_i}{\partial x_j}\right) + g_i\left(\rho - \rho_0\right) \tag{3.13}$$

where:

$$\mu_{eff} = \mu + \mu_T \tag{3.14}$$

and P' is a modified pressure defined by:

$$P' = P + \tfrac{2}{3}\rho k + \left(\tfrac{2}{3}\mu_{eff} - \zeta\right)\frac{\partial U_i}{\partial x_i} - \rho_0 \phi \tag{3.15}$$

In this case ζ is a bulk viscosity (which may be neglected for most Newtonian fluids) and ϕ is a gravitational quantity, such that:

$$\frac{\partial \phi}{\partial x_i} = g_i \tag{3.16}$$

All that remains now is try to calculate this eddy viscosity. Turbulence models that take this approach are called eddy viscosity or mean field closure models. Using dimensional analysis it is shown that:

$$\text{Eddy viscosity} = \rho \times \text{coefficient} \times \text{velocity scale} \times \text{length scale} \tag{3.17}$$

So calculation of a length and velocity scale leads to an eddy viscosity, which is then used directly in Equation (3.13). There are a number of methods to calculate the eddy viscosity.

The simplest is the zero-equation model. Here, the eddy viscosity is either set as constant throughout the flow or prescribed algebraically as a function of flow parameters such as Reynolds number. The other type of zero-equation model is the mixing length hypothesis put forward by Prandtl. Here a mixing length is prescribed, or again is a simple function of the flow geometry, which together with a velocity gradient gives the Reynolds stress. These types of models are rarely used in CFD today as more complex and accurate models can be efficiently utilised.

The next step up is a one-equation model. Here, a length scale is prescribed as in a mixing length zero-equation model but the velocity scale is taken to be the square root of the turbulent kinetic energy, k. To obtain k, a differential transport equation is used with k as the dependent variable. The transport equation can be derived exactly from the Navier–Stokes equations but simple approximations are used to obtain the modelled equation for k.

The final type of model in this branch is the two-equation model. A model of this type was used as one of the turbulence models employed in this study. The eddy viscosity is evaluated from the solution of two differential equations, one for k as in the one-equation model, and another for ε, the rate of dissipation of k. The latter is related to the length scale via $k^{2/3}$.

3.2.1.1 k–ε model

In this two equation model the eddy viscosity, using Equation (3.17), is defined as:

$$\mu_T = C_\mu \rho \frac{k^2}{\varepsilon} \tag{3.18}$$

The transport equations for k and ε are:

$$\frac{\partial \rho U_i k}{\partial x_i} = \frac{\partial}{\partial x_i}\left(\left(\mu + \frac{\mu_T}{\sigma_k}\right)\frac{\partial k}{\partial x_i}\right) + \mathbf{P} + \mathbf{G} - \rho\varepsilon \tag{3.19}$$

$$\frac{\partial \rho U_i \varepsilon}{\partial x_i} = \frac{\partial}{\partial x_i}\left(\left(\mu + \frac{\mu_T}{\sigma_\varepsilon}\right)\frac{\partial \varepsilon}{\partial x_i}\right) + C_1 \frac{\varepsilon}{k}\left(\mathbf{P} + C_3 \mathbf{G}\right) - C_2 \rho \frac{\varepsilon^2}{k} \tag{3.20}$$

where **P** is the shear production defined as:

$$\mathbf{P} = \mu_{eff} \frac{\partial U_i}{\partial x_j}\left(\frac{\partial U_i}{\partial x_j} + \frac{\partial U_j}{\partial x_i}\right) - \tfrac{2}{3}\frac{\partial U_i}{\partial x_j}\left(\mu_{eff}\frac{\partial U_i}{\partial x_j} + \rho k\right) \tag{3.21}$$

The second term in **P** is only present in compressible flows. **G** is the production of turbulence kinetic energy due to buoyancy, and is given by:

$$\mathbf{G} = -\frac{\mu_{eff}}{\rho\sigma_T} g_i \frac{\partial \rho}{\partial x_i} \tag{3.22}$$

When employing the Boussinesq approximation for buoyancy, Equation (3.22) can be rewritten as:

$$\mathbf{G} = \frac{\mu_{eff}}{\sigma_T} \beta g_i \frac{\partial T}{\partial x_i} \tag{3.23}$$

The empirical constants that this model uses are shown in Table 3.1.

Table 3.1 Values of the *k*–ε turbulence model constants

C_μ	0.09
C_1	1.44
C_2	1.92
C_3	1.0
σ_T	0.9
σ_k	1.0
σ_ε	1.217

3.2.1.2 RNG *k*–ε model

This model is a modification of the standard *k*–ε model using renormalisation group analysis of the Navier–Stokes equations. It is part empirical and part analytical. The only modifications are a modified term relating to the production of energy dissipation in the ε–equation and a different set of model constants. This RNG model is applicable to high Reynolds number flows. The new equations for *k* and ε become:

$$\frac{\partial \rho U_i k}{\partial x_i} = \frac{\partial}{\partial x_i}\left(\left(\mu + \frac{\mu_T}{\sigma_k}\right)\frac{\partial k}{\partial x_i}\right) + \mathbf{P} + \mathbf{G} - \rho\varepsilon \tag{3.24}$$

$$\frac{\partial \rho U_i \varepsilon}{\partial x_i} = \frac{\partial}{\partial x_i}\left(\left(\mu + \frac{\mu_T}{\sigma_\varepsilon}\right)\frac{\partial \varepsilon}{\partial x_i}\right) + \left(C_1 - C_{1\mathrm{RNG}}\right)\frac{\varepsilon}{k}\left(\mathbf{P} + C_3\mathbf{G}\right) - C_2\rho\frac{\varepsilon^2}{k} \tag{3.25}$$

The new constant $C_{1\mathrm{RNG}}$ is given by the equations:

$$C_{1\mathrm{RNG}} = \frac{\eta\left(1 - \eta/\eta_0\right)}{\left(1 + \beta\eta^3\right)} \tag{3.26}$$

and:

$$\eta = \sqrt{\frac{\mathbf{P}}{\mu}\frac{k}{\varepsilon}} \tag{3.27}$$

In this case η_0 and β are additional model constants, the latter not to be confused with the coefficient of thermal expansion. These new constants have the values 3.38 and 0.015, respectively.

3.2.1.3 Low Reynolds number *k*–ε model

Just as the RNG model is applicable to high-Reynolds number flows, this model has been derived for application at low-Reynolds numbers (Launder and Sharma 1974). Four modifications have been made to the *k* and ε equations. These are made to ensure a damping of the eddy viscosity when the local turbulent Reynolds number is low, a modification to the ε–equation to ensure that it goes to zero at the walls and also modifications of the source terms. The model should be used for flows with Reynolds numbers in the range of 5,000 to 30,000. The modified equations that make up this low Reynolds number flow are:

$$\mu_T = C_\mu f_\mu \rho \frac{k^2}{\varepsilon} \tag{3.28}$$

$$\frac{\partial \rho U_i k}{\partial x_i} = \frac{\partial}{\partial x_i}\left(\left(\mu + \frac{\mu_T}{\sigma_k}\right)\frac{\partial k}{\partial x_i}\right) + \mathbf{P} + \mathbf{G} - \rho\varepsilon - D \tag{3.29}$$

$$\frac{\partial \rho U_i \varepsilon}{\partial x_i} = \frac{\partial}{\partial x_i}\left(\left(\mu + \frac{\mu_T}{\sigma_\varepsilon}\right)\frac{\partial \varepsilon}{\partial x_i}\right) + C_1 \frac{\varepsilon}{k}\left(\mathbf{P} + C_3\mathbf{G}\right) - C_2 f_2 \rho \frac{\varepsilon^2}{k} + E \tag{3.30}$$

The additional functions are defined by:

$$f_\mu = \exp\left(-3.4 \Big/ \left(1 + {}^{R_T}\!/_{50}\right)^2\right) \tag{3.31}$$

$$f_2 = 1 - 0.3\exp\left(-R_T^2\right) \tag{3.32}$$

$$D = 2\mu\left(\frac{\partial \sqrt{k}}{\partial x_i}\right)^2 \tag{3.33}$$

$$E = 2\frac{\mu\mu_T}{\rho}\left(\frac{\partial^2 U_i}{\partial x_j \partial x_k}\right) \tag{3.34}$$

And the turbulent Reynolds number is given by:

$$R_T = \frac{\rho k^2}{\mu\varepsilon} \tag{3.35}$$

3.2.1.4 Differential flux model

When using a differential flux model (DFM) the turbulent viscosity hypothesis is discarded. Instead, each Reynolds stress and flux is determined from its own transport equation directly (the modelling of thermal turbulent fluctuations is covered in Section 3.2.1.5; this differential model is described as a flux model as it predicts both stresses *and* fluxes using differential transport equations). This enables anisotropic effects to be captured and so in theory at least, this type of model should be far superior to any two–equation model.

Whereas both laminar and turbulent viscosity were combined into an effective viscosity when using the *k*–ε model, the DFM neglects molecular stresses altogether and so the momentum equation becomes:

$$\frac{\partial}{\partial x_j}\left(\rho \overline{U}_i \overline{U}_j\right) = -\frac{\partial P}{\partial x_i} + \frac{\partial \rho \overline{u_i' u_j'}}{\partial x_j} + g_i\left(\rho - \rho_0\right) \tag{3.36}$$

Where the pressure is given in Equation (3.15). The transport equation for each individual Reynolds stress is:

$$\frac{\partial}{\partial x_i}\left(\rho U_i \overline{u_i' u_j'}\right) = \frac{\partial}{\partial x_i}\left(\rho \frac{C_S}{\sigma_{DS}} \frac{k}{\varepsilon} \overline{u_i' u_j'} \frac{\partial \overline{u_i' u_j'}}{\partial x_j}\right) + \mathrm{P} + \mathrm{G} + \phi - \tfrac{2}{3}\rho\varepsilon \mathrm{I} \tag{3.37}$$

P is the shear stress production term and G is the buoyancy stress production term given by:

$$P = -\rho\left(\overline{u_i'u_j'}\frac{\partial \overline{U_j}}{\partial x_j} + \overline{u_i'u_j'}\frac{\partial \overline{U_i}}{\partial x_i}\right) \tag{3.38}$$

and:

$$G = -\rho\beta\left(g_j\overline{u_i h} + g_i\overline{u_j h}\right) \tag{3.39}$$

The pressure–strain correlation, ϕ, is given by:

$$\phi = \phi_1 + \phi_2 + \phi_3 \tag{3.40}$$

where:

$$\phi_1 = -\rho C_{1S}\frac{\varepsilon}{k}\left(\overline{u_i'u_j'} - \tfrac{2}{3}kI\right) \tag{3.41}$$

$$\phi_2 = -C_{2S}\left(P + \tfrac{2}{3}I\rho\overline{u_i'u_j'}\frac{\partial \overline{U_i}}{\partial x_j}\right) \tag{3.42}$$

and:

$$\phi_3 = -C_{3S}\left(G + \tfrac{2}{3}I\rho\beta g_i\overline{u_i h}\right) \tag{3.43}$$

As the dissipation of turbulence energy appears in Equation (3.37) it too has to be modelled. A slightly different equation than that adopted in the k–ε model (Equation 3.20) is used here. It now has the form:

$$\frac{\partial \rho U_i \varepsilon}{\partial x_i} = \frac{\partial}{\partial x_i}\left(\rho \frac{C_S}{\sigma_\varepsilon}\frac{k}{\varepsilon}\overline{u'_i u'_j}\frac{\partial \varepsilon}{\partial x_i}\right) + C_1\frac{\varepsilon}{k}\left(P + C_3 G\right) - C_2 \rho \frac{\varepsilon^2}{k} \qquad (3.44)$$

The empirical constants used in the differential stress transport equations are shown in Table 3.2.

Table 3.2 Differential stress transport equation constants

C_μ	0.09
C_1	1.44
C_2	1.92
C_3	1.0
C_{1S}	1.8
C_{2S}	0.6
C_{3S}	0.5
C_S	0.22
σ_T	0.9
σ_k	1.0
σ_ε	1.375
σ_{DS}	1.0

3.2.1.5 Modelling of Reynolds fluxes

So far, only the calculation of the Reynolds stress components has been discussed. The approach taken to model the Reynolds fluxes is analogous to the approach for the stresses. The simplest way, as in the gradient hypothesis of Equation (3.12), is to relate the Reynolds flux to an appropriate gradient with the necessary proportionality term. As it is conjectured that there is an eddy viscosity which links the mean strain with the Reynolds stresses, so there is an eddy diffusivity that relates the mean temperature gradients to the Reynolds fluxes. This relationship is written as:

$$-\rho\overline{u'_i h'} = \Gamma_T\left(\frac{\partial \overline{T}}{\partial x_i}\right) \qquad (3.45)$$

Here, Γ_T is the eddy diffusivity and is prescribed by:

$$\Gamma_T = \frac{\mu_T}{\sigma_T} \tag{3.46}$$

where σ_T is the turbulent Prandtl number, the ratio between eddy viscosity and eddy diffusivity. As both stresses and fluxes are assumed to be diffused by the same mechanisms then the turbulent Prandtl number is prescribed as a constant. It is this relationship (Equations 3.45 and 3.46) that is used when modelling the Reynolds fluxes in conjunction with the k–ε model.

When the DFM is used the Reynolds stresses are derived from their own differential transport equations, as are the Reynolds fluxes. The form of the transport equation for the fluxes is much the same as the transport equations we have encountered so far:

$$\frac{\partial \rho U_i \overline{u_i' h'}}{\partial x_i} = \frac{\partial}{\partial x_i}\left(\rho \frac{C_S}{\sigma_{DF}} \frac{k}{\varepsilon} \overline{u_i' u_j'} \frac{\partial \overline{u_i' h'}}{\partial x_j}\right) + P_F + G_F + \pi \tag{3.47}$$

P_F and G_F are the mean field and buoyancy production, respectively. P_F is defined by:

$$P_F = -\rho\left(\overline{u_i' u_j'} \frac{\partial \overline{H}}{\partial x_i} + \overline{u_i' h'} \frac{\partial \overline{U_i}}{\partial x_i}\right) \tag{3.48}$$

and G_F by:

$$G_F = -\frac{\beta}{C_P} \overline{h'^2} \tag{3.49}$$

The pressure–scalar gradient term, π, is written as the sum of the three terms

$$\pi = \pi_1 + \pi_2 + \pi_3 \tag{3.50}$$

where:

$$\pi_1 = -\rho C_{1F} \frac{\varepsilon}{k} \overline{u_i' h'} \tag{3.51}$$

$$\pi_2 = \rho C_{2F} \overline{u_i' h'} \frac{\partial \overline{U}_i}{\partial x_j} \tag{3.52}$$

and:

$$\pi_3 = -C_{3F} G_F \tag{3.53}$$

The enthalpy correlation, $\overline{h'^2}$, appearing due to buoyancy effects in Equation (3.49), requires a further transport equation to be used, thus closing the equation set:

$$\frac{\partial \rho U_i \overline{h'^2}}{\partial x_i} = \frac{\partial}{\partial x_i}\left(\rho \frac{C_S}{\sigma_{HF}} \frac{k}{\varepsilon} \overline{u_i' u_j'} \frac{\partial \overline{h'^2}}{\partial x_j} \right) + P_h - \rho \frac{\overline{h'^2}}{k R_F} \varepsilon \tag{3.54}$$

where the production term is:

$$P_h = -2 \rho \overline{u_i' h'} \frac{\partial H}{\partial x_i} \tag{3.55}$$

The empirical constants used in the Reynolds flux transport equations are shown in Table 3.3.

Table 3.3 Differential flux transport equation constants

R_F	0.5
σ_{DF}	1.467
σ_{HF}	2.0
C_{1F}	3.0
C_{2F}	0.5
C_{3F}	0.33

3.2.1.6 Modelling of turbulence due to buoyancy

Buoyant effects are present in many engineering and environmental applications. It is therefore important to understand how buoyancy modifies not only the velocity field (as seen in the body force term in the momentum Equation 3.6), but also the turbulence field. This section will briefly identify the terms introduced into the turbulence modelling equations that account for the effects of buoyancy.

Normally it is found that a strain of some sort is instrumental in producing turbulence. When buoyant effects are present, it is a density gradient that gives rise to turbulence production and subsequent increase in mixing. This can be clearly seen in Equation (3.22). A negative sign implies that for stable stratification (i.e. density decreases in the opposite direction in which gravity acts) turbulence is damped. Unstable stratification (i.e. a lower density area lying beneath a high-density region), especially in steady state, has higher turbulence levels associated with it. In the ε transport equation (Equation 3.20) the production of k due to buoyancy is linked to the production of ε via a constant C_3. The effect of including or omitting this increase in production of ε is covered in Section 5.2.2.

When using the DFM the same treatment for buoyancy is applied. Now, however, buoyancy is responsible for the increase in the individual Reynolds stress components. Equation (3.39) is much like Equation (3.22); the density gradient (actually a temperature gradient when employing the Boussinesq approximation as seen in Equation 3.23) is replaced by the Reynolds flux component associated with the direction in which gravity acts, and so includes any directional effects that the buoyancy is responsible for.

In non-isothermal flows turbulence is not solely quantified by the Reynolds stresses. Reynolds fluxes are even more indicative of the level of mixing between 'hot' and 'cold' fluids. Buoyancy itself increases these Reynolds fluxes directly. This is seen in Equation (3.47) through the action of the production term G_F. It is due to this term that yet another transport equation is required to model the variance $\overline{h'^2}$.

The final effect that buoyancy has on turbulence levels is via the pressure–strain correlations in the Reynolds stress and flux transport equations (Equations 3.43, 3.54).

3.2.2 Discussion of governing equations

The three basic time–averaged governing equations of the conservation of mass, momentum and thermal energy (Equations 3.5, 3.6 and 3.7, respectively) are all theoretically derived. As long as the assumptions on which they were derived are not contradicted, no errors will be introduced by their use. This does not hold true for the more empirical turbulence modelling equations. They are either derived using relationships that have analogies with differing flow conditions or rely heavily on empirically determined coefficients or both! In high-Reynolds number flows, where turbulence plays such a dominant role, it is imperative that the strengths and failings of the methods by which turbulence is modelled are covered.

As mentioned already, the main assumption of zero–, one– and two–equation models is that they all rely on the assumption of the existence of an eddy viscosity. This eddy viscosity is assumed to be a property of the flow and so can vary from point to point. It is also treated as a scalar; Equation (3.12) has the same eddy viscosity for all Reynolds stresses. The debate at this point is whether the laminar analogy that has been made is merited or not. The fact that dimensionally the two relationships, Equations 3.11 and 3.12, are equal does not ensure that the analogy is justified. There is also the concept of a negative eddy viscosity. Turbulence energy can, under special circumstances, be transferred to larger length scales, resulting in a negative energy dissipation. This is something that the eddy viscosity assumption does not take into account. Beyond the eddy viscosity argument lies the problem of the determination of μ_T. The form of the relationship of Equation (3.18) is again dimensionally determined, but it is at this stage that empirical coefficients begin to be introduced. When these coefficients are used the entire relationship could be restricted to the flow conditions under which they were measured. The next level of uncertainty comes from the transport equations which are used to determine the variables that define μ_T. Although the transport equation for k can be derived quite readily from the mechanical energy equation, the equation for ε is a little more problematic. Although it can be derived exactly, it is extremely complex and contains many unknown and almost unmeasurable terms. The form of the ε–equation is therefore modelled on that for k. In all, the k–ε model contains five empirical coefficients. They have been determined from experimental data and also from computer optimisation. However, for flows that are similar to those used for the determination of the coefficients, and which obey the isotropic assumption of a scalar eddy viscosity, the k–ε model performs adequately.

The differential flux model is, in theory, much more advanced than any two–equation model. An exact transport equation can be derived (again from the Navier–Stokes equations) for each individual Reynolds stress. The terms for the convection and production of the stresses can be readily calculated. The remaining five terms, describing diffusion, redistribution and dissipation of the Reynolds stresses, pose unknown correlations that must themselves be modelled to close the equation set. This introduces a further six coefficients. These constants are determined from experiments, including:

- return to isotropy of grid generated turbulence;
- response of isotropic turbulence to sudden distortion;
- homogeneous free shear flow data;
- equilibrium free shear flows;
- shear-stress collapse in a stably curved layer;
- computer optimisation.

It could be argued that a DFM is just as limited to certain applications as the k–ε model with respect to the determination of these coefficients. This, however is outweighed by the more analytical derivation of the form of the transport equations themselves. The fact that each Reynolds stress and flux is determined from its own equation allows the solution to become anisotropic under the appropriate conditions. It is this freedom of the DFM that makes its choice more attractive, or even necessary, for so-called complex flows.

The problems of efficiency and solution stability should not be overlooked. The k–ε model has two differential equations to calculate the eddy viscosity whereas a DFM has eleven to obtain the stresses and fluxes directly (six for the stresses, three for the fluxes, one for ε and one for $\overline{h'^2}$). One of the main problems this introduces is the need for vastly increased computer memory capacity. Looking at it another way, for a given computer memory size, use of a DFM would limit the complexity of the geometry to be modelled, possibly to an unacceptable level. Another negative aspect of the DFM is its sensitivity during the solution procedure. The solution procedure (covered in Section 3.5) is iterative in nature. Using the equations found in the DFM, many of them linked, can easily result in the divergence and collapse of the solution procedure altogether. At best, convergence of the solution will take much longer when compared to the relatively stable k–ε model.

3.3 DISCRETISATION OF THE GOVERNING EQUATIONS

Although the equations defined in the preceding section are closed, they cannot be solved directly. To do so, we turn to numerical methods. All the equations are derivative in nature. By integrating them over a small or finite volume we can determine how much each variable changes over that volume. If we know the value of the variables at the limits of the solution domain then, using this form of integration (discretisation), we can ascertain their values within the domain. So, by starting with the governing equations, fixing variables at the solution domain boundary (boundary conditions), beginning with an initial guess of values at each cell (initial condition), and then integrating the equations over many adjacent finite volumes (grid), we obtain a converged solution field for each variable. The process of integrating the governing equations is covered below.

3.3.1 Basic principles of the finite volume method

The governing equations must be integrated over a grid of adjacent finite volume cells or 'bricks'. Previously, it has been common to use what is known as a staggered grid. An example of this can be seen in Figure 3.2.

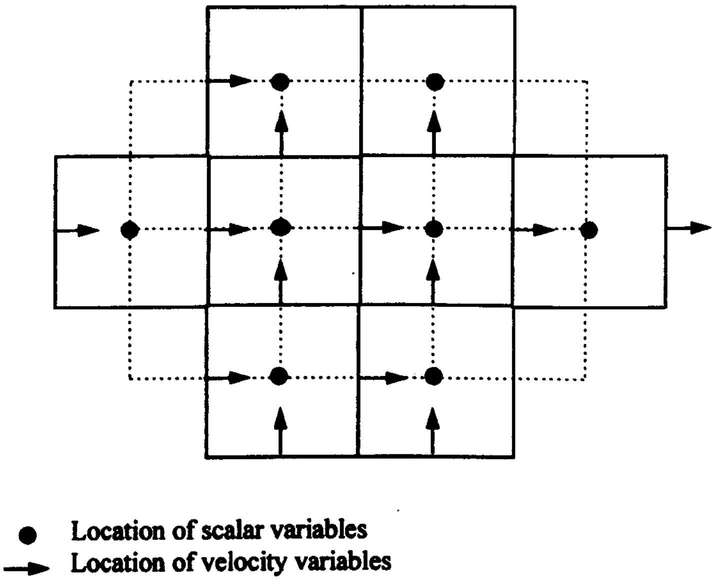

Figure 3.2 Staggered grid array.

Here, we see that all scalar variables are stored at the centre of each cell, or rather the scalar variable has the same value throughout all of that cell. The vector variables are stored on the centre of each face of the cell so that fluxes flowing through the cell can be calculated directly. This results in four grids: one for scalars and three for the velocities. Heavy memory requirements are therefore made on the computer. With a staggered grid there also exists complications in accurately gridding complex geometries. To overcome these problems a non-staggered approach is taken in this study (Figure 3.3). With a non-staggered grid all scalars and variables are stored on a single grid at the centre of each cell. The process by which velocities are extrapolated to the cell faces for flux calculations is covered in Section 3.3.5. This approach enables accurate gridding of complex geometries with efficient use of memory capabilities.

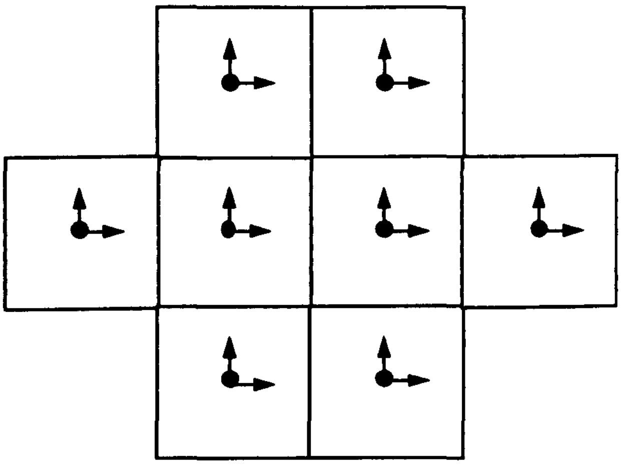

Figure 3.3 Non-staggered grid array.

It is not wise to grid an entire solution domain uniformly. In regions where there are high variable spatial gradients it is essential to have a high grid density of cells so as to 'capture' this gradient. If a gradient exists, but there is only a coarse grid present, then a numerical error called numerical diffusion is likely to occur. This has the effect of smoothing out, or diffusing, any large local variable peaks. The result can be an overestimation of a variable in places or an underestimation where there should be a high value. To ensure that there are none of these grid dependent errors, a grid sensitivity test should be conducted. Here, the number of cells in the domain is raised continuously until such time as the variables (or at least those variables of interest) cease to vary at any point upon further cell density increases. This form of test is described in Section 4.3.3.6.

Once the solution domain has been gridded then each governing equation must be integrated over each cell. Only when the laws of conservation, as well as the turbulent transport equations, are satisfied at each cell (to within a tolerable degree) is the solution complete.

For simplicity of coding, all the governing equations are organised into a similar form. This generic form can be written as:

$$\frac{\partial \rho \overline{U_i} \phi}{\partial x_i} - \frac{\partial}{\partial x_i}\left(\Gamma \frac{\partial \phi}{\partial x_j}\right) = S \tag{3.56}$$

The first term represents the convection of any variable, ϕ, by the mean fluid velocity, $\overline{U_i}$; the second term represents diffusion where Γ is the diffusion coefficient; and the third term is a source or sink term where ϕ is either created or destroyed. When integrating over a control volume we obtain:

$$\int \rho \phi \overline{U_i} . \mathbf{n} dA - \int \Gamma \frac{\partial \phi}{\partial x_j} . \mathbf{n} dA = \int S dV \tag{3.57}$$

The calculation of these integrals is the centre of the discretisation process. Figure 3.4 shows a single orthogonal cell and some of its neighbours. With a non-staggered grid all variables are stored at the centre of the cell at point P. Neighbouring points include points E, W, WW, etc. In the schemes that follow a lower case subscript (n, e, s, w) refers to values at the appropriate face whereas an upper case subscript (N, E, S, W) refers to values at the appropriate cell centres.

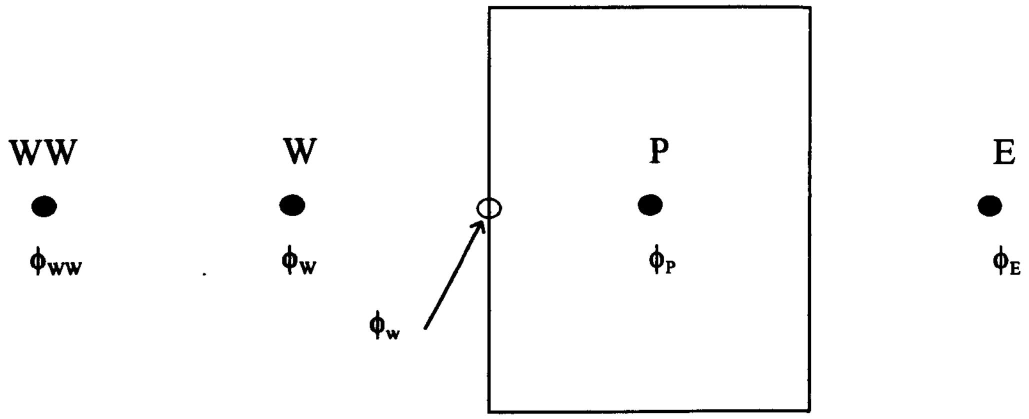

Figure 3.4 Control volume notation.

Discretisation over the cell results in the formulation of the finite volume equation:

$$a_P\phi_P = \sum_{nn} a_{nn}\phi_{nn} + S \tag{3.58}$$

The coefficients (a_P etc.), that express the contribution of convection and diffusion across the cell boundaries, are called matrix coefficients. Each matrix coefficient is composed of a contribution from the diffusive term and one from the convective term. How each coefficient is derived is now explained.

3.3.2 Treatment of the diffusion terms

The diffusion term is the simplest to integrate. By looking at the diffusive flux at the west face of the cell we can write:

$$\int \Gamma \frac{\partial \phi}{\partial x_j}.\mathbf{n}dA = \frac{\Gamma A_w}{h_w}(\phi_P - \phi_W) \tag{3.59}$$

Where h_w is the height of the west face of the cell. Equation (3.59) can be rewritten as:

$$\frac{\Gamma A_w}{h_w}(\phi_P - \phi_W) = D_W(\phi_P - \phi_W) \tag{3.60}$$

Such that D_W is the west-face diffusion coefficient. There is a diffusion coefficient for each face of the cell.

3.3.3 Treatment of the convective terms

The integration of the convective (sometimes referred to as advective) term can be accomplished by a wide variety of methods. The more accurate methods often tend to be slower and less robust during the solution process. In this study a choice of three methods were chosen for the integration of this term. All the schemes require calculation of the variable at the face in question (unlike treatment for the diffusive term which relies purely on a difference between cell centres). This is because each convective term requires the normal velocity at the face in question.

3.3.3.1 The 'hybrid' scheme

This scheme is a combination of two separate methods; upwind differencing and central differencing. When using upwind differencing, the value of the variable ϕ at the west face of the cell (ϕ_w) is taken to be the same as the value at the upstream point W (ϕ_W) (for the case where the flow is from west to east). So, if we integrate over the west face:

$$\int \rho\phi\overline{U_i}.\mathbf{n}dA = \rho\overline{U_w}A_w\phi_W \equiv C_W\phi_W \tag{3.61}$$

Where C_W is the convection coefficient at the west face. Again, there are coefficients for each face of the cell though they can be either positive or negative depending on the direction of the flow.

Central differencing is the most obvious discretisation for the convection term. Looking again at the west face:

$$\int \rho\phi\overline{U_i}.\mathbf{n}dA = \rho\overline{U_w}A_w\tfrac{1}{2}\left(\phi_W + \phi_P\right) \tag{3.62}$$

The hybrid scheme consists of the use of central differencing if the cell Peclet number is less than 2.0, otherwise it uses upwind differencing but ignoring the diffusive term. This scheme can therefore be either second-order accurate or first-order accurate, respectively. The matrix coefficient, *a* (in Equation 3.58), is defined as:

$$a_W = \max\left(\tfrac{1}{2}C_W, D_W\right) + \tfrac{1}{2}C_W \qquad (3.63)$$

3.3.3.2 The QUICK scheme

This is a third order accurate upwind scheme. This scheme, instead of using only the immediate neighbouring points, uses two upstream and one downstream point:

$$\int \rho\phi\overline{U_i}.\mathbf{n}dA = \rho\overline{U_w}A_w\left(\tfrac{3}{8}\phi_P + \tfrac{3}{4}\phi_W - \tfrac{1}{8}\phi_{WW}\right) \qquad (3.64)$$

Again, the matrix coefficient at this face is defined as:

$$a_W = \tfrac{5}{8}\max\left(C_W, 0\right) + \tfrac{1}{8}\max\left(C_E, 0\right) + D_W \qquad (3.65)$$

3.3.3.3 The CCCT scheme

This scheme is a bounded form of the standard QUICK scheme. For continuity we look again at the integration over the west face:

$$\int \rho\phi\overline{U_i}.\mathbf{n}dA = \rho\overline{U_w}A_w\left(\left(\tfrac{3}{8} - \alpha\right)\phi_P + \left(\tfrac{3}{4} + 2\alpha\right)\phi_W - \left(\tfrac{1}{8} + \alpha\right)\phi_{WW}\right) \qquad (3.66)$$

The term α depends on the curvature of the variable ϕ.

3.3.3.4 Discussion of discretisation techniques

The above three methods each have their own strengths and failings. The hybrid scheme is simple and very robust. A converged solution can be reached quickly thus relaxing the requirements on computer resources. However, when the cell Peclet number exceeds 2.0, i.e. when convection dominates diffusion, and first-order accurate upwind differencing is used, the results can suffer from numerical, or false, diffusion due to the inability of this first-order scheme to capture any high gradients. This problem also occurs when the main flow is skewed with respect to the grid alignment, which lessens the dominance of 'upstream' effects.

To overcome these low-order accuracy problems of the hybrid scheme the QUICK scheme can be used. As it is third-order accurate it is capable of capturing a much steeper gradient on an equivalent grid. However, as a side effect, this unbounded scheme can suffer from overshoots or undershoots. This is where the gradient itself is captured, but at either end of this slope the QUICK scheme overpredicts or underpredicts (depending on which 'end' of the gradient we refer to) the value of the variable. This may not be too serious if the overshoot is only a small percentage of the variable value or difference in the variable across the gradient. However, when negative values are predicted of variables that can only be positive this overshooting can give rise to unrealistic or impossible results. This can happen with turbulence kinetic energy, k, or its rate of dissipation, ε. Undershooting of k or ε can either produce results that are meaningless or even cause the solution process to diverge.

So, to overcome the problems associated with the QUICK scheme, the CCCT scheme can be employed. The CCCT scheme is a modification of the standard QUICK scheme. The CCCT scheme is said to be bounded, i.e. the overshoots found when using QUICK are truncated by CCCT. Out of all three schemes this one is the least stable. Although a converged solution will be obtained it will take much longer than with QUICK which in turn takes much longer than the hybrid scheme. To overcome any numerical diffusion errors the grid density can either be increased so as to minimise the problem associated with lower-order schemes, or a higher order scheme can be used, which in turn is less stable. The former case will increase memory requirements whilst the latter will increase convergence time. In this respect it can be argued that the computer resources play an important role in the choice of CFD model parameters.

All the above discretisation theory is applicable to simple orthogonal grids. When using body fitted grids (bfg) the cells no longer have simple 90° vertices. BFGs enable gridding of very complex geometries including curves and slopes. Therefore, the whole process of calculating fluxes, diffusion and convection coefficients becomes much more involved. The theory of the transformation from simple Cartesian systems to general curvilinear ones is covered in CFDS-FLOW3D (1994).

3.3.4 Procedure for the derivation of pressure

Although the governing equation set is now closed, there is no obvious method for the derivation of pressure. Pressure does not have an equation of its own, so to speak. The SIMPLE (Semi-implicit method for pressure-linked equations) pressure correction algorithm (Patankar & Spalding 1972) is therefore used. Pressure is obtained via an iterative method within the main solution process itself. The following equations relate to the simple orthogonal grids. Again, the extension to non-orthogonal bfgs is not covered here for the purposes of simplicity.

There are two steps in the pressure correction process. The first is the predictor step. The momentum equation, when applied to the east face of a control volume at any given stage in the solution, can be written as:

$$a_e U_e^* = \sum a_m U_m^* + A_e \left(P_P^* - P_E^* \right) + S_e \tag{3.67}$$

Note that this equation is used iteratively in the solution process. It would be justified to assume that the problem has not yet converged during the solution process so a new pressure and velocity field is required, e.g.:

$$\begin{aligned} P^{**} &= P^{*} + P' \\ U^{**} &= U^{*} + U' \end{aligned} \qquad (3.68)$$

The first terms are the updated fields, the second terms are the present fields and the final terms are the differences needed to conserve mass continuity. The updated fields also obey the momentum equation:

$$a_e U_e^{**} = \sum_{nn} a_{nn} U_{nn}^{**} + A_e \left(P_P^{**} - P_E^{**} \right) + S_e \qquad (3.69)$$

Within the method for calculation of the neighbouring velocity in Equation (3.69) lies the difference between SIMPLE and SIMPLEC. The velocity is approximated by:

$$U_{nn}^{**} = U_{nn}^{*} + \alpha \left(U_P^{**} - U_P^{*} \right) \qquad (3.70)$$

where $\alpha = 0$ for SIMPLE and $\alpha = 1$ for SIMPLEC (the latter used in this study). By subtraction of Equation (3.69) from Equation (3.67) we obtain:

$$a_e U_e' = \sum_{nn} a_{nn} U_{nn}' + A_e \left(P_P' - P_E' \right) \qquad (3.71)$$

For nearly orthogonal grids, the off-diagonal components (i.e. the contributions from diagonally neighbouring cells) can be ignored. Hence, the algorithm is semi-implicit. Assuming that the corrected fields do actually satisfy continuity, we can write:

$$a_P P_P' = \sum_{nn} a_{nn} P_{nn}' + m_P \qquad (3.72)$$

where:

$$a_P = \sum_{nn} a_{nn} \tag{3.73}$$

and the mass source residual for the cell:

$$m_P = -C_u^* + C_d^* - C_n^* + C_s^* - C_e^* + C_w^* \tag{3.74}$$

Where C^* is the mass flow through the cell face. The second stage is called the corrector step. Here, we first correct for pressure by using:

$$P_P^{**} = P_P^* + \alpha_P P_P' \tag{3.75}$$

The α term is called an under-relaxation factor and is used to introduce the modified variable slowly (i.e. $0.0 < \alpha < 1.0$) to ensure stability. Secondly, we correct for the velocities in a similar fashion. Ultimately, the problem will converge when the mass source residual of Equation (3.74) reaches a tolerably small value.

3.3.5 Rhie-Chow interpolation

The use of non-staggered grids means that all variables, both scalar and vector, are located at the centre of each cell. It is necessary to obtain the normal velocity at a cell face for calculation of the convection coefficients and mass source terms used during the pressure correction procedure. Instead of using weighted linear interpolation, which leads to the well-known checkerboard oscillations in pressure and velocity, a modified momentum equation is used. This is procedure is called the Rhie-Chow interpolation method (Rhie & Chow 1983).

3.4 BOUNDARY CONDITIONS

Just as the equation set must be closed, so must the grid be to enable solving. This means that values at the edge of the grid must either be prescribed or a method given for their calculation. These so-called boundary conditions are critical because, as they are set, they have a very strong influence on the solution within the domain itself. There are different kinds of boundary conditions available according to where the boundary lies. All the conditions used in this study are detailed in the following sections.

3.4.1 Near wall treatment

At a solid–fluid boundary the fluid velocity is zero with respect to the wall. How the fluid velocity changes from zero at the wall to the free-stream value introduces complications. Within this wall boundary layer there are many complex mixing processes present. There are two methods for predicting the flow field in this region.

3.4.1.1 Wall function method

It has been found that the variation in velocity with vertical distance from the wall in a boundary layer follows a self-similar non-dimensional shape. This is shown in Figure 3.5. By looking at the relationship between these non-dimensional terms, u^+ and y^+, we see that there is an area within the boundary layer where u^+ is some function of the log of y^+. This is called the logarithmic region. This relationship takes the form:

$$u^+ = \frac{1}{\kappa}\ln\left(\mathrm{E}y^+\right) \text{ for } y^+ > y_0^+ \qquad (3.76)$$

This is true for y^+ values above 11.23 (y_0^+) and less than 1000. The constant E, empirically derived, has the value 9.793. So, by knowing the height from the wall of the first grid cell the velocity can then be calculated. From here on into the solution domain, the momentum equation is used to calculate the velocity. The value of turbulent kinetic energy is solved, using the k transport equation in the k–ε model, at the grid cell nearest to the wall and then the energy dissipation is given by:

$$\varepsilon = \frac{C_\mu^{3/4} k^{3/2}}{\kappa y} \tag{3.77}$$

It is critical to keep the grid cells nearest the walls at a y^+ value within the range 11.23–1000 for the assumption that this wall function relies on to be valid. Near-wall velocities will be overestimated if the first cell lies beyond a y^+ value of 1000.

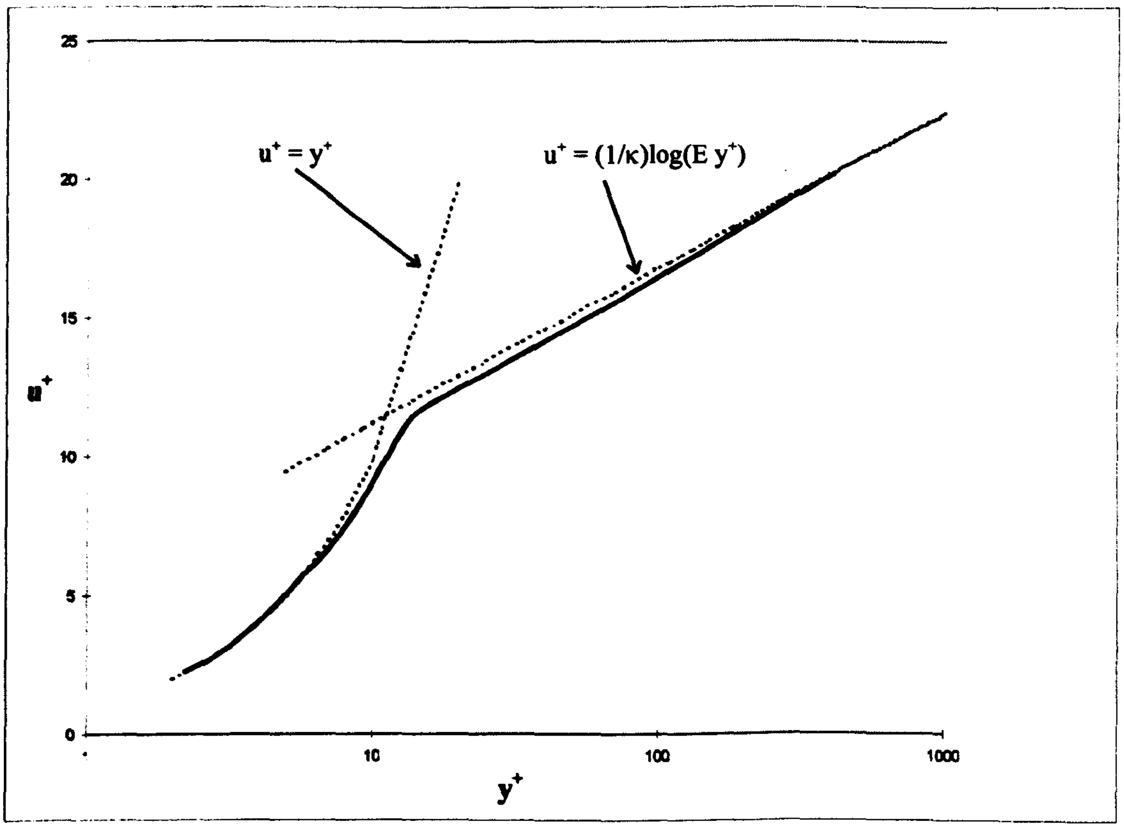

Figure 3.5 Schematic graph of a wall boundary layer.

3.4.1.2 Low–Reynolds number near-wall approach

When using the low-Reynolds number k–ε model there is no assumption made about the shape of the wall boundary layer. Instead, the governing equations are integrated directly to the wall, through the boundary layer. By doing this, however, a very fine grid density is needed to capture the high gradients encountered in this region. All regions of the boundary layer must be captured and the nearest grid cell must be no more than $y^+ = 1$ from the wall.

3.4.2 Symmetry plane

In the majority of cases where physical symmetry exists in a solution domain, a computational symmetry can also be applied. This means that only 50% of the domain needs to be gridded, thus offering a massive saving on computer memory requirements. There are cases, such as vortex shedding from a cylinder and other transient states, where although physical symmetry exists, computational symmetry does not. The symmetry boundary condition acts like a computational mirror. The main effect is that no flux crosses this plane. To implement this, and other boundary conditions, a row of dummy cells is defined on the outer edge of the solution domain. All variables are mathematically symmetrical across the plane (i.e. the value within the dummy cell assumes the value of its neighbouring cell within the domain). The component of velocity normal to the symmetry boundary and the component of the Reynolds shear stress and Reynolds flux involving this normal velocity component are both anti-symmetrical (i.e. the value within the dummy cell assumes the negative value of its neighbouring cell within the domain).

At the symmetry boundary all variable gradients are normal to the symmetry plane. There are two conditions where this is true. The first is, as already mentioned, at a physical symmetry plane. The second is in a region of homogeneous flow. Here, there are no changes across the plane. This is true at or above the top of a boundary layer or even vertically within a boundary layer as long as there are no end effects present. Thus, if the plane of symmetry is positioned in or near an area of gradient, then an error would be introduced at the boundary that could affect the results well into the domain itself.

3.4.3 Inlet plane

At an inlet plane values for variables at an edge of the domain are prescribed exactly. All variables are specified except for pressure, which is extrapolated from downstream. Variables can either have a 'top-hat' profile where they are constant across the inlet boundary or a FORTRAN user routine can be implemented to prescribe a more complex inlet profile.

3.4.4 Mass-flow boundary

This boundary condition is used where fluid exits the domain. In this study a Neumann boundary condition is used. Just as continuity is assured through each cell, the mass flow boundary condition ensures that mass conservation is obtained throughout the entire domain. There are three stages in implementing this condition:

1 The velocity field is normalised to the exit plane thus all components of velocity parallel to the plane are set to zero.

2 The discrepancy between the actual mass flow rate out of the domain and the desired flow rate (the sum of all inlet mass flow rates) is calculated.

3 An increment is added to all normalised velocities at outlet faces to force outlet mass flow to the desired value.

Stage one introduces an error itself. By normalising the velocities at the mass–flow plane we are forcing fully-developed conditions upon the flow. Where this may be valid, or already exists, e.g. at the end of an exit duct or after a long period of development, it is not the case within regions of undeveloped flow. These include regions of recirculation, sudden expansion, etc.

3.5 SOLUTION OF THE DISCRETISED EQUATIONS

Having covered the derivation of all linearised equations from the governing partial differential equations, the process by which they are solved will now be explained. As already mentioned, an iterative process is used, starting from an initial estimate of the values of all variables at each cell through to the converged solution where the final values obey their respective conservation equations to within an acceptable degree of accuracy.

3.5.1 Solution procedure

The solution process consists of two loops. An initial guess or initial condition is taken for the values of all variables at each cell. The two loops are then iterated in a nested manner. The inner loop solves the linearised equations for each variable in turn at each cell assuming all other fields are fixed. The outer loop involves updating all variable fields with the values calculated in the inner loop. As this process progresses, the flow field approaches its final or converged state. The iterative process stops when the error in global mass continuity in the entire flow field reaches an acceptably small value. A detailed understanding of this process is essential for 'tweaking' of solution parameters so as to ensure quick and efficient convergence.

3.5.1.1 The inner iteration

The inner iteration consists of taking each variable in turn, whilst assuming all the others to be fixed, and passing the relevant equations for each cell to iterative linear equation solvers. All updated variable values are not passed on to the other linearised equations until the completion of the inner loop. It is within the outer loop that this takes place.

There are a number of solution methods for each variable. These are listed in Table 3.4.

Table 3.4 Equation Solvers

U, V, W	Stone
P	ICCG
H	Stone
All Reynolds stresses, fluxes, k and ε	Line relaxation

It is useful to visualise each cell having a set of equations for each variable associated with it. Stone's method takes all the equations for the variable in question, for every cell in the domain, and collects them into a large matrix. It is this matrix that is solved in an iterative way. The line relaxation solver takes only a single line of cells at a time. A matrix with all the equations for the present variable at each of the cells in the line is formed and solved directly. The line then moves one cell location in a predetermined direction (set to be in the same direction as the main flow) and the process is repeated. This can be called an iterative method also as the line sweep up and down the domain.

At some point the iterative process must be terminated so that the inner iteration can proceed onto the next variable. There are two ways by which to stop the inner iteration for each variable. The first is by setting sweep information. This is easiest to visualise with the line relaxation method. A minimum and maximum number of sweeps can be set for each variable. This forces there to be at least a set number of sweeps, but which are not repeated indefinitely. The second, and more sound method, is by setting a residual reduction factor. Each variable at each cell during the solution process does not satisfy its respective conservation law, i.e. the amount by which the linear equation is not satisfied. By summing all these residuals for each cell we obtain the total amount by which the equations are not satisfied. The residual reduction factor ensures that the sweeping takes place until the sum of the residuals for each variable has been cut by the reduction factor itself (0.0 < reduction factor < 1.0). This is a more realistic way with which to stop the inner loop. Therefore, the number of sweeps should be kept high enough to ensure that the reduction in residuals is satisfied first. This sweeping also applies to Stone's method and the preconditioned conjugate gradient solvers as well.

The values for the number of sweeps and the reduction factor mainly used in this study are given in Table 3.5.

Table 3.5 Number of sweeps and reduction factors

Variable	Minimum number of sweeps	Maximum number of sweeps	Residual reduction factor
U, V, W	1	5	0.25
P	1	30	0.1
All Reynolds stresses, fluxes, k and ε	1	5	0.25
H	1	30	0.1

It is necessary to make small changes to ease convergence in some cases. For example, the effect of buoyancy sensitises the solution process by linking the enthalpy and momentum equations via the body force term in the latter. A decreased reduction factor for enthalpy ensures accurate solution for H in the inner iteration, which aids convergence in the outer iteration.

3.5.1.2 The outer iteration

Once the inner loop has been completed, i.e. each variable taken in turn and iteratively solved until the stopping criteria has been met, the outer iteration is performed. The main aim of the outer loop is to update all variables in all equations by the values calculated in the inner loop. It is within this outer loop that the velocity–pressure coupling algorithm, SIMPLEC, covered in Section 3.3.4, is implemented.

Instead of directly updating the cells, only part of the difference between the values in this outer loop when compared to the values from the previous loop are added. The fraction of the difference passed on is called an under-relaxation factor (URF, where $0.0 < \text{URF} < 1.0$). No under-relaxing (i.e. URF = 1.0) means that all of the difference in a variable between this iteration and the previous one is passed on. With greater under-relaxing, i.e. a smaller URF, the solution process is slowed down with only a fraction of the difference added to the previous value. The main purpose of under-relaxing is to stabilise the solution process. By choosing a smaller URF two effects are generated.

Firstly, the matrix of equations are made strongly diagonally dominant and thus a more accurate solution of the equations is gained with a fixed amount of work. Secondly a smaller URF corresponds to a small pseudo-time step bringing the stability benefits of small time steps. The URFs used mainly in this study are given in Table 3.6.

Table 3.6 Under-relaxation factors

Variable	URF
$U, V, W,$	0.65
P	1.0
k, ε	0.7
T	1.0
H	0.7
Reynolds stresses and fluxes	0.5

It is also possible in this loop to force another inner iteration solution for a group of variables. When the DFM is used this is implemented for k, ε and Reynolds stresses and fluxes transport equations. These equations are iterated twice in the inner iteration when compared to all the other variables. This forces a very accurate solution of these turbulent quantities, which plays a critical role in solution stability.

The outer loop is stopped when the problem is said to have converged. There are a number of criteria for stopping the outer loop. There can be a time limit or a maximum number of outer iterations. These two criteria are driven more by computing resources than by a physically realistic criteria. The condition for convergence in this study is for the sum of mass source residuals (see Equation 3.74) from each cell in the domain dropping below a predefined value. The convergence can also be monitored at specific locations. As the iteration progresses the value of the sum of mass source residuals decreases as the monitoring point should approach a constant value. Therefore, a minimum sum of mass source residuals, together with monitoring of the variable values during the solution procedure are combined to obtain a satisfactory convergence.

3.5.1.3 Computer software

The commercial CFD package used is CFDS-FLOW3D from the Atomic Energy Authority at Harwell in Oxfordshire. Also in the suite of CFDS programs is the grid generator (SOPHIA) and post-processing visualisation package (JASPER).

Chapter 4. Problem Under Consideration

This chapter outlines the problem under consideration in this study. The main aim of the investigation is to understand more fully the effect of multiple plumes, issued in close proximity to each other, and their dispersion into a cross-flowing ambient. The following chapter will therefore cover the real-life, physical cooling tower plume arrangement, how this has already been modelled in a wind tunnel and finally, how this study approaches the problem in a mathematical light.

4.1 ACTUAL PROBLEM

Evaporative type cooling is by far the most common method used in the UK. Here, the water to be cooled is brought into direct contact with colder air whereupon evaporation leads to a decrease in the temperature of the hot water. A less common type of cooling is performed by dry towers. Here, there is no direct contact between hot water and cool air. Heat transfer occurs across dry surface coil sections, hence the water is cooled totally by sensible heat. A mixture of these two types of cooling can be found in plume abatement and water conservation type towers.

When using evaporative cooling, the hot air leaving the tower can be highly visible due to its elevated temperature and moisture content relative to the surrounding ambient air. A decrease in density and persistence of the plume can be achieved by using plume abatement towers. Such towers cool some of the hot water by dry cooling as well as using evaporative cooling for the remaining water. The combined cooling air leaves the tower at subsaturated conditions and cools to ambient temperatures without entering the supersaturated, visible state.

There are two conditions that lead to the plume spreading down to ground level when using mechanical hybrid type towers. The first, called touchdown, is where a bent-over plume spreads naturally by entraining ambient air, but whose centreline is close enough to the ground so that the increased plume width eventually coincides with ground level. Secondly, there is plume downwash. In low exit velocity conditions the plume can be bent-over so quickly that it interacts with the tower wake. Accelerated cross-wind around the sides of the tower structure lead to areas of low pressure in the lee of the tower. These areas can drag the underside of the plume down which inhibits plume rise in the early stages. At worst, some plume material can be pulled into the recirculation region within the wake leading to reingestion of hot, high-humidity air back into the tower. Both these situations are highly undesirable. The most common form of restricting these problems is to increase the height of the tower so that the plume is issued into the cross-wind at a greater height above the ground. This is done either by increasing the stack or plenum height.

If these last options are not available then great care has to be taken when siting mechanical tower arrays. More often than not the only factor that is controllable is the orientation of the arrays as source conditions will be defined by loading requirements and there is little hope of controlling ambient wind conditions. An understanding of how adjacent plumes merge, and thus how effectively they will rise, is therefore required in an attempt to achieve greatest combined rise through informed array positioning.

4.2 WIND TUNNEL MODEL REPRESENTATION

National Power plc commissioned wind tunnel studies to characterise and quantify the interaction and possible downwash of cooling tower plumes from various cooling tower arrays. This work was carried out by TNO Environmental and Energy Research of Holland (TNO, 1995). These tests are to be modelled computationally in this study and the results compared. A full description of the wind tunnel arrangement will therefore be given.

4.2.1 Description of experimental wind tunnel tests

The work was done in an open type wind tunnel, the relevant dimensions of which are shown in Figure 4.1. A linear scaling factor of 300 was chosen when converting the full-scale down to wind tunnel scales. An atmospheric boundary layer was simulated in the wind tunnel with a full-scale surface roughness length of 0.1m. A rough carpet on the floor of the conditioning section of the tunnel was used with a tripping fence of height 130mm and shark fins at the entrance.

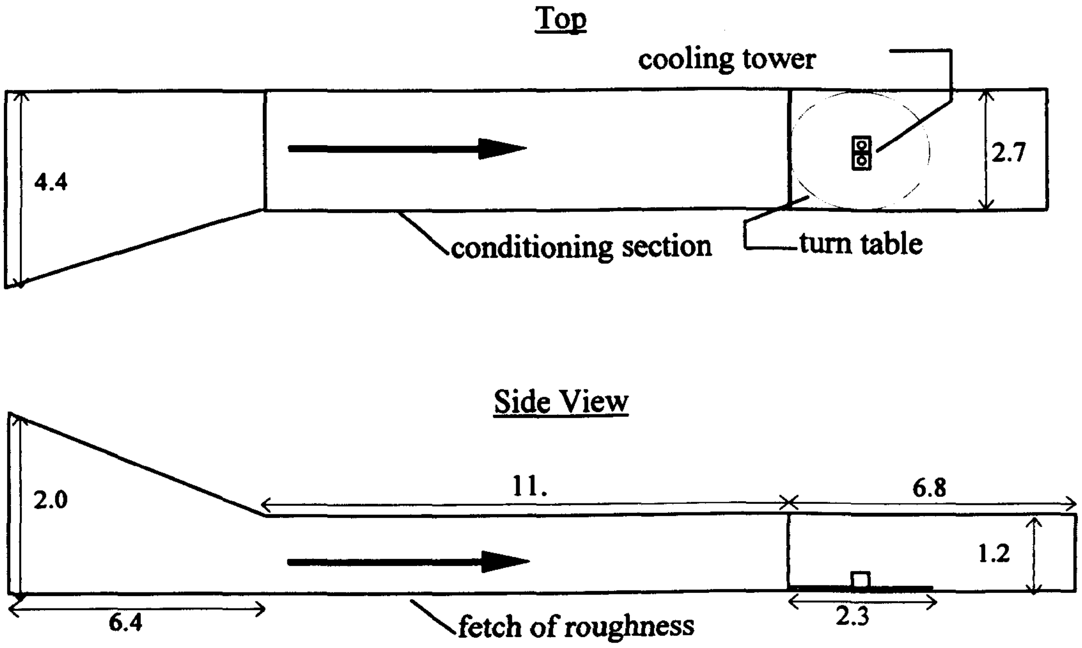

Figure 4.1 Experimental wind tunnel arrangement (all dimensions in metres)

The rather complex outline of a real-life mechanical tower, shown in Figure 4.2, is simplified in the wind tunnel work to a cubic building with the full-scale dimensions 20 × 20 × 20m with an internal cylindrical development duct 10m in diameter. The wind tunnel model dimensions are therefore 66 × 66 × 66mm and the diameter of the opening is 33mm. A gauze was mounted at the bottom of the tower development section to promote a uniform profile of velocity at that plane. This simplified tower model is shown in Figure 4.3.

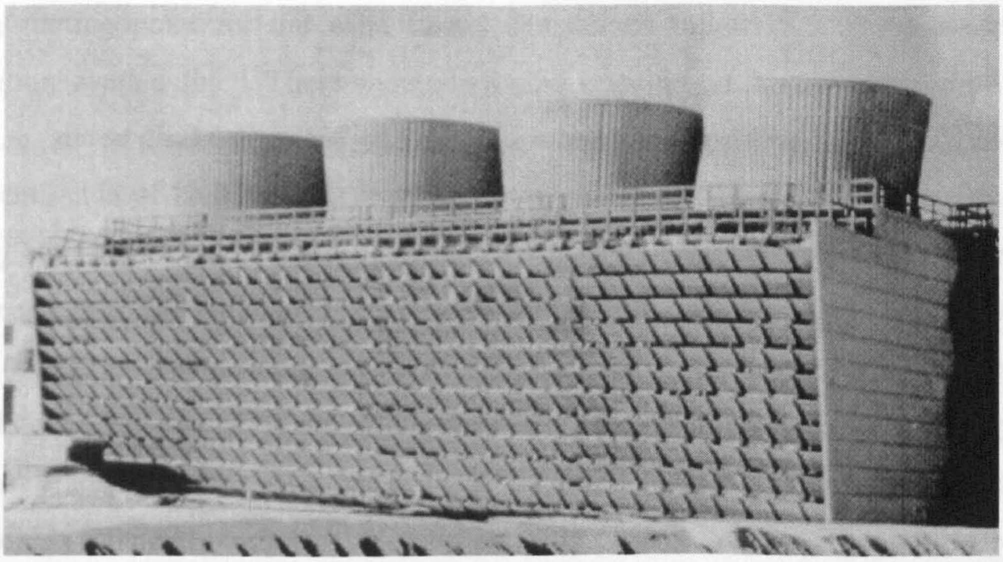

Figure 4.2 Array of hybrid cooling towers (Hensley, 1985).

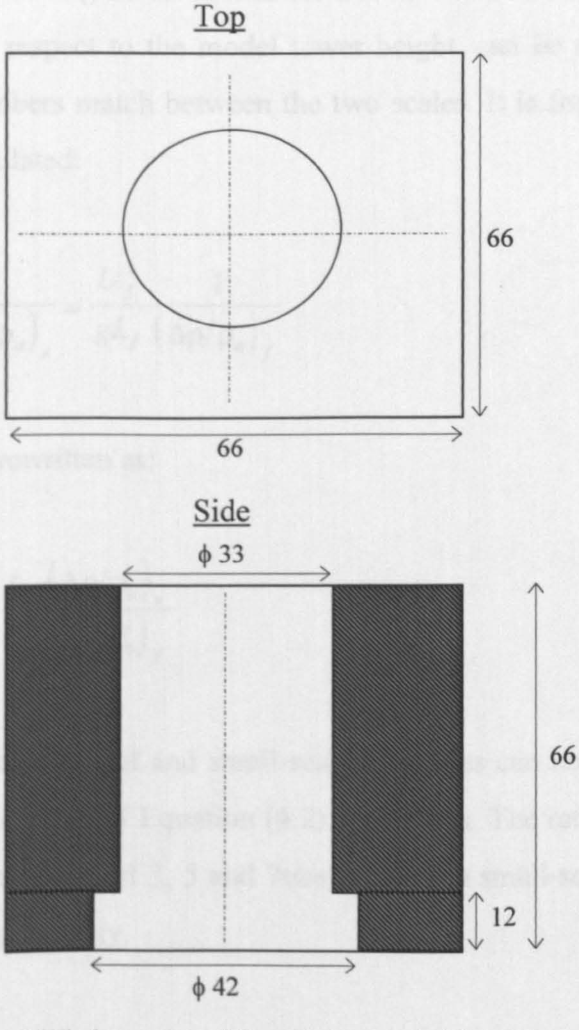

Figure 4.3 Wind tunnel model cooling tower (all dimensions in millimetres).

As a starting point for the wind tunnel simulations full-scale source and ambient conditions were defined. These were cross-wind velocities at the tower top of 3, 5 and 7m/s, a source discharge speed of 7m/s and a temperature difference of 15K over an ambient value of 288K. Correct scaling between full and small-scales would involve fixing both the Froude and Reynolds number as well as the relative density difference between source and ambient. The full-scale density ratio between source and ambient is 0.95 (due to the temperature excess of 15K over the ambient of 288K). Wind tunnel simulation of this value would lead to very low wind speeds and correspondingly low Reynolds numbers. This would be difficult in terms of stability as well as the discharge not being sufficiently turbulent. A compromise is therefore made. A density difference of 0.74 in the wind tunnel is achieved by adding 30% helium to the flow through the cooling tower. Higher air speeds are now allowed and a minimum Reynolds number of 1800, with respect to the model tower height, can be realised. It is still essential that Froude numbers match between the two scales. It is from this that the velocity scaling can be calculated:

$$\frac{U_s^2}{gL_s}\frac{1}{\left(\Delta\rho/\rho_a\right)_s}=\frac{U_f^2}{gL_f}\frac{1}{\left(\Delta\rho/\rho_a\right)_f} \tag{4.1}$$

this can be rewritten as:

$$\left(\frac{U_s}{U_f}\right)^2=\frac{L_s}{L_f}\frac{\left(\Delta\rho/\rho_a\right)_s}{\left(\Delta T/T_0\right)_f} \tag{4.2}$$

The ratio between full and small-scale velocities can now be calculated as all terms on the right-hand side of Equation (4.2) are known. The ratio is equal to 0.1307 and so the full-scale velocities of 3, 5 and 7m/s convert to small-scale velocities of 0.39, 0.65 and 0.91m/s, respectively.

A tracer is added to the helium and air mixture of the tower source discharge so that the concentration of the plume may be measured at various downstream locations. 0.3%

volume of isobutylene is therefore added to the source. To measure the concentrations of the tracer gas a rake consisting of 12 sampling tubes on a line was used. The distance between the tube mouths was 70mm. The outer and inner diameters of a sampling tube were 2.7 and 1.5mm, respectively. Three photo ionisation detectors, operating simultaneously, were used to record the concentration of the tracer gas. Values were averaged over a period of 1 minute. Air speed in the wind tunnel was recorded using a thermistor probe. Flow rates of the air, helium and isobutylene to the towers were measured using rotameters and mass-flow controllers.

4.2.2 Wind tunnel experimental results

Cross-wind inlet profiles were measured 1.5m upstream of the centre of the tower array. The measured profiles of cross-wind velocity, three components of turbulence intensity and a length scale profile are shown in Figure 4.4.

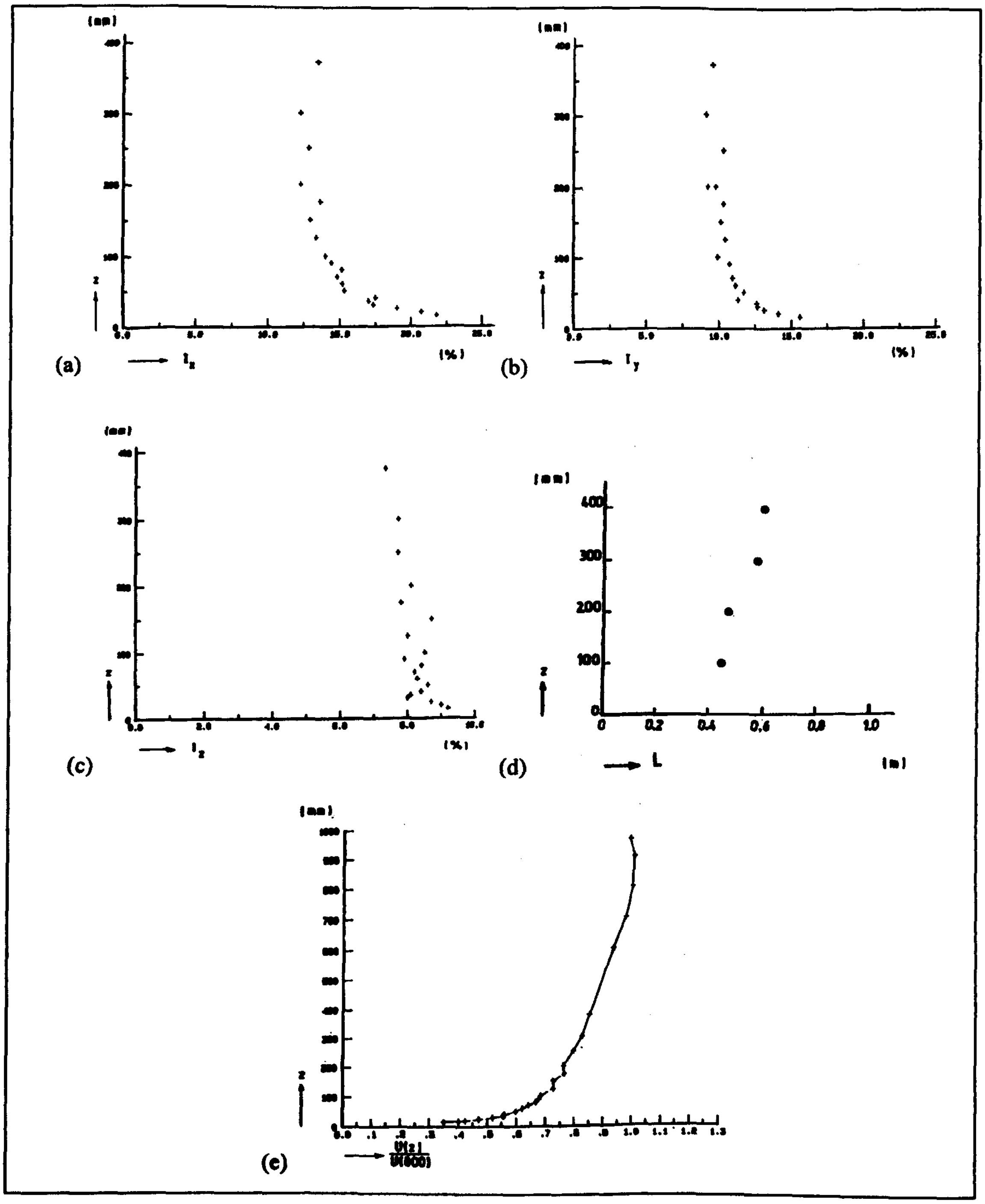

Figure 4.4 Inlet profile graphs of turbulence intensity in three directions (a, b, c), turbulent length scale (d) and cross-wind velocity (e) (TNO, 1995)

Concentration measurements were taken at four downstream locations: 0.33, 1.33, 2.66 and 4.0m (full-scale distances of 100, 400, 800 and 1200m) from the front of the tower array. At each of these locations vertical and horizontal concentration profiles were measured. The exact procedure, taken from the TNO report, was as follows.

"At first the vertical profile has been measured at the lateral location where the concentration proved to be the highest. In general the lateral co-ordinate of this location proved to be close to the lateral co-ordinate of the centre of the cooling tower array. Subsequently a horizontal profile has been measured at the vertical height of the maximum concentration from the vertical profile." (TNO, 1995)

The full TNO study covered six tower array types (1×1, 1×2, 1×4, 2×2, 1×10 and 2×5) and three wind directions at each of the three wind speeds for each configuration. This is approximately 30 configurations in total (in addition, four configurations with no helium were also studied). For each configuration eight concentration profiles were measured. Not all configurations are modelled in this study. An example of the raw TNO data is given in Appendix A. The 'y-correction' referred to in this raw data is the lateral off-centre distance mentioned in the above quote. This could be attributed to lateral drift within the wind tunnel. It may also correspond to one of the off-centre thermal cores found within the plume's kidney-shaped cross-section. The vertical peak in concentration (which was used to define the vertical height at which the horizontal profiles were measured) could be the highest for those positions measured. It may also coincide with the exact point of the peak. Because of the way the measurement positions were chosen, a certain degree of uncertainty exists which should be noted here. These points are covered more fully when comparing the computational results to the experimental data in Chapter 5.

4.2.3 Discussion of experimental results

It is important to try to asses not only the accuracy of any experimental data but to also question any assumptions that the experiment was based upon. An awareness of all errors and tolerances will go some way in quantifying the overall accuracy of the comparison between experimental and computational results.

A CFD code produces a vast amount of data that is spatially highly accurate. The method of obtaining concentration values in the wind tunnel introduces smoothing errors that should be addressed. The external diameter of the wind tunnel sampling tubes is 2.7mm corresponding to a full-scale diameter of 0.8m. So, just as a computational grid limits the ability to capture a spatial gradient, the experimental method also introduces a form of averaging of concentration gradients. Any high peaks of concentration that exist in reality, smaller than 0.8m in the full-scale, will therefore be smoothed out somewhat by this measuring process.

The scaling assumptions outlined in Section 4.2.1 would be of critical importance when comparing the wind tunnel data with actual full-scale data. When using a computational model the question arises whether to model the wind tunnel scale, copying the wind tunnel geometry and boundary conditions exactly, or to model the full-scale set-up directly. The former would certainly provide the best method for validation of the code itself, whilst the latter should give an indication as to not only the accuracy of the numerical model, but also to the accuracy of the experiment to model the full-scale.

4.3 COMPUTATIONAL MODEL

There a number of advantages, as well as disadvantages, in using CFD as a predictive tool compared to standard experimental techniques. One of the benefits of CFD lies in the freedom to model a great number of geometries and flow conditions with ease. Once a geometry has been created it can be modified or copied to quickly produce a new arrangement. With wind tunnel work once a model has been manufactured it is geometrically fixed. To then go on to model a different arrangement requires the manufacture or modification of existing parts. This can be a costly and time-consuming process. The difference between modelling small or large scales computationally is simply a matter of differing numerical values. This itself can overcome the errors of scaling assumptions and compromises found in wind tunnel work. Another benefit is the shear quantity of data produced by a CFD code. It will always far outweigh that which can be as easily derived from an equivalent experimental rig. Within a single CFD result data file lies information on not only readily measurable variables such as velocities and temperatures, but also on more complex parameters such as heat transfer coefficients, wall shear stresses and Reynolds fluxes and stresses.

Computing power, or lack of it, introduces the problems encountered in CFD work. Although the exact equations governing fluid flow are known, present computing resources mean that drastic simplifying assumptions on the behaviour of fluids have to be made. A direct numerical simulation (DNS) with a grid dense enough to capture all turbulent structures down to the Kolmogarov scale with time steps of the appropriate order would be as accurate as the accuracy of its boundary conditions. At present though it would take in the order of millennia to simulate the problem at hand using this method. Assumptions are therefore made to simplify the computational model. The most important area is the treatment of turbulence, covered in Section 3.2.1. Other sources of error are found in the density of the grid used, the discretisation of the governing equations and also in some boundary conditions. As with wind tunnel studies, the results generated will only be as accurate as the definition of the model itself.

The work carried out in this study comprises the modelling of both the wind tunnel work as well as the full-scale. For direct comparison with experimental data the wind tunnel geometry is modelled as closely as possible. Differing number of sources, wind direction and wind speed are investigated as well as the effects of buoyancy. The results themselves are given in Chapter 5. Below is an outline of the geometries and scales studied as well as the boundary conditions used.

4.3.1 Cooling tower geometries

Three cooling tower arrays are modelled. These are a single source, the wind approaching normal to one face of the tower, a 1 x 2 array and also a 2 x 1 array. The two double source arrangements have the wind approaching normal to firstly the minor (shorter) axis of the line array and secondly normal to the major axis.

4.3.1.1 Single tower

The simplest geometry is that of the single tower, shown in Figure 4.5. The only difference between this and the wind tunnel model (see Figure 4.3) is that the development duct is now purely cylindrical. A top-hat profile for all inlet variables is set at the bottom of this duct. Physical symmetry has been utilised so only half of the entire domain needs to be modelled.

4.3.1.2 Tandem arrangement

An increase in the number of sources quickly increases the number of required grid cells. Therefore, just a 1×2 arrangement is modelled, again making use of the existence of physical symmetry. The effect of wind direction is also incorporated into the geometry. The two extremes of the wind direction, parallel and normal to the towers, are investigated.

The tandem arrangement refers to a 1×2 array where the wind approaches at 0° to the long axis of the array. This is shown in Figure 4.6. The plume inlet boundary conditions are identical to the single source case, although there is now an upstream and downstream source.

4.3.1.3 Side-by-side arrangement

This geometry is identical to the tandem arrangement except now the cross-wind approaches from an angle of 90° to the long axis of the array, as shown in Figure 4.7. As the physical symmetry plane now bisects the centre of the long axis of the array an entire source is modelled to one side of the symmetry plane. Again, source inlet boundary conditions are the same as for the previous two geometries.

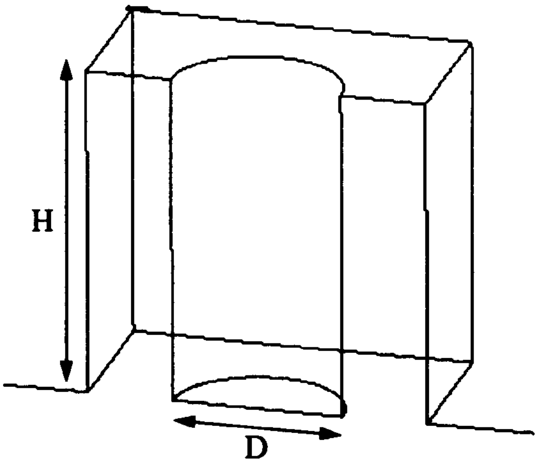

Figure 4.5 Single source tower geometry.

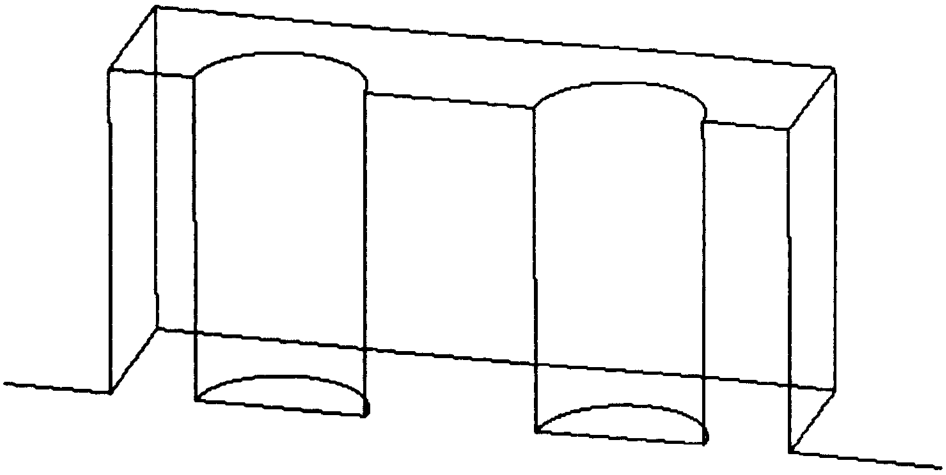

Figure 4.6 Tandem sources tower geometry.

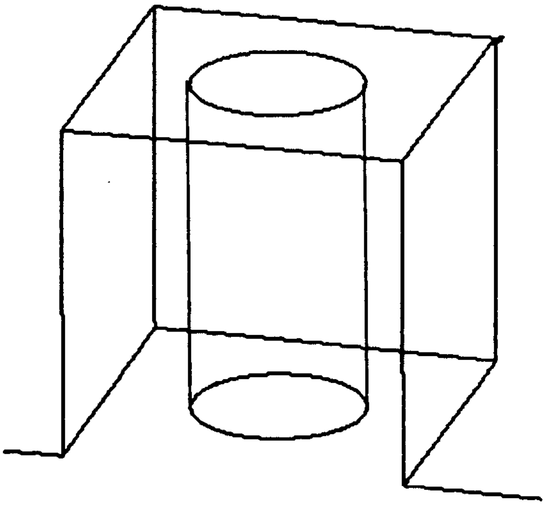

Figure 4.7 Side-by-side sources tower geometry.

4.3.2 Geometric scales

4.3.2.1 Small-scale

The flow field geometry modelled, essentially a section of the wind tunnel geometry, is shown in Figure 4.8. Although the experimental inlet profiles were measured 1.5m (22.7H) upstream of the tower array, the cross-wind inlet to the computational domain is 0.76m (11.1H) upstream. This is primarily to reduce, as far as possible, the number of grid cells used. As this computational plane is only 0.74m (11.2H) upstream from where the experimental inlet profiles were measured it can be shown by simple empirical laws that very little boundary layer development occurs within this region, therefore the foreshortening of the domain is acceptable. The inlet plane is still far enough upstream of the towers so as not to be affected by windward tower gradients so that the prescribed cross-wind inlet condition still holds. The top plane is positioned above the top of the boundary layer so that symmetry boundary conditions can be applied. Another possible option (which was considered but not implemented) included a much lower top plane where a 'dummy' inlet would have been set, i.e. an inlet parallel to the plane itself. Downstream of the tower this plane would have had to rise to accommodate the rising plume. It would also have been difficult to allow the boundary layer to develop over the length of the domain, something that an elevated symmetry plane can cope with. The side plane, opposite the physical symmetry plane, also has symmetry boundary conditions imposed. Again, it is positioned far enough to the side of the developing plume so that it is in a region where there are no fluxes across it, even at the domain exit plane where the plume is at its widest. The exit plane's position was determined by allowing comparisons for the first two downstream experimental measuring stations, x = 0.33m (5H) and x = 1.33m (20H) and ensuring that the experimental plume width was less than the computational domain width. The domain extends downstream 2.0m (30H) from the tower array so that any back propagating errors introduced by the Neumann mass flow boundary condition are minimised at the 1.33m measuring location.

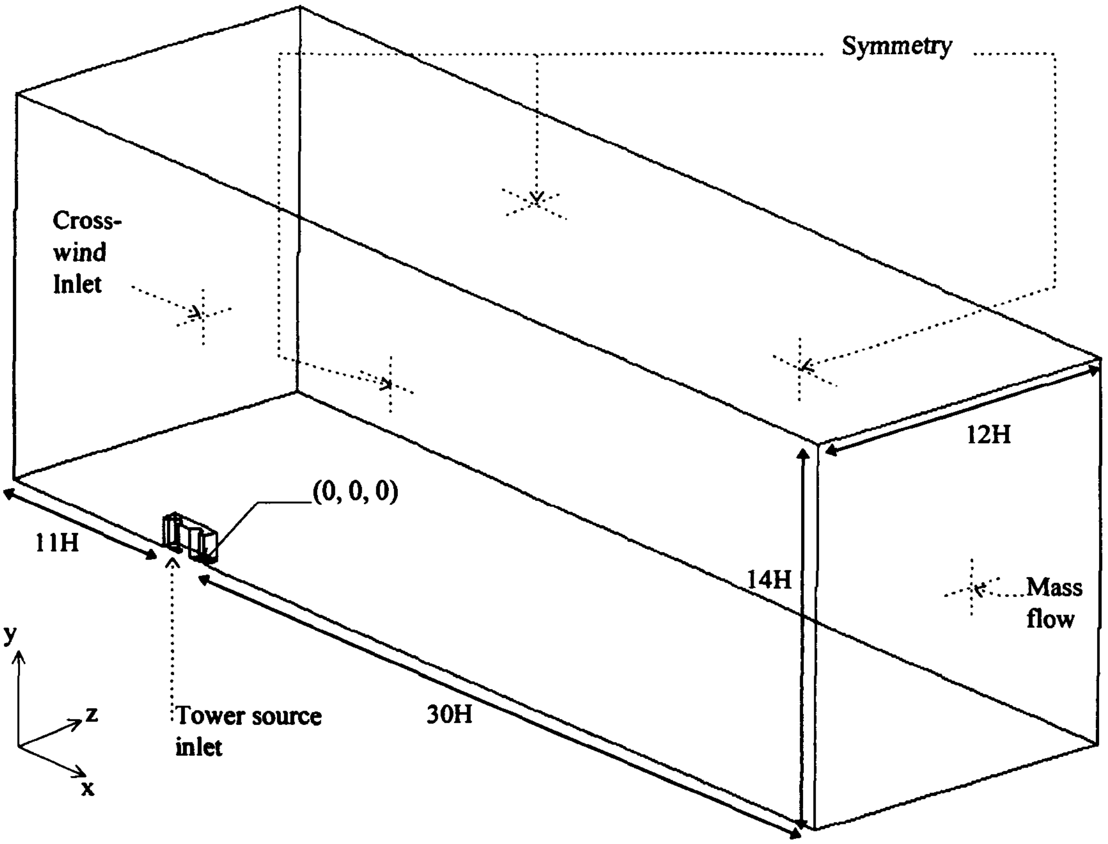

Figure 4.8 Small-scale computational domain.

To model the wind tunnel work directly, the density difference achieved by the addition of hydrogen in the experiment was achieved in the computational model by setting an elevated source temperature (100K over an ambient of 288K) so as to produce the same density ratio as in the experiments (0.74). This could also have been achieved (although not used here) by introducing two species, one at the cross-wind inlet and the other at the tower source. Both would have been the same phase but with different densities. Following the former choice, the large density differences involved now mean that the Boussinesq assumption can no longer be utilised. Instead the method referred to as the weakly compressible method (see Section 3.2) was adopted. Instead of introducing a passive tracer at the source, as was done in the wind tunnel work, the concentration and temperature fields were assumed to be linked as:

$$\frac{C-C_a}{C_0-C_a}=\frac{T-T_a}{T_0-T_a}=T^* \qquad (4.3)$$

As the ambient concentration in the wind tunnel, C_a, is equal to zero, the above relationship becomes:

$$\frac{C}{C_0} = \frac{T - T_a}{T_0 - T_a} \qquad (4.4)$$

The experimental concentration data was given in terms of the ratio between actual and source concentrations. Equation (4.4) is therefore used to convert the experimental data into a form that can be readily compared to the computationally predicted temperature field.

4.3.2.2 Full-scale

By modelling the full-scale the hope is to predict directly that which the experimental work set out to model. By doing this it is intended to overcome the compromises taken in the wind tunnel study and so hopefully obtaining a more accurate prediction of the real-life problem. The transition from small to full-scale geometries is relatively simple. A global scaling factor of 300 was applied to all geometric points, the shape of the domain remained identical to the small-scale. All boundary conditions, and their relative locations, also remained the same. In the full-scale the ratio of source to ambient density was equal to 0.95, resulting in an elevated source temperature of 15K above ambient. Therefore, the Boussinesq assumption for buoyancy was applied. The conversion of experimental concentrations to the comparable non-dimensionalised temperature, T^*, was handled in the same way as in the small-scale work.

4.3.3 Parametric variations

A CFD code has, what can be euphemistically called, a wide choice of parameters, settings and assumptions that are by no means fixed. There are varying degrees of accuracy that can be obtained, although normally at the expense of computer time. There are methods that can increase the speed of the convergence process, although normally at the expense of convergence stability. An outline is now given of some specific parametric variations that will be employed and investigated in this study.

4.3.3.1 Buoyant and non-buoyant tests

For the case of a single source, the wind tunnel work modelled a jet-type source ($Fr_0 = \infty$). To try to isolate the effects of buoyancy, this scenario was also computationally modelled. Experimentally this was achieved by the omission of helium at the source. Computationally, the buoyancy can be neglected simply by the omission of the body force term in Equation (3.2) as well as those terms which describe the effects of buoyancy on turbulence production and/or destruction.

4.3.3.2 Variation in cross-wind speed

The wind tunnel work included three different cross-wind speed profiles, each having a boundary layer-type logarithmic shape. These are shown in Figure 4.4. The computational study considers both the slowest and fastest of the three. In the full-scale these profiles are defined by the velocities at the tower top, having values of 3 and 7m/s. In the small-scale these are 0.39 and 0.91m/s, respectively. The boundary layer shape can be mathematically fitted to the measured wind tunnel profile, to a high degree of accuracy, by the following relationship:

$$\frac{U_{y1}}{U_{y2}} = \frac{\ln(y_1 / z_0)}{\ln(y_2 / z_0)} \qquad (4.5)$$

Where y_1 and y_2 represent different heights and z_0 is the surface roughness. It is assumed that the full-scale cross-wind also follows this relationship. Knowing the tower height and the cross-wind speed at that elevation together with the surface roughness, the vertical profile of the cross-wind velocity can be defined at the cross-wind inlet plane. A full-scale surface roughness of 0.1m was assumed. Therefore, the small-scale surface roughness was 0.00033m. The given profiles of turbulence intensity and length scale are then used in the calculation of turbulence energy and its rate of dissipation of the cross-wind at the inlet plane. Three turbulence intensity profiles are expressed in non-dimensional form by:

$$TI_x = -13.5^{-1} \log\left(\frac{y}{11.4 \times \partial}\right) \tag{4.6}$$

$$TI_y = -21.8^{-1} \log\left(\frac{y}{33.5 \times \partial}\right) \tag{4.7}$$

$$TI_z = -65.4^{-1} \log\left(\frac{y}{2800 \times \partial}\right) \tag{4.8}$$

where:

$$TI_x = \frac{\sqrt{u'^2}}{U},\ TI_y = \frac{\sqrt{v'^2}}{U} \text{ and } TI_z = \frac{\sqrt{w'^2}}{U} \tag{4.9}$$

These three profiles of turbulence intensity are derived from best fits to the experimental profiles in Figure 4.4. The turbulence energy is now defined by:

$$k = \tfrac{1}{2}U^2\left(TI_x^2 + TI_y^2 + TI_z^2\right) \tag{4.10}$$

Since the turbulence energy is zero at the wall, a linear variation of turbulence energy was assumed between the wall and a point at 0.002δ distance from the wall. The length scale used to calculate the cross-wind profile of energy dissipation rate, ε, is also derived from a best fit plot of the profile in Figure 4.4. For the small-scale, the length scale profile was obtained from:

$$L_x = (y + 0.8)/2.0 \tag{4.11}$$

The full-scale profile was taken to be a factor of 300 times larger. The profile for ε is then defined by:

$$\varepsilon = \frac{k^{3/2}}{L_x} \qquad (4.12)$$

4.3.3.3 Tower source turbulence levels.

All tower source values are set assuming uniform, i.e. 'top-hat', profiles, constant across the tower inlet plane. Velocities of 7.0 and 0.91m/s, for full and small-scales respectively, are used. The sum of the three turbulence intensities at the tower source was assumed to be 6.3%. The value of k was then calculated from Equation (4.10). The value of ε was obtained from Equation (4.12). The length scale used in this case was the source diameter and the normalising velocity was V_0. The sensitivity of the results to the assumed level of turbulence at this inlet plane were investigated by also setting a turbulence intensity of 3% and 12%. By comparing these results the importance of the correct value of source turbulence intensity can be ascertained.

4.3.3.4 The constant C_3.

The turbulence production due to buoyancy is modelled in Equation (3.19), the equation for the transport of turbulent kinetic energy, by a source term, G, defined in Equation (3.22). How it is incorporated into Equation (3.20), the transport of energy dissipation, is less exact. A proportion of the term G is included in the term describing the production of the rate of dissipation of turbulence energy. The proportion being implemented via a constant C_3 where $0 < C_3 < 1$. The relationship between the production and dissipation of turbulence due to buoyancy is not known exactly and so the value of C_3 is debatable and probably varies for differing flow geometries. Because of this ambiguity two values are tried, i.e. 0 and 1. It may well be the case that under certain boundary conditions the trajectory of the plume may be sensitive to this constant. However, if the source is sufficiently jet-like it is unlikely that C_3 will be of importance.

4.3.3.5 Turbulent Prandtl number

With Reynolds numbers of the order of 10^6 encountered in the full-scale, laminar viscosity will always be far outweighed by turbulent viscosity. This is also true for diffusion of the temperature field. The transport of heat due to turbulent fluctuations (i.e. Reynolds fluxes) are related to mean temperature gradients via an eddy diffusivity (see Section 3.2.1.5). The eddy diffusivity is related to the eddy viscosity via a turbulent Prandtl number (Equation 3.46). The value of the turbulent Prandtl number has been experimentally determined for certain flow geometries, the commonly accepted value is 0.9. Mompean (1994) has shown however, that under certain circumstances a lower value yields more accurate results. This is also substantiated by the renormalised group theory analysis of the Navier Stokes equations by Yakhot & Orszag (1986). This work produced a theoretically derived value of the turbulent Prandtl number of 0.716. For such an important parameter, especially for the flow field under consideration, three values were used in this study, i.e. 0.4, 0.6 and 0.9.

4.3.3.6 Gridding

Although the geometry of small and full-scale models is identical, there are differences in gridding between the two. The grid for the small-scale is described here first. To be able to capture the critical spatial gradients very near where the plume enters the cross-wind at the tower top, a very fine grid was adopted in this region. Due to this, the grid cells nearest to the wall are located within the viscous sub-layer. If the standard logarithmic law of the wall was used, then the first cell in the log layer would have been too far from this critical area. Therefore, instead of employing the law of the wall, the governing equations are integrated up to the wall. This process is part of the low Reynolds number turbulence model and is used for all small-scale work. To accurately capture the wall boundary layer the first grid cell next to the wall was located within a distance of $y^+ = 1$. Approximately five further cells were included outside the viscous sublayer, mainly in the logarithmic layer. The gridding of the small-scale domain is shown in Figure 4.9. A multiblock approach was taken where the geometry is broken down into many adjacent blocks. A more complex geometry requires a greater number of blocks to capture it. Downstream from the tower the orthogonal shape of the blocks is changed slightly so as to maintain as high a grid density within the rising spreading plume as possible. A compromise in this block modification had to be taken as some source configurations resulted in fast rising plumes, whilst in others the plume bends over very quickly and may not rise much further downstream at all. The grid is 'elevated' just downstream of the tower so that grid density can be maintained for all source configurations.

Having to integrate up to the wall in the small-scale resulted in a very high total number of cells within the entire domain. This, together with the solution for a weakly compressible flow, greatly increased both solution time and computer memory storage requirements. It was therefore decided to perform the bulk of the comparative studies for the full-scale case. The sensitivity tests were also done using the full-scale models, this includes the grid dependency tests. The full-scale grid is essentially a slightly modified form of the small-scale grid. The cells below the viscous sub-layer were removed, the near wall cells now resided at a value of $y^+ = 100$ on average. The same distribution of cells above the near wall cell was maintained in both small and full-scales. The total number of cells is greatly reduced in the full-scale case. An initial assumption is made that if grid independency is achieved in the full-scale, then it must also be in the small-scale, as the latter has an even denser grid.

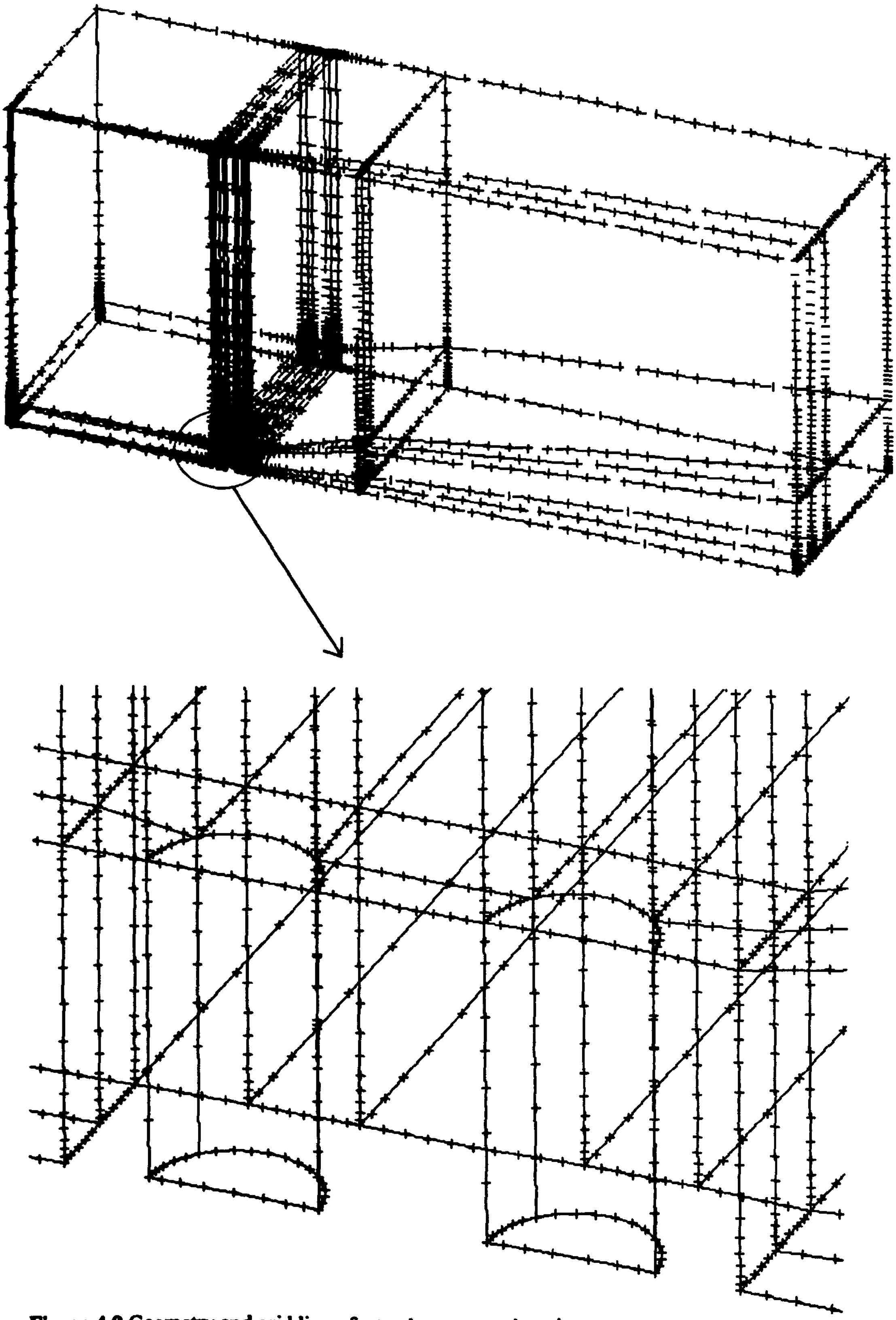

Figure 4.9 Geometry and gridding of a tandem source domain.

Gridding of the solution domain is probably the most important aspect of an accurate prediction. Any spatial gradients that exist must be captured by a sufficiently dense grid. If not, then the predicted gradient will be smoothed by numerical diffusion. Numerical errors can also be introduced if the predominant flow direction is not aligned with main grid orientation. These errors can lead to disastrous affects on the final solution. It is imperative that any CFD investigation is not affected by grid-related errors. To this end a grid dependency test was carried out and the following procedure was followed. An initial grid was created and an approximate solution was generated. This solution gave some indication as to the location of high gradients and the grid was modified in these areas. Having set the ratio of cell density from one domain area to another, the number of grid cells was scaled globally to create another denser grid. Runs were performed on these different grids and results compared. When there was no change in the results for successively denser grids then the results are said to be grid independent. It may be the case that one variable or one area of the domain may achieve independence before another. It is important that a variable of primary interest, in an area of concern, is chosen when analysing the grid independency tests. In this study, sensitivity tests were carried out on a single and tandem source arrangement. This is to ensure grid independency on all runs between these two extremes of theoretical plume rise height.

4.3.3.7 Discretisation scheme

The role of grid and discretisation scheme are closely related. A scheme of higher order should be able to capture a gradient accurately with fewer grid cells than a lower order scheme with the same number of cells. Conversely, a lower order scheme will be as accurate with a denser grid in the correct regions than a higher order scheme with fewer cells. Unfortunately, higher order schemes tend to be more unstable and so may well take longer to converge, whilst a denser grid will take up more computer memory and also increase solution time. It is because of this that two schemes were investigated. Firstly, the hybrid scheme was applied to all governing equations (see Section 3.3.3.1). Secondly, for comparison, the QUICK scheme (see Section 3.3.3.2) was employed. Because there can be unphysical under- and over-shoots of captured gradients generated by the QUICK scheme, the bounded form, CCCT (see Section 3.3.3.3), was also used for the equations of k and ε to ensure that they remain positive at all times. Negative values of these variables invalidate the eddy viscosity assumption of Equation (3.18). This bounded scheme was not used for all governing equations as it proved to be not unstable, but difficult to ensure efficient convergence.

4.3.3.8 Turbulence model

The role of turbulence, and its effects on a flow field, will always be of critical importance in engineering applications. The theory of turbulence modelling remains the main area where a majority of research is being conducted. There exists many ways in which to accommodate turbulence, from the simplest zero equation models right up to full Reynolds flux models. As it is likely that any one model will perform differently under various applications, a number of models are compared in this study. To enable CFD to be used as an economical engineering research and design tool, a turbulence model has to be chosen that is both stable and also of a satisfactory accuracy.

This study therefore compares results from four turbulence models. The low Reynolds number k–ε model (see Section 3.2.1.3) is used for all small-scale work. The standard k–ε model (see Section 3.2.1.1), the RNG k–ε model (see Section 3.2.1.2) and a differential flux model (see Section 3.2.1.4) are all used for the full-scale. It is hoped that an understanding of the reasons for the comparative accuracy of these four models will lead to a more informed approach when choosing turbulence models for other applications.

Cross-wind inlet profiles of turbulence energy and its rate of dissipation required by the first three models have already been defined in Section 4.3.3.2. For the Reynolds flux model more specific profiles of individual Reynolds stresses and fluxes have to be defined. Individual normal Reynolds stress profiles of the cross-wind were calculated directly from Equations (4.6–4.9). The numerical model solved for enthalpy relative to an ambient value, in this case the cross-flow. Therefore, there were no mean or fluctuating enthalpy values at the cross-wind inlet plane.

At the tower source the three normal Reynolds stresses were set to 2/3k. A similar approach to the calculation of k in Equations 4.9 and 4.10 was then used when determining the Reynolds fluxes. An intensity of the fluctuations of the velocity/enthalpy correlations was assumed such that:

$$TI_{uh} = \frac{\overline{u_i'h'}}{V_0 H_0} \tag{4.13}$$

The three fluxes can then be calculated by setting an intensity and also knowing the source velocity and enthalpy. The same reasoning was used for the enthalpy/enthalpy correlation of Equation (3.54):

$$TI_{hh} = \frac{\sqrt{\overline{h'^2}}}{H_0} \tag{4.14}$$

In both cases an intensity of 3% was assumed. It was assumed that if this value was not physically accurate then the short development region between the tower source and tower exit will give these correlations time to 'settle-down' into more stable values. Theoretically these correlations are produced by mean gradients of velocity and enthalpy at the inlet plane. However, as a top-hat profile is set at the plume source these values should all be very small. Setting zero values for these correlations causes severe convergence problems when using a differential flux model. It could be the case that in reality these turbulent fluxes and stresses are convected from more complex flow regions downstream of the computational inlet plane. It is the belief here that plume trajectory and spreading will not be highly sensitive to inaccuracies in the setting of these source fluxes.

4.3.4 Cases studied

There are two main areas under which all the computational work in this study fall. Firstly, work was conducted to investigate the sensitivity of the results to parametric variations already discussed. These variations included grid density, turbulent Prandtl number, the value of the constant C_3 and also tower source turbulence intensity. Secondly, the main body of the work centred upon comparison with the experimental data. Therefore, both small and full-scales are modelled using various combinations of discretisation schemes, turbulence models and exit velocity ratios. Tables 4.1 and 4.2 list the cases studied. The two scales modelled, full and small, are denoted by FS and SS respectively. Buoyant runs are denoted by a B, non-buoyant runs by NB.

4.3.4.1 Case solution details

The majority of the cases were solved on a CONVEX C3860 supercomputer at the University of London Computer Centre. Grid generation and flow visualisation was performed on a SUN SPARC 10 workstation at Brunel University.

The number of grid cells used for each geometry was dependent on the number and arrangement of sources investigated. For a single source 94000 cells were employed. A tandem arrangement used 122000 cells and a side-by-side configuration 136000. As shown in Figure 4.9, most cells were concentrated in regions close to the tower. When performing the grid sensitivity tests a global scaling factor was applied to the number of grid cells in each section of the domain. A scaling factor of 1.3 resulted in a 'fine' gird and a factor of 0.7 resulted in a 'coarse' grid. The average solution time for each outer iteration was 0.00014s per cell. The number of outer iterations required for convergence varied considerably, depending on discretisation scheme and turbulence model. This varied from 350 outer iterations for the baseline case up to 1500 iterations when using the QUICK scheme and the side-by-side tower configuration.

Once the sensitivity tests were completed it was possible to choose an optimised grid as well as noting the effect of the other parametric variations. A base-line model was then defined from which the other combinations listed in Table 4.2 were investigated and compared with the experimental data. The results of the runs that have been defined are presented in Chapter 5.

Case number	Geometry	R	Turbulence model	Discretisation scheme	Parametric Variation
1	Single	2.33	k-ε	Hybrid	Coarse grid
2	Single	2.33	k-ε	Hybrid	Medium grid
3	Single	2.33	k-ε	Hybrid	Fine grid
4	Single	2.33	k-ε	QUICK	Coarse grid
5	Single	2.33	k-ε	QUICK	Medium grid
6	Single	2.33	k-ε	QUICK	Fine grid
7	Tandem	1.0	k-ε	Hybrid	Coarse grid
8	Tandem	1.0	k-ε	Hybrid	Medium grid
9	Tandem	1.0	k-ε	Hybrid	Fine grid
10	Tandem	1.0	k-ε	QUICK	Coarse grid
11	Tandem	1.0	k-ε	QUICK	Medium grid
12	Tandem	1.0	k-ε	QUICK	Fine grid
13	Tandem	2.33	k-ε	Hybrid	Coarse grid
14	Tandem	2.33	k-ε	Hybrid	Medium grid
15	Tandem	2.33	k-ε	Hybrid	Fine grid
16	Tandem	2.33	k-ε	QUICK	Coarse grid
17	Tandem	2.33	k-ε	QUICK	Medium grid
18	Tandem	2.33	k-ε	QUICK	Fine grid
19	Tandem	2.33	k-ε	Hybrid	Modified coarse grid
20	Tandem	2.33	k-ε	Hybrid	Modified medium grid
21	Tandem	2.33	k-ε	Hybrid	Modified fine grid
22	Tandem	2.33	k-ε	QUICK	Modified coarse grid
23	Tandem	2.33	k-ε	QUICK	Modified medium grid
24	Tandem	2.33	k-ε	QUICK	Modified fine grid
25	Single	2.33	k-ε	Hybrid	$\sigma_T = 0.4$
26	Single	2.33	k-ε	Hybrid	$\sigma_T = 0.6$
27	Single	2.33	k-ε	Hybrid	$\sigma_T = 0.9$
28	Single	2.33	k-ε	QUICK	$\sigma_T = 0.4$
29	Single	2.33	k-ε	QUICK	$\sigma_T = 0.6$
30	Single	2.33	k-ε	QUICK	$\sigma_T = 0.9$
31	Single	2.33	k-ε	Hybrid	$C_3 = 0$
32	Single	2.33	DFM	Hybrid	$C_3 = 0$
33	Single	2.33	k-ε	Hybrid	$TI_0 = 3\%$
34	Single	2.33	k-ε	Hybrid	$TI_0 = 6.3\%$
35	Single	2.33	k-ε	Hybrid	$TI_0 = 12\%$
36	Single	2.33	k-ε	QUICK	$TI_0 = 3\%$
37	Single	2.33	k-ε	QUICK	$TI_0 = 6.3\%$
38	Single	2.33	k-ε	QUICK	$TI_0 = 12\%$

Table 4.1 Sensitivity Tests

Case number	**Geometry**	**Scale**	***R***	**Turbulence model**	**Discretisation scheme**	**Buoyancy**
39	Single	SS	2.33	Low Re. k-ε	Hybrid	B
40	Single	SS	2.33	Low Re. k-ε	QUICK	B
41	Side-by-side	SS	2.33	Low Re. k-ε	Hybrid	B
42	Side-by-side	SS	2.33	Low Re. k-ε	QUICK	B
43	Tandem	SS	2.33	Low Re. k-ε	Hybrid	B
44	Tandem	SS	2.33	Low Re. k-ε	QUICK	B
45	Single	FS	2.33	k-ε	Hybrid	NB
46	Single	FS	2.33	k-ε	QUICK	NB
47	Single	FS	2.33	RNG k-ε	Hybrid	NB
48	Single	FS	2.33	DSM	Hybrid	NB
49	Single	FS	2.33	k-ε	Hybrid	B
50	Single	FS	2.33	k-ε	QUICK	B
51	Single	FS	2.33	RNG k-ε	Hybrid	B
52	Single	FS	2.33	DFM	Hybrid	B
53	Side-by-side	FS	2.33	k-ε	Hybrid	B
54	Side-by-side	FS	2.33	k-ε	QUICK	B
55	Side-by-side	FS	2.33	RNG k-ε	Hybrid	B
56	Side-by-side	FS	2.33	DFM	Hybrid	B
57	Side-by-side	FS	1.0	k-ε	Hybrid	B
58	Side-by-side	FS	1.0	k-ε	QUICK	B
59	Side-by-side	FS	1.0	RNG k-ε	Hybrid	B
60	Side-by-side	FS	1.0	DFM	Hybrid	B
61	Tandem	FS	2.33	k-ε	Hybrid	B
62	Tandem	FS	2.33	k-ε	QUICK	B
63	Tandem	FS	2.33	RNG k-ε	Hybrid	B
64	Tandem	FS	2.33	DFM	Hybrid	B
65	Tandem	FS	1.0	k-ε	Hybrid	B
66	Tandem	FS	1.0	k-ε	QUICK	B
67	Tandem	FS	1.0	RNG k-ε	Hybrid	B
68	Tandem	FS	1.0	DFM	Hybrid	B

Table 4.2 Main body of work

Chapter 5. Results and Discussion

5.1 GRID SENSITIVITY

Grid sensitivity tests are carried out on two full-scale geometries, a single and a tandem source arrangement. To analyse grid dependency effects, temperature contours are plotted on the y-z plane at the two downstream locations where the experimental data is measured (x = 10D and x = 40D). Graphs are also plotted of vertical temperature profiles on the symmetry plane (z = 0D) and also vertically through the thermal core of the plume, referred to as 'peak' (see Section 4.2.2). By viewing both centre line and peak profiles, rates of grid independency can be ascertained. The scale of all y-z plane temperature contour plots can be gauged by the inclusion of the internal development duct within the tower on each individual contour plot (as shown in Figure 5.1a, b). The vertical line near the symmetry plane is therefore 2D high and at a distance of z = 0.5D. Each contour figure has a temperature key ranging from 0.1K to 1.1K above ambient (288.1K to 289.1K). A more accurate determination of temperature can be achieved by counting the 0.067K gap between each contour.

The main aim of grid independency tests is to assure that the grid is fine enough to minimise numerical diffusion effects. However, a greater understanding of the discretisation schemes used, and therefore how they should be applied in other engineering problems, can be gained by this analysis. There will always be a compromise between the stability of a lower order discretisation scheme and the greater accuracy of either an extremely fine grid or a higher order scheme. This is also true of any turbulence model employed. It is important, therefore, to prioritise the behaviour of the predicted flow field. An efficient CFD investigation will have ensured that those results that are to be utilised are grid independent. In the problem at hand the two primary parameters are plume rise height and its rate of dilution. This should be considered in the following discussion.

5.1.1 Single source

By far the simplest, and most common, form of tower arrangements is the single source. As much of the analysis of multiple plume interaction will be discussed with reference to that of a single plume it is essential that this configuration is modelled accurately.

Figure 5.1 shows temperature contours for the three grid densities of Cases 1, 2 and 3 (low, medium and high, respectively) using the hybrid scheme and k-ε turbulence model. It is this combination of parameters that can be viewed as the baseline model. Figure 5.2 shows temperature contours for Cases 4, 5 and 6; the same single source geometry, using the QUICK scheme. Graphs of the vertical profiles for all the single source grid sensitivity Cases (1–6) are shown in Figure 5.3. The rise height is defined as the location of the maximum temperature in the centre (on the physical symmetry plane) of the plume.

Results predicted when using the hybrid scheme are discussed first (see Figure 5.1). The first result to note is a marked decrease in plume rise with denser grids as well as a decrease in dilution rates at both downstream locations. Grid independent rise height is achieved at a lower grid density at x = 10D than at x = 40D. Rise height is almost grid independent at all three grid densities at x = 10D and at the two higher densities at x = 40D. Dilution levels on the other hand appear to be more sensitive to grid effects (there is greater change in peak dilution levels with a denser grid than there is with plume rise height as seen in Figure 5.3a). These levels become grid independent sooner (with respect to an increasing grid density) at x = 40D than at x = 10D and also reach the independent state earlier on the physical symmetry plane than through the thermal core. There is a grid-related effect that is smoothing, or diffusing, the thermal field near the source. This can attributed to the errors introduced when the flow is misaligned, or skewed, with respect to the predominant orthogonal grid orientation in the bending over region the plume experiences in the near-field. Even though the grid orientation was elevated in this area to accommodate the bending over and rising plume, near to the source errors are still apparent. At these full-scale Reynolds numbers (in the order of

10^6) cell Peclet numbers will always be greater than 2 (i.e. convection dominated) in the majority of the domain. The hybrid scheme uses first order accurate upwind differencing under these conditions (see Section 3.3.3.1). This, together with the skewed flow, results in excessive numerical diffusion and subsequent vertical spreading of the plume at x = 10D. Little or no grid-related spreading in the horizontal direction occurs as there is much less gradient curvature in this direction as well as a finer grid compared to the vertical grid density. This analysis of these spreading effects is further reinforced when studying the QUICK results.

At x = 40D the QUICK results have achieved grid independency much sooner than the hybrid results (see Figure 5.3d). There is little or no change for all three densities in both rise height and dilution at this downstream location. The results from both hybrid and QUICK calculations are identical at this downstream location. At x = 10D rise height prediction is also the same for both schemes on the symmetry plane. The main difference here between the hybrid and QUICK results is the dilution and spreading of the plume. Thermal core T^* values predicted by the QUICK scheme are 100% higher than those predicted by the hybrid scheme. The fundamental question at this stage is 'which scheme is the most accurate?' If there were sufficient cells in all areas of the domain, then grid independent results generated by both hybrid and QUICK should be identical, as indeed they are at x = 40D. However, this is not true at x = 10D. The answer to this lies in how QUICK captures high gradients on coarse, or skewed, grids such as those encountered between the source and x = 10D. At the upper part of the plume QUICK overpredicts the temperature gradient as well as predicting temperatures slightly below ambient at the plume boundary (an undershoot). Because of this the plume contracts, accelerates and the peak internal temperature increases accordingly. The solution to these grid-related problems is to ensure that there is a sufficiently dense grid (or one that is at least aligned with the main flow direction) at the thermal boundaries of the plume especially in the near-field. From a gridding perspective, with the computational resources available, this is not feasible. A pragmatic summary of the analysis is that grid independent and equal plume rise is predicted by both the hybrid and QUICK schemes, at both downstream locations, when using the medium density grid. Vertical spreading is overpredicted somewhat by the hybrid scheme near the source whilst comparatively high temperatures near the source occur when using the QUICK scheme. The validity of this reasoning is further reinforced when the small-scale results are studied and also when both the full and small-scale predictions are compared to the experimental data.

One trend of these grid tests is that plume rise *decreases* with an increase in grid density. This is contrary to usual understanding which dictates that any diffusion experienced by the plume, thus entraining cold ambient, should weigh the plume down thus deterring rise in coarse grids. The explanation of this apparent contradiction, and thus a greater understanding of the processes involved in plume bending, is formulated when analysing the grid independency results from a tandem arrangement.

5.1.1.1 Conclusions

- Increased vertical plume spreading is due to numerical diffusion in the relatively coarse grid region in the bending-over region close to the source. This is especially true when the upwind part of the hybrid discretisation scheme is used.
- Grid independency is achieved sooner when using QUICK than when using the hybrid scheme.
- Contraction of the plume when using QUICK leads to T^* peak levels twice as high as the hybrid predictions close to the source.
- Diffusion near the source leads to increased plume rise, not decreased rise due to entrainment of cold ambient.

5.1.2 Tandem sources

This arrangement was chosen to perform grid dependency tests as this source configuration theoretically results in the largest rise heights. To be able to capture the very high gradients from both sources near the tower top the grid density at higher y values does suffer (i.e. is coarser) especially vertically above the two towers. As parametric tests are to be performed on a number of source geometries it is important that the grid does not vary greatly from one geometry to another. Comparison of results can then be made without varying grid structures being blamed for any added differences. Three grid densities are again used with both the hybrid scheme (Table 4.1; Cases 13, 14 and 15) and also with the QUICK scheme (Table 4.1; Cases 16, 17 and 18). The results are presented in a similar fashion as the single source. Figure 5.4 shows the hybrid cross-section temperature contours on the y-z plane at x = 10D and x = 40D downstream, Figure 5.5 shows the QUICK results. Figure 5.6 presents the graphs of the vertical temperature profiles through both the centreline and 'peak' of the plume for both the hybrid and QUICK cases.

The hybrid results suffer from the same excessive vertical spreading as the single source. Not only is there a more complex arrangement of curved gradients with respect to the grid, but also, as there are two sources, the thermal gradients between the centre of the plume and ambient are much greater than the single source case. Also, bending-over occurs over a larger region that includes more coarse grid area. It is therefore not surprising that the spreading in this case is even more severe than the single source case. Again, the QUICK results do not suffer from this spreading but the thermal undershoot is predicted as well as the contracted cross-section and high peak temperatures. Grid independent dilution is not achieved anywhere, with either scheme. Unlike the single source there are two trends in grid dependent dilution. On the symmetry plane there is a decrease in temperature with progressively denser grids, whilst through the thermal core of the plume temperature is seen to increase. This is caused by the numerical diffusion of the velocity field and the subsequent inability to capture the vorticity within the two counter-rotating cells of the plume. These cells are responsible for maintaining the thermally bifurcated state of the plume cross-section. They are initially generated by the cross-wind as it is accelerated around the vertical plume near the source. This motion is then sustained by a buoyant up-flow in the centre of the plume and the down-flow at the cooler plume edges. The addition of diffusion, in this case numerical, although a diffusive turbulence model can also produce the same effect, causes the smoothing of this flow feature.

The most obvious grid-related effect in this case is the plume rise height. This is most apparent with the hybrid results where rise height is elevated to such an extent that the plume actually coincides with the symmetry plane at the top of the domain by x = 40D (see Figure 5.4d). With denser grids the plume does not rise as high, and also reduces in spreading, although never approaches a grid independent state. This behaviour is due to the vertical grid density between the tower top and the top of the domain. Whereas the middle density was sufficient for the single source, none of the three grid densities is high enough for this tandem arrangement. This is not surprising as the merging tandem plumes cover much more of the domain, and thus are prone to greater diffusive problems. The only difference between these grids and those used for the single source is the inclusion of the extra tower. To further obtain independent solutions for this tower arrangement three further grids are generated where additional cells are added only in the vertical section between the tower top and domain top. The six additional cases comprise of three modified grids used with the hybrid scheme (Table 4.1; Cases 19, 20 and 21) and the same three modified grids used with the QUICK scheme (Table 4.1;Cases 22, 23 and 24).

The results from these refined grids are presented in the same manner as the previous two geometries in Figures 5.7, 5.8 and 5.9. It is immediately apparent that the increase in grid density in the vertical region has resulted in grid independent rise for the QUICK scheme and near-independence for the hybrid scheme. The diffusion of the bifurcated structure of the plume is apparent with the hybrid results as there is an ongoing reduction in centreline and increase in core temperatures with increase densities. The QUICK results show independent dilution on the centreline and core independent solutions with the two finer grids. Indeed, there is hardly any difference at all between the two finer grid results using the QUICK scheme. It should be noted however that convergence stability using the finest grid and QUICK scheme (Case 24) was severely affected resulting in extremely excessive convergence times. Again, a pragmatic analysis results in the choice of the medium grid as a compromise between stability and accuracy. The QUICK results are totally grid independent although the hybrid predictions result in a 2% overestimation in rise height at x = 10D and a 17%

overestimation at x = 40D. From an engineering perspective these quantified inaccuracies can at most be equated to the inaccuracies in setting the source and cross-wind boundary conditions such as mass flow and enthalpy levels etc. It is assumed that the shape of the cross-section itself is grid independent though there is an upwards shift in rise due to numerical diffusion effects in the bending-over region. The cause for this shift, and how it highlights the main mechanism affecting plume trajectory, is further highlighted and finally explained after a final grid sensitivity test is performed.

A tandem source arrangement is used again although with a higher cross-wind velocity leading to an exit velocity ratio, R, of 1.0. The same grid as employed initially for the tandem arrangement is used again. Where it failed badly for the tandem sources with $R = 2.33$ it is envisaged that the results will achieve grid independency with the boundary conditions used. This is because there is a much shorter bending over region, thus less skew and coarse grid-related numerical diffusion errors, for the $R = 1.0$ case. The results are presented in a similar fashion in Figures 5.10, 5.11 and 5.12. Again, the hybrid scheme is used on the three grid densities (Table 4.1; Cases 7, 8 and 9) and compared to the QUICK results (Table 4.1; Cases 10, 11 and 12). Comparing the contour plots of both hybrid and QUICK results at x = 10D, it is apparent that although there is still vertical spreading on the upper section of the plume, the hybrid results are more comparable to the QUICK results. There is no thermal core temperature in these cases, the only peak in temperature lies on the symmetry plane. As the vertical section of the plume is so much shorter before it is bent-over due to the elevated cross-wind speeds there is little or no time for the vorticity to be generated within the plume itself. There is therefore no bifurcated structure. If the plume was more buoyant it could be that the bifurcated structure would develop further downstream but does not do so in this case. Rise height is grid independent for all grid densities, at both locations using either scheme. Whatever grid-related factor was causing an increase in plume rise on coarser grids is now not present. Both the non-bifurcated structure as well as the grid independence in rise overestimation are a product of the speed of which the plume bends over.

To investigate the grid dependence, or independence, in rise overestimation, and therefore understand the mechanisms that dominate plume trajectory, a graph is constructed from a horizontal line passing 1 m ($y = 2.1D$) above the tower top at the physical symmetry plane ($z = 0D$) for the single source case. This graph is shown in Figure 5.13. The lowest and highest grid densities are chosen using both the hybrid and QUICK schemes (Cases 1 and 3 then 4 and 6, respectively). Velocity in the x-direction is plotted together with the pressure (relative to a reference pressure at a point at the top of the oncoming atmospheric boundary layer) against x/D whose origin is at the windward side of the development duct. Plume bending in this region is dominated by the inviscid interaction of the cross-wind with the vertically issued plume. The pressure distribution both upstream and downstream of the source will therefore determine the forces acting on both sides of the plume, characterising initial bending. In reality this pressure distribution extends all along the plume edges in the bending over region. By looking at the profiles immediately adjacent to the source an understanding of the initial bending process can be gained. There is little or no difference in the upstream pressure gradient with either scheme on either grid density. It is the pressure variation between $0.75 < x/D < 1.5$ that is most sensitive to numerical diffusion. The diffusion contribution due to coarse grid regions reduces velocity gradients that in turn affect the predicted pressure variation. One component of the force bending the plume can be obtained from this pressure gradient. The pressure gradient in the wake region immediately behind the source is much the same for both grid densities when using the QUICK scheme, only the absolute value of pressure is shifted slightly. The hybrid scheme predicts a considerably steeper gradient when using the denser grid when compared to that predicted by the coarsest grid. The fact that these differences appear only in the wake region downstream of the source explains the grid independence of rise overestimation when using $R = 1$. In that case plume bending is achieved so quickly that there is hardly any wake region for these differences to manifest themselves. The velocity profiles show the strength of the recirculation behind the source and are also indicative of the strength of the vorticity within the plume itself. The stronger wake region predicted by the QUICK scheme explains the higher vorticity (i.e. a more thermally bifurcated structure) within the plume at further downstream locations. Although this line of analysis is not a direct explanation of the difference in rise for varying grid densities and the strength of the plumes vorticity, it is indicative of the processes and mechanisms involved.

5.1.2.1 Conclusions

- For the tandem arrangement greater excessive rise prediction for low grid densities is due to larger thermal gradients and bending-over in coarse grid region compared to the single source case.
- Numerical diffusion of vorticity field near to the source leads to less thermal bifurcation on lower grid densities.
- Increase in grid density between the tower top and domain top leads to grid independent plume rise and spreading for the QUICK scheme and near independence for the hybrid scheme.
- This modified grid density used in conjunction with the QUICK scheme results in a very unstable solution process and subsequent excessive solution times.
- There is a 17% overestimation in rise height when using the hybrid scheme at x = 40D but plume spreading and dilution are assumed to be grid independent.
- When $R = 1.0$ there is no thermal bifurcation as the rotational motion within the plume is not established in the very small bending-over region.
- Grid independent rise height is achieved for *all* grid densities and discretisation schemes for the tandem source arrangement when $R = 1.0$. This is due to the fast bending-over and associated lack of skewed flow with respect to the grid.
- Sensitivity to rise height prediction is due to differences in predicted gradients of speed and pressure in the wake region for different grids and discretisation schemes.

5.2 OTHER SENSITIVITY TESTS

Although commonly accepted parameters cannot be redefined with so little experimental validation data it is still important to investigate the sensitivity of the results to variations in these parameters. There is a large number of both empirically derived coefficients as well as additional equation terms in the governing equations used in this study. With most of these it is difficult to gauge their sensitivity to the results, there are however some that are obviously important or are subject to much debate in the literature. Three parameters are therefore investigated in this study to determine the effects of their inclusion or variation. These are the turbulent Prandtl number, the contribution of turbulence due to buoyancy in the standard *k*–ε turbulence model and plume source turbulence levels.

5.2.1 Turbulent Prandtl number

The theory of turbulence modelling has warranted a vast amount of research and study. Much of this has been centred on the calculation of both the shear and normal stresses in the momentum equation (i.e. Reynolds stresses) that are a result of velocity decomposition. In comparison, relatively little work has been carried out on the calculation of the velocity–enthalpy correlation (i.e. Reynolds fluxes) that determine the turbulent transport of thermal energy. The two-equation *k*–ε turbulence model leads to the calculation of an eddy viscosity. An eddy diffusivity is then defined that is related to the eddy viscosity via a constant turbulent Prandtl number (see Equation 3.46). The commonly accepted empirical value for the turbulent Prandtl number is 0.9. That is to say, for any quantified ability of a flow to transport momentum by turbulent fluctuations (i.e. eddy viscosity), thermal energy is transported due to turbulence more efficiently by a factor of Pr_T^{-1}. As the turbulent Prandtl number is constant this factor remains the same regardless of the value of the eddy viscosity. It is not the aim of this study to investigate the turbulent mechanisms by which momentum and thermal energy are transported. It is valid, however, to question the value of this constant and its range of applicability beyond the experimental conditions of its determination. Recent studies, including the work on renormalised group theory (Yakhot & Orszag, 1986), have seen more accurate predictions when a lower value of turbulent Prandtl number has been used. Tennekes (1981) also discussed the variation of Pr_T. Experimentally it is suggested that a value as low as 0.7 is valid for stable flows and that it decreases under unstable conditions. In high Reynolds number flows encountered in this study the turbulent Prandtl number is of critical importance in the accurate prediction of the temperature field. With diffusion, either numerical or due to turbulence, playing such a dominant role in the results any added diffusion due to a more efficient turbulent enthalpy field must be investigated fully.

Three values of turbulent Prandtl number are tested, i.e. 0.4, 0.6 and the standard value of 0.9. A wide range of values was chosen so as to determine not only the sensitivity of the results but to also to understand the trends of the predictions at extreme values. The baseline model of a single source with the k–ε model is used with both the hybrid scheme (Table 4.1; Cases 25, 26 and 27, $Pr_T = 0.4$, 0.6 and 0.9, respectively) and also with the QUICK scheme (Table 4.1; Cases 28, 29 and 30, $Pr_T = 0.4$, 0.6 and 0.9, respectively). Temperature contour plots are presented for the hybrid results in Figure 5.14 and QUICK results in Figure 5.15. Graphs of both vertical and horizontal temperature profiles are shown in Figure 5.16.

There is less additional turbulent thermal diffusion with the hybrid results than with QUICK for the two lower values of Pr_T as seen in Figures 5.14 and 5.15. The temperature gradients predicted when using the hybrid scheme have already been diffused slightly due to grid-related errors in the near-field. Any subsequent diffusion due to a lower turbulent Prandtl number (diffusion that is directly proportional to temperature gradients) is not as strong as the additional diffusion experienced by the much less diffusive QUICK scheme. The 34% reduction in Pr_T from 0.9 to 0.6 leads to a 4% reduction in peak temperature with the hybrid scheme but a 10% reduction with the QUICK scheme at x = 10D. By x = 40D this reduction has increased to 11% and 29%, respectively. This increase in the reduction of peak temperature further downstream is due to the spreading of the plume's own momentum and the subsequent dominance of turbulent diffusion. At x = 10D any reduction in peak temperature is compensated for by an increase in temperature on the symmetry plane. The bifurcated cross-section is being diffused away, against the action of the counter-rotating vortices. By x = 40D the bifurcated structure is absent when $Pr_T = 0.4$ using QUICK. These results have shown a strong sensitivity to a slight reduction in Pr_T even with the moderately buoyant plume under consideration here. A strongly buoyant plume, whose bifurcated structure is highly dependent upon the buoyant up-flow in the centre of the plume, would be severely sensitive to any reduction in Pr_T. The accuracy of a lower value of Pr_T will be re-examined when the computational results are compared with the experimental data.

5.2.1.1 Conclusions

- Reduction in Pr_T leads to greater dilution of the plume at x = 40D than at x = 10D due to the dominance of turbulent diffusion of the temperature field at the further downstream location.
- Increased thermal dilution at lower values of Pr_T when using the QUICK scheme is due to the less diffused thermal gradients to start with.

5.2.2 The constant C_3

Turbulence production due to buoyant flow is accommodated for in the *k* equation of the *k*–ε model by a production term, G (Equation 3.22). How the production term in the ε equation, affected by a stratified flow, is modelled is less exact. In the present study the standard modification of the ε equation (Equation 3.20) is employed. It has been noted in the literature that this modification should fail badly for bent-over plumes where the horizontal plume velocity results in negligible generation of ε due to buoyancy (Rodi, 1982). A single buoyant source is therefore modelled using the baseline case of the *k*–ε model and the hybrid scheme both including and excluding the constant C_3 through which the production of ε is included in Equation (3.20) (Table 4.1; Cases 2 and 31, respectively). The same geometry and discretisation scheme is also used with the full differential flux model, again, with and without C_3 (Table 4.1; Cases 52 and 32, respectively). The latter two cases are carried out to see if the more generic approach of this second order closure model is more sensitive to this constant than the two-equation model.

Temperature contours at x = 10D and x = 40D are shown in Figure 5.17. The two cases of $C_3 = 1$ and $C_3 = 0$ are shown side-by-side for both turbulence models. There is practically no difference at all in the predicted temperature field with the inclusion or exclusion of this constant for the boundary conditions used in this study. The only visible difference is in the differential flux results at x = 40D. Here there is a very slight increase in size of the inner contour of the plume (288.4 K) as it extends slightly closer to the physical symmetry plane. This variation, small as it is, is in keeping with the expected behaviour of the plume without the inclusion of C_3. When $C_3 = 0$ there is less production of energy dissipation in areas of stratification, ε does therefore not increase and so the eddy viscosity increases comparatively to when $C_3 = 1$. The resultant increase in eddy viscosity leads to greater mixing thus the more spread inner contour that is observed.

The dilution of the plume to approximately 0.5K above ambient by x = 40D results in very weak stratification in this downstream region. It is in this region though where turbulent entrainment of ambient dominates the plume's growth. In more buoyant sources it is therefore expected that the role of the constant C_3 and the modelling of turbulence production and destruction due to stratification will become far more critical than in the present study.

5.2.2.1 Conclusions

- Practically no sensitivity to the choice of C_3 is seen due to the high dilution rates, thus very low levels of stratification, at both x = 10D and x = 40D.

5.2.3 Source turbulence levels

Turbulence levels at the tower source are the only prescribed boundary conditions that are not available from the experimental work. To test the sensitivity of predicted plume trajectory and dilution three inlet turbulence intensity levels, namely 3, 6.3 and 12%, were chosen and corresponding values of k and ε were prescribed. Both the hybrid (Table 4.1; Cases 33, 34 and 35) and QUICK (Table 4.1; Cases 36, 37 and 38) discretisation schemes are used.

Two graphs that highlight the effect on the plume dilution and trajectory are presented in Figure 5.18. For clarity only the lowest and highest of the intensities are presented so that trends in the extreme may be analysed. The first graph shows vertical T^* profiles at x = 10D on the physical symmetry plane for both schemes and both intensities. As can be seen clearly, there is no difference at all in the predicted temperature profiles using either source intensity levels. To further investigate why this is so, another graph is presented showing vertical profiles of k and speed through the centre of the development duct on the physical symmetry plane. Again, there is no difference in the speed profiles for either intensity. Turbulence kinetic energy for the 12% intensity is seen to decrease slightly in the development duct. This is due to the initial top-hat velocity profile not being able to sustain such high levels of turbulence energy. The lower intensity produces levels of turbulence kinetic energy that are more in keeping with the lack of strain in the development duct and thus do not change at all within it. As soon as the plume interacts with the cross-flow the overall speed of the flow is reduced. Because of this high level of strain turbulent kinetic energy increases considerably due to the gradient hypothesis of Equation (3.12). The higher gradient of speed predicted by the QUICK scheme results in higher levels of k. Above this strain region all values of k converge to the same level. For the prescribed levels of turbulence used the creation of turbulent kinetic energy in the bulk flow is a result of the strain produced by the inviscid interaction of plume and cross-wind. For the levels investigated they do not have a direct bearing on either the velocity or the temperature fields. If extremely high levels were set at the tower source and convected in the initial interaction region they could go on to diffuse strains and thus affect the resulting plume trajectory and dilution. The middle value of 6.3% was chosen as it is high enough to aid iterative convergence yet low enough not to affect subsequent plume development.

5.2.3.1 Conclusions

- No sensitivity was seen on plume trajectory and dilution for source turbulence intensity levels of 3% and 12% set at the tower source.
- Mean strains, where the plume interacts with the cross-wind, generate turbulent levels that dominate the turbulence convected up from the source.

5.3 COMPARISON WITH EXPERIMENTAL DATA

There are three main aims in the analysis of the bulk of the work in this study. They are firstly to compare the computational predictions with the experimental data, secondly to gain an understanding of the performance of discretisation scheme and turbulence model. The third aim is obtain a better understanding of the interaction mechanism between adjacent plumes. Three cooling tower arrays in both small and full-scales are modelled (see Table 4.2). For ease of comparison the results are presented in a standardised way for each geometry. The contours of plume cross-section temperature are plotted on the y-z plane at the two downstream locations where the experimental data was recorded (x = 10D and x = 40D). The experimental profiles were said to be taken through the location of the highest plume concentration at both downstream locations (see Section 4.2.2). Where this location differs from the location of the computational thermal core, additional profiles are plotted to gauge any increase in comparative accuracy. Therefore, vertical and horizontal lines are superimposed onto these contour plots to indicate the location of the recorded experimental concentration profiles as well lines bisecting the thermal core of the plume cross-section should the latter be in a different location. Four graphs are then included showing vertical concentrations at the two downstream locations as well as the two corresponding horizontal profiles. It is on these graphs that the experimental data is also plotted to investigate the accuracy of the computational model in the small-scale and the accuracy of the wind tunnel scaling assumptions when compared with the full-scale computational results. Velocity vectors and temperature contours are then plotted on the physical symmetry plane for the single and tandem sources. These plots are not included for the side-by-side arrangements as the physical symmetry plane is not common to all stages of the interaction process. Finally, both velocity vectors and temperature contours are plotted on four planes in the near-field, close to the tower. The locations of these planes are shown in Figure 5.19. By understanding the velocity and temperature fields in the near-field, explanations as to the behaviour and accuracy of the different models and schemes at x = 10D and x = 40D may be formulated.

5.3.1 Small-scale work

The small-scale work is presented and discussed first. For each of the three arrays two discretisation schemes are used, hybrid and QUICK. Because of the nature of the low Reynolds numbers encountered in some areas of the flow only one turbulence model is used, namely the low Reynolds number turbulence model (see Section 3.2.1.3). The analysis therefore highlights the differing performances of the two forms of discretisation as well as the general accuracy of the turbulence model via comparison with the experimental data.

5.3.1.1 Single source

Cross-section temperature contours are shown in Figure 5.20. In consideration of this, and the subsequent plots of this type, good agreement with experiment can be seen when there are no dotted blue lines present. Under these circumstances the location of the computational thermal core coincides exactly with the experimental position. In this case of a single source the lateral offset of the core is the same with both schemes and experiment at x = 10D. However, the experimental vertical location is lower. At x = 40D both vertical and horizontal locations differ, although only slightly. There is very little difference between the two schemes compared to the differences observed during the grid sensitivity tests. This is due to the increase in grid density at the tower top, necessitated by integration direct to the wall, and subsequent higher density between tower top and top symmetry plane. Indeed, by x = 40D there is little difference between them at all. Also, the lower Reynolds numbers of the small-scale result in the reduction of cell Peclet numbers. Under these conditions (i.e. when the Peclet number falls below 2) the hybrid scheme uses second order accurate central differencing. The combination therefore of a gridded tower top boundary layer and the more frequent use of a higher order discretisation leads to the greater similarity of the hybrid results when compared to QUICK. The remaining difference is near the source where QUICK predicts higher temperatures (T^* values 45% higher than hybrid at x = 10D). There is no physical undershoot due to a sufficiently high grid in the extremely high gradient regions at the source/cross-wind interaction. Comparison with the grid sensitivity tests of Figure 5.2 shows a much cooler thermal core in the small-scale using QUICK. It appears that when the QUICK scheme encounters coarse grid regions it is likely to predict an undershoot, in this case in temperature, and also an overshoot in the core of the plume as seen in the full-scale sensitivity work. This is in keeping with the findings of Klimetzek, (1996), who noted an inaccuracy of higher order unbounded schemes used in conjunction with coarse and skewed grids. The higher grid density used in the small-scale work suffers less from these problems than the full-scale computations, although there still exists the higher core temperatures.

The quantified comparison with the experimental results is shown in Figure 5.21. The lateral and vertical offsets, for the vertical and horizontal profiles, respectively, in the figure caption refer to the exact location at which the experimental data were recorded. If these are different from the location of the computational thermal core a profile through the latter is also included, drawn as a dotted line and referred to as 'peak'. When judging the accuracy of the computational model there are three plume parameters that can be compared. These are rise height, dilution and spreading. The rise height of the wind tunnel plumes have been calculated by curve fitting the experimental data and noting the resultant peak. Computational rise height is determined by the vertical location of the peak in temperature of the T^* profile. A summary of rise height comparisons for the small-scale work is shown at the end of this chapter in Table 5.1 (the empirical rise heights will be compared and discussed in Section 5.5). Results are presented in multiples of source diameter, the comparative percentage accuracy is also included. The overestimation in rise height of 8 and 13% at x = 10D by the hybrid and QUICK results respectively can be viewed as good agreement with the experiment, especially from an engineering perspective. The rise heights at x = 40D are of the same accuracy. The higher peak temperatures at x = 10D for the QUICK results, but similar plume cross-sectional areas compared to the cooler hybrid results, means that the QUICK plume has contracted and accelerated near to the source. This is so that global thermal continuity throughout the solution domain is maintained (i.e. the enthalpy residuals at the end of the iterative solution process were very close to zero for both hybrid and QUICK cases). This behaviour is discussed shortly.

The accuracy of the shape of the cross-section can be determined by studying the horizontal temperature profiles (Figure 5.21c, d). At x = 10D the horizontal profiles through the thermal core are in excellent agreement with the experimental data. The apparent overestimation of temperature in the thermal core for both hybrid and QUICK predictions may be a result of the spatial inaccuracy of the experimental measuring method. At x = 10D the shape of the cross-section can be said to be correct, although the rise height is overpredicted by approximately 1D (Figure 5.21a). At x = 40D rise height is again overpredicted by about 1D (Figure 5.21b) although there is good agreement for the dilution which is as low as 2% of source levels ($T^* = 0.02$). The horizontal profiles (Figure 5.21c) of this, and all subsequent cases, appear to underestimate the horizontal spreading of the plume at this further downstream location. The actual location where T^* becomes zero is almost identical for both experiment and computational results. The shape of the horizontal profile, however, is very different for both. The computational profile is Gaussian but the experimental profile is much broader in the centre of the plume, quickly decreasing towards the edges. Further analysis of this phenomena is given when both small and full-scales have been studied. It is too soon to accurately determine the cause for this discrepancy.

The velocity and temperature fields on the physical symmetry plane is shown in Figure 5.22. Figure 5.23 shows these vectors and temperature contours on the four planes defined in Figure 5.19. Where specific points on these figures are referenced a i, ii, iii etc. is included in both the text (e.g. Figure 5.23a–i) and also on the figure itself. The differences between the results for Case 39 (hybrid) and Case 40 (QUICK) can be attributed to the concepts of gradient capturing and grid-related diffusion. The plume predicted by QUICK maintains high velocities (i.e. > 1 m/s) for far longer than the hybrid plume. This leads to a contraction of the thermal plume. In turn this leads to a higher recirculation behind the vertical section of the plume (Figure 5.22–i). Dilution and vertical spreading on the symmetry plane occurs faster with the hybrid plume. The reasons for this are apparent with reference to Figure 5.23. Higher velocity gradients are predicted in the recirculation region behind the vertical section of the plume using QUICK (Figure 5.23a–i). In spite of this, as well as slightly higher velocities approaching the plume from the leading edge of the tower, it is the hybrid results that show greater spreading of the temperature field. By the 45° plane (Figure 5.23b), it is evident that the hybrid plume has spread further away from the symmetry plane than the QUICK plume. The reasons for this depend upon the formation of a recirculation zone behind the core of the momentum plume (Figure 5.23b–ii) that goes on to develop into the characteristic counter-rotating vortex pair. When this recirculation forms behind the slower and weaker hybrid plume, the thermal core diffuses into the vortex (Figure 5.23b–iii). Even though a stronger recirculation forms behind the QUICK momentum plume, less plume material is drawn into it compared to the hybrid case (Figure 5.23b–iv). By x = 1D the stronger QUICK recirculation, now becoming part of the counter-rotating vortex pair, has resulted in a more bifurcated cross-section. A stronger up-flow through the centre of the plume maintains a contracted cross-section, although plume material has started to be convected into the centre of the vortex (Figure 5.23c–v). By x = 5D both cross-sections look almost identical. The QUICK plume has a higher temperature in the thermal core that persists beyond the x = 10D experimental comparison location. The reason for this, i.e. the interaction between plume wake recirculation and the momentum plume in the near-field, has now been determined. This is an advance upon more basic analyses that would have relied purely on the more diffusive nature of the hybrid scheme in explaining the higher dilution rates.

5.3.1.1.1 Conclusions

- Plume cross-sections are more similar at x = 10D using hybrid and QUICK schemes than in the full-scale sensitivity comparisons. This is due to higher grid densities in the boundary layer at the tower top and also greater use of central differencing at these lower levels of cell Peclet numbers in this low Reynolds number environment.
- There is good agreement for plume dilution levels at x = 40D compared with the experimental data. Spreading is underpredicted at the horizontal plume boundaries.
- The plume predicted by the QUICK scheme is more contracted, sustaining higher velocity and levels of vorticity than the hybrid predictions.
- The thermal core of the QUICK plume does not diffuse into the rotating vortex part of the cross-section, unlike the hybrid case, at x = 10D. By x = 40D the near-field differences between both schemes have diminished considerably.

5.3.1.2 Side-by-side sources

This tower configuration is the most simple adaptation of the single source. Experimentally, rise will not be enhanced as efficiently compared to when two sources are positioned behind each other. The reasons for this lack of 'merging efficiency' will be determined through the analysis in this section.

Temperature contour plots at x = 10D and x = 40D are shown in Figure 5.24. The hybrid solution is Case 41 whilst the QUICK solution is Case 42. The cross-section shape at x = 10D is again very alike for both schemes. The QUICK scheme predicts higher thermal core temperatures than hybrid and is also slightly more contracted. At x = 40D the two cross-sections are almost identical. There is good agreement between computational and experimental rise height, thus the absence of any horizontal blue dotted lines in Figure 5.24. The horizontal location of the thermal core is positioned nearer the physical symmetry plane in the experiments than predicted computationally. This may, in part, be due to the increased width of the combined plume and therefore less defined horizontal peak location. When comparing Figure 5.24 with Figure 5.20

(single source) the delay in plume interaction with side-by-side sources can be clearly seen. There is a similarity in shape between Figures 5.20a and 5.24b. It takes at least another 30D for the side-by-side sources to merge into a single plume (characterised by the bifurcated cross-section of a single source) compared to the case of the single source. The reason for this delay, or inefficiency of interaction, is partly due to the fact that the inner sides of the adjacent plumes will only coincide after each has grown due to turbulent entrainment of ambient. The other reason is due to the velocity, or rather vortex, field and will be discussed after the quantified comparison with the experimental data.

Vertical and horizontal profiles of temperature are shown in Figure 5.25. The vertical profiles at x = 10D (Figure 5.25a) show excellent agreement in the vertical width of the plume, especially at the lower, buoyantly stable, side. The QUICK scheme predicts a steeper gradient at the top surface compared to the hybrid solution. Both schemes predict higher core temperatures, although the QUICK peak is only 25% higher. The underestimation in the spreading at the top side of the plume at x = 10D is extenuated at x = 40D. Both schemes predict the lower plume surface accurately though the experimental plume experiences much more mixing at the top surface. Computationally, the only way of accommodating increased mixing due to a thermally unstable layer is via the production term **G** (see Equation 3.22) in the turbulent kinetic energy equation. As noted by Tennekes (1981) the value of the turbulent Prandtl number decreases with an increase in instability, which results in a spreading of the temperature field (see Section 5.2.1). If Pr_T were allowed to vary in proportion with a stability parameter (such as the Richardson number) this would in turn allow more spreading on the top surface of the plume. The problems of numerical diffusion in the coarse and skewed grid region in the near-field produced increased diffusion on the top surface of the plume in the full-scale grid sensitivity tests (see Section 5.1.1). The consequence can be seen as a cancelling out of effects. The less diffusive Pr_T value of 0.9 is compensated for by the combination of diffusive grids and schemes. The decrease in numerical diffusion in this small-scale work highlights this effect. These effects are more dominant when there is a wide horizontal top plume surface from which unstable spreading can occur. Prediction of rise height is again in good agreement with the experimental data (Table 5.1) with differences of less than 7% at x = 10D and 11% at x = 40D. The horizontal profiles are also in good agreement (Figure 5.25c, d). The predicted centre line temperatures match exactly with experiment at both x = 10D and x = 40D. The horizontal profiles seem to capture the peak in temperature whilst the experimental points either miss the exact location of the peak or smooth it somewhat. The horizontal profile at x = 40D provides the most accurate comparison with the experimental data in this study.

The near-field velocity vectors and temperature contours are shown in Figure 5.26. The cross-wind is accelerated not only around the sides of the two sources, but also in between them. This causes the reattachment point to be shifted (Figure 5.26a–i) when compared to the single source case. The accelerated flow between both sources and the resulting recirculation limits the size of the inner vortices compared to the growth of the outer vortices at the 45° plane (Figure 5.26b–ii). The QUICK solution increases this effect by the prediction of a faster plume (Figure 5.26b–iii) and stronger recirculation that also produces a more bifurcated structure at this location (Figure 5.26b–iv). By x = 1D (Figure 5.26c) the two vortices predicted by QUICK are much stronger and more contracted than those predicted by the hybrid scheme. There is a larger inflow through the bottom of the plume (Figure 5.26c–v) which, together with the stronger vortices, maintain the outer lobes of the cross-section compared to hybrid (Figure 5.26c–vi). By x = 5D (Figure 5.26d) the QUICK cross-section still has a more bifurcated structure and is less spread than the hybrid solution. In general, the inability of the hybrid scheme to capture the high swirling velocity gradients leads to the diffusion of the temperature field into regions of lower velocity. The higher velocity gradients of the QUICK solution maintain a more concentrated thermal cross-section.

Efficient merging of adjacent sources would entail a fast mixing of each plume's thermal material before such time as turbulent entrainment cools the thermal core. To explain the interaction process an analysis of the interaction at the physical symmetry plane is therefore required. Up until, and including, the 45° plane, the cross-wind penetrates between the two plumes. After bending over is completed the mixing of the two plumes is due solely to the interaction of the two inner vortices. The conflict and reorganisation stage of Figure 2.3 refers to this part of the interaction process. The down-flow of the inner vortices at the symmetry plane is counteracted by the buoyant body force generated by the high temperatures at this location. Mixing is then determined by the strength of the weakening inner vortex and the diffusion of the temperature field across the symmetry plane. Figure 5.26c illustrates this point well. The stronger inner vortex predicted by QUICK results in higher velocities at the symmetry plane. This contracts the temperature gradients away from the physical symmetry plane. The hybrid results predict a weaker vortex that allows the increased diffusion across the symmetry plane leading to greater mixing at an earlier stage. Although the hybrid side-by-side results show the expected diffusion, in this case it leads to a decrease in the ratio of plume surface area to cross-sectional area of the merged plumes compared to the large surface area of the still distinct two single plumes predicted by QUICK. As dilution is proportional to this ratio this explains the smaller difference between hybrid and QUICK temperatures (Figure 5.26d) than predicted with a single source (Figure 5.23d).

5.3.1.2.1 Conclusions

- Merging of adjacent side-by-side sources into a single type cross-section does not occur until x = 40D.
- Spreading from the plume upper surface is underpredicted by the computational model. This behaviour is amplified due to the much wider top surface of the side-by-side merging plumes.
- Higher vorticity levels predicted by the QUICK scheme leads to a more contracted, bifurcated plume, especially near the symmetry plane.
- Plume interaction is dominated by the conflict and reorganisation stage in Figure 2.3 as the bent-over plumes begin to merge at the symmetry plane. Merging at this location is dominated by the predicted strength of the inner rotating vortices.

5.3.1.3 Tandem sources

Two sources positioned behind each other with respect to the oncoming cross-wind is the final double tower arrangement. Experimentally this combination offers the most efficient rise enhancement. Why this is so will be determined in this section.

Temperature contours at the location of the experimental profiles are shown in Figure 5.27. At x = 10D there is good agreement for the location of the lateral offset of the thermal core, although rise height is overpredicted. At x = 40D rise height is predicted well but the predicted thermal core is slightly further from the symmetry plane. With side-by-side sources a single plume-like cross-section did not develop until at least x = 40D. With tandem sources, however, a single combined-type plume is apparent at x = 10D. This is indicative of the more efficient mixing and greater rise enhancement obtained with tandem sources compared to the side-by-side case. The trend of higher temperatures and a more contracted cross-section of the QUICK results is maintained at x = 10D. Compared to previous results for the first time, at x = 40D, the hybrid results show a very slight increase in core temperature over the QUICK results.

The vertical and horizontal profiles are shown in Figure 5.28. Although the predictions of rise height are less accurate at x = 10D than the results so far (Table 5.1) the vertical width of the plume is captured well, both at the lower and upper boundaries, by both schemes. The computational model predicts the thermal core above the centre point of the vertical cross-section. Experimentally the vertical profile is more symmetrical. At x = 40D the agreement for rise height is to within 3% (Table 5.1). The bottom section of the plume is captured well, although at the top there is again a lack of vertical spreading. All horizontal computational profiles show narrower plumes than were experimentally measured (Figure 5.28c, d). At x = 10D neither the experimental nor the peak location profiles are in good agreement with experiment. At x = 40D the shape of the horizontal computational profile is more like the experimental data, although again narrower. Once merging has been completed and the cross-section settles down to that of purely a single source then the agreement between experiment and computation is improved. As both hybrid and QUICK results are similar in shape and have the expected differences in temperature, the reason for the apparent inaccuracy at x = 10D lies in the turbulence model. So far little has been said about the mathematical accommodation of turbulent diffusion because the main differences and inaccuracies in the results were due to the discretisation schemes. The flow field of this tandem arrangement contains the most complex strains encountered so far. Under these conditions any two-equation model will suffer due to the isotropic assumption upon which it is based. The reason why it fails will require comparison to more advanced turbulence models. This is done when the full-scale is modelled.

The velocity and temperature fields on the physical symmetry plane is shown in Figure 5.29. The QUICK results once again predict higher velocities within both plumes and a subsequent contraction (Figure 5.29b). Both the recirculation between the two sources (Figure 5.29a–i) as well as the larger recirculation behind the downstream source (Figure 5.29a–ii) are stronger and vertically more persistent when the QUICK scheme is used. This decreases the amount of thermal diffusion in these areas when compared to the hybrid results. The shielding that the upstream plume offers the downstream plume near to the source is one of the primary mechanisms of rise enhancement. As there is little difference between the two schemes in plume rise height at x = 10D and x = 40D then this form of enhancement is not affected by the slight diffusion of the temperature field seen in the hybrid results. This shielding is purely due to the inviscid interaction of plume and cross-wind. The other near-field vectors and contours are shown in Figure 5.30. Figure 5.30a shows very little difference in the velocity fields. The increase in thermal diffusion of the hybrid results (Figure 5.30a–i) does indicate that scheme's inability to capture the reverse velocities as well as the QUICK scheme. The QUICK scheme also predicts a larger recirculation behind the downstream plume in Figure 5.30a–ii. By the 45° plane there is only one distinct cross-section visible. There is a small lobe on the QUICK cross-section (Figure 5.30b–iii) that coincides with the point highlighted by Figure 5.30a–ii. By x = 1D this lobe is more apparent (Figure 5.30c–iv) and is reinforced by the less diffused vortex predicted by QUICK. By x = 5D the effect of the weaker vortex inflow predicted by the hybrid scheme (Figure 5.30d–v) can be seen in the higher temperatures in that region when compared to QUICK. The second mechanism of rise enhancement is the reinforced buoyant up-flow in the centre of the combined plumes. The vertical velocities at the physical symmetry plane in Figures 5.30c and d are approximately twice as big as those of the single source plume (see Figure 5.23c, d). The vertical velocity at the symmetry plane for the side-by-side sources at the same locations (see Figure 5.26c, d) is almost zero. Apart from a reduction in the rate of dilution, this has demonstrated the increased effect of buoyancy and subsequent high rise generated when the plumes merge in the early stages of their trajectory.

5.3.1.3.1 Conclusions

- Efficient merging of the plume is seen by the prediction of a single plume type cross-section by x = 10D.
- The plume predicted by the QUICK scheme is more rounded and contracted at x = 10D. By x = 40D the difference between the QUICK and hybrid predictions has disappeared.
- Discrepancies in the accuracy between QUICK and hybrid results and the experimental data may be attributed to turbulence model deficiency.
- Rise enhancement is due to two factors. Firstly, the upwind source offers the downstream source an inviscid shielding against the oncoming cross-wind. Secondly, there is an increased buoyant up-flow due to the lower dilution rates seen in the merged plume close to the source.

5.3.2 Full-scale work

The full-scale computational study bypasses the scaling assumptions upon which the wind tunnel work relies. Potentially this approach will produce results that will bear greater resemblance to the real-life situation. As in the wind tunnel work, the full-scale plume is still assumed to be dry. A real cooling tower plume will contain water in both droplet and saturated states, during rise latent heat is released that will aid buoyancy thus increasing rise. There will still remain differences therefore between this computational study and an actual plume. In the full-scale, Reynolds numbers in the order of 10^6 are encountered. Unlike the wind tunnel work that contained both fully turbulent as well as transitional states, the full-scale falls well into the fully turbulent regime. From a modelling perspective this enables the use of some of the many turbulence models available. The problem at hand contains buoyancy, swirl and streamline curvature, all complex types of flow that can lead to anisotropic turbulence and are common to many engineering applications. The analysis of the relative performance of different models used in this study will enable informed choice of certain models in other studies containing similar complex fields. The relative accuracy of these models compared to the experimental data will be less clear. Not only can the full-scale predictions suffer from slight numerical diffusion in the near-field but also the full-scale Reynolds numbers may produce flow fields, especially in the cooling tower wake, that cannot be scaled accurately to those found in the small-scale. The experimental data is still included though to highlight areas where the differences are substantial. The results are presented in the same fashion as the small-scale work. The order in which plots are presented across the page at the various planes is consistent throughout. To minimise reference to Table 4.2 the order is as follows:

k–ε model hybrid scheme	k–ε model QUICK scheme	RNG k–ε model hybrid scheme	DFM hybrid scheme

5.3.2.1 Non-buoyant single source

The simplest of cases studied in both scales is the single tower with a jet like ($Fr = \infty$) source. Temperature is still solved for, but buoyancy is ignored. In this case the temperature field acts as a passive contaminant. The temperature field is simply representative of the convected and diffused momentum field.

Temperature contours at x = 10D (100m) and x = 40D (400m) are shown in Figure 5.31. Rise height for all four combinations of model and scheme are in excellent agreement with the experimental prediction at x = 10D. All hybrid cases suffer from the numerical diffusion of the upper section of the plume encountered in the grid sensitivity tests. It should be noted at this stage that this apparently extreme diffusion only affects the outer four or five contours (288-288.3K). For the rest, the shape of the cross-section resemble, much more closely, the cross-section as predicted by QUICK. The excess temperature at the thermal core of the QUICK results at x = 10D are present and are attributed to the overshoot due to the behaviour of this third order accurate scheme in coarse and skewed grid regions near the source. The RNG based turbulence model predicts a bifurcated structure at x = 10D, unlike any of the other cases. The modifications to the standard k-ε model that comprise the RNG form are especially suited to flows with high rates of strain such as the ones encountered here. The similarity of the RNG k–ε model results compared to the DFM, and conversely the differences between standard k–ε model results and the RNG form, are of critical interest in evaluating the accuracy and efficiency of these models throughout the full-scale analysis. With this in mind, the RNG results at both x = 10D and x = 40D bears slightly more resemblance to the DFM results than the standard k–ε model. Both RNG and DFM have a more contracted bottom section compared to the k–ε model. The QUICK cross-section is much more rounded and, although the height of the thermal peak is the same as the other cases, the bottom of the plume extends closer to the ground. By x = 40D the slight differences at x = 10D have been exaggerated. As there is no aid by buoyancy after the plume has bent-over, the plume shape and position at this location will be strongly dependent upon that closer to the source. The hybrid k-ε and DFM cases are in good agreement for rise height, QUICK is lower and RNG is higher. There is no lateral offset of the thermal core for all computational predictions at x = 40D (all thermal cores are on the physical symmetry plane). The experimental location is far to one side. This wide offset, under these circumstances where a buoyancy aided bifurcated section is not expected, could be due to drift within the wind tunnel. At both x = 10D and x = 40D the RNG case has exhibited similar features as the DFM, only more exaggerated. It may be that the modifications to accurately capture anisotropic behaviour overcompensate under other conditions. Further study of the other tower arrangements will explore this behaviour.

The quantified comparison to the experimental data is shown in Figure 5.32. When comparing both the experimental and computational profiles the difference in Reynolds number between the two scales must not be ignored. Although it is known that there is little or no effect upon plume trajectory due to atmospheric turbulence until very far downstream, there is a marked change in the structure of the tower wake from transitional to fully turbulent regimes. A non-buoyant plume is more likely to suffer from downwash than a buoyant source. This interaction with the tower wake may invalidate the comparison between predicted and experimental results in this case. The vertical profiles at x = 10D (Figure 5.32a) show the smoothed thermal gradient on the top surface of the plume when the hybrid scheme is used. The QUICK scheme appears to capture the top part of the cross-section but predicts a peak temperature twice as large as the hybrid results. The similarity between RNG and DFM results at x = 10D is clear, although the lack of spreading on the plume underside with these two models seems to be contrary to the experimental measurements. At x = 40D there is a large difference between the lateral location of the plume core between prediction and experiment (see Figure 5.31b). The computational physical symmetry vertical profiles are in closer agreement with experiment and so the offset may be a product of wind tunnel drift or measuring error. The QUICK scheme predicts the ground level concentration correctly but predicts a low rise height. The hybrid results are in closer agreement with the more spread experimental data. The agreement seen in Table 5.2 for the rise height prediction at both locations is highly accurate considering the possible discrepancies due to Reynolds number differences. Indeed, the lower rise height predicted by QUICK may in fact be a more accurate representation of plume-wake interaction in the full-scale. The diffusive hybrid scheme appears to predict a full-scale tower wake that is more like the small-scale case and so results in greater comparative accuracy between the two scales.

The horizontal profiles show a lack of spreading of the hybrid plumes compared to the QUICK profiles (Figure 5.32c, d). At x = 40D it is the RNG profile that has maintained the hottest thermal core, even more so than QUICK, and is the most inaccurate. All of the other cases are in relatively good agreement for horizontal spreading at this location. The reasons for the differences between RNG and the other cases is explored when studying the symmetry plane velocity vectors and temperature contours in Figure 5.33 and the near-field planes in Figure 5.34.

The plume wake predicted by both RNG and DFM turbulence models is stronger than the standard k–ε model as seen in Figure 5.33c–i compared to the equivalent location in Figures 5.33a, b. It is this that results in the lack of spreading on the plume underside with these two models further downstream. The plume wake structure predicted by QUICK at the leeward edge of the tower is very different from the hybrid predictions (see Figure 5.33b–ii). These features can be further understood by examining the cross-sectional planes in Figure 5.34.

The wake structure behind the plume predicted by the RNG and DFM models is clearly seen (Figure 5.34a–i). The higher wake velocities predicted by QUICK seen in Figure 5.33b–ii are also seen in Figure 5.34a–ii and are due to the higher velocities predicted as the cross-wind is accelerated around the side of the source (see Figure 5.34a–iii). It is this attribute of the QUICK scheme to capture these velocities that are aligned more horizontally (i.e. higher w velocities) to the main flow direction that results in the wider QUICK plume already noted. By the 45° plane this is even more apparent in the rounder vortex with higher w velocities, as shown in Figure 5.34b–iv. The stronger wake vortex that 'pinches' the thermal cross-section on the symmetry plane predicted by RNG and DFM is seen in Figure 5.34b–v. Here there are reverse velocities in the order of 1 m/s compared to an almost stagnant flow at this location predicted by the standard k-ε model. At $x = 1D$ the differences in both tower wake and plume vortex as predicted by the four cases is clear (Figure 5.34c). The dominance of higher w velocities predicted by QUICK and the subsequent wider vortex (Figure 5.34c–vi) determine the thermal structure. The lack of diffusion on the upper surface of the plume in this coarser grid region is also apparent (see Figure 5.34c–vii). The RNG tower wake is much like that predicted by the DFM with a very strong up-flow on the symmetry plane all the way through the plume (Figure 5.34c–viii). The RNG scheme predicts a continuation of the plume wake vortex highlighted in Figure 5.34a–i (Figure 5.34c–ix). The DFM predicts a relatively low velocity at this location, although this wake has nearly vanished. There is more spreading on the lower right section of the plume (Figure 5.34c–x) than the RNG case. By x = 5D the cross-sections are similar to those seen at x = 10D. The RNG counter-rotating vortex is still persistent (Figure 5.34b–xi) and it is this that results in the bifurcated structure at x = 10D and the horizontal contraction at x = 40D. The wider QUICK counter-rotating vortex has now diminished as it loses the bifurcated structure. The larger *w* velocities were a result of the ability of this scheme to capture cross-flow gradients of the counter-rotating vortices that are created by the cross-wind and vertical plume interaction close to the source.

These non-buoyant cases detach the effect of temperature induced rise from the velocity field. The differences in prediction of temperature do therefore not affect the plume's trajectory. The performance of the velocity field prediction for the different models and schemes has been explained without the added complexity of the effects of buoyancy. How the four combinations of scheme and model perform when the source is plume like is examined in the next section.

5.3.2.1.1 Conclusions

- The QUICK plume predicts temperatures 80% higher in the thermal core of the plume compared to all hybrid cases. This difference vanishes by x = 40D.
- The RNG plume alone predicts a bifurcated thermal structure at both x = 10D and x = 40D.
- Both RNG and DFM models predict a more pronounced plume wake recirculation and a strong rotating flow on the underside of the plume at x = 10D.
- Non-buoyant plume rise in the near-field is dominated by tower wake interaction and so differences in the prediction of the flow in this region by the four models result in the differing rise predictions.

5.3.2.2 Buoyant single source

Temperature contours at x = 10D and x = 40D are shown in Figure 5.35. At x = 10D all four cases predict the lateral and the vertical location of the thermal core accurately. At x = 40D the QUICK scheme predicts a lower rise height than experiment, whilst all but the RNG model predict the lateral offset of the thermal core accurately. Compared to the equivalent non-buoyant cases in Figure 5.31, there is a much wider difference between the results especially at x = 40D. This is especially true of the RNG and DFM results. The theoretical accuracy of the DFM and the simplicity of the standard k-ε model should bound the predictions of the modified RNG k-ε model. In this case, however, the RNG results are very different than both k-ε model and DFM. Exactly why this is so will be covered in Section 5.4.

Figure 5.36 shows the comparison with the experimental data. The trend of the QUICK scheme to capture the top surface of the plume is apparent, as is the overprediction of core temperature. The top surface is diffused when the hybrid scheme is used, although the RNG model predicts less spreading than both the standard k-ε model and DFM. By x = 40D the differences between the cases is very apparent. Both standard k-ε model and DFM predict much higher rise than QUICK and the RNG model. The accuracy of these predictions is dependent upon the scaling assumptions used for the wind tunnel work. The difference in Reynolds number between the two scales will not be as critical in this case as it was in the downwash affected non-buoyant case. It appears that the RNG k-ε model is on average more accurate than the other three cases. This is a result of diffusion effects, both numerical and turbulent, that the plume experiences. The lower rise height of the RNG model at x = 40D may be due to the same non-diffusive behaviour than the QUICK scheme. The horizontal profiles again show RNG to be more accurate especially at x = 10D. The RNG model predicts a wider plume at both downstream locations, even more so than QUICK at x = 40D. The non-buoyant results showed QUICK's ability to predict high lateral velocities within the counter-rotating vortex that created a more rounded thermal cross-section. It is possible that the same is happening here with RNG or more probably it is due to higher levels of predicted lateral turbulent diffusion and spreading of the plume.

The physical symmetry plane velocity vectors and temperature contours are shown in Figure 5.37. Compared to the cross-sectional profiles of Figure 5.38 relatively little understanding can be gained form these plots. The two main differences already highlighted in Figure 5.33 are also present in this buoyant case. Figure 5.37b–i shows the different wake structure as predicted by QUICK compared with the hybrid results. The similarity between RNG and DFM predictions in the plume wake and up-flow region into the lower side of the plume for the non-buoyant case is not as strong for this buoyant source. The recirculation region in Figure 5.37c–ii, and in the entire tower wake in general, is more similar to the standard k-ε model than to the DFM. The second order closure model predicts a stronger reversed flow than all other cases (Figure 5.37d–iii). At this stage it is not obvious as to whether this variation in the prediction of the wake and recirculation is responsible for the large differences in rise height further downstream. To understand more fully why rise varies so much at x = 40D the near-field is presented in y-z plane cross-section in Figure 5.38.

The cross-wind is accelerated much faster around the QUICK source than the other three hybrid cases (Figure 5.38a–i) as well as any of the non-buoyant cases (Figure 5.34a). The higher vertical velocities induced due to buoyancy even this close to the source play an important role in the wake region behind the vertical plume. At the 45° plane the recirculation on the symmetry plane as predicted by the DFM (Figure 5.38b–ii) is much greater than that of the RNG model. The rotating vortex predicted by the RNG model has some similarity to the QUICK vortex in so much as there is a wider section of high w velocity (Figure 5.38b–iii) that creates a more rounded section. The reason for this apparent similarity between QUICK and RNG that leads to both predicting lower rise heights is due to two separate mechanisms. Firstly, the QUICK scheme is able to capture gradients that are normal to the predominant flow direction (i.e. normal to the predominant *upwind* direction, v and w velocities). The benefit of this is a better ability to capture the rotating vortex. This is seen in the high lateral velocities in Figure 5.38c–iv compared to the velocities predicted by the other three schemes at the equivalent locations. Even though the temperatures predicted by QUICK are very high, the ratio of buoyancy generated v velocities to the w velocities is such that a rounded vortex is predicted. The RNG model does not have this high proportion of lateral velocity, although still predicts a rounded section. The second reason is due to lower proportion of buoyancy induced *v* velocities due to a more diffused temperature field for the RNG model, lower in fact than the other three cases. This is seen in the magnitude of the velocity on the symmetry plane at the height of the thermal core (Figure 5.38c–v). By x = 10D the more contracted RNG and QUICK cross-sections both have smaller *v* velocities in the centre of the cross-section. Conversely, the other two hybrid schemes have vertically diffused thermal cross-sections that result in higher velocities especially on the upper surface of the plume (Figure 5.38d–vi). This leads to the higher rise of these two cases seen in Figure 5.35.

The addition of buoyancy leads to a greater sensitivity in the performance of each scheme and model. In this case the structure of the counter-rotating vortex has shown to be dependent on the relationship between cross-stream gradients and vertical buoyancy induced velocities. It is the higher dilution rates predicted by the RNG that lead to a similarity in performance between the QUICK discretisation scheme and the RNG k–ε turbulence model. The actual cause of this faster dilution can only be determined by a detailed study of the predicted turbulence field. If the DFM is accepted as performing with greater theoretical accuracy under these complex strain conditions, then it is not unreasonable to assume that the RNG model is performing spuriously.

5.3.2.2.1 Conclusions

- Compared to the non-buoyant cases, the prediction of the buoyant plume differ greatly by the four models.
- Both plume rise and height and the lateral location of the thermal core are predicted accurately by all four models compared with the experimental results at x = 10D. By x = 40D rise height is overpredicted by both QUICK and RNG models.
- These lower rise similarities can be attributed to QUICK's ability to predict a more rounder rotating vortex and the higher dilution rate exhibited by the RNG model.

5.3.2.3 Side-by-side sources

The full-scale side-by-side source geometry is investigated in Cases 53–56 (see Table 4.2). Temperature contour plots at x = 10D and x = 40D are shown in Figure 5.39. Vertical and horizontal profiles of temperature are shown in Figure 5.40, whilst the near-field velocity vectors and temperature contours are presented in Figure 5.41. An obvious comparison to be made is to the equivalent small-scale side-by-side model already discussed and shown in Figures 5.24 to 5.26.

Due to the very fine near-wall gridding in the small-scale work there was little difference between both hybrid and QUICK results. By x = 40D there was hardly any difference at all (see Figure 5.24b). In the full-scale there is the expected differences between hybrid and QUICK results but surprisingly little change in the predicted cross-sections using the three different turbulence models. At x = 10D all cases agree well with experimental rise height and the lateral offset of the thermal core is in better agreement than the small-scale results in Figure 5.24a. By x = 40D all hybrid plumes have risen to the same height whilst the QUICK plume is substantially lower. The full-scale results at x = 40D show a much less uniform cross-section than the equivalent small-scale cross-sections in Figure 5.24b. The discrepancy in rise height between hybrid and QUICK results can be attributed to numerical diffusion effects nearer the source. Yet all four cross-sections in the full-scale at x = 40D are much more bifurcated than the characteristic single plume cross-section at this location in the small-scale. The effect of the low Reynolds number turbulence model used in the small-scale has aided the combining of the adjacent sources. This is compared to the more bifurcated structure of the cross-section in the fully turbulent full-scale. Whether this is due to the action of turbulent diffusion or to the cross-flow gradient capturing performance of the QUICK scheme on a relatively coarse grid is investigated in this section.

The vertical profiles of temperature in Figure 5.40 shows a predicted dilution down to 16% for the QUICK scheme through the core of the cross-section compared to a level of 13% in the small-scale (see Figure 5.25a). The addition of turbulent diffusion in the full-scale seems to be outweighed by the overestimation of temperature due to the behaviour of the QUICK scheme in coarse grid regions. The hybrid results in the full-scale show the opposite behaviour: a lower predicted temperature compared to the small-scale. Similar rise heights at x = 10D are predicted in both small and full-scales (Table 5.2). At x = 40D more spreading of the upper surface of the plume is predicted in the full-scale than the small-scale. The horizontal profiles show good agreement for physical symmetry plane dilution levels, although again there is a lack of spreading in the horizontal direction.

The near-field analysis once again provides the best explanation of the dominant interaction processes. The full-scale near-field of Figure 5.41 is compared to the equivalent small-scale results in Figure 5.26. The location of the reattachment point on the leeward side of the plume is the same as the small-scale location. The QUICK scheme predicts a higher acceleration of both the cross-wind around the side of the plume (Figure 5.41a–i) as well as of the plume itself (Figure 5.41a–ii). Both RNG and DFM once again predict a stronger recirculation in the wake of the source (Figure 5.41a–iii), the RNG model actually has a stronger reversed flow than the DFM. At the 45° plane, interaction with the adjacent plume has begun. The baseline model shows some mixing across the symmetry plane (Figure 5.41b–iv) more so than both the RNG and DFM cases. The QUICK scheme is already merged with the adjacent plume (Figure 5.41b–v) due to the prediction of a much greater lateral convection than any of the hybrid cases (Figure 5.41b–vi). The lack of lateral velocities predicted by the hybrid scheme means that interaction is more a function of turbulent diffusion towards the symmetry plane. The stronger rotating vortices predicted by the QUICK scheme convect the thermal core to the symmetry plane whereupon interaction occurs far more readily. The stronger reversed flow in both the RNG and DFM cases (Figure 5.41b–vii) results in less spreading against the predominant flow direction. The actual shape of the thermal cross-section is not affected greatly by the reversed flow region as can be seen in the comparison of the baseline case with both RNG and DFM sections. By x = 1D the strong up-flow into the centre of the plume in both the RNG and DFM cases (Figure 5.41c–viii) brings cold ambient into the plume which leads to a strengthening of the bifurcated structure. Once again this is more evident with the RNG model although it should be noted that this effect is only slight and there is still little difference between baseline, RNG and DFM cases. The higher lateral velocities within the outer rotating cell predicted by QUICK is evident (Figure 5.41c–ix). This leads to the wider cross-section and subsequent reduction in up-flow despite of the apparent efficiency of interaction. By x = 5D the trend of both RNG and DFM to retain their bifurcated structure is still apparent. The QUICK scheme, although the earliest to merge and to lose its double bifurcated structure unlike the hybrid cases, predicts a cross-section similar to a single plume although far more bifurcated itself. Compared to the equivalent small-scale section (see Figure 5.26d) the full-scale QUICK case is more rotated, retains a less diffused thermal core and also has faster up-flows through its centre.

5.3.2.3.1 Conclusions

- All plumes retain a more bifurcated structure, and thus take longer to merge, in the full-scale compared to the equivalent small-scale models.
- The QUICK plume predicts a low dilution rate near the source and much lower rise, especially at x = 40D, compared to the hybrid cases.
- Merging across the physical symmetry plane occurs much earlier with the QUICK scheme, yet at x = 40D the cross-section is more bifurcated compared to the hybrid cases.
- Prediction of the interaction process is dominated by the model's ability to predict the inner rotating vortex.

5.3.2.4 Side-by-side sources, *R* = 1

When the cross-wind velocity at the tower-top is the same as the plume source velocity an extremely complex flow field is produced. Any wake regions are surrounded by much higher velocities and so more severe levels of streamline curvature exist. These conditions theoretically lead to turbulence anisotropy and so greater differences in the predictive ability of the turbulence models used is expected, more so than in the relatively 'softer' flow conditions encountered so far.

Figure 5.42 shows the y-z plane temperature contours at x = 10D and x = 40D. All cases predict a bifurcated section at x = 10D where experimentally there was no lateral offset of the thermal core. Rise height at x = 10D is in good agreement for all cases except the DFM which predicts a slightly higher rise. By x = 40D all cases apparently overestimate the rise height and only the baseline model and the QUICK variation have thermal cores on the symmetry plane. As expected, there is now a large difference between DFM, RNG and standard k-ε model. The RNG model is now more in line with the baseline model compared to the DFM. Once again the QUICK scheme predicts a more rounded cross-section compared to the hybrid cases.

The vertical and horizontal profiles are shown in Figure 5.43. At x = 10D the QUICK scheme captures the underside of the plume much more accurately than all hybrid cases. Downwash has occurred, where the ground level concentration rises above zero, and is predicted by QUICK. This scheme also appears to capture the top section of the plume as well but again overestimates the thermal levels within the plume itself. The DFM predicts considerably lower thermal levels on the symmetry plane than the other cases but quickly becomes similar further away from this plane. As can be seen in Table 5.2, the actual level of rise height prediction is in good numerical agreement with experiment. At x = 40D it is the DFM that predicts reasonable dilution levels on the symmetry plane in the core of the plume compared to the other cases. The QUICK scheme accurately predicts the ground level concentration whilst the baseline and RNG cases capture the upper side of the plume well. At x = 40D it is the DFM that is in best agreement with experiment. The dotted lines of the profiles through the predicted thermal cores agree much better with the experimental vertical width of the plume. The temperature within the plume is yet again much higher than experiment. The horizontal width of the plume is best predicted by the QUICK scheme but it is the hybrid cases that result in the correct dilution levels. At x = 40D the DFM horizontal profile is in good agreement with experiment but fails to spread far enough due to the hybrid scheme's inability to capture the lateral velocity component of the rotating vortex.

The near-field velocity and temperature contours are shown in Figure 5.44. The reattachment point is further from the symmetry plane than in the $R = 2.33$ case (Figure 5.44a–i). The recirculation around this stagnation point is sensitive to both discretisation scheme (Figure 5.44a–ii) and turbulence model (Figure 5.44a–iii). The DFM in particular predicts a much larger recirculation. The cross-flow accelerated in-between the sources is predicted to decelerate more quickly using RNG and DFM (Figure 5.44a–iv) compared to both the baseline model and the QUICK variation (Figure 5.44a–v). This accelerated through-flow, and the expected stronger reversed flow (Figure 5.44a–vi), deters both the RNG and DFM thermal cross-sections from spreading across the symmetry plane. This is also partly true of the standard k-ε model. The mixing across the symmetry plane at this early stage can therefore be attributed to QUICK's ability to capture the vortex initiation shown by the high velocities in Figure 5.44a–vii. By the 45° plane both RNG and DFM have maintained their bifurcated structure due to the strong reversed flow (Figure 5.44b–viii). There is not the same formation of the counter-rotating vortices as in the $R = 2.33$ case (Figure 5.41b). This is due to the strong cross-flow bending the plume over so quickly that there is not a sufficiently long enough vertical section for the cross-wind to accelerate around and initiate the rotating vortex pair. At x = 1D the RNG and DFM near symmetry vortices are stronger and less diffused (Figure 5.44c–ix) than those predicted by the standard k-ε model. The QUICK plume has diffused further towards the ground due to the low predicted velocities between 0D < y < 2D (Figure 5.44c–x). The DFM predicts a rotating flow developing near the ground that none of the other cases predict (Figure 5.44c–xi). It is fair to say that these flow fields are the most complex encountered so far and also the first time where the DFM predicts velocities very different from the other cases. By x = 5D a single rotating vortex has developed in all cases that is characteristic of a single combined plume. This is in comparison to Figure 5.41d (side-by-side sources but with a weaker cross-flow) where merging was not yet completed. The location of the thermal core is always above the rotating momentum plume in all cases. The complex strain field at x = 1D (Figure 5.44c), the heart of the interaction and reorganisation stage of Figure 2.3, has the highest concentration of temperature in the top section of the plume. By x = 5D the strain field has quickly settled down and organised itself into the simple single rotating vortex. The thermal core still resides though in the top section of the plume.

5.3.2.4.1 Conclusions

- Unlike the experimental results, all computational cross-sections show a bifurcated thermal structure at x = 10D.
- All four models overpredict rise height at x = 40D.
- The QUICK scheme predicts a wider thermal cross-section due to higher lateral velocities within the merged rotating vortex.
- Under these extreme strain conditions the DFM predicts stronger recirculating and rotating flow features compared to the other hybrid cases.
- Merging of adjacent plumes into a single plume occurs much earlier compared to the $R = 2.33$ case.

5.3.2.5 Tandem sources

In comparison to the complexity of the interaction of side-by-side plumes, a tandem source arrangement, and subsequent mixing, is relatively simple. Temperature contours at x = 10D and x = 40D are shown in Figure 5.45. At x = 10D all three hybrid cases are almost identical. The QUICK plume is more contracted with a stronger thermal core. All schemes overpredict rise height, although the lateral location of the thermal core is in good agreement with experiment. This overestimation in rise height is expected, and has been quantified in Section 5.1.2. At x = 40D all cross-sections look almost identical. The RNG and DFM plumes have risen slightly higher than the baseline model.

The temperature profiles are shown in Figure 5.46. The QUICK scheme vertical temperature profile at both x = 10D and x = 40D is almost identical to the equivalent small-scale case seen in Figure 5.28. The horizontal QUICK profile shows a lower dilution rate than the small-scale case at the thermal core. Rise height prediction is much more sensitive under these boundary conditions at this downstream location, whereas the shape of the plume seems not to be. Spreading in the horizontal direction in the full-scale is again less than both the small-scale and the experimental results.

The symmetry plane vectors and contours for both baseline and QUICK cases look almost identical (Figure 5.47). Both cases predict a rotational flow on the symmetry plane (Figure 5.47a–i). This feature is predicted more strongly by the RNG model (Figure 5.47c–ii). The DFM predicts a substantially different velocity and thermal field on the symmetry plane. The rotating feature is present although it is lower and more rounded (Figure 5.47d–iii). The flow immediately above the centre of this rotating feature has a much stronger downward component. The thermal plume is much more spread on the symmetry plane with a much steeper thermal gradient at both the upper and lower surfaces (Figure 5.47d–iv). Comparing the baseline, RNG and DFM cases, the RNG case predicts less merging between the sources on the symmetry plane (Figure 5.47c–v) compared to the DFM case. This is only true in the near-field, however, as can be seen in the subsequent similarity in thermal cross-sections shown in Figure 5.45a, b.

The y-z plane near-field vectors and contours are shown in Figure 5.48. The spreading of the DFM plume temperature field is evident even close to the source (Figure 5.48a–i). By the 45° plane the high thermal gradients at the boundary of the DFM plume are already established (Figure 5.48b–ii). Once again, the QUICK scheme predicts cross-stream velocities that result in a more rounded vortex (Figure 5.48b–iii). In general, the interaction of tandem sources is highly efficient with the formation of a single counter-rotating vortex pair before the plumes have fully bent-over. The predicted plume wake varies considerably between all four cases. By $x = 1D$ all hybrid cases predict taller diffused plumes whilst the QUICK scheme is again more contracted due to the higher w velocities within the vortex (Figure 5.48c–iv). The small rotation below the plume is in the same vertical position in both baseline and DFM cases (Figure 5.48c–v). This rotation predicted by the RNG is of the same strength as the DFM case but is higher (Figure 5.48c–vi). By $x = 5D$ the RNG and baseline cases have a similar bifurcated structure whilst the DFM is far more diffused. Dispite these differences at $x = 5D$, by $x = 10D$ all hybrid cases appear similar (Figure 5.54a). The complex flow fields in the near-field (i.e. x < 10D) result in a wide range of predicted cross-sections. Further downstream, however, under less severe strain, the plumes predicted using the hybrid scheme become much more similar. The QUICK scheme leads to lower rise, although it too predicts cross-sections similar to the hybrid cases but only at a downstream distance of x = 40D.

5.3.2.5.1 Conclusions

- Rise height is overpredicted at x = 10D by all cases, compared with the experimental results, although only slightly by the QUICK scheme.
- By x = 40D there is the grid-related expected overprediction of rise by the hybrid cases. The shape of the thermal cross-sections predicted by all four models at x = 40D are very similar.
- Horizontal spreading is underpredicted by all cases at both downstream locations.
- Large differences in the shape of the predicted cross-sections between x = 1D and x = 10D have vanished by x = 40D.
- Merging occurs very early with the formation of a single plume-type thermal cross-section at the 45° plane.

5.3.2.6 Tandem sources, *R* = 1

The final source configuration modelled is again a tandem tower arrangement but with *R* = 1.0. Figure 5.49 shows temperature contours at x = 10D and x = 40D. As experienced throughout the analysis, the QUICK plume is more rounded and has a hotter thermal core than the hybrid cases. All hybrid cases show spreading from the upper section of the plume due to slight numerical diffusion effects experienced at the plume/cross-wind interaction region close to the source. At x = 10D all cases agree well with experiment for rise height. The DFM predicts a bifurcated structure at x = 10D, the location of which is in excellent agreement with experiment. The possible cause of differences between small-scale and full-scale is the tower wake interaction with the bent-over plume. At x = 10D this is not apparent, although at x = 40D, as with the side-by-side cases when $R = 1.0$, rise height is overpredicted by all cases. Again, it is the DFM that more accurately predicts the lateral offset of the thermal core at x = 40D, whilst all other cases show no bifurcated structure.

Vertical and horizontal temperature profiles are shown in Figure 5.50. At x = 10D rise height is accurate to within 18% (Table 5.2). The QUICK scheme captures the position of the top surface of the plume but overestimates the core temperature level by 300%. The vertical profiles of all hybrid cases show little differences between each other. This graph resembles very closely that of the single buoyant source vertical profiles in Figure 5.36a. This is indicative of how quickly this tandem arrangement merges to form a characteristic single plume. Profiles through the computational core and at the location of the experimental measurement both overpredict rise by 25%–40%. The horizontal profiles once again show the underestimation in spreading of all cases at both downstream locations. Overall the comparison with the experimental data is poorer than expected. As merging occurs so quickly the resulting single plume field should be relatively simple compared to the more complex and longer interaction regimes encountered so far. As will be seen however in the near-field figures, due to the high cross-wind speeds, interaction between bent-over plume and tower wake does occur. Any difference in tower wake structure between wind tunnel-and full-scales would result in differing trajectories between small- and full-scale plumes in this case.

The near-field velocity vectors and temperature contours on the physical symmetry plane are shown in Figure 5.51. Due to the strong cross-wind, merging of the temperature fields between both sources is achieved on the symmetry plane. Both baseline and QUICK cases show similar tower wake velocity fields and the ‘pulling down’ of the underside of the plume into the wake itself (Figure 5.51a–i). There is much less dilution of the thermal plume on the symmetry plane predicted by QUICK. Both RNG and DFM cases show the existence of separation at the leading edge of the tower (Figure 5.51c–ii). The RNG tower wake is similar to that of the DFM with higher reversed velocities (Figure 5.51b–iii) compared to the baseline case (Figure 5.51b–i).

The DFM predicts reverse velocities in the tower wake that extend right up to the leeward tower wall itself (Figure 5.51c–iv). There is also a more predominant up-flow into the underside of the plume (Figure 5.51c–v). In the other three cases this up-flow was quickly converted into a forward flow. It seems that the DFM is less diffusive in this respect and can sustain flows against the dominant flow direction.

The near-field y-z plane plots are shown in Figure 5.52. The acceleration of the source as it interacts with the cross-wind is much higher when using QUICK compared to the hybrid cases (Figure 5.52a–i). It is this initiation of the rotation vortex pair that results in the wider, more rounded, plumes predicted by QUICK. The recirculation between the sources varies greatly amongst different cases. The DFM predicts a recirculation behind the upwind source (Figure 5.51a–ii). This feature is predicted to some extent by the baseline case but not by the RNG model. As with the previous tandem configuration, merging is complete by the 45° plane with the existence of the characteristic single counter-rotating. The QUICK scheme predicts slightly higher w velocities on the upper side of the plume vortex (Figure 5.52b–iii). The reversed flow in the wake of the tower results in a 'pinching' of the lower thermal cross-section contours in both RNG and DFM cases (Figure 5.52b–iv). This is far more apparent, due to the higher reversed velocities, in the DFM case. By x = 1D both baseline and QUICK cases have wider cross-sections than RNG and DFM cases. This is due to the lower up-flow velocities in the plume on the symmetry plane. The stagnant region on the underside of the plume predicted by both standard k-ε model cases (Figure 5.52c–v) is partly present in the RNG case but not at all in the DFM case. The wake rotation in the DFM case has resulted in a strong vortex feature below the plume (Figure 5.52c–vi). The RNG case shows signs of this (Figure 5.52c–vii), although it is far more diffused. By x = 5D the four cases have settled into the behaviour encountered so far in this analysis. The RNG case is very similar to the DFM case, both having bifurcated sections (Figure 5.52d–viii). The QUICK section is much more rounded with the centre of the rotating vortex further from the symmetry plane (Figure 5.52d–ix). The baseline case shows a diffused thermal core with a non-bifurcated structure on the symmetry plane.

These source and boundary conditions again highlight the main behaviour of turbulence model and discretisation scheme that have been encountered throughout this analysis. Fundamental interaction processes are predicted by all cases, the differences are in associated flow features and the exact location of the thermal core.

5.3.2.6.1 Conclusions

- Rise height prediction is in good agreement with experiment at x = 10D but overpredicted slightly by x = 40D.
- Plume temperatures are overpredicted at both x = 10D and x = 40D, especially by the QUICK scheme at x = 10D.
- A strong reversed flow in the tower wake is predicted by both RNG and DFM. The DFM also predicts higher vertical velocities through the lower section of the bent-over plume near to the source.
- Merging occurs extremely quickly when $R = 1.0$. Differences in the predicted velocity fields, especially by the DFM, are only present in the near-field and do not affect plume trajectory greatly.

5.4 TURBULENT FLOW FIELD CHARACTERISTICS

The full-scale modelling conducted in this study is at Reynolds numbers in excess of 10^6 based on tower height. The contribution of turbulent effects on the diffusion of momentum and thermal energy will far outweigh the contribution due to molecular viscosity and molecular thermal diffusivity. The ratio of eddy to molecular viscosity is contained in the turbulent Reynolds number which reaches values of 10^5. The accurate prediction of both the Reynolds stresses and fluxes, or rather their spatial gradients, is of critical importance in determining levels of diffusion. The similarity of mean primary variable values, such as plume temperature, for the three turbulence models employed in this study may only be indicative of the dominance of convection over diffusion. The differences between these turbulence models, in terms of the predicted ability of the flow to become turbulently diffused (i.e. the eddy viscosity) as well as the levels of Reynolds stress contribution, are investigated in this section. The DFM eddy viscosity is calculated from the turbulent kinetic energy (calculated exactly from the three normal stresses) and its rate of dissipation as per Equation (3.18).

5.4.1 Near field eddy viscosity prediction

Instead of studying every cooling tower source arrangement, only one is selected to look at the turbulent nature of the predicted flow field. A side-by-side arrangement is chosen with an exit velocity ratio, *R*, of 1.0 (Table 4.2; Cases 57-60). As discussed in Section 5.3.2.4, this configuration results in complex flows that should in theory lead to anisotropic effects due to strong streamline curvature.

It is important at this stage to explain the conception of turbulence anisotropy and isotropy. The commonly used phrase for turbulence isotropy is that turbulent levels are the same in all three directions. This is a slightly ambiguous definition. When talking about isotropy or anisotropy a qualifier must be included to explain what exactly is the same in all three directions. The following three definitions are formulated.

1. *The ability of the flow to become turbulently diffused (i.e. the eddy viscosity) is the same in all three directions.*

2. *The contribution from all six Reynolds stresses are the same, as are the three Reynolds fluxes.*

3. *The amount of turbulent diffusion exhibited by the mean primary variables is the same in all three directions.*

The third definition, i.e. the diffusive flux is the same in all three directions with reference to the finite volume under consideration, is the most generic. This definition allows both the eddy viscosity and the mean strain rate to be anisotropic in themselves, but the resulting total diffusive contribution to be equal in all directions at any one point. This, however, is hard to gauge both experimentally and computationally and as a result remains an abstract construct.

The most common definition, that of a constant eddy viscosity at any one point, is investigated further in this section. Instead of simply looking at the eddy viscosity field and relating it to the velocity field, both the k and ε fields are studied to see exactly what it is that dominates the prediction of μ_T (as per Equation 3.18). Figure 5.53 shows the predicted temperature, velocity, μ_T, k and ε fields at both the horizontal and first vertical cross-section planes defined in Figure 5.19. The contours are plotted for the standard k–ε model, the RNG k–ε model and the DFM.

5.4.1.1 Horizontal plane comparisons at y = 2.1D

The main differences in the prediction of the velocity field in the horizontal plane just above the tower top are in the wake region downstream of the vertically issuing plume. The standard k–ε model predicts an almost stagnant flow in this region with an elongated recirculation region (Figure 5.53a–i). The DFM, in comparison, predicts a strong reversed flow and a more contracted recirculation in this region (Figure 5.53c–ii). The RNG k–ε model shows a reversed flow that is almost identical to the DFM (Figure

5.53b–iii). The reason for this commonly encountered behaviour, i.e. the similarity between DFM and RNG results, becomes evident when looking at the eddy viscosity contours.

There are extremely high levels of eddy viscosity predicted in the region just upstream of the leading edge of the tower (Figure 5.53a–iv). Eddy viscosity values reach in excess of 10 kg/ms at this location. The fact that there is a clear demarcation line of this high μ_T region that coincides with the leading edge of the tower and the block boundary, away from the symmetry plane (Figure 5.53a–v), hints at a possible numerical (grid) reason for this behaviour. The fact that these errors are visible only in the turbulence parameters mean that this is due to errors in the prediction of mean velocity gradients at the thin end of the high aspect ratio cells along this demarcation line. The fact that these errors are not visible in the mean primary variables goes to highlight the insensitivity of pressure and velocity distribution to the turbulent field in the homogeneous flow away from the tower corner. These levels fall sharply as the flow is accelerated between the two sources but rises rapidly again to a peak that is spread along the stagnant wake region on the symmetry plane (Figure 5.53a–vi). The levels of μ_T predicted by the DFM are up to six times smaller than that predicted by the standard k–ε model. Instead of there being a peak on the symmetry plane there is a small increase in μ_T to the side of the wake away from the symmetry plane (Figure 5.53c–vii). The RNG k–ε model predictions are fall between both standard k–ε model and DFM. Absolute levels of μ_T are only slightly higher than the DFM levels but are well below the levels of the k–ε model. It is these low levels of μ_T predicted by the RNG model that allow the flow to reverse in the plume wake region. The standard k–ε model is so diffusive to the extent that the flow is unable to reverse due to the excessively high levels of μ_T.

Having related the eddy viscosity field to the plume wake region it now remains to explain *why* the eddy viscosity predictions by the three turbulence models vary so much. The turbulent kinetic energy predicted by the standard k–ε model is far higher than the levels predicted by the other two turbulence models just upstream of the plume (Figure 5.53a–viii). As with the eddy viscosity field, the distribution of the turbulent kinetic energy field of both k–ε models are similar but the values of k predicted by the DFM and RNG models are almost identical. In the wake region on the symmetry plane all three models predict a peak in k, the standard k–ε model producing levels only slightly higher than the other two models (Figure 5.53a–ix). The DFM predicts another local peak in k that coincides with the peak in eddy viscosity shown in Figure 5.53c–vii (Figure 5.53c–x). So why do neither RNG or DFM predict the very high levels of eddy viscosity shown in Figure 5.53a–vi? The answer to this lies in the ε field. The standard k–ε model predicts a relatively weak peak in ε at the same location as the peak in k (Figure 5.53a–xi). Both RNG and DFM models predict much higher levels of ε at the same location (Figure 5.53b–xii). This behaviour is by far the most dominant factor in the similarity between RNG and DFM velocity fields.

The increased levels of ε predicted by the RNG is due to the additional terms that constitute the RNG k–ε model (Equations 3.26, 3.27). Under high strain conditions these terms substantially increase the production of ε. These higher levels of ε, together with more moderate levels of k, result in the absence of the peak in eddy viscosity on the symmetry plane predicted by the standard k–ε model. The peak in Figure 5.53a–vi is due to the different comparative rates at which both k and ε reduce from their peaks seen in Figure 5.53a–ix and 5.53a–xi.

5.4.1.2 Vertical plane comparisons at x = 1D

Having now gained an understanding of why the velocity fields vary between the three turbulence models studied, we now look at the vertical cross-sectional plane taken at x = 1D to see if the conclusions drawn for the horizontal plane still hold.

Whereas the horizontal flow field of Figure 5.53 a, b and c included a wake recirculation region, the flow seen in the vertical plane, both within the bent-over plume and also between the plume and the ground, is of a more swirling nature. The thermal plume predicted by the standard k–ε model is more diffused than both RNG and DFM plumes at the symmetry plane (Figure 5.53d–xiii). This is due to the high levels of eddy viscosity (and subsequent high levels of eddy diffusivity) seen in Figure 5.53d–xiv that are convected in from the peak in Figure 5.53d–xv. So far this behaviour is much the same as that seen in the horizontal plane. The similarity between RNG and DFM velocity fields is much weaker, however, in this plane. Although there is a stronger upflow into the plume in the RNG model (Figure 5.53e–xvi) compared to the standard k–ε model, the swirling flow between the plume and the ground as seen in the DFM case (Figure 5.53f–xvii) is absent in the RNG model. The eddy viscosity predicted by the RNG model is still much lower than that predicted by the standard k–ε model but not sufficiently low (i.e. as low as the DFM levels) to sustain this swirling motion. This is especially true in the near-wall region where the RNG model predicts a sharp rise in eddy viscosity through the ground boundary layer where this is absent in the DFM predictions.

An alternative explanation could be that it is the anisotropic nature of the eddy viscosity in this region that gives rise to this secondary flow that could *only* be captured by the DFM. This is further supported when comparing both the k and ε fields of the RNG and DFM models. The behaviour of the RNG model, in terms of the similarity between RNG and DFM k and ε fields, is the same as the horizontal plane comparisons. The location of the RNG peak in k (Figure 5.53e–xviii) is the same as that of the DFM (Figure 5.53f–xix). The similarity in the location and strength of the peak in ε is even more similar (Figure 5.53e–xx).

This swirling feature predicted by the DFM leads to more plume material being brought down closer to ground level but does not seriously affect the prediction of plume rise height as discussed in Section 5.3.2.4. It appears that the major differences in flow field prediction by the various turbulence models are of associated flow features that are not directly related to plume rise and only slightly related to plume dilution in the moderately buoyant cases investigated. A configuration where buoyancy plays a more dominant role, especially in low exit velocity ratio conditions that lead to plume downwash, would lead to much larger differences in the comparative accuracy of the different turbulence models. The over prediction in eddy viscosity by the standard k–ε model in decelerated regions leads to excessively high levels of eddy diffusivity that causes increased spreading that could dominate adjacent plume interaction and subsequent rise in highly buoyant sources.

5.4.2 Near-field turbulence anisotropy prediction

The preceding section discussed the comparison of the three turbulence models using essentially isotropic parameters such as turbulent kinetic energy, *k*, and its rate of dissipation, ε. The DFM results were reduced down to a form where comparison to the two equation models could be conducted. By doing this any anisotropic flow behaviour (anisotropic in terms of differing Reynolds stresses or eddy viscosities; see Section 5.4.1 points 1 and 2) is essentially averaged out. For flow features that are dominated by secondary turbulent motion the amount of anisotropy is extremely important. This section will highlight those flow regions where anisotropic behaviour of the Reynolds stresses and fluxes are most apparent. Graphs showing the variation in Reynolds stresses and fluxes in the horizontal and vertical planes looked at in the previous section are presented and discussed.

5.4.2.1 Horizontal Reynolds stress and flux profiles

Figure 5.54a shows the horizontal profiles of the three normal Reynolds stresses at $Y = 21D$ and at a z location above the centre of the tower development duct. The leading edge of the tower is at X/D = -2.0 and the trailing edge at X/D = 0. Each normal Reynolds stress is created by a combination of mean strains. The variation therefore in each stress is strongly related to the velocity field along the profile line. Just upstream of the plume source there is an increase in all three stresses (Figure 5.54a–i) that reaches a maximum at the cross-wind/plume interface before decreasing to low levels within the plume itself (Figure 5.54a–ii). As the profile line lies above the centre of the source the lateral velocity gradients are small. This results in the lateral $\overline{w'^2}$ stress being the smallest compared to both the vertical and streamwise fluctuations. Between the downwind edge of the source and the trailing edge of the tower a small recirculation exists. Here the lateral velocity gradients dominate the vertical and streamwise gradients (Figure 5.54a–iii) and so the $\overline{w'^2}$ stress is by far the largest. In the wake region further downstream. The streamwise fluctuations dominate but all three normal stresses tend to the same value as the flow 'recovers' (i.e. loses the streamline curvature, swirl, etc.) and turbulence returns to isotropy in terms of the normal stresses.

The previous section compared both DFM and two-equation predicted eddy viscosity values. It could be possible to calculate all three eddy viscosities for each normal stress from the DFM results using Equation (3.12) and compare the three values at each point to the single values predicted by the two-equation models. This would give an indication as to the validity of a two-equation approach. However, Equation (3.12) requires the calculation of mean strains that were not available from the results. It is the authors belief however that the anisotropy of the normal stresses is indicative of an anisotropy of the eddy viscosity.

The Reynolds flux profiles in Figure 5.54b are produced by a combination of not only the mean strains but also by the mean enthalpy gradients. The largest values are found at the cross-wind/plume interface (Figure 5.54b–iv) where the enthalpy gradients are the largest in the flow field. The difference in signs of $\overline{v'h'}$ and $\overline{u'h'}$ is due to difference in signs of the mean gradients. The very small values of $\overline{w'h'}$ are due to the small mean enthalpy gradients laterally across the plume at this source centreline location. Downstream from the source, as the plume begins to spread and dilute and so mean enthalpy gradients decrease, values of Reynolds fluxes also decrease.

Anisotropy of the Reynolds fluxes, and the possible anisotropy of the eddy diffusivity at the same locations, as seen near the source should in theory result in large predictive differences between two-equation and DFM models. The fact that the differences are not as large as the amount of stress and flux anisotropy that are present leads to two conclusions. Firstly, the plume development near the source is dominated by inviscid processes, pressure gradients formed as the plume interacts with the cross-wind. This high Peclet number type flow is relatively insensitive to differences in the prediction of the diffusive contribution. Secondly, it is not the anisotropy of the turbulence, either in stress and flux differences or variation in point eddy viscosity values, but the absolute levels of eddy viscosity predicted that sensitises the results. The fact that eddy viscosity predicted by the standard *k*–ε model was up to six times higher than levels predicted by the DFM far outweighs the fact that the former model is unable to account for anisotropy of the eddy viscosity itself.

5.4.2.2 Vertical Reynolds stress and flux profiles

Figure 5.54c shows the vertical profiles of the normal Reynolds stresses at a downstream distance of X/D = 1 and at the same source centreline lateral offset as before. Again, it is the mean strains that generate the normal stresses which decrease rapidly above the plume beyond Y/D = 4.5. The swirling flow feature seen in Figure 5.53f–xvii, between the ground and the top of the tower, leads to equal levels of vertical and lateral normal stresses (Figure 5.54c–v). Within the centre of the plume the turbulence becomes very anisotropic with the streamwise normal stresses more than twice as large as the normal vertical fluctuations.

The Reynolds flux profiles along the same line are shown in Figure 5.54d. Both the most negative and most positive of the fluxes coincide with the lower and upper boundaries of the thermal plume. The positively stable layer on the plume underside leads to negative flux values whilst the unstable upper side results in positive values. Above the plume, where there is no enthalpy gradient, the fluxes return to zero. The fluxes themselves are indicative of the rate at which the plume is diluting, i.e. entraining ambient.

5.4.3 Conclusions

This section has attempted to describe what the failings and abilities are of the two most common types of turbulence model. From an engineering perspective the use of large eddy simulation or direct numerical simulation is far too computationally expensive to perform this type of engineering investigation. Conversely, the use of zero or one-equation models, although computationally efficient, are not sufficiently accurate for the complexity of this type of flow. Both two-equation and DFM models lie in the middle of these two extremes.

It has been shown that the standard k–ε model severely overestimates the eddy viscosity in regions of stagnation, due to a combination of high levels of turbulence kinetic energy and low levels of energy dissipation compared to the DFM results. The modified RNG model predicts much lower levels of eddy viscosity (up to six times lower in the stagnation regions) primarily due to a modified production term in the ε equation that increases production in regions of high strain (i.e. around a stagnation). The DFM model predicts levels of eddy viscosity slightly lower than the RNG levels producing a less diffusive flow that contains recirculations that neither two-equation models could predict. By its very nature it allows the flow to become anisotropic (in terms of Reynolds stresses, fluxes and as a consequence, eddy viscosity) and so can predict secondary flow features.

For the type of flow considered there is surprisingly little difference between the predicted plume rise, interaction and dispersion when using both types of turbulence model. However, for flows where the exact nature of the turbulent contribution is critical (e.g. highly buoyant, combusting, wall heat transfer) the comparative accuracy of these models has to be re-evaluated.

5.5 COMPARISON WITH EMPIRICAL RISE HEIGHT PREDICTIONS

Simple 1D formula such as those discussed in Section 2.1.1 will always offer the quickest method for determining plume rise height under neutral atmospheric conditions. The simplifications upon which these equations are based mean that they may not accurately predict plume rise in the more complex environment found in reality. The computational approach taken in this study incorporates the effects of an oncoming logarithmic type atmospheric boundary layer not accounted for in the 2/3 law relationship (see Equation 2.6). This study also includes the effect of the cooling tower wake as well as non-uniform plume source profiles. Comparisons between the experimental and computational rise height with the empirical predictions are therefore made to asses the sensitivity of the assumptions on which the empirical equations are based. Empirical predictions for all small-scale and full-scale plumes are included in Tables 5.1 and 5.2, respectively.

5.5.1 Calculation of empirical rise heights

There are three equations that can be used to predict single plume rise height far from the source. The first is the '1/3' law for jet type sources (see Equation 2.5), the second is the '2/3' law for buoyant type sources (see Equation 2.6) and the third is a combination of the two for sources with significant amounts of momentum and buoyancy flux (see Equation 2.7).

Both the small-scale and full-scale buoyant plume sources studied here produce a moderately buoyant plume (i.e. a Froude number of 10). When the '2/3' law is used to predict the rise height, an overestimation, in comparison to both experiment and computation, of rise height at the far downstream location occurs. Because of this, Equation (2.7) is used which results in a more accurate prediction especially at the $x = 40D$ location. The rise height for adjacent sources is calculated via an enhancement factor that gives the amount by which the adjacent plume rise exceeds that of a single source (see Section 2.2.1). Equation 2.14 is used first to check whether an enhancement factor is required. The non-dimensionalised spacing factor of Equation (2.14) includes both source buoyancy flux, cross-wind speed and wind direction. Because the wind directions set in this study are 0° and 90° (tandem and side-by-side, respectively) then enhancement will only be used for the tandem arrangement where $S' = 0$. Equation (2.13) is therefore used for the tandem tower arrangements and the rise heights predicted by Equation (2.7) modified accordingly.

5.5.1.1 Small-scale empirical rise prediction

The small-scale empirical prediction for the single source at x = 10D is in good agreement with both experimental and computational rise heights (Table 5.1). At x = 40D the predicted rise is 22% higher than the value of the experimental results (all subsequent errors are given in relation to the experimental data). The empirical rise height prediction for the side-by-side sources are in even better agreement with the experimental results at x = 10D. This lends weight to the 'enhancement-or-not' formula of Equation (2.13). By x = 40D the error is 10% compared to the -11% error for the computational results. The tandem source empirical rise heights underestimate the amount of enhancement at both downstream locations, although only by a small amount. The fact that the single and non-enhanced side-by-side empirical rise height predictions nearly always overpredict rise, compared to both the experimental and computational results, indicates two things. Firstly, the buoyancy part of Equation (2.17) is too dominant for the more jet-type source considered here. Secondly, the empirical equation is based upon a 'top-hat' profile of the oncoming cross-wind. The plume encounters higher cross-wind velocities the higher it rises (as in both experimental and computational cases) that results in a lower overall rise. The fact that the enhanced rise of the tandem sources is *lower* than both experimental and computational results indicates that the true enhancement factor is larger than the empirical value.

5.5.1.2 Full-scale empirical rise prediction

The empirical prediction for the full-scale jet type source is in perfect agreement with the experimental result at x = 10D (Table 5.2). By x = 40D the empirical '1/3' law overpredicts rise. Because the jet is non-buoyant the inaccuracy at the further downstream location is due solely to the higher cross-wind speeds encountered by the jet at this height of y = 7.7D. Conversely, the accuracy of the empirical prediction at x = 10D is due to the similarity between empirical assumptions and actual conditions (i.e. little or no variation in cross-wind speed with height and a purely non-buoyant source). The empirical rise prediction for the single buoyant source, as in the small-scale case, is in good agreement with the experimental results at x = 10D but over predicts rise at x = 40D. Again, this is due to the two factors of non-uniform cross-wind speed and the overestimation of the contribution of buoyancy in Equation (2.17). The accuracy of the empirical prediction at both downstream locations for the side-by-side source configuration with $R = 2.33$ again justifies the non-enhanced assumption of Equation (2.13). When $R = 1.0$, the agreement between experimental and empirical prediction is even better nearer the source. By x = 40D the empirical prediction once again overestimates rise due to the same two factors. The similarity between small-scale and full-scale empirical predictive trends continues with the underestimation of rise height for the tandem arrangement at both downstream locations when $R = 2.33$. When $R = 1.0$, enhancement is underpredicted again at x = 10D but overpredicted slightly at x = 40D. This again tends to indicate that the true enhancement factor is larger than that predicted by Equation (2.13).

5.5.2 Conclusions

In general, empirical predictions for both small and full-scales are in the same order of accuracy as the computational results. The non-enhanced assumption for the side-by-side sources is justified. The effect of the tower wake from the side-by-side towers has a greater effect upon rise enhancement (or rather rise limiting) than any enhancement due to the merging of the adjacent plumes. The apparent underprediction of enhancement factor for the tandem sources, although only in the order of 10%, may actually be greater in reality.

Small-scale	x = 10D				x = 40D			
Tower array	Experiment	hybrid	QUICK	Empirical	Experiment	hybrid	QUICK	Empirical
1 × 1 single	5.3	5.7 8%	6.0 13%	5.7 8%	9.5	10 5%	10.7 13%	11.6 22%
1 × 2 side-by-side	5.6	6.0 7%	5.4 -4%	5.7 2% *(no enhancement)*	10.5	9.3 -11%	9.3 -11%	11.6 10% *(no enhancement)*
2 × 1 tandem	7.9	10.1 28%	9.6 22%	6.8 -14% *(enhanced)*	14.9	15.4 3%	15.4 3%	14.3 -4% *(enhanced)*

Table 5.1 Comparison of small-scale computational work to experimental results and empirical predictions for plume rise height y/D (%: comparison to experimental result)

Full-scale	x = 10D						x = 40D					
Tower array	Experiment	hybrid *k*-ε	QUICK *k*-ε	hybrid RNG*k*-ε	hybrid DFM	Empirical	Experiment	hybrid *k*-ε	QUICK *k*-ε	hybrid RNG*k*-ε	hybrid DFM	Empirical
1 × 1 single Non-buoyant	4.9	4.6 -6%	4.6 -6%	4.6 -6%	5.0 2%	4.9 0%	6.1	5.6 -8%	4.8 -21%	6.6 8%	6.6 8%	7.7 26%
1 × 1 single Buoyant	5.3	5.8 9%	5.2 -2%	5.8 9%	5.8 9%	5.5 4%	9.5	11.4 20%	9.3 -2%	9.6 1%	11.4 20%	10.9 15%
1 × 2 side-by-side $R = 2.33$	5.6	6.3 13%	6.3 13%	6.3 13%	6.3 13%	5.5 -2% *(no enhancement)*	10.5	13.0 24%	11.0 5%	13.0 24%	13.0 24%	10.9 4% *(no enhancement)*
1 × 2 side-by-side $R = 1.0$	2.9	3.2 10%	3.4 17%	3.2 10%	2.7 -7%	2.9 0% *(no enhancement)*	4.4	5.5 25%	5.5 25%	5.5 25%	4.6 5%	5.3 20% *(no enhancement)*
2 × 1 tandem $R = 2.33$	7.9	10.1 28%	8.5 8%	10.7 35%	10.7 35%	6.8 -14% *(enhanced)*	14.9	18.2 22%	16.6 11%	18.2 22%	18.2 22%	13.3 -11% *(enhanced)*
2 × 1 tandem $R = 1.0$	3.9	4.6 18%	4.6 18%	4.6 18%	4.6 18%	3.4 -13% *(enhanced)*	5.9	7.4 25%	7.4 25%	7.4 25%	8.2 40%	6.3 7% *(enhanced)*

Table 5.2 Comparison of full-scale computational work to experimental results and empirical predictions for plume rise height y/D (%: comparison to experimental result)

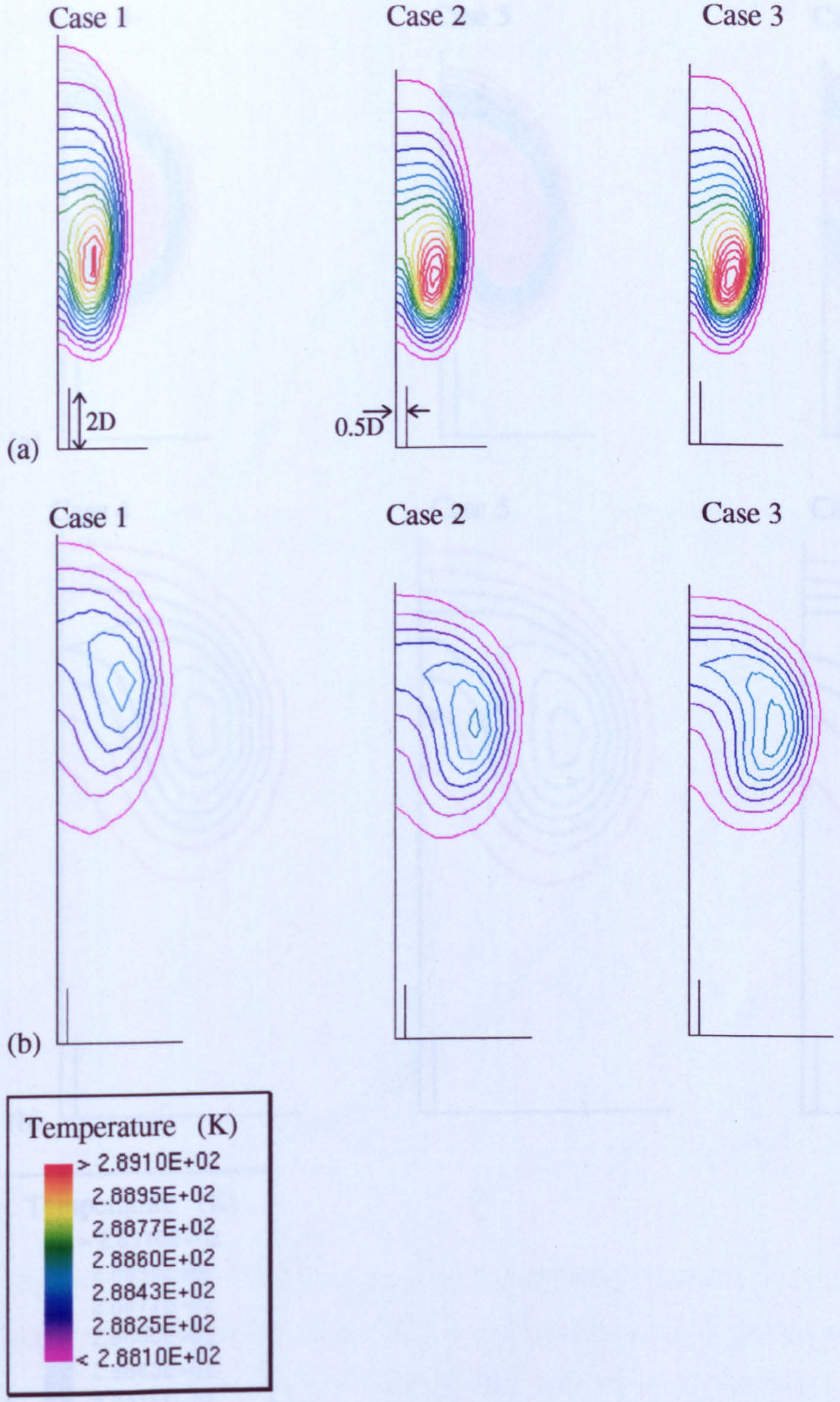

Figure 5.1 Single buoyant source grid sensitivity tests using the hybrid scheme (Cases 1–3), temperature contours where (a) refers to x = 10D and (b) to x = 40D. External contour = 288.1K subsequent gaps = 0.067K. (Original in colour.)

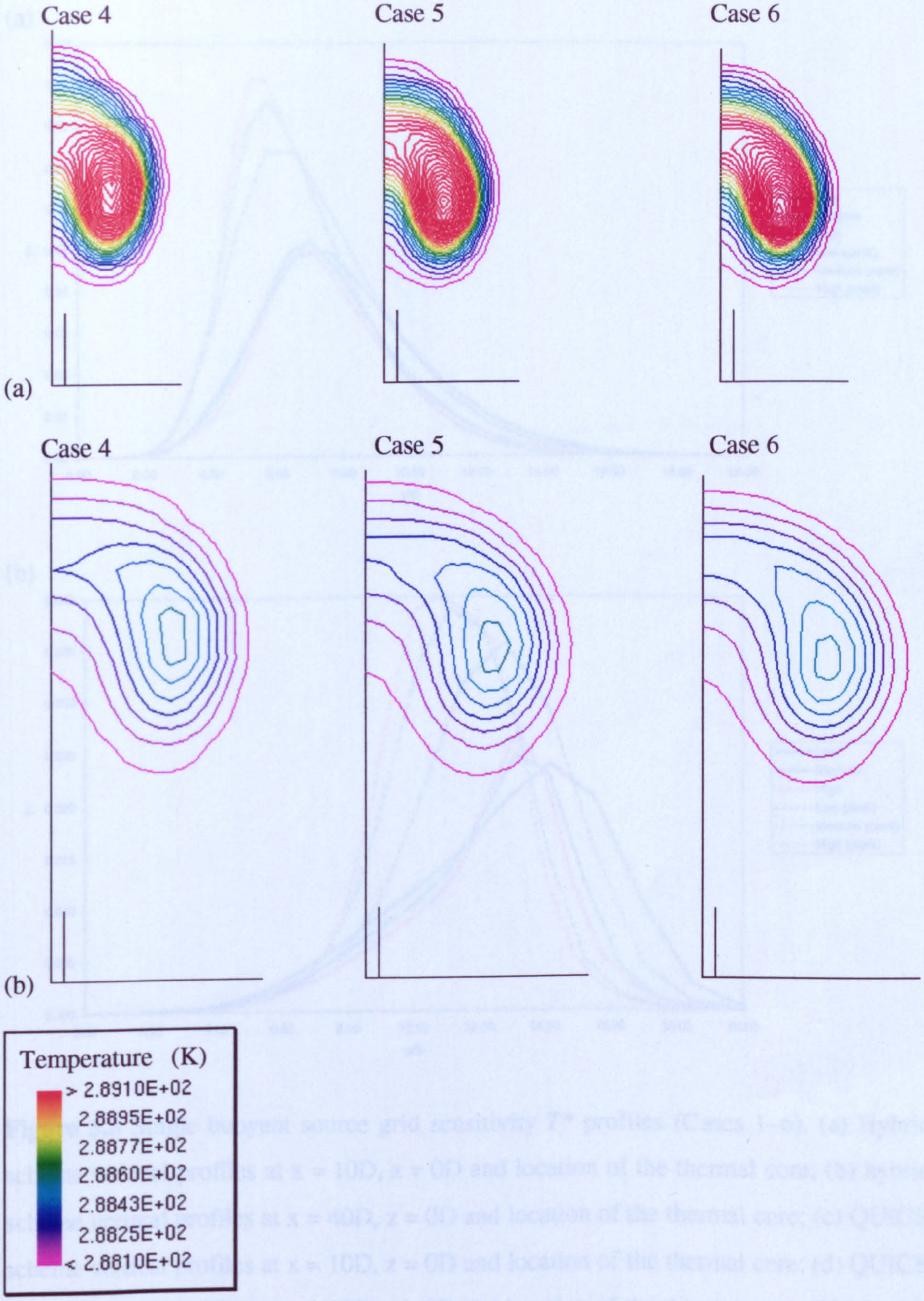

Figure 5.2 Single buoyant source grid sensitivity tests using the QUICK scheme (Cases 4–6); temperature contours where (a) refers to x = 10D and (b) to x = 40D. (Original in colour.)

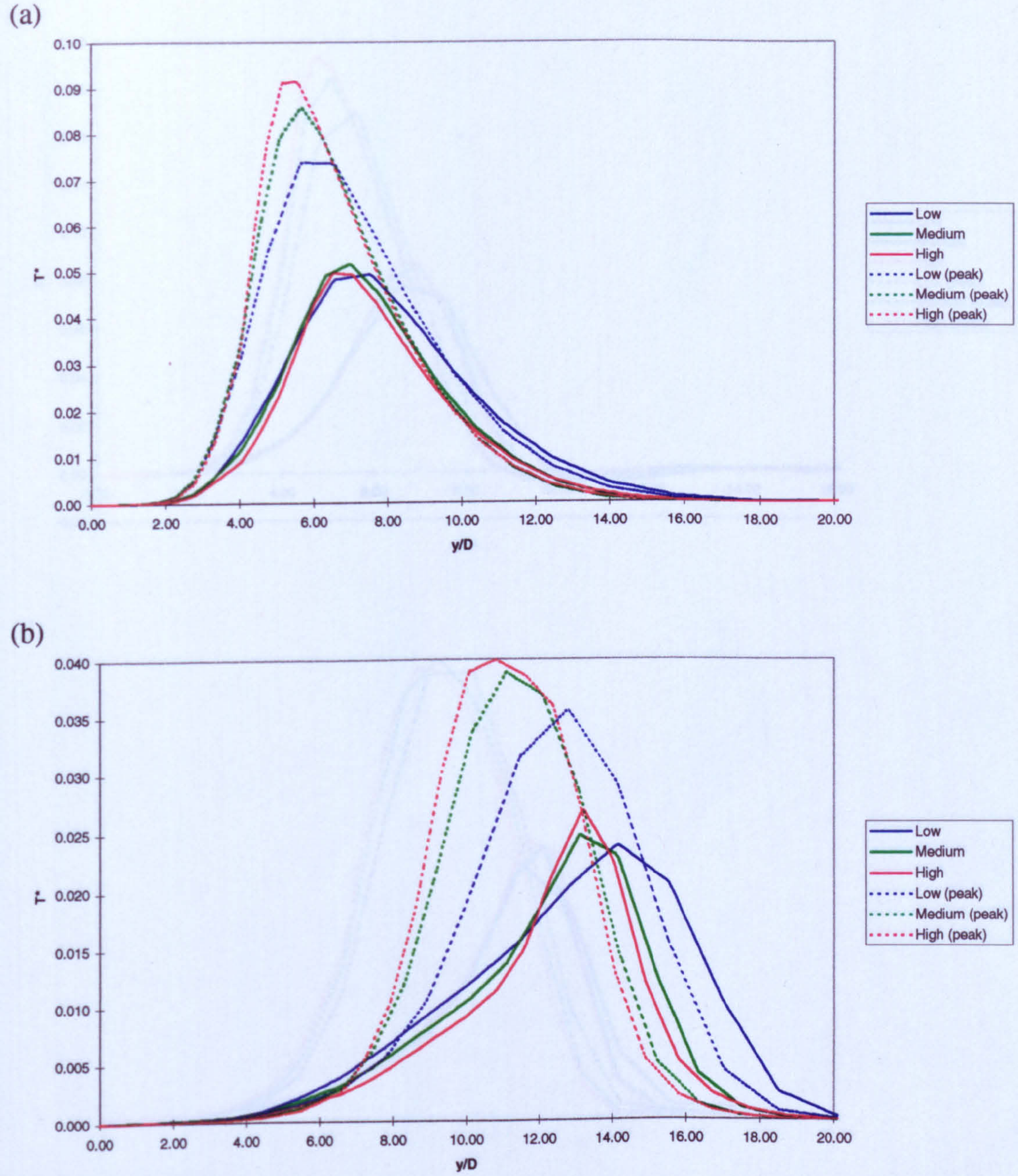

Figure 5.3 Single buoyant source grid sensitivity *T** profiles (Cases 1–6). (a) Hybrid scheme vertical profiles at x = 10D, z = 0D and location of the thermal core; (b) hybrid scheme vertical profiles at x = 40D, z = 0D and location of the thermal core; (c) QUICK scheme vertical profiles at x = 10D, z = 0D and location of the thermal core; (d) QUICK scheme vertical profiles at x = 40D, z = 0D and location of the thermal core. (Original in colour.)

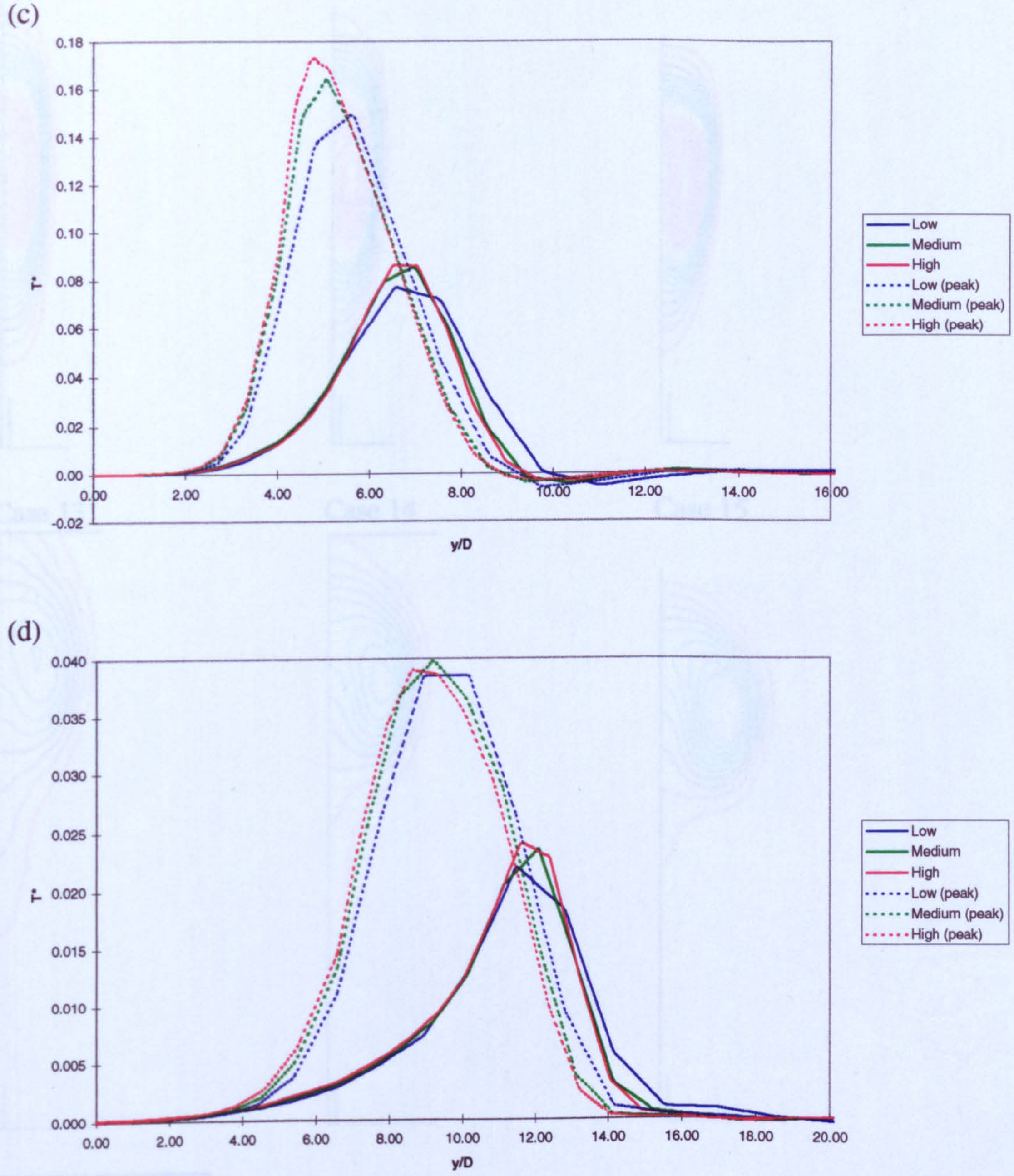

Figure 5.3 *Continued.*

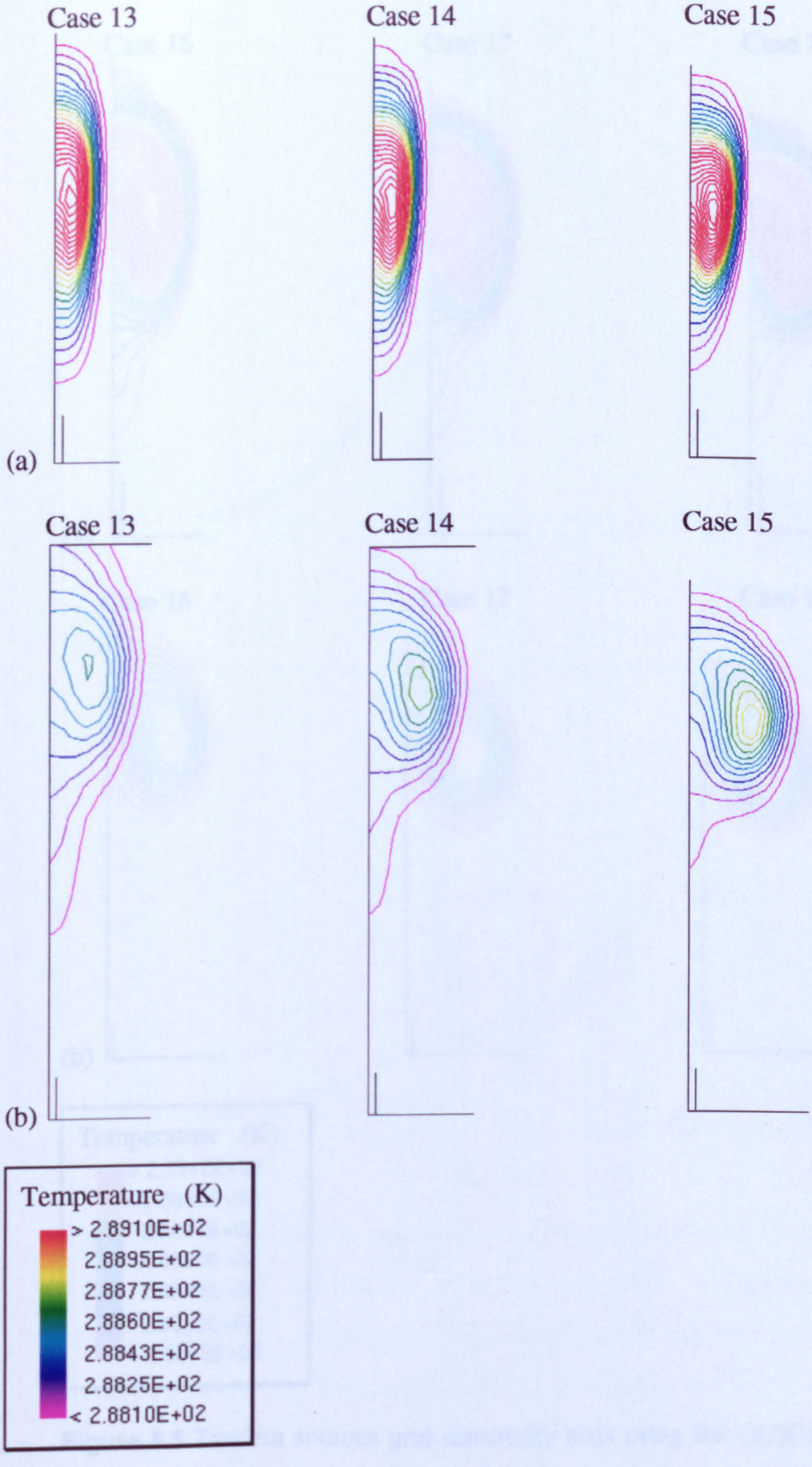

Figure 5.4 Tandem sources grid sensitivity tests using the hybrid scheme (Cases 13–15); temperature contours where (a) refers to x = 10D and (b) to x = 40D. (Original in colour.)

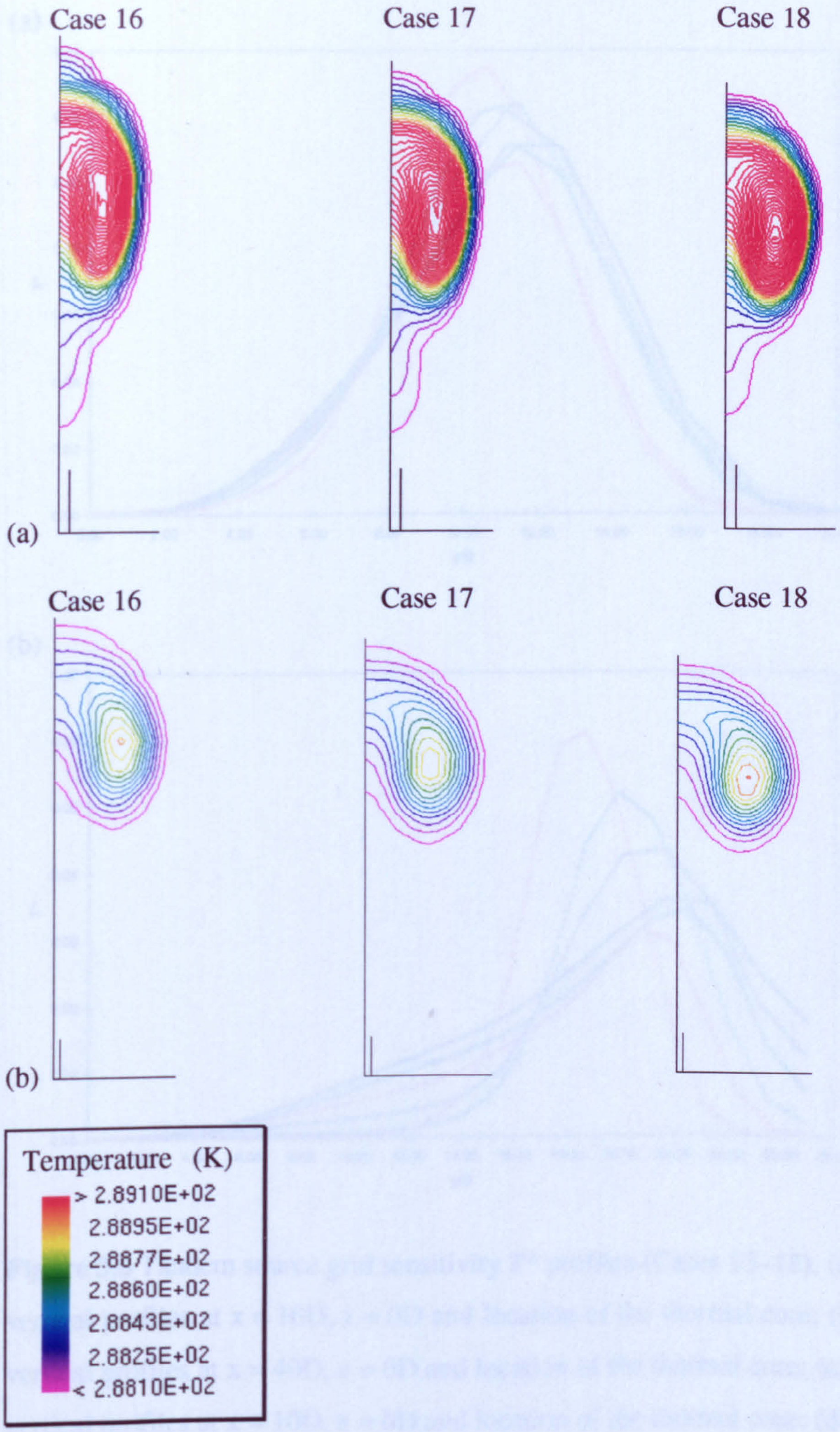

Figure 5.5 Tandem sources grid sensitivity tests using the QUICK scheme (Cases 16–18); temperature contours where (a) refers to x = 10D and (b) to x = 40D. (Original in colour.)

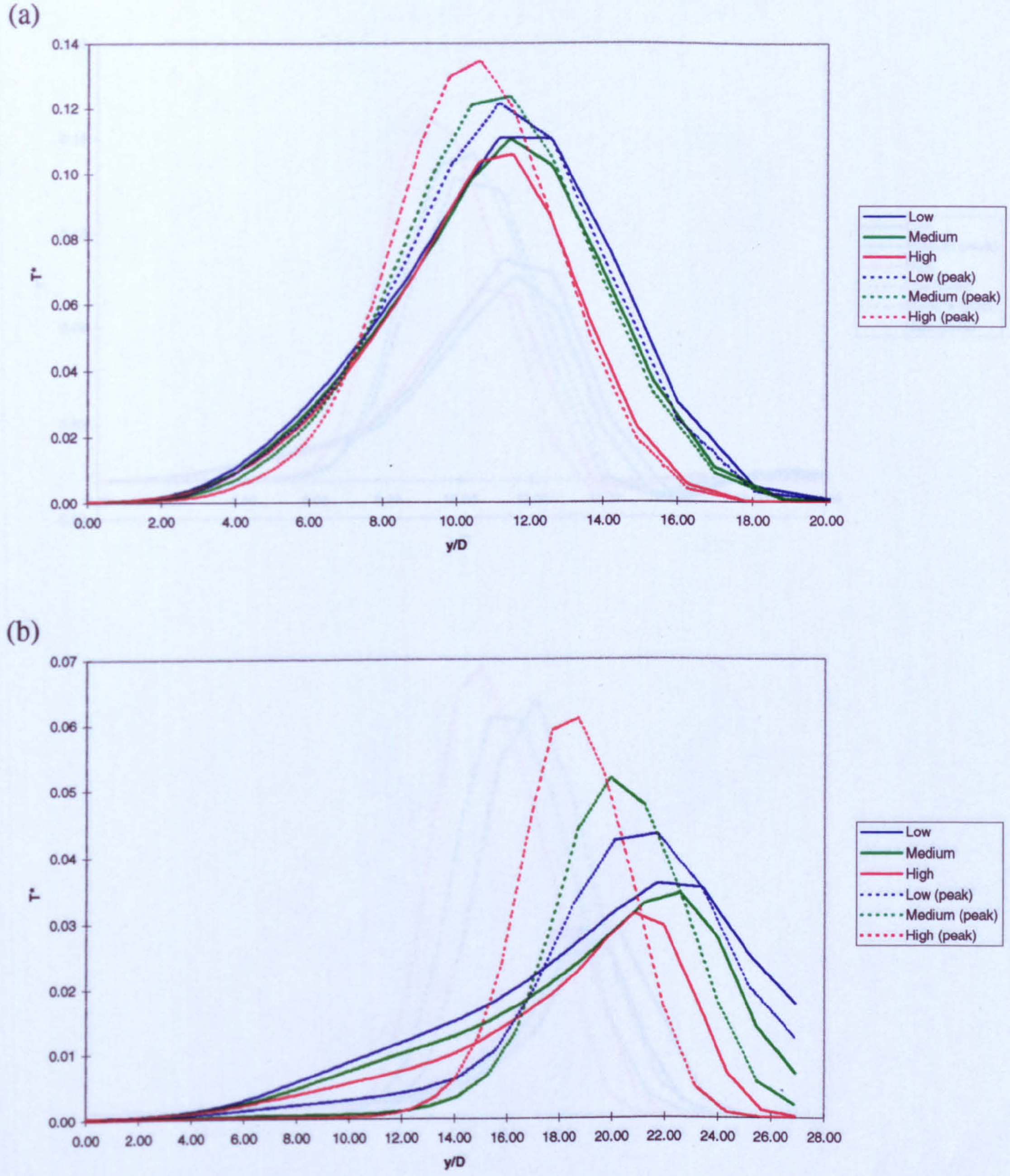

Figure 5.6 Tandem source grid sensitivity T^* profiles (Cases 13–18). (a) Hybrid scheme vertical profiles at x = 10D, z = 0D and location of the thermal core; (b) hybrid scheme vertical profiles at x = 40D, z = 0D and location of the thermal core; (c) QUICK scheme vertical profiles at x = 10D, z = 0D and location of the thermal core; (d) QUICK scheme vertical profiles at x = 40D, z = 0D and location of the thermal core. (Original in Colour)

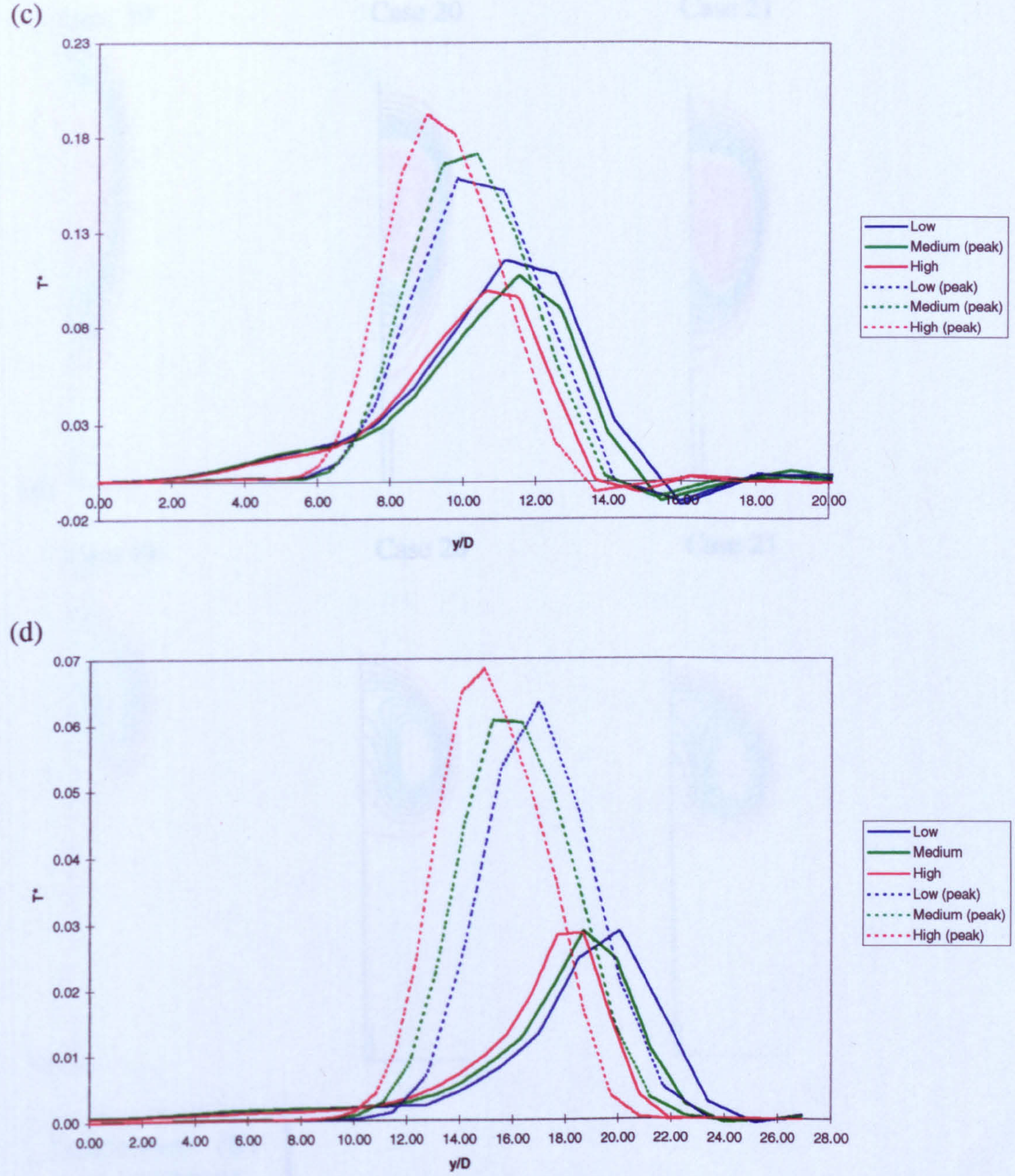

Figure 5.6 *Continued.*

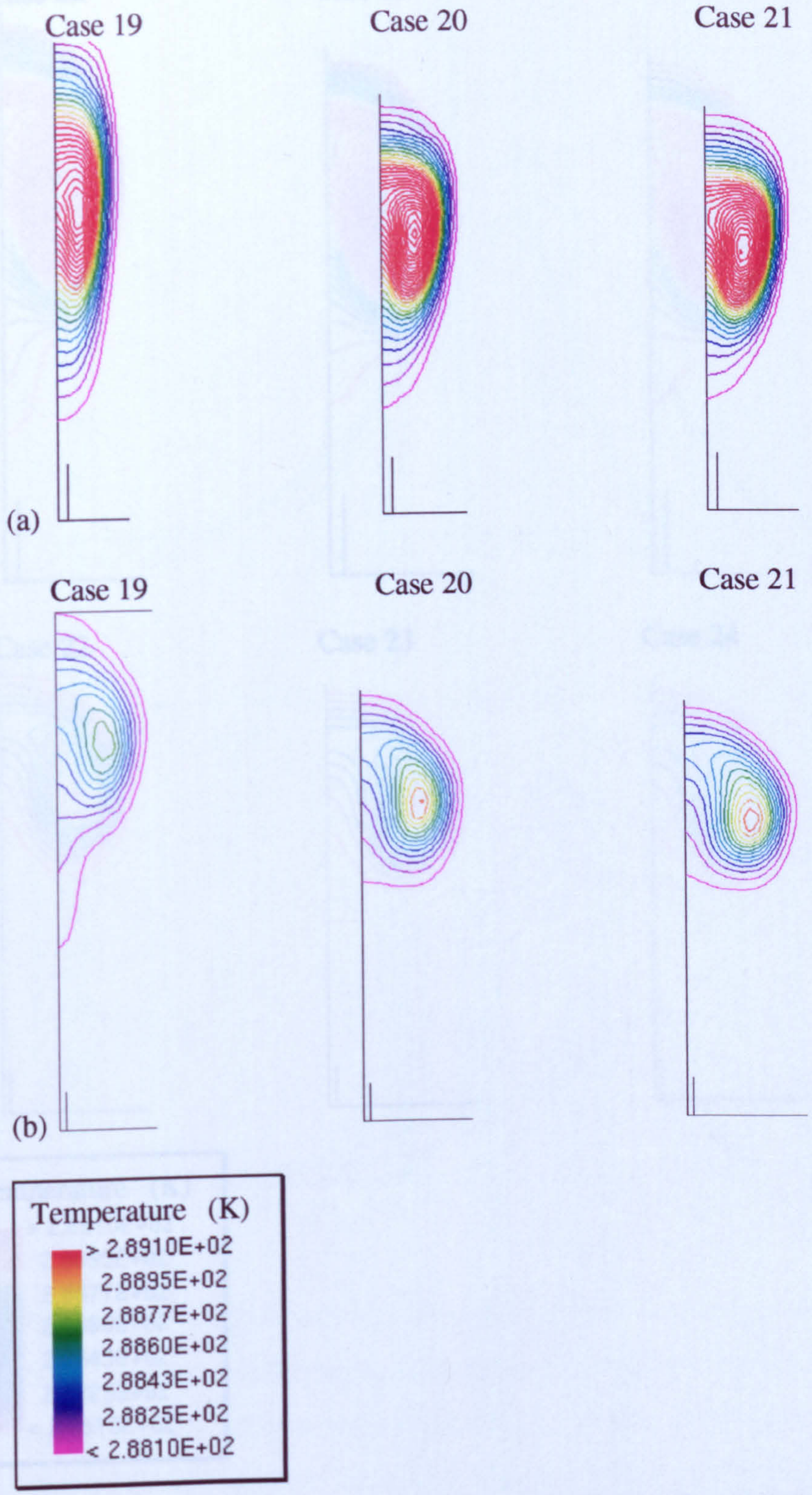

Figure 5.7 Tandem sources grid sensitivity tests using the hybrid scheme and a modified grid distribution (Cases 19–21); temperature contours where (a) refers to x = 10D and (b) to x = 40D. (Original in colour.)

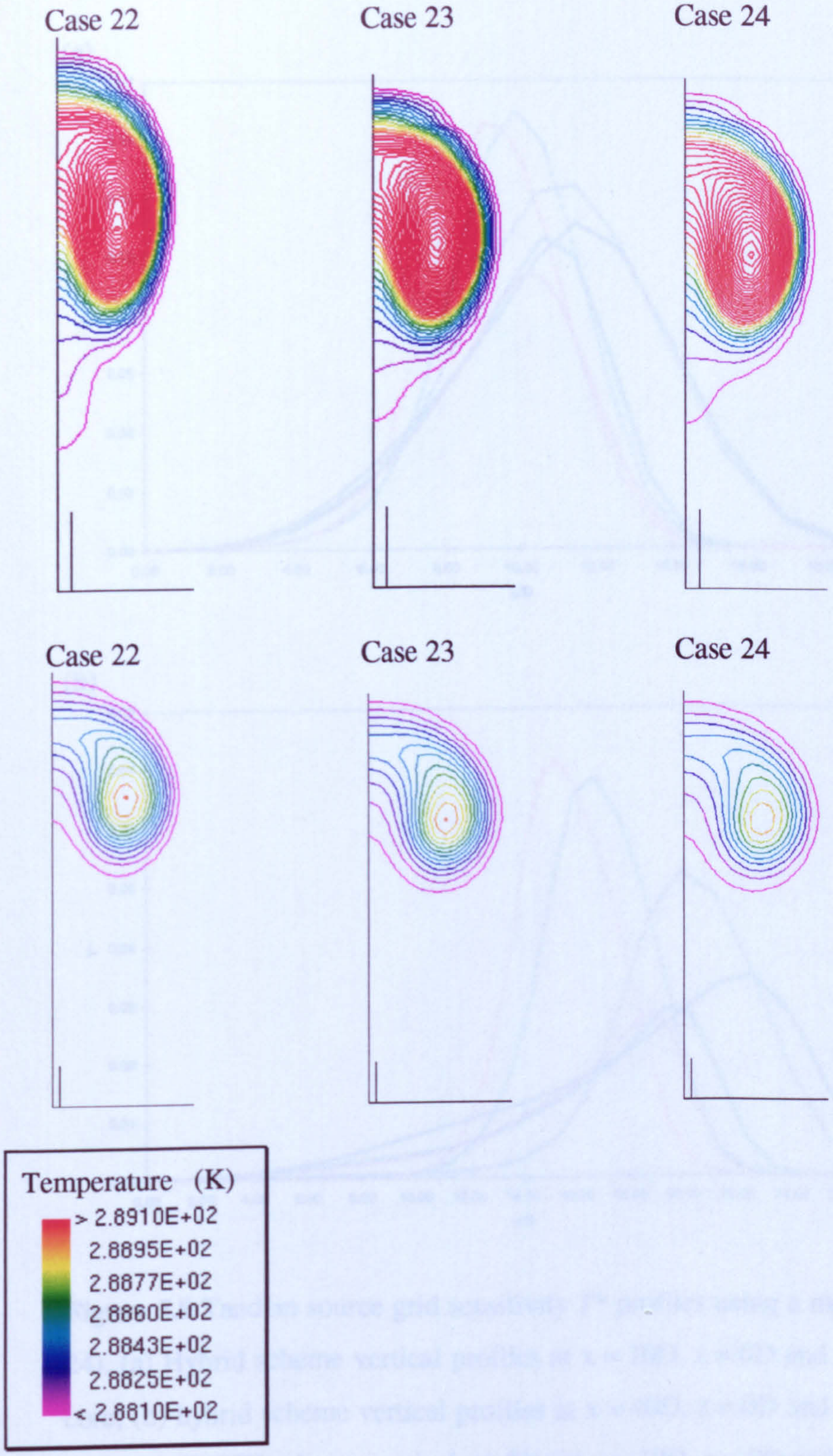

Figure 5.8 Tandem sources grid sensitivity tests using the QUICK scheme and a modified grid distribution (Cases 22–24); temperature contours where (a) refers to x = 10D and (b) to x = 40D. (Original in colour.)

(a)

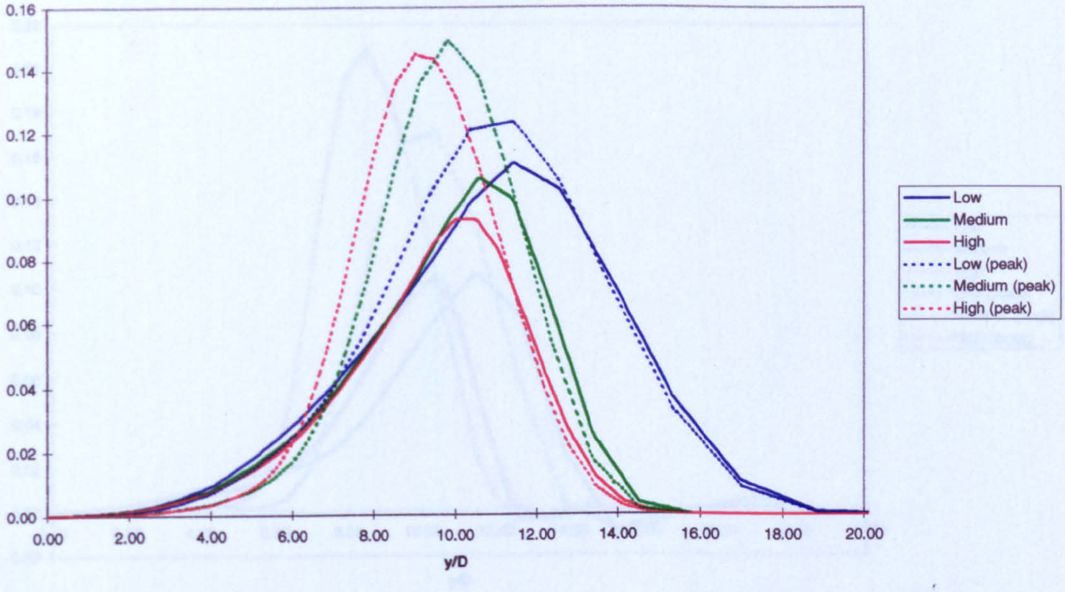

(b)

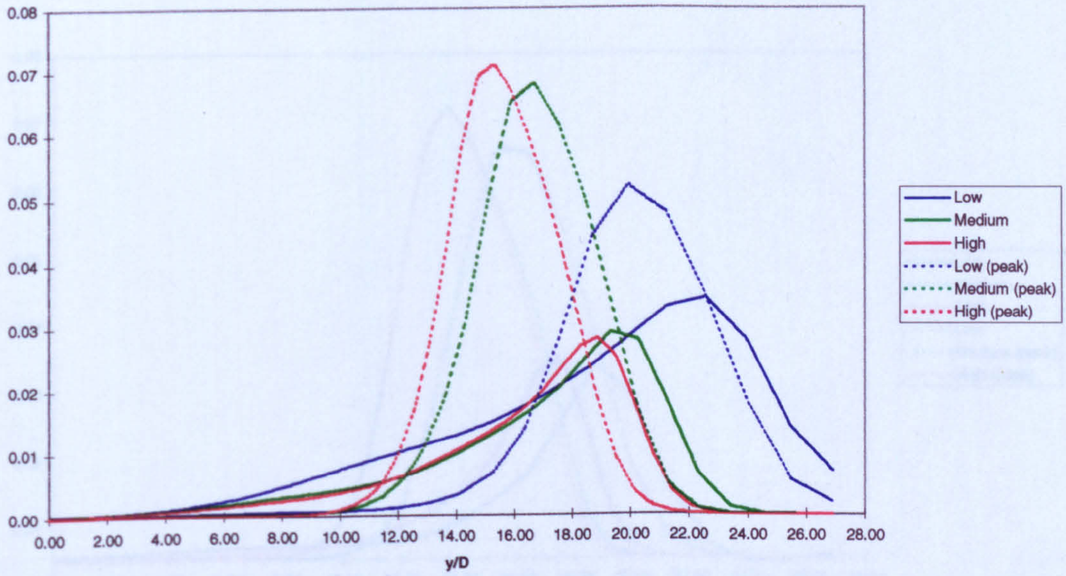

Figure 5.9 Tandem source grid sensitivity T^* profiles using a modified grid (Cases 19–24). (a) Hybrid scheme vertical profiles at x = 10D, z = 0D and location of the thermal core; (b) hybrid scheme vertical profiles at x = 40D, z = 0D and location of the thermal core; (c) QUICK scheme vertical profiles at x = 10D, z = 0D and location of the thermal core; (d) QUICK scheme vertical profiles at x = 40D, z = 0D and location of the thermal core. (Original in colour.)

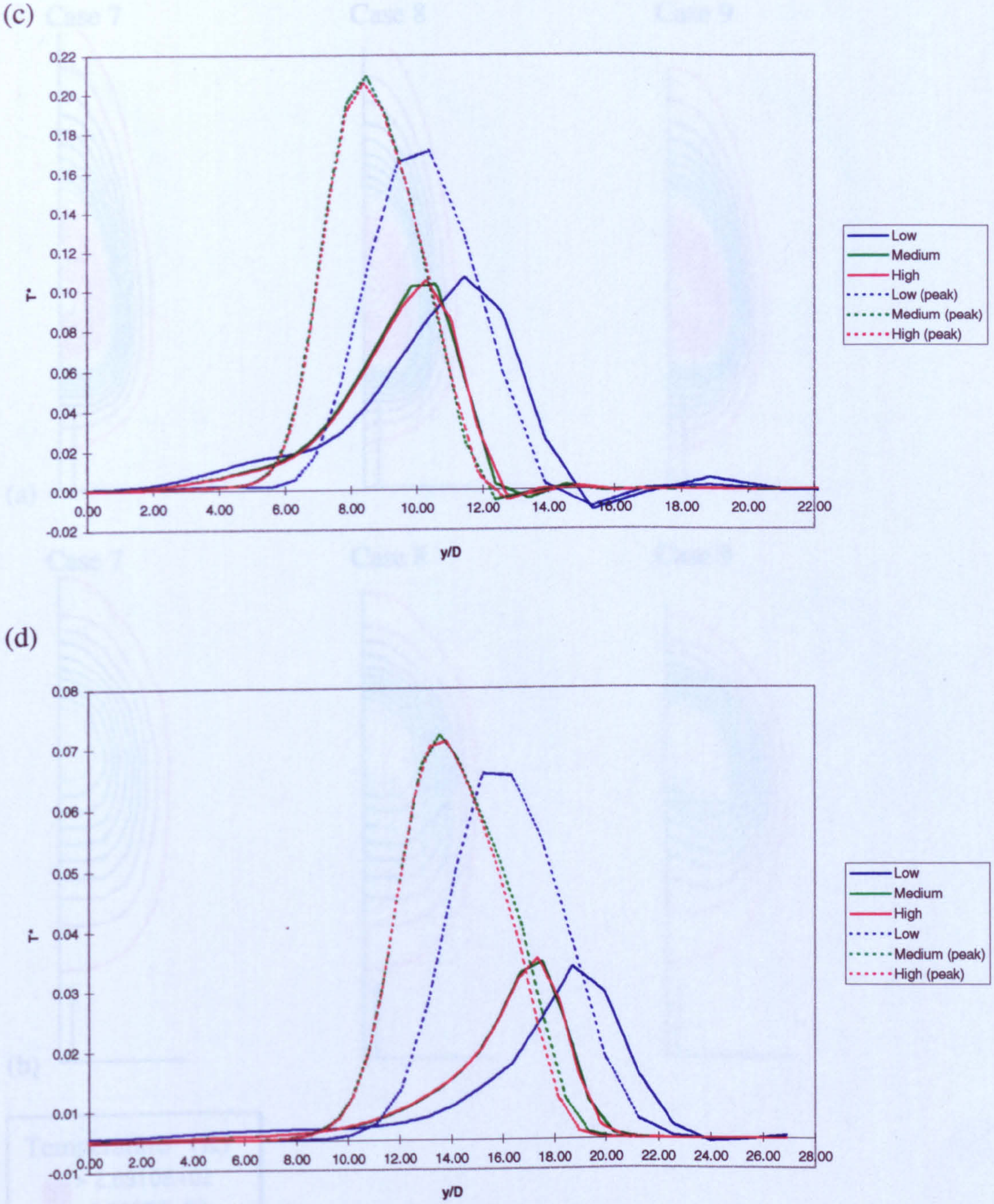

Figure 5.9 *Continued.*

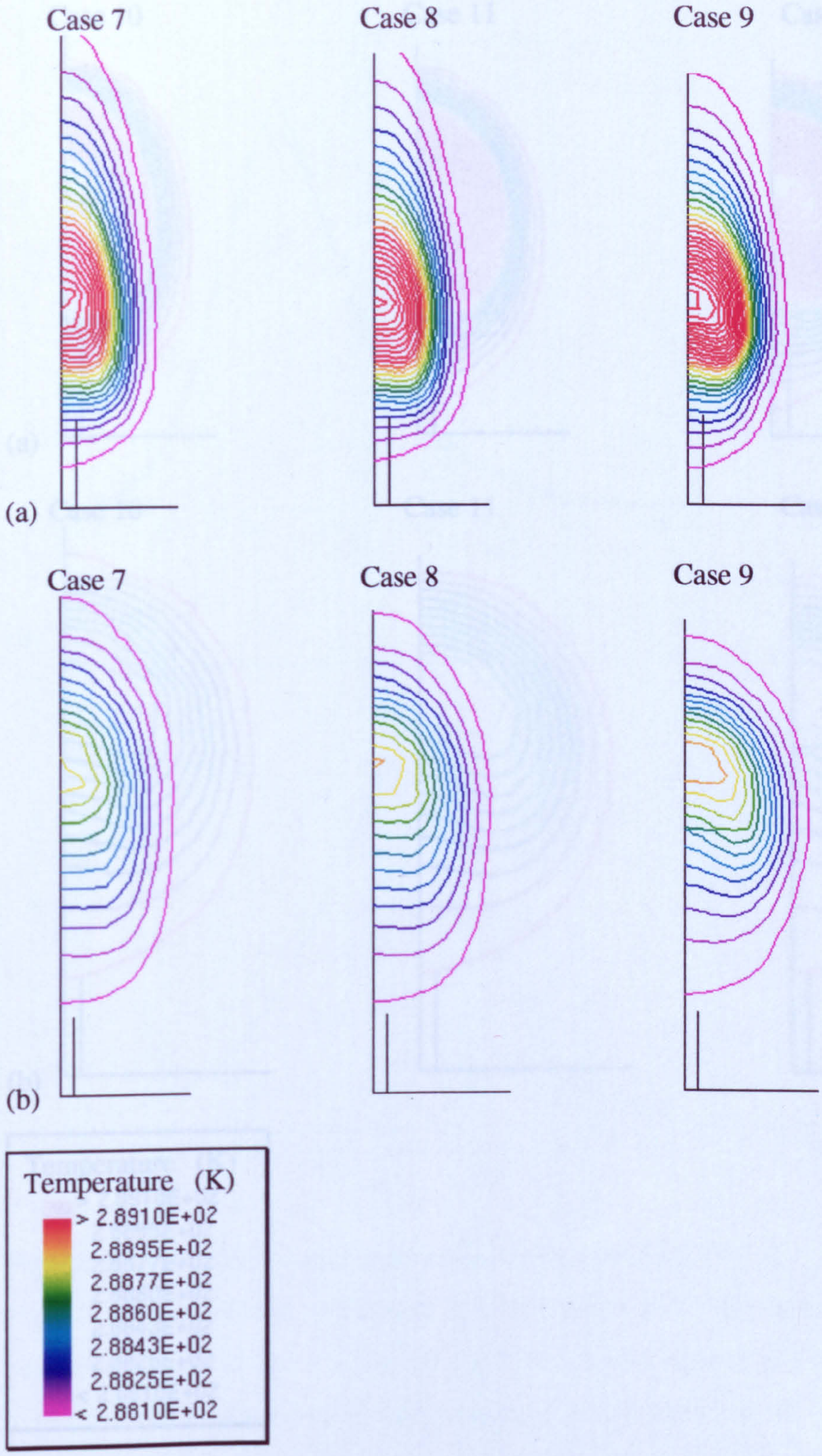

Figure 5.10 Tandem sources grid sensitivity tests using the hybrid scheme with $R = 1$ (Cases 7–9); temperature contours where (a) refers to x = 10D and (b) to x = 40D. (Original in colour.)

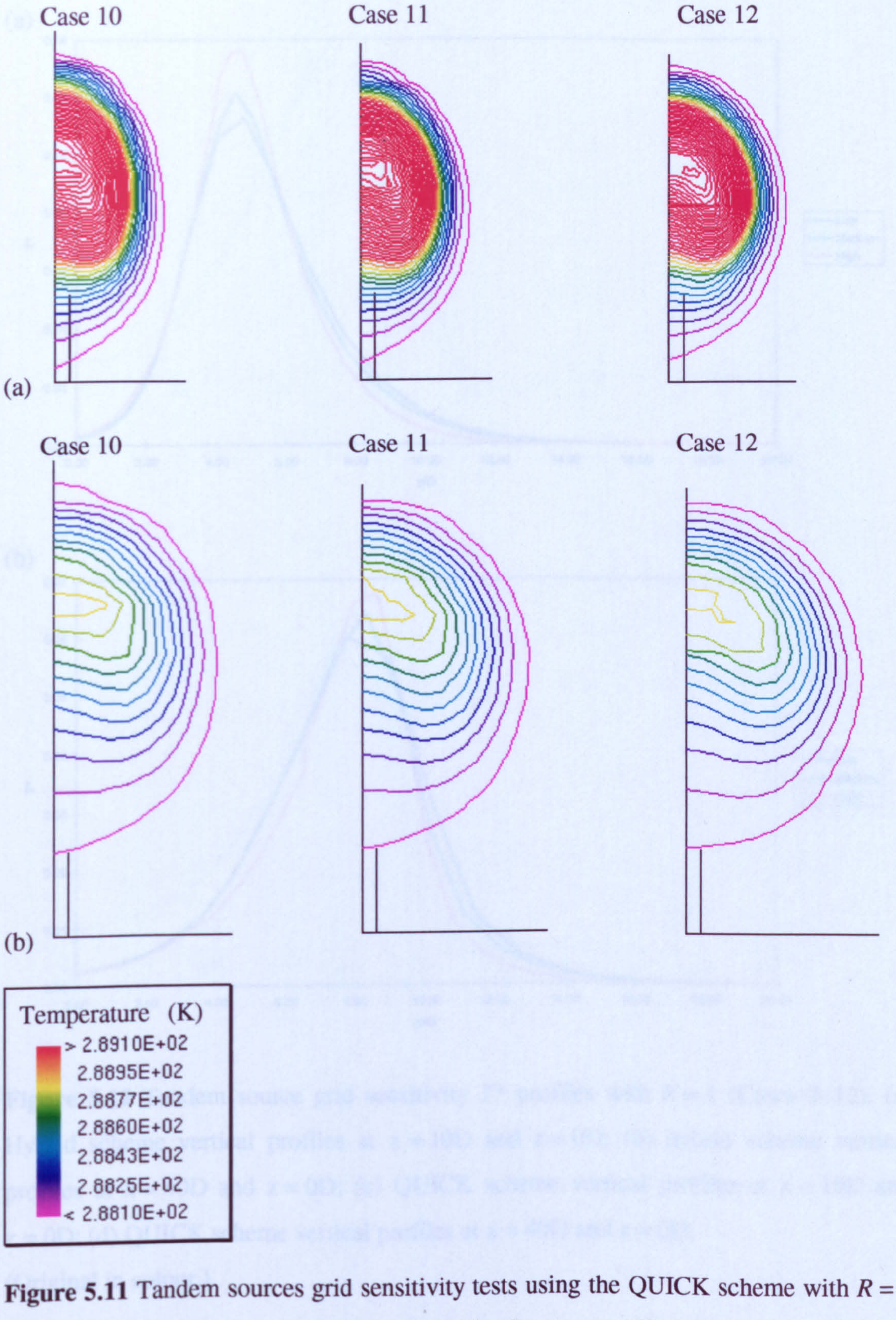

Figure 5.11 Tandem sources grid sensitivity tests using the QUICK scheme with $R = 1$ (Cases 10–12); temperature contours where (a) refers to x = 10D and (b) to x = 40D. (Original in colour.)

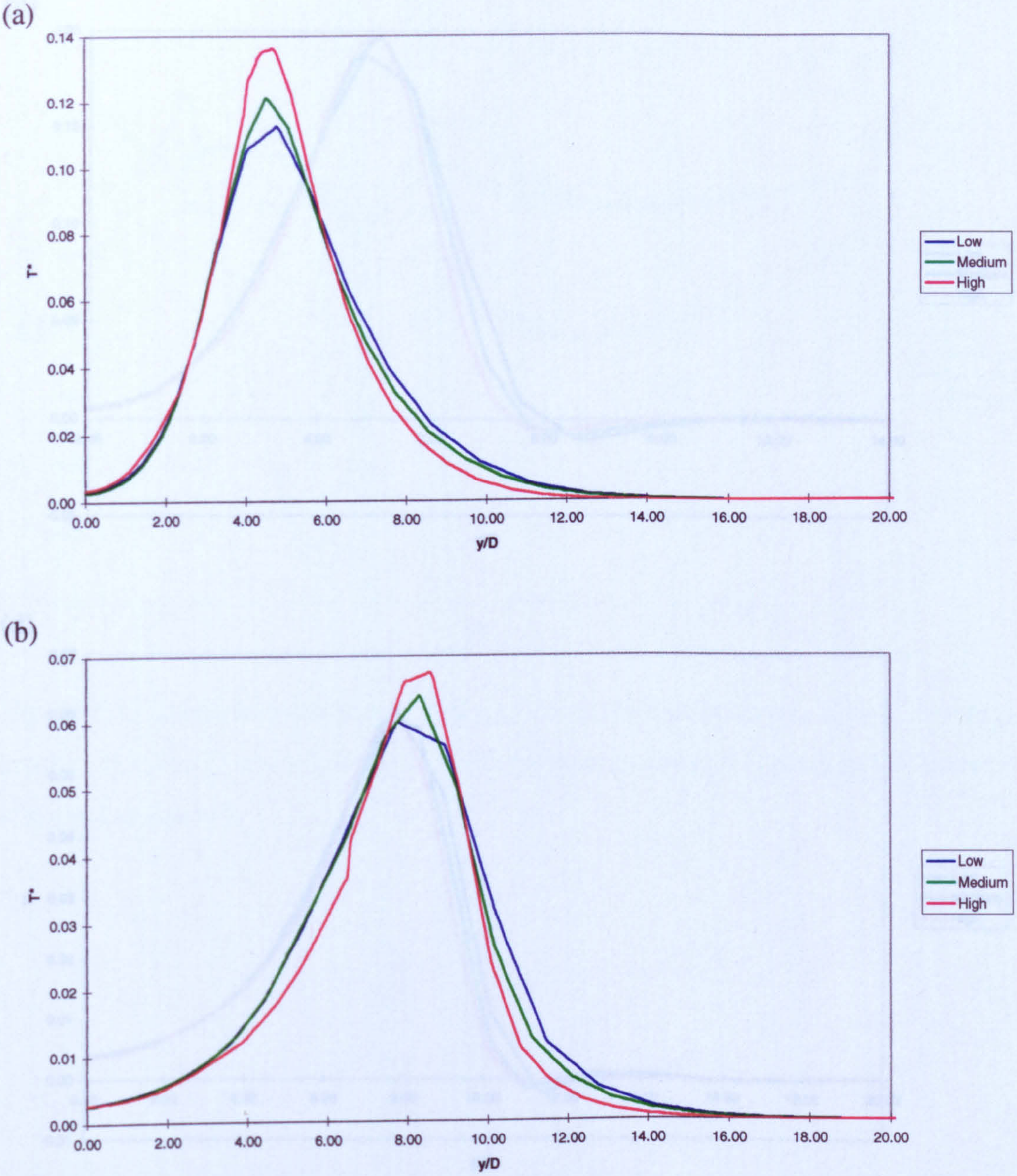

Figure 5.12 Tandem source grid sensitivity T^* profiles with $R = 1$ (Cases 7–12). (a) Hybrid scheme vertical profiles at x = 10D and z = 0D; (b) hybrid scheme vertical profiles at x = 40D and z = 0D; (c) QUICK scheme vertical profiles at x = 10D and z = 0D; (d) QUICK scheme vertical profiles at x = 40D and z = 0D.

(Original in colour.)

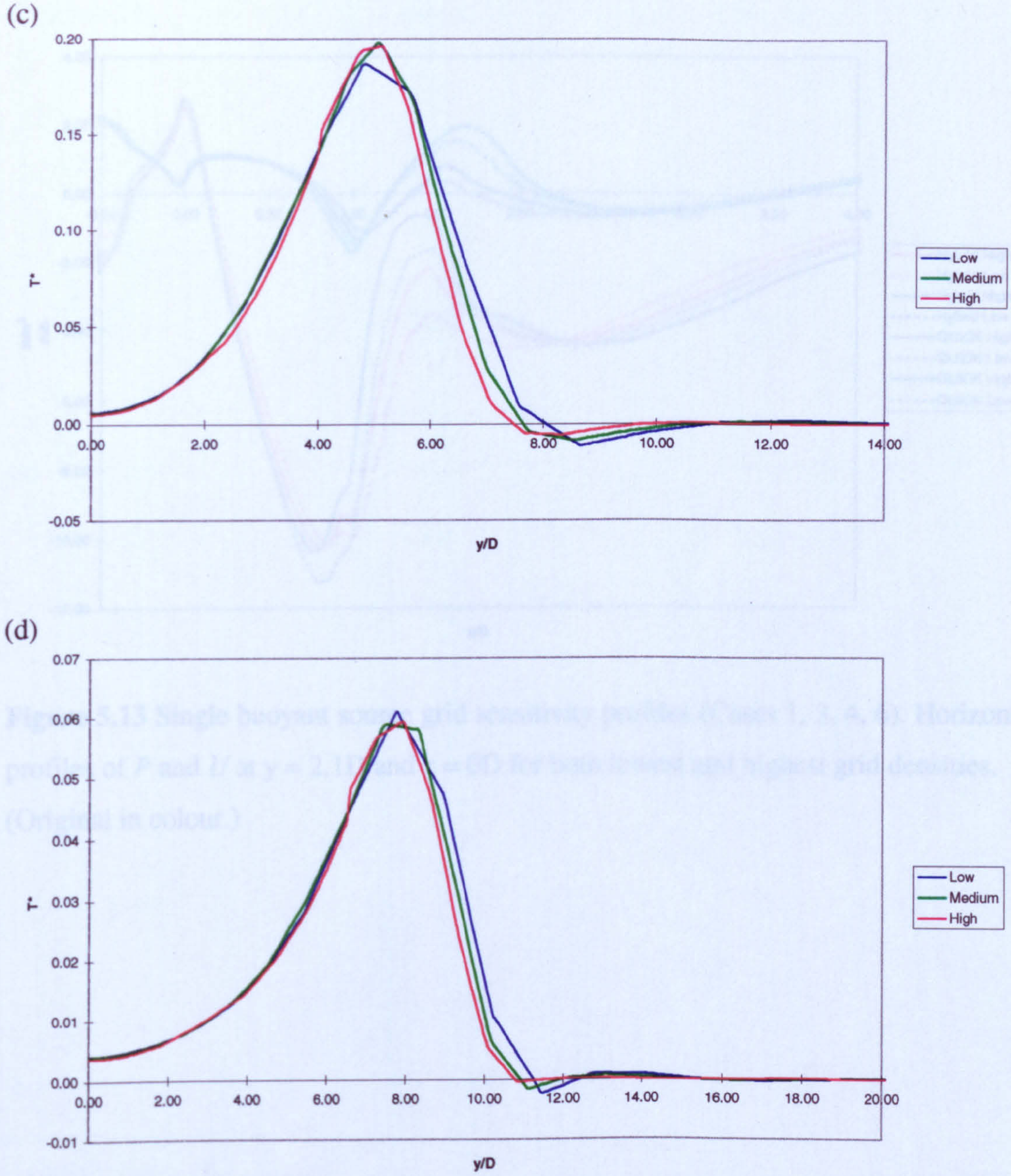

Figure 5.12 *Continued.*

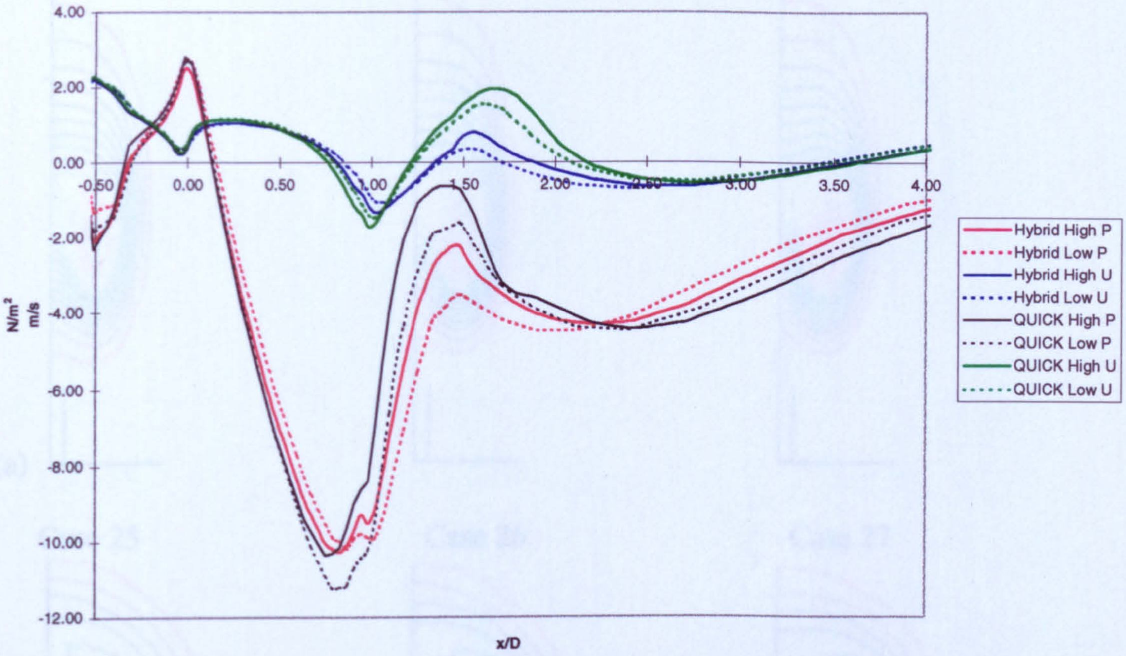

Figure 5.13 Single buoyant source grid sensitivity profiles (Cases 1, 3, 4, 6). Horizontal profiles of *P* and *U* at y = 2.1D and z = 0D for both lowest and highest grid densities. (Original in colour.)

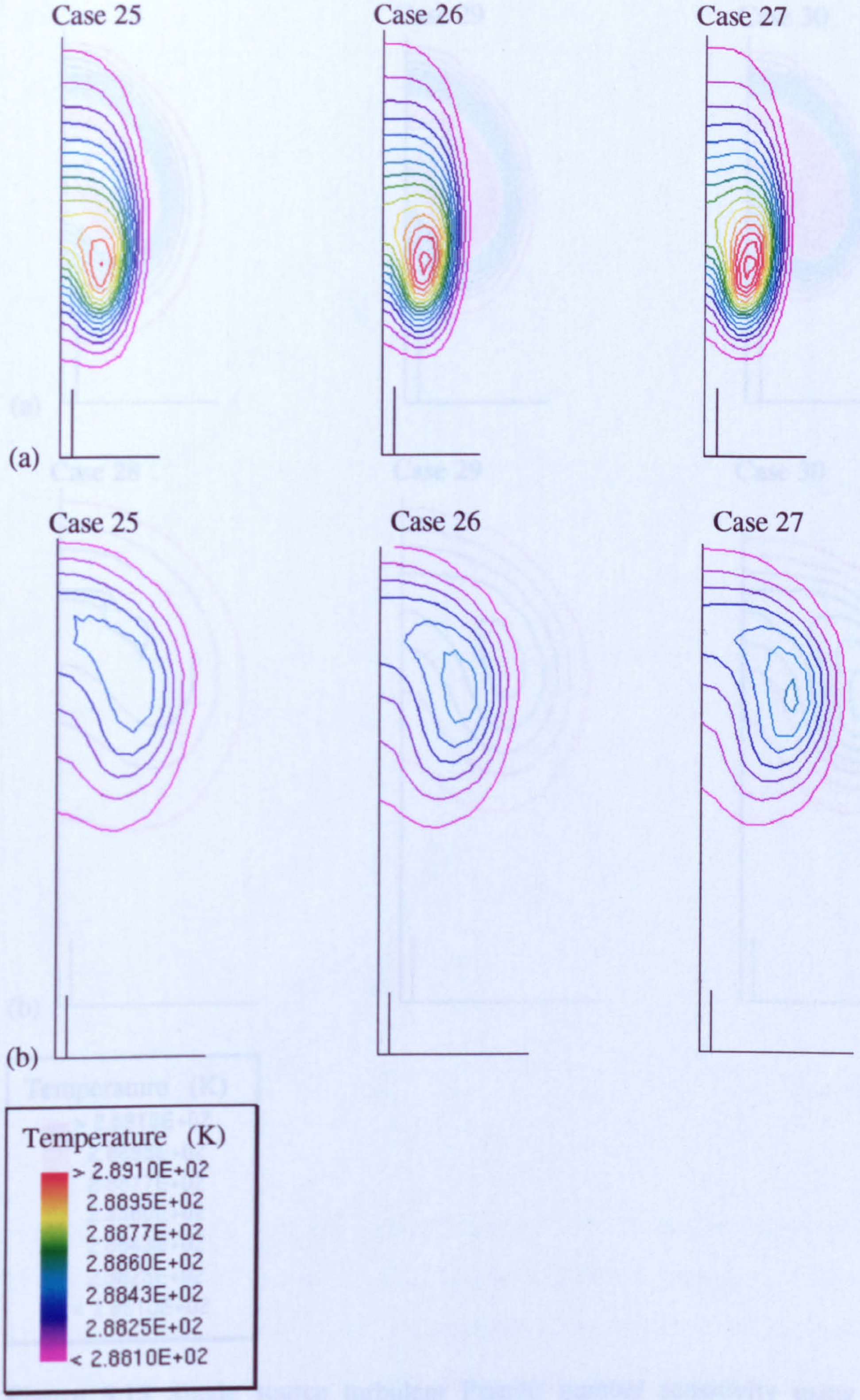

Figure 5.14 Single source turbulent Prandtl number sensitivity test using the hybrid scheme (Cases 25–27, Pr_t = 0.4, 0.6 and 0.9 respectively); temperature contours where (a) refers to x = 10D and (b) to x = 40D. (Original in colour.)

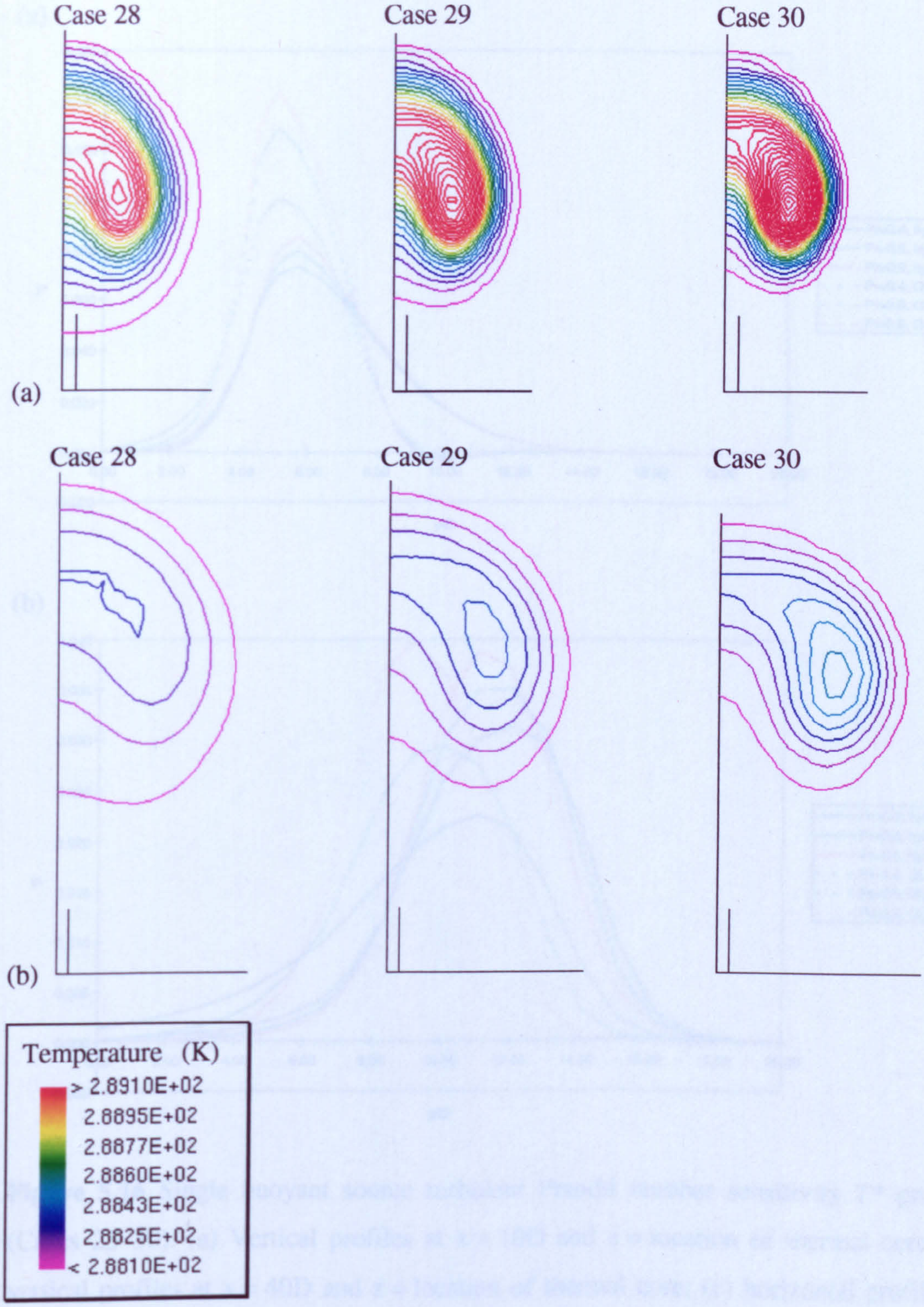

Figure 5.15 Single source turbulent Prandtl number sensitivity using the QUICK scheme (Cases 28–30, Pr_t = 0.4, 0.6 and 0.9 respectively); temperature contours where (a) refers to x = 10D and (b) to x = 40D. (Original in colour.)

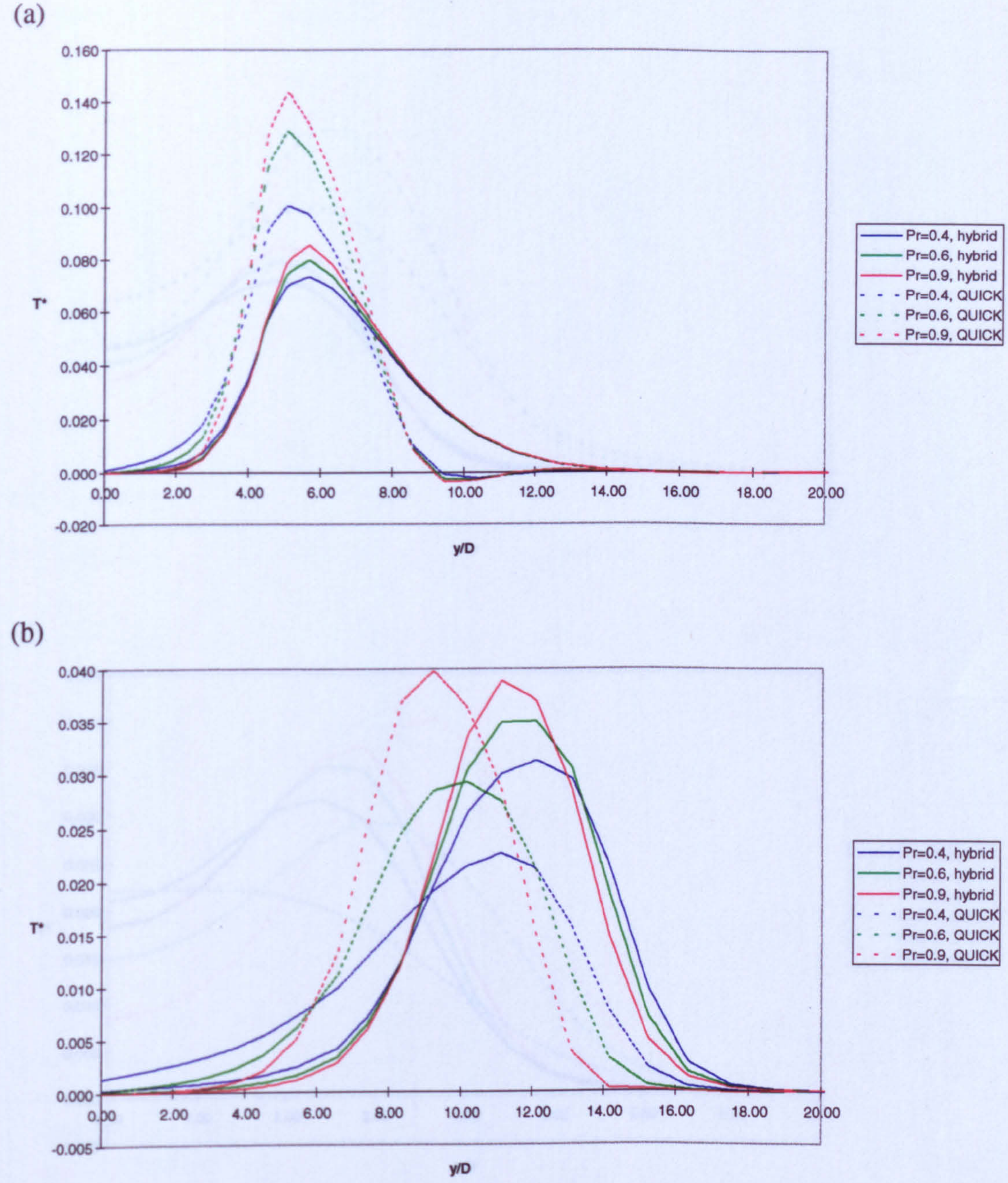

Figure 5.16 Single buoyant source turbulent Prandtl number sensitivity *T** profiles (Cases 25–30). (a) Vertical profiles at x = 10D and z = location of thermal core; (b) vertical profiles at x = 40D and z = location of thermal core; (c) horizontal profiles at x = 10D and y = location of thermal core; (d) horizontal profiles at x = 40D and y = location of thermal core. (Original in colour.)

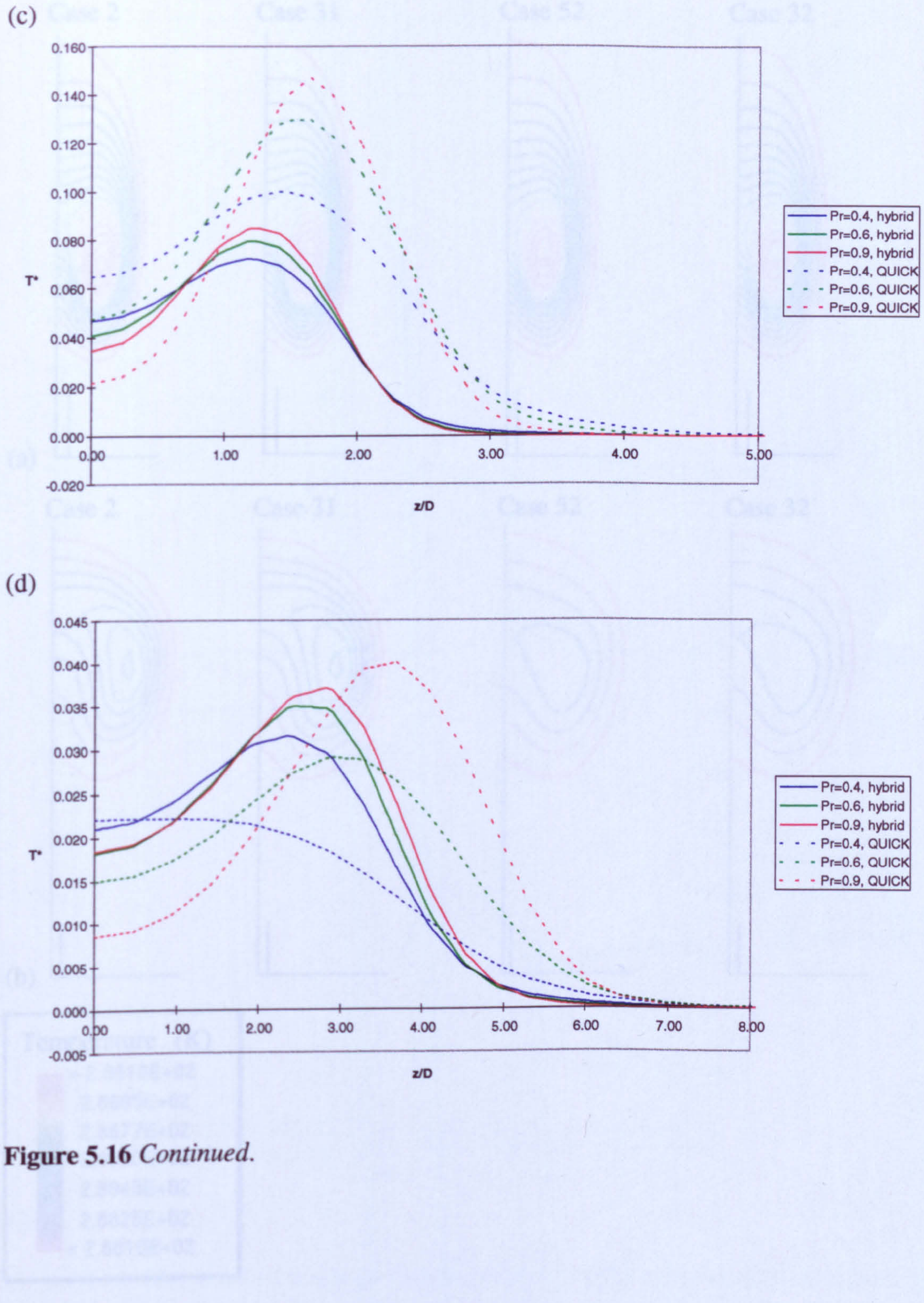

Figure 5.16 *Continued.*

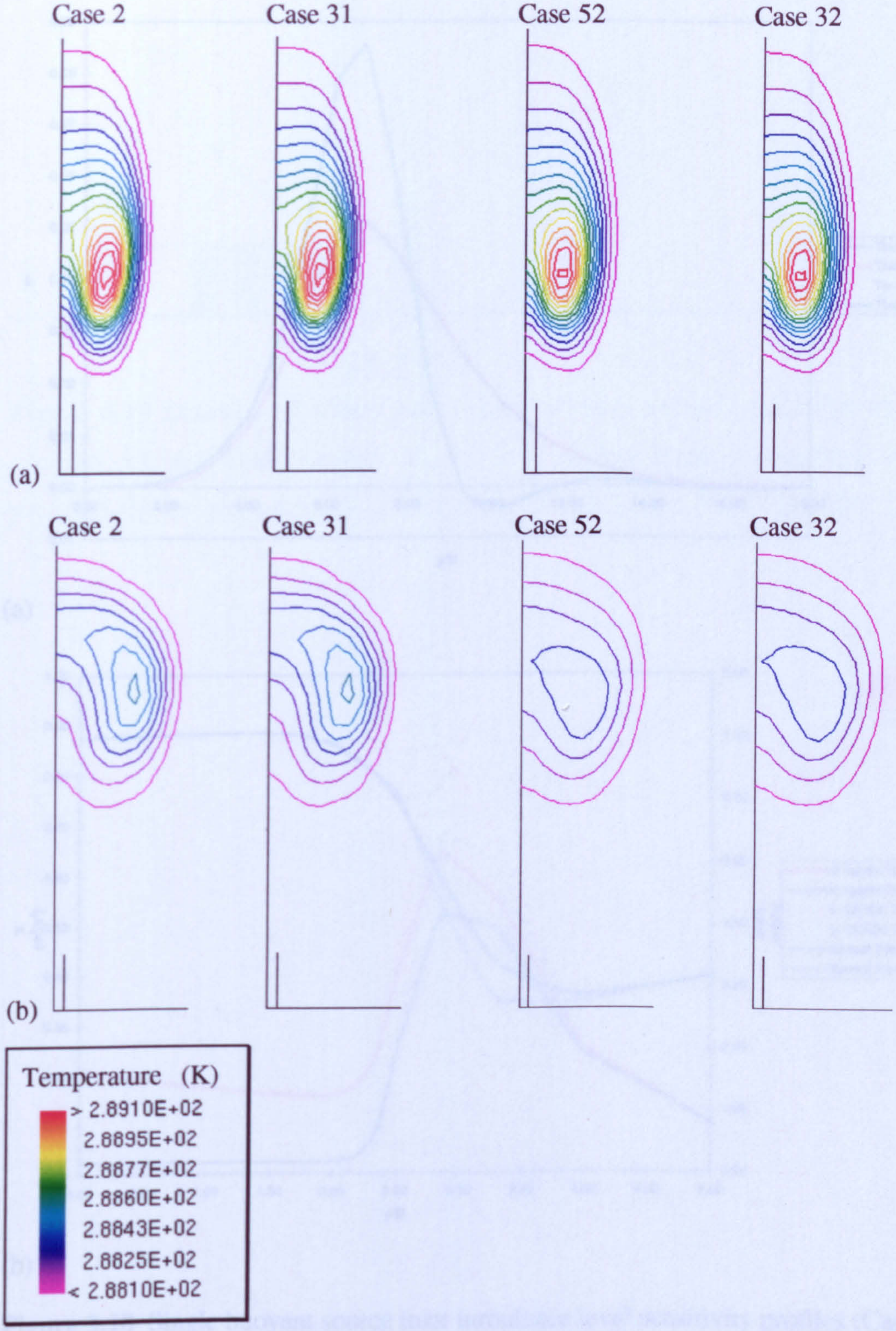

Figure 5.17 Single buoyant source C_3 sensitivity (Cases 2, 31, 52, 32; where *k*-ε $C_3 = 1$, *k*-ε $C_3 = 0$, DFM $C_3 = 1$ and DFM $C_3 = 0$ respectively), temperature contours where (a) refers to x = 10D and (b) to x = 40D. (Original in colour.)

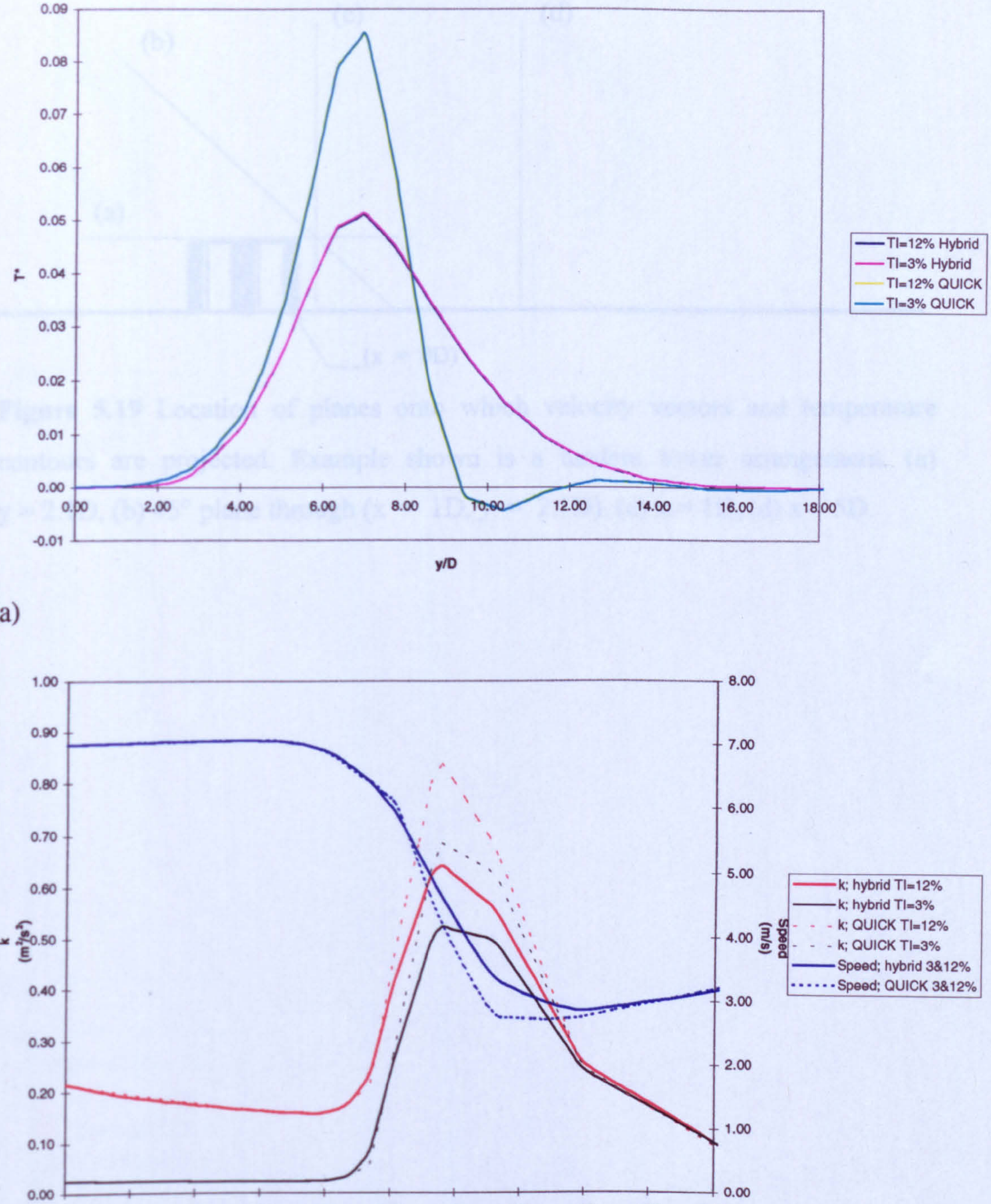

(a)

(b)

Figure 5.18 Single buoyant source inlet turbulence level sensitivity profiles (Cases 33–35). (a) Vertical T^* profiles at x = 10D and z = 0D; (b) vertical profiles of k and speed at x = -1D (centre of the tower development duct) and z = 0D.

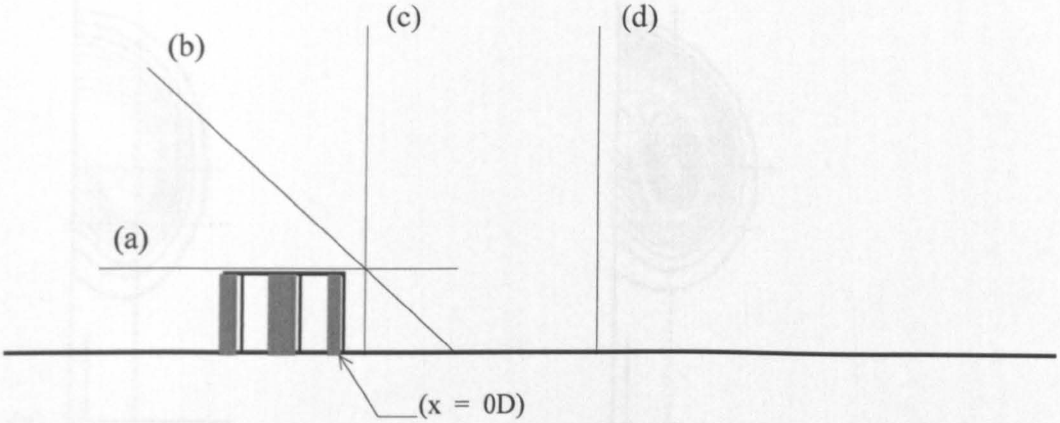

Figure 5.19 Location of planes onto which velocity vectors and temperature contours are projected. Example shown is a tandem tower arrangement. (a) y = 2.1D, (b) 45° plane through (x = 1D, y = 2.1D), (c) x = 1D, (d) x = 5D.

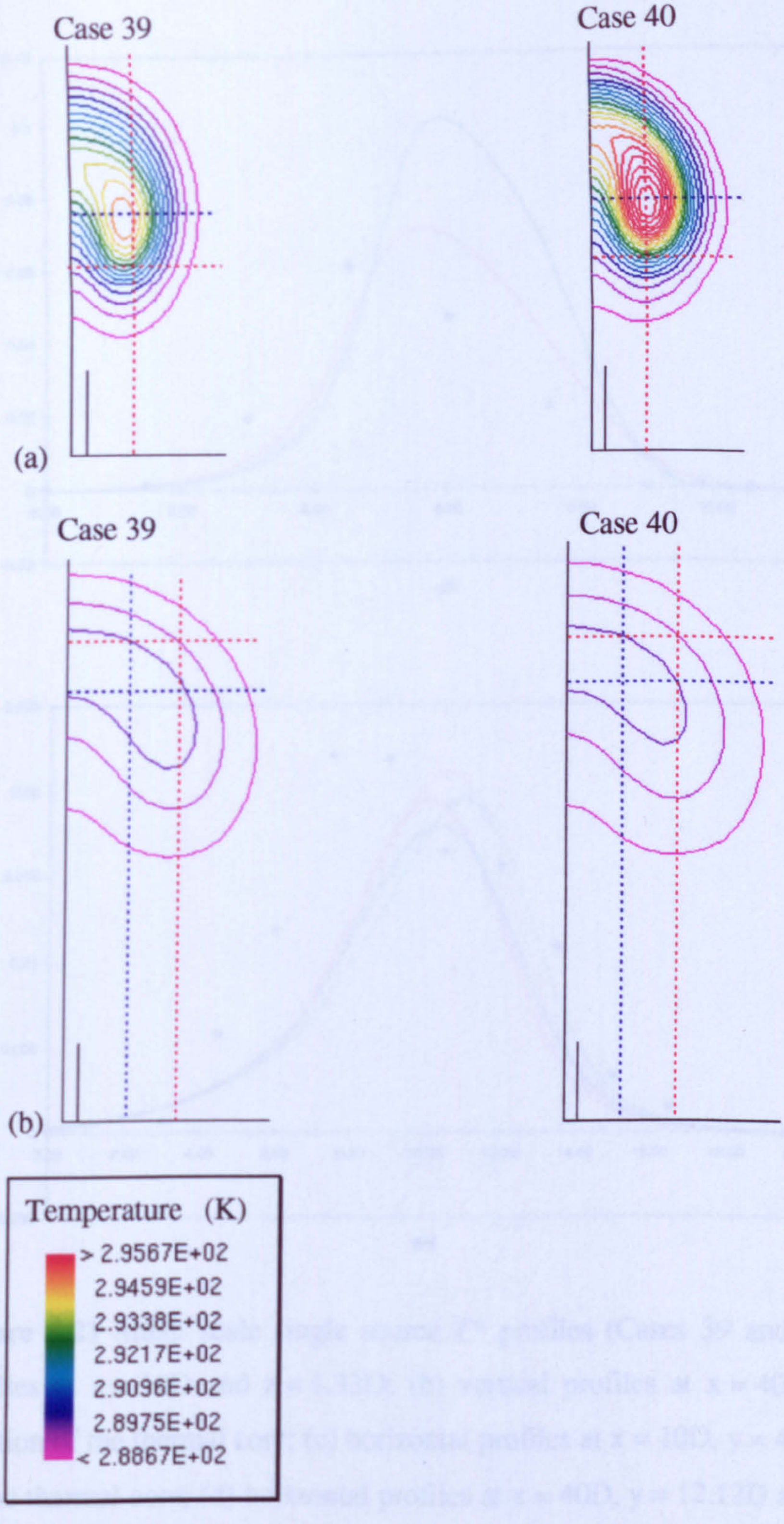

Figure 5.20 Small-scale single source (Cases 39 and 40); temperature contours where (a) refers to x = 10D and (b) to x = 40D. Red dotted lines refer to the location of experimental profiles, blue lines bisect the thermal core. External contour = 288.67K subsequent gaps = 0.46K. (Original in colour.)

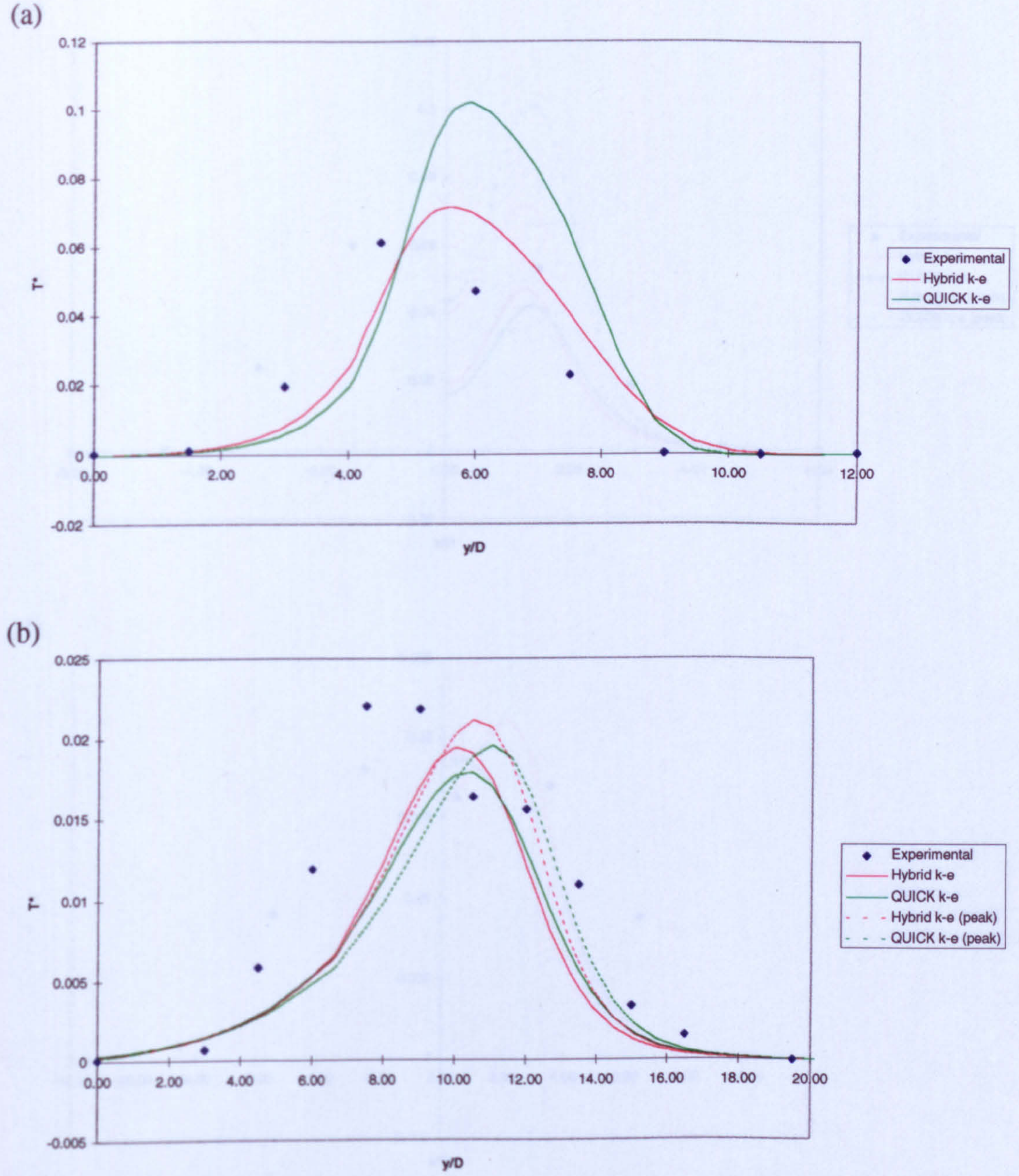

Figure 5.21 Small scale single source *T** profiles (Cases 39 and 40). (a) Vertical profiles at x = 10D and z = 1.33D; (b) vertical profiles at x = 40D, z = 2.89D and location of the thermal core; (c) horizontal profiles at x = 10D, y = 4.54D and location of the thermal core; (d) horizontal profiles at x = 40D, y = 12.12D and location of the thermal core. (Original in colour.)

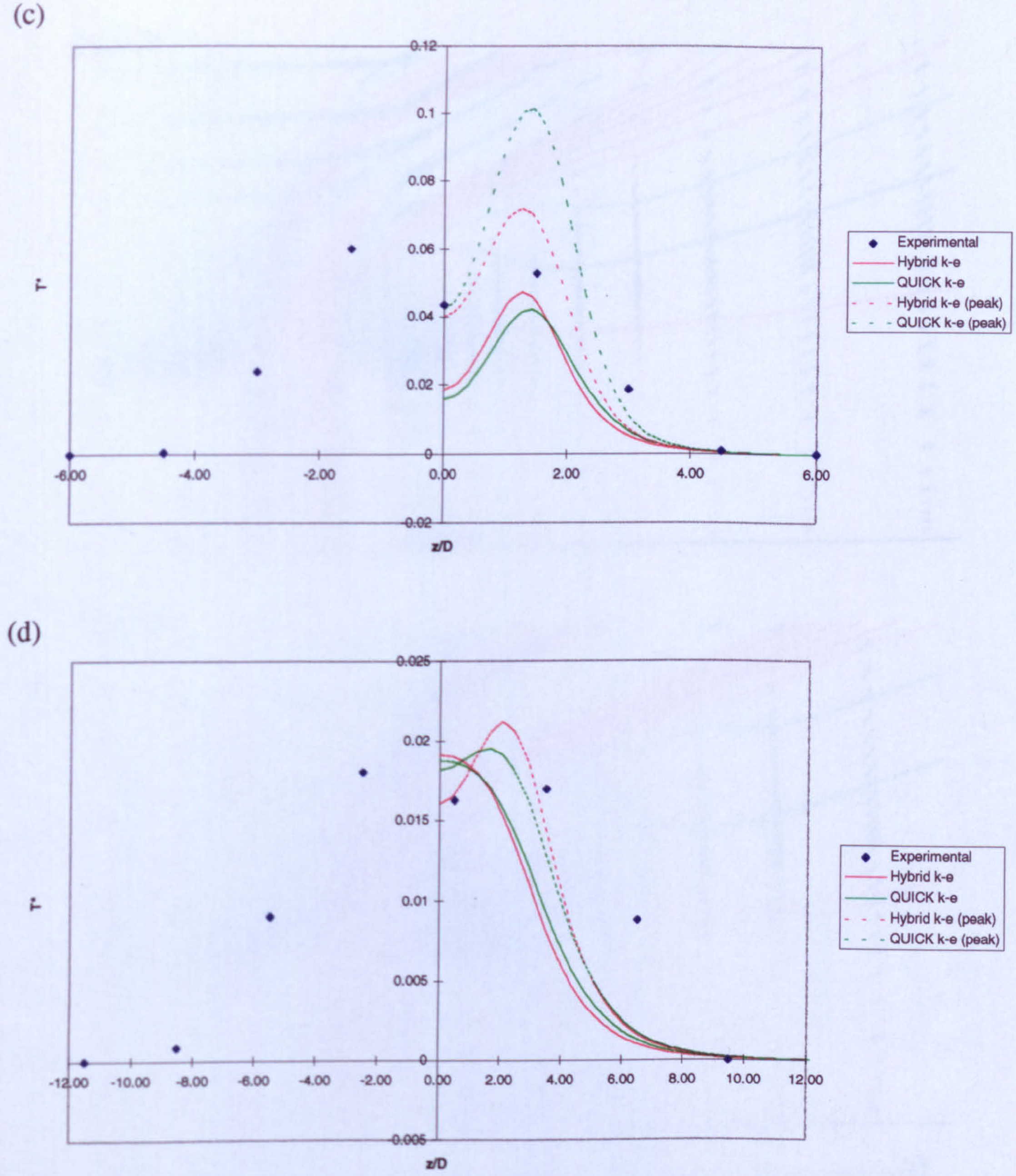

Figure 5.21 *Continued.*

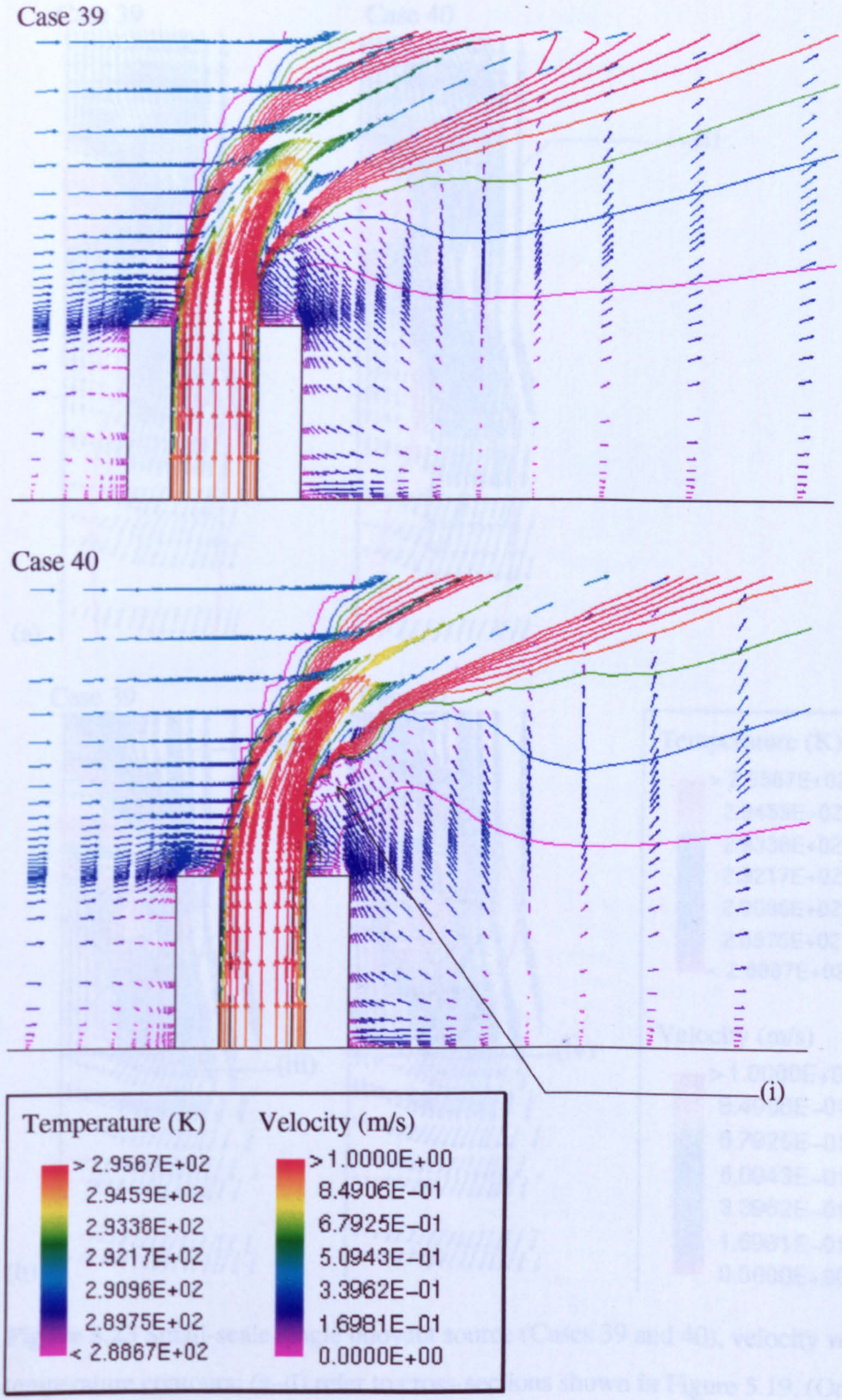

Figure 5.22 Small scale single buoyant source (Cases 39 and 40), velocity vector and temperature contours on the physical symmetry plane. (Original in colour.)

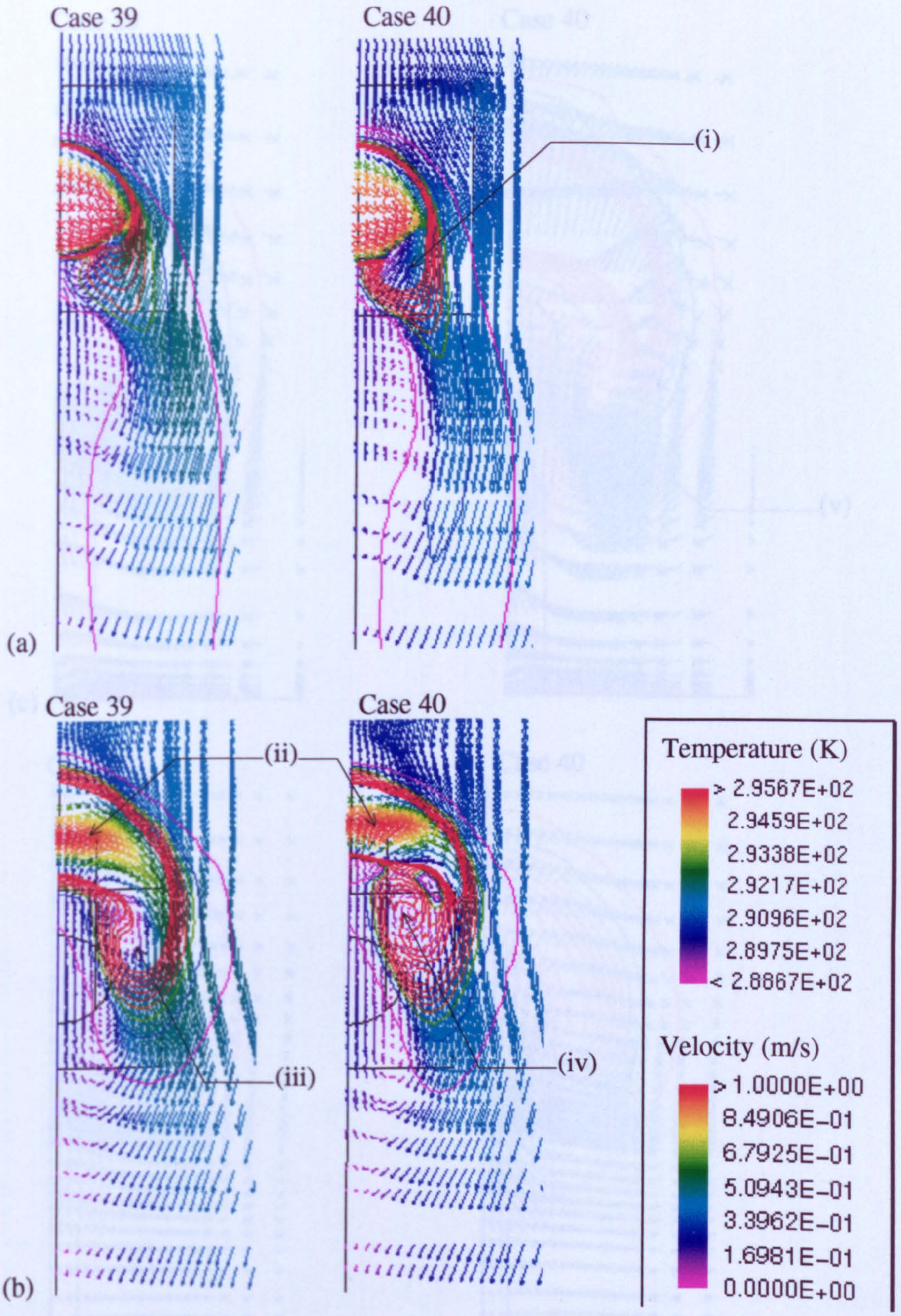

Figure 5.23 Small-scale single buoyant source (Cases 39 and 40), velocity vector and temperature contours; (a–d) refer to cross-sections shown in Figure 5.19. (Original in colour.)

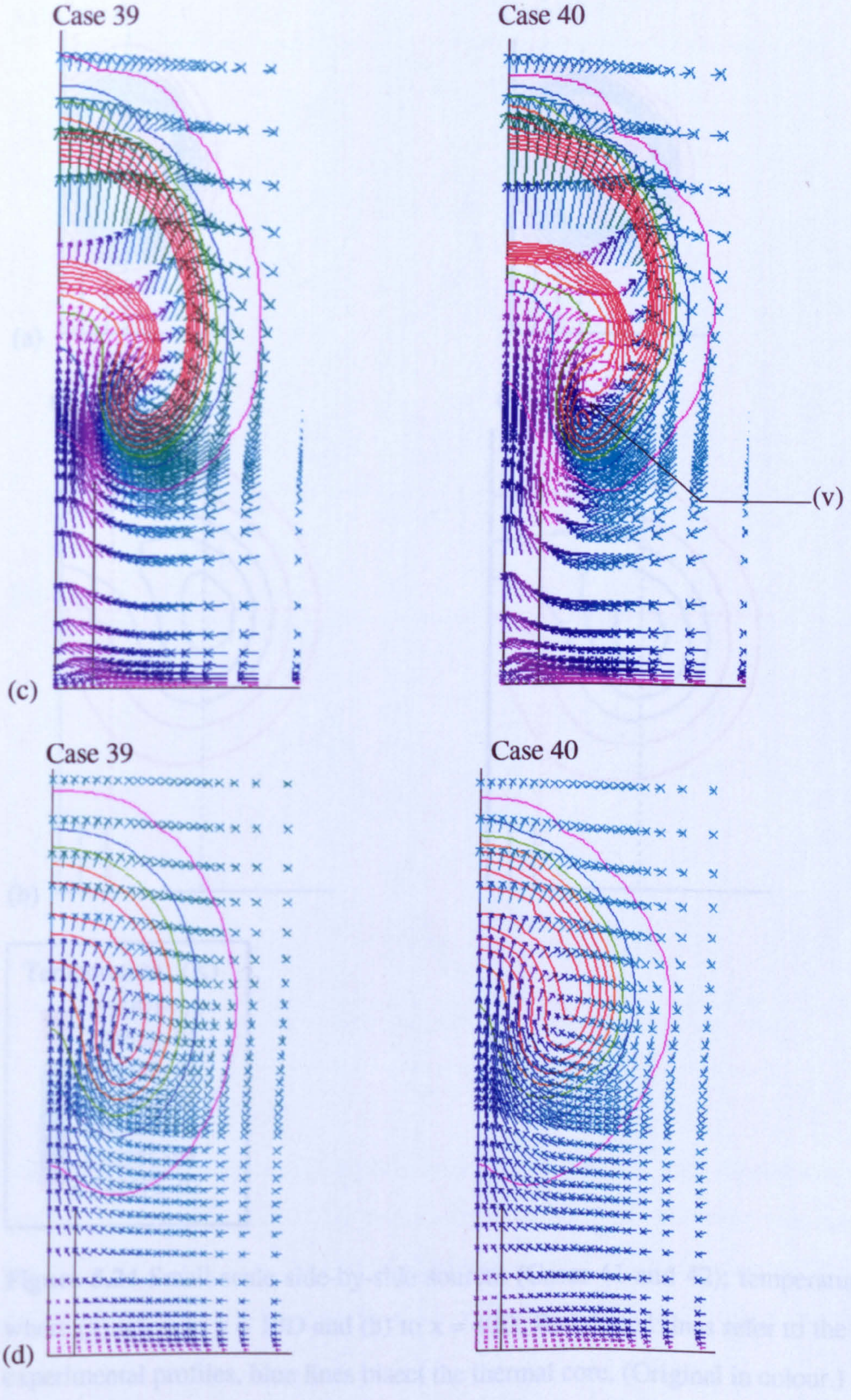

Figure 5.23 *Continued.*

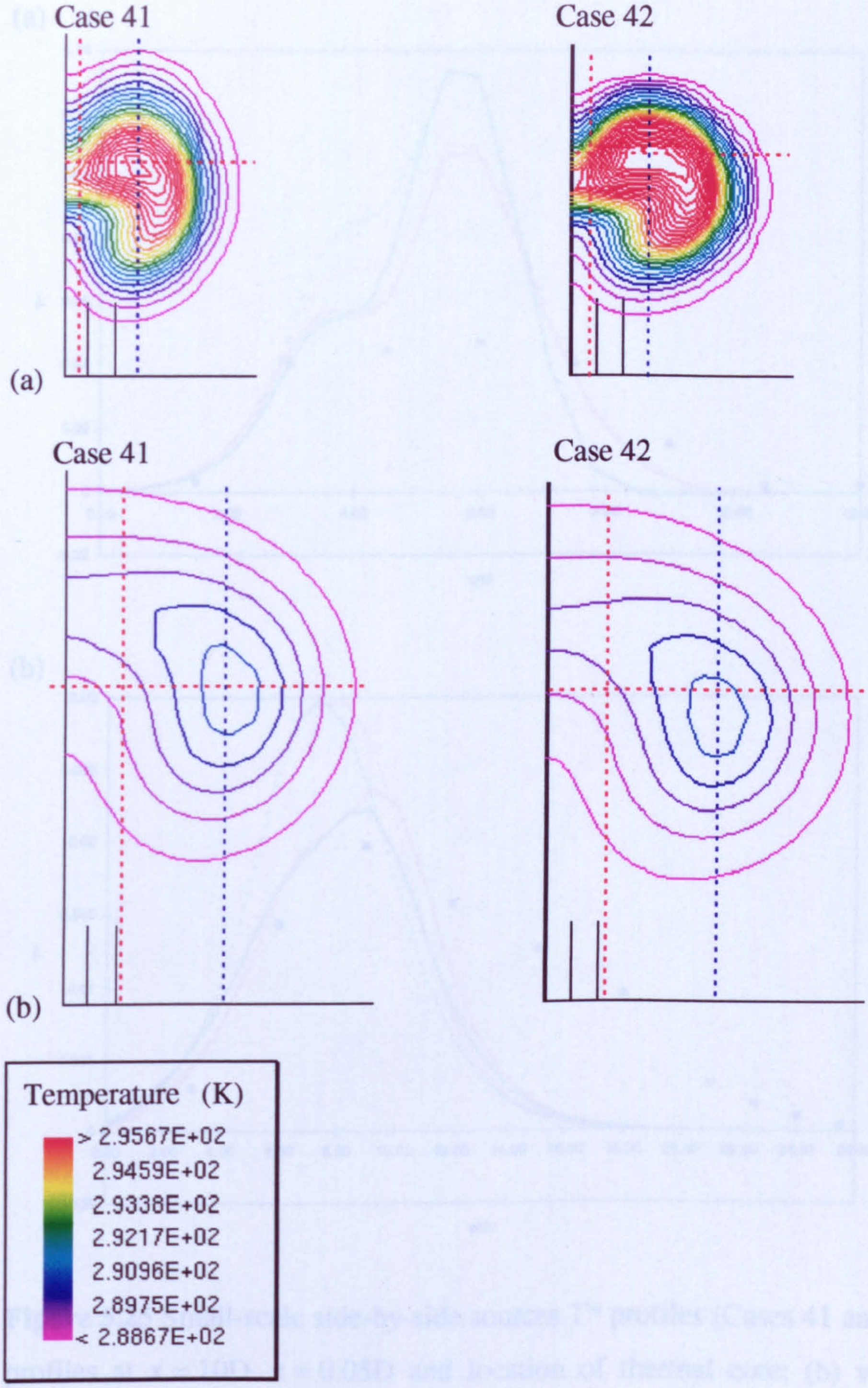

Figure 5.24 Small-scale side-by-side sources (Cases 41 and 42); temperature contours where (a) refers to x = 10D and (b) to x = 40D. Red dotted lines refer to the location of experimental profiles, blue lines bisect the thermal core. (Original in colour.)

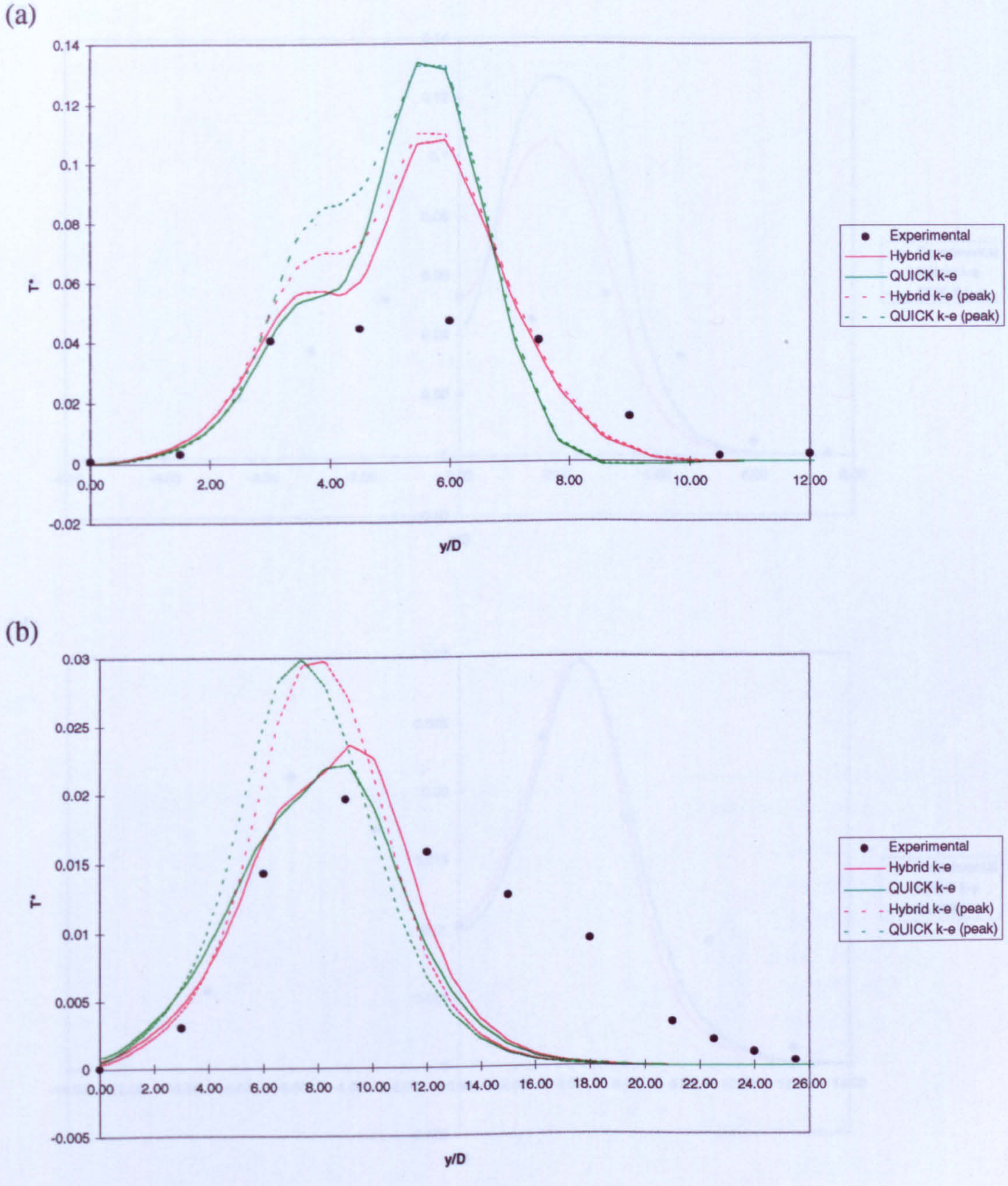

Figure 5.25 Small-scale side-by-side sources *T** profiles (Cases 41 and 42). (a) Vertical profiles at x = 10D, z = 0.05D and location of thermal core; (b) vertical profiles at x = 40D, z = 1.69D and location of the thermal core; (c) horizontal profiles at x = 10D and y = 6D; (d) horizontal profiles at x = 40D and y = 9.09D. (Original in colour.)

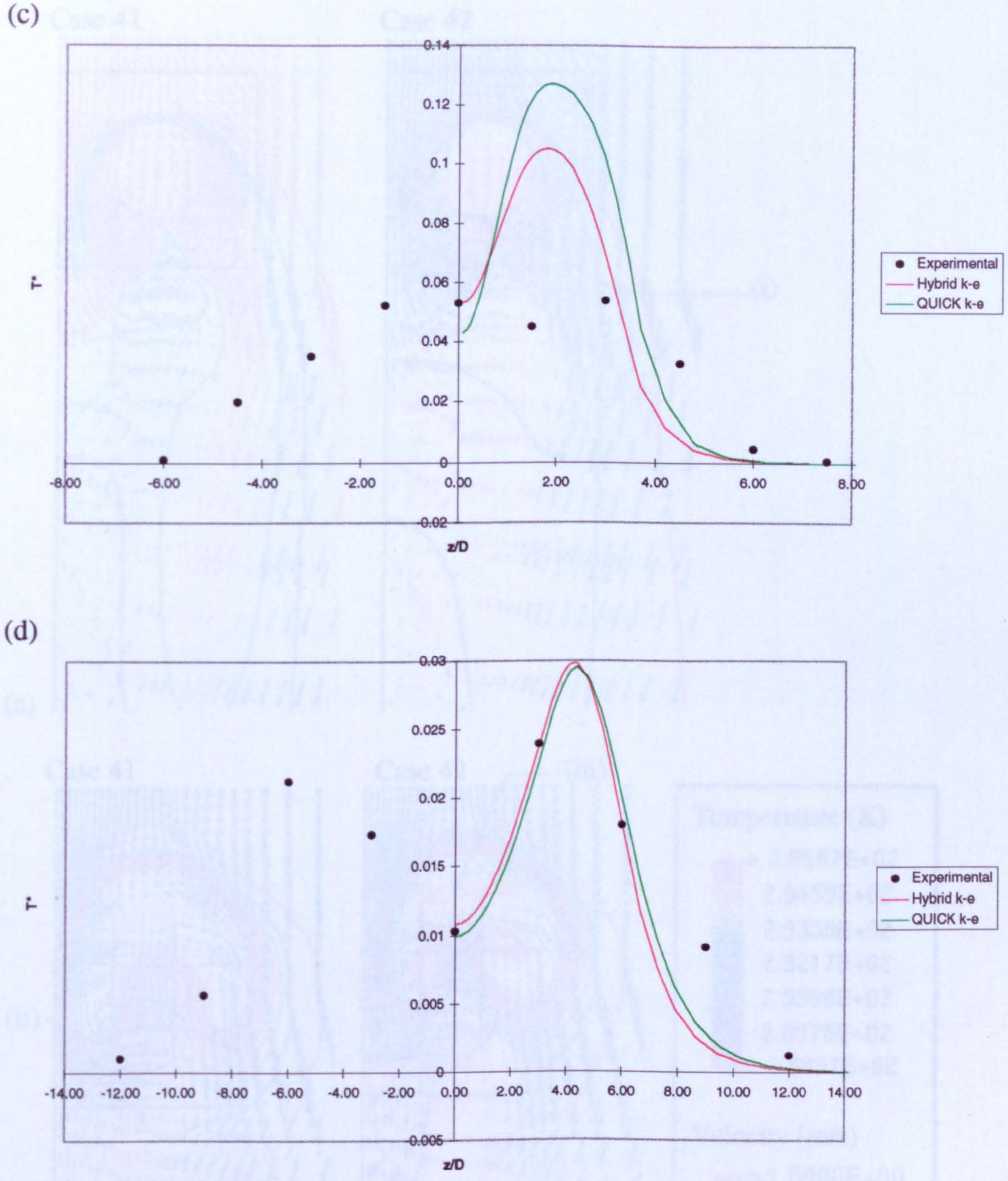

Figure 5.25 *Continued.*

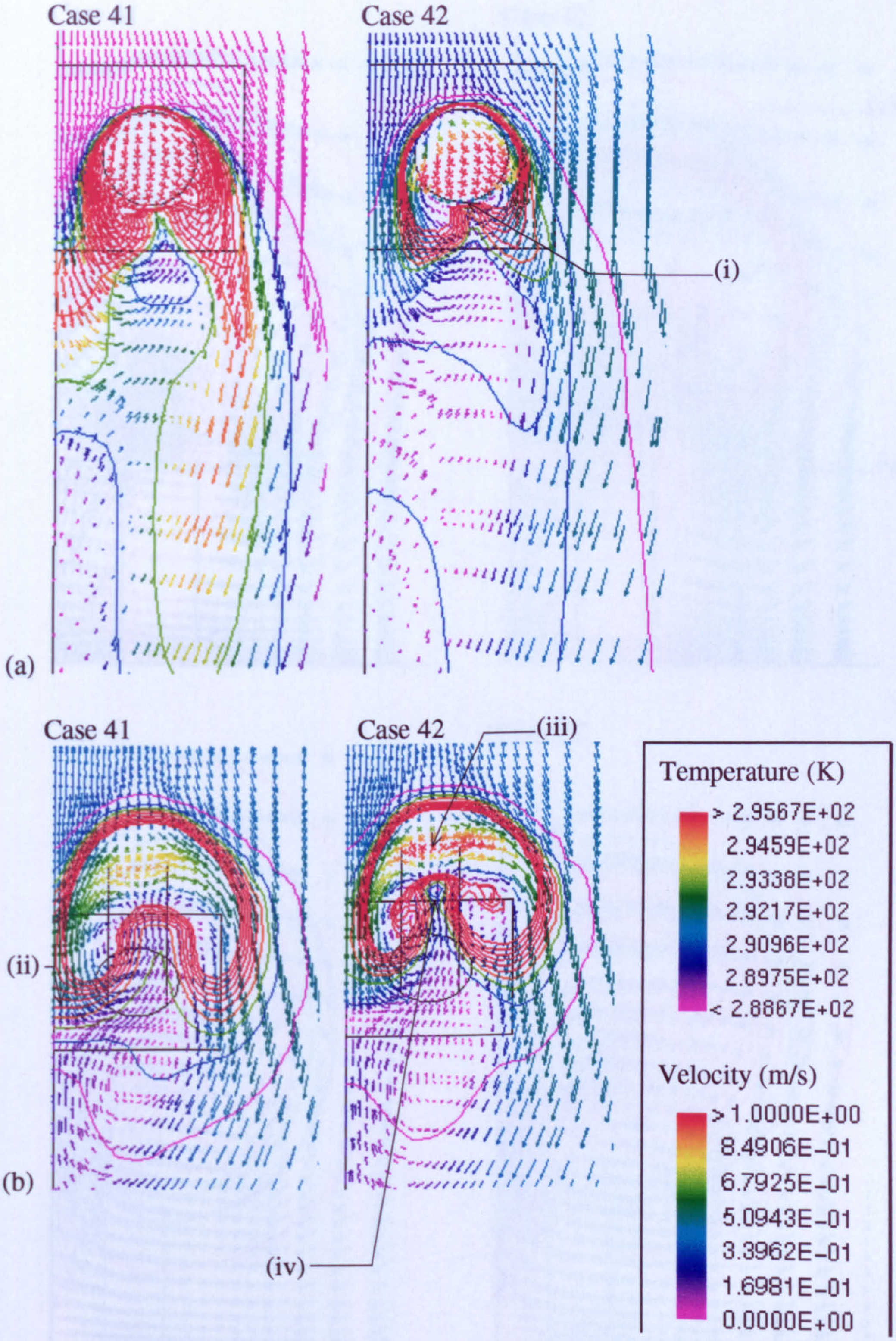

Figure 5.26 Small-scale side-by-side sources (Cases 41 and 42), velocity vector and temperature contours; (a–d) refer to cross-sections shown in Figure 5.19. (Original in colour.)

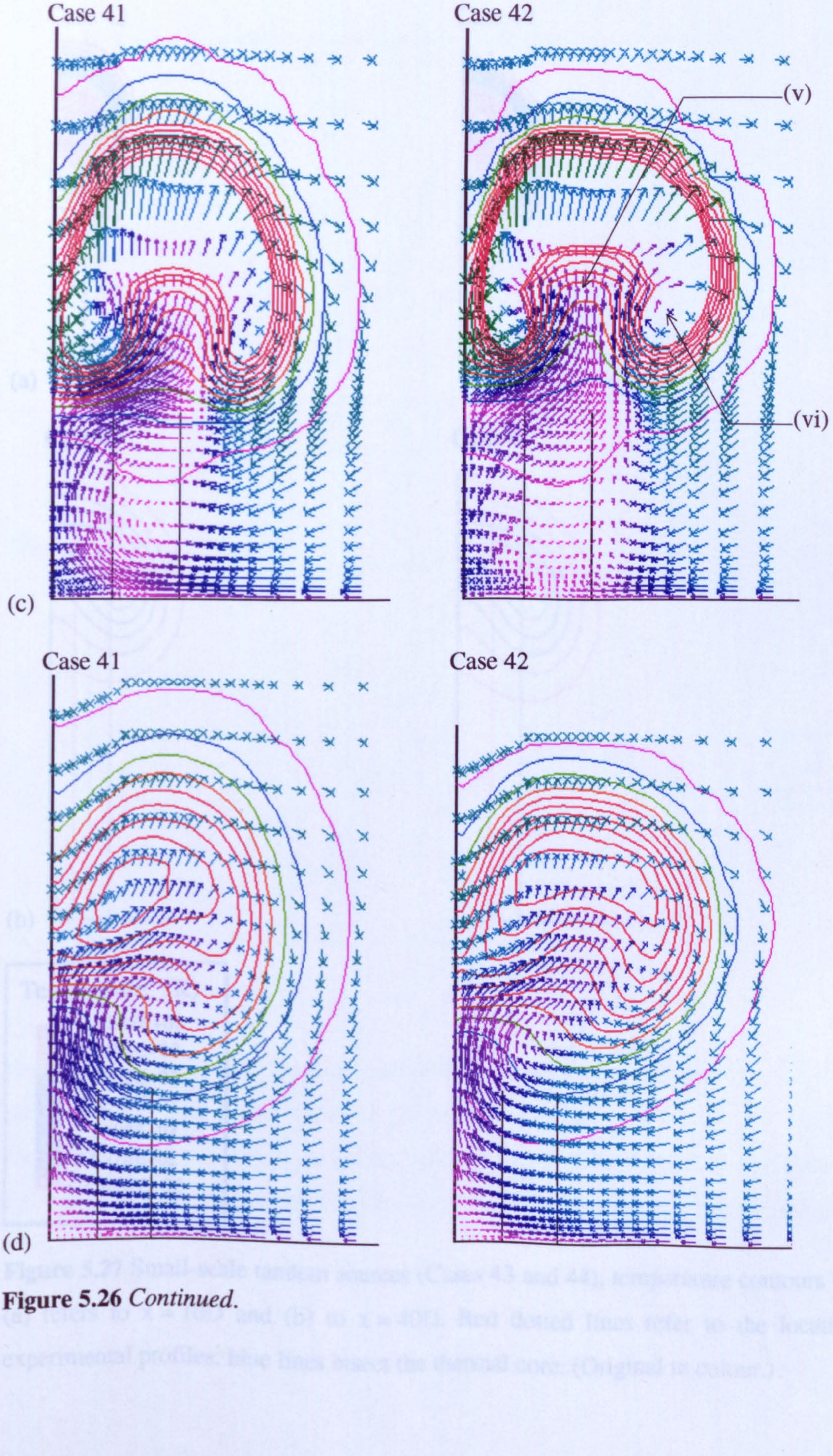

Figure 5.26 *Continued.*

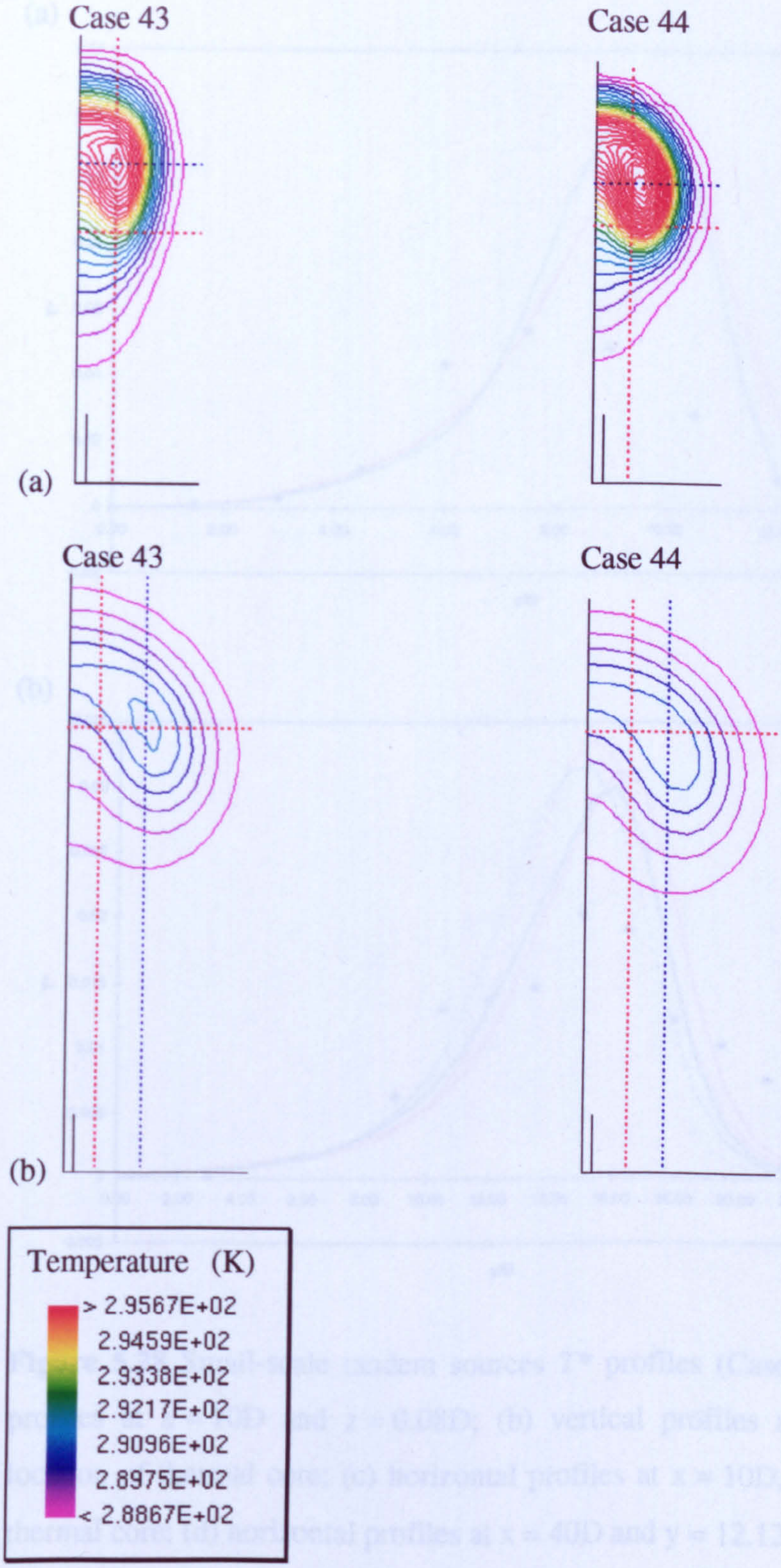

Figure 5.27 Small-scale tandem sources (Cases 43 and 44), temperature contours where (a) refers to x = 10D and (b) to x = 40D. Red dotted lines refer to the location of experimental profiles, blue lines bisect the thermal core. (Original in colour.)

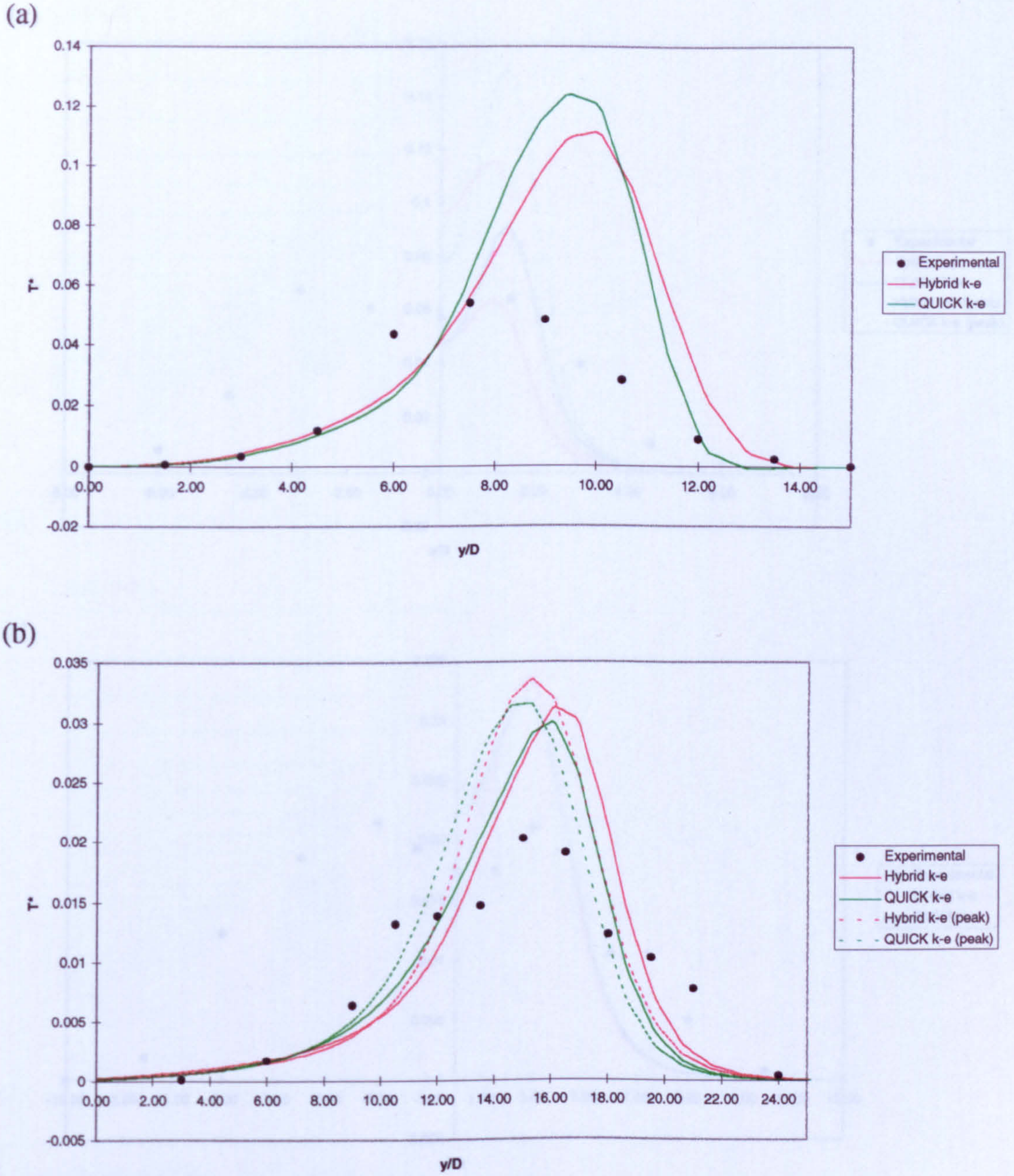

Figure 5.28 Small-scale tandem sources T^* profiles (Cases 43 and 44). (a) Vertical profiles at x = 10D and z = 0.08D; (b) vertical profiles at x = 40D, z = 1.69D and location of thermal core; (c) horizontal profiles at x = 10D, y = 7.75D and location of thermal core; (d) horizontal profiles at x = 40D and y = 12.12D. (Original in colour.)

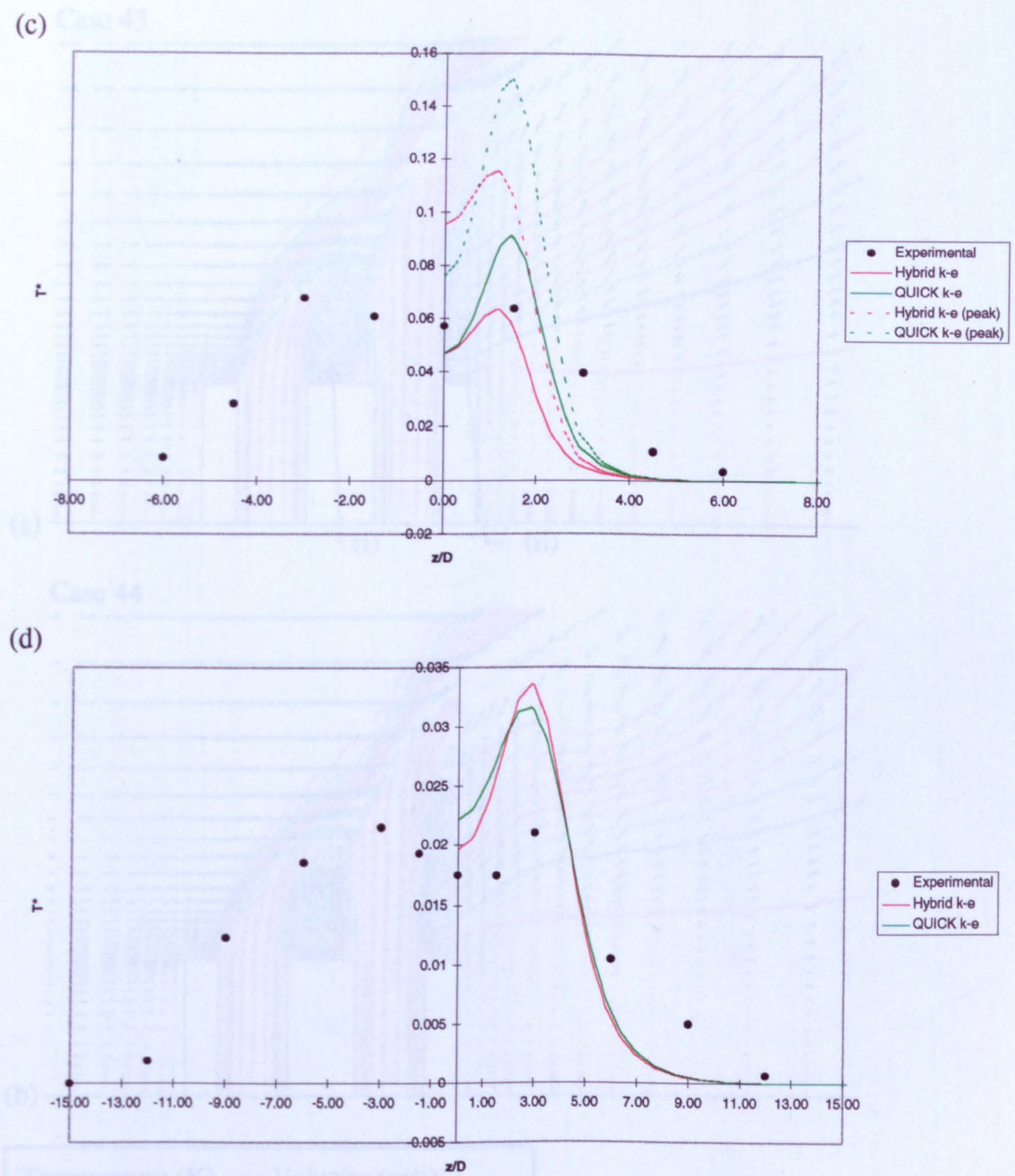

Figure 5.28 *Continued.*

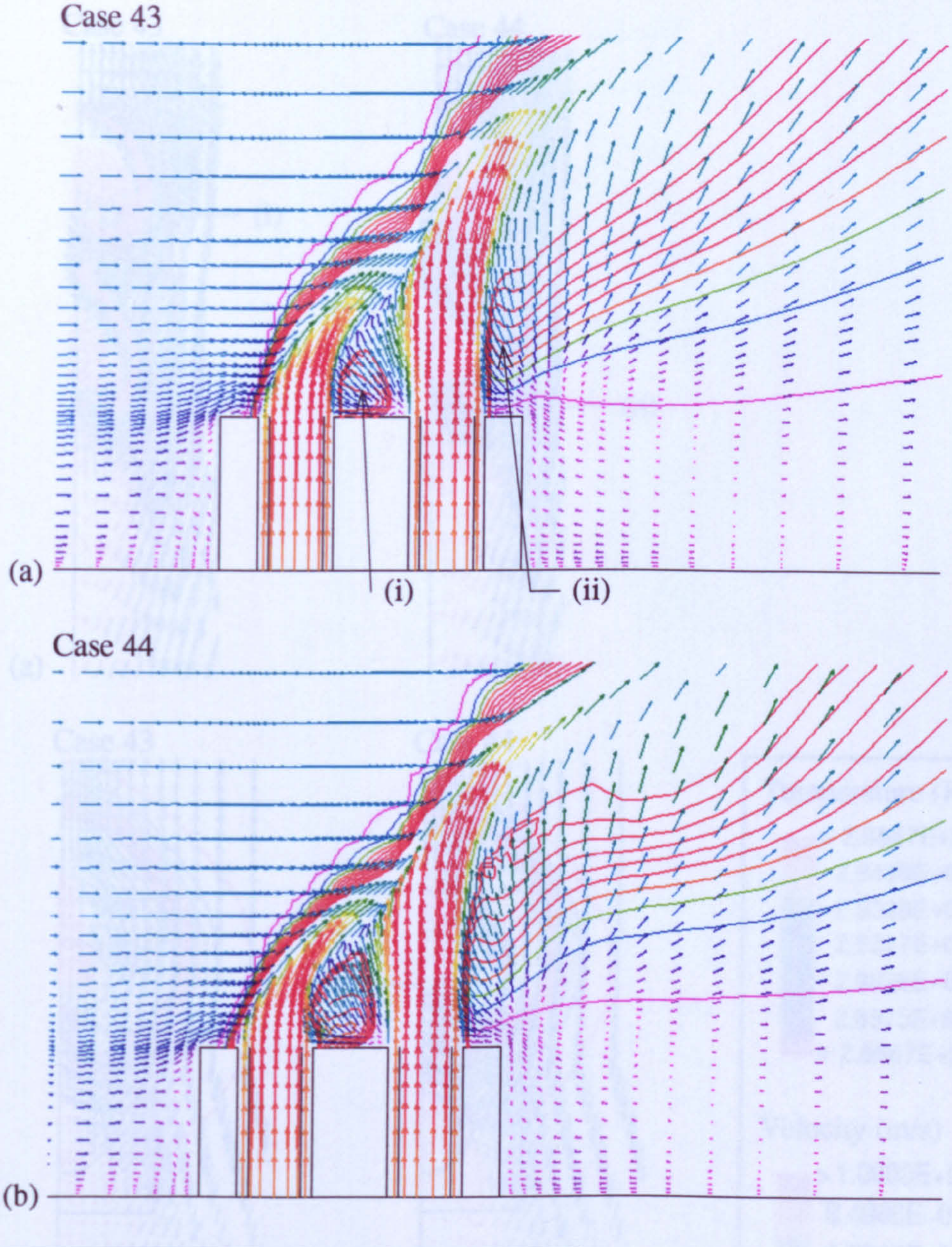

Figure 5.29 Small-scale tandem sources (Cases 43 and 44), velocity vector and temperature contours on the physical symmetry plane. (Original in colour.)

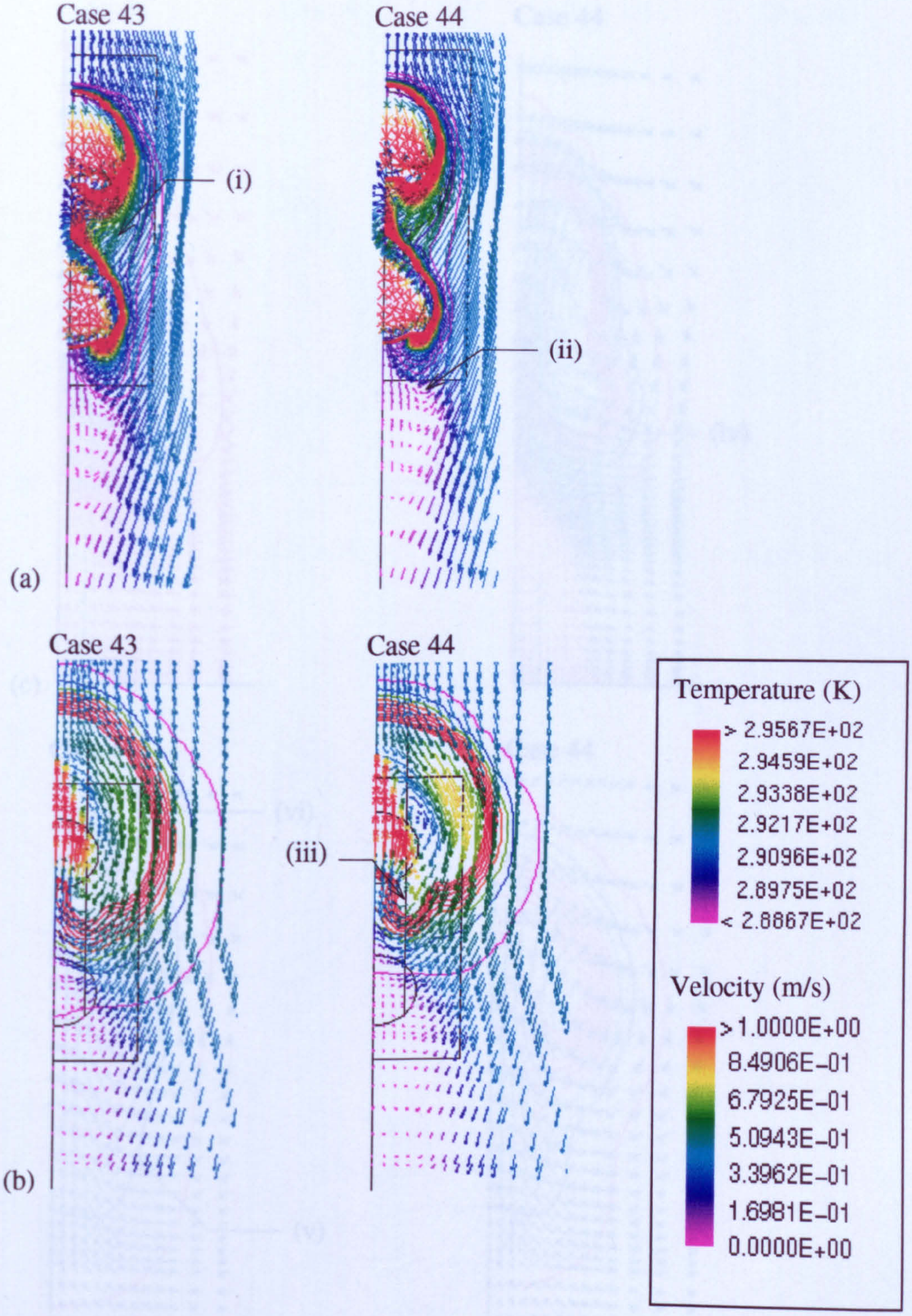

Figure 5.30 Small-scale tandem sources (Cases 43 and 44), velocity vector and temperature contours; (a–d) refer to cross-sections shown in Figure 5.19. (Original in colour.)

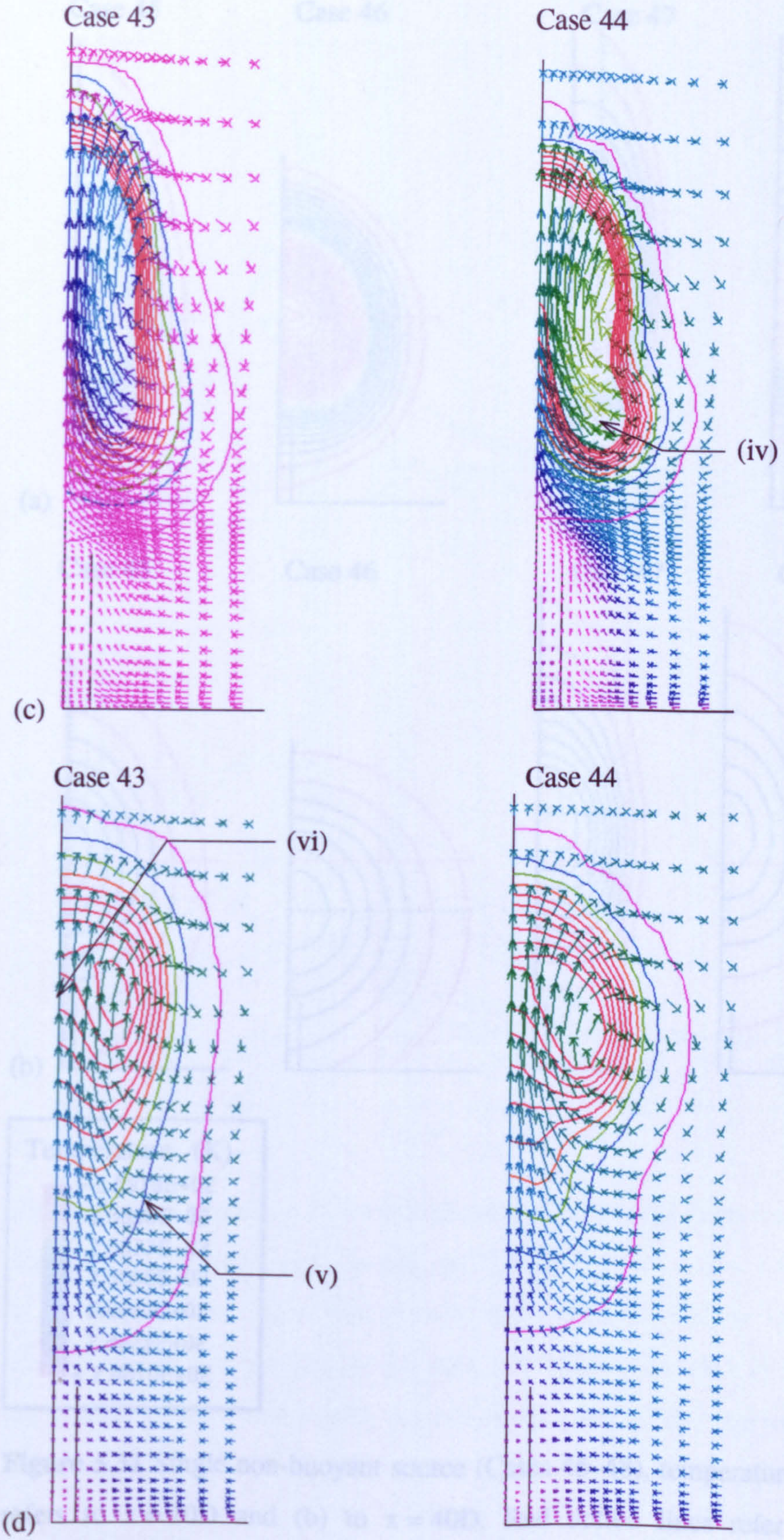

Figure 5.30 *Continued.*

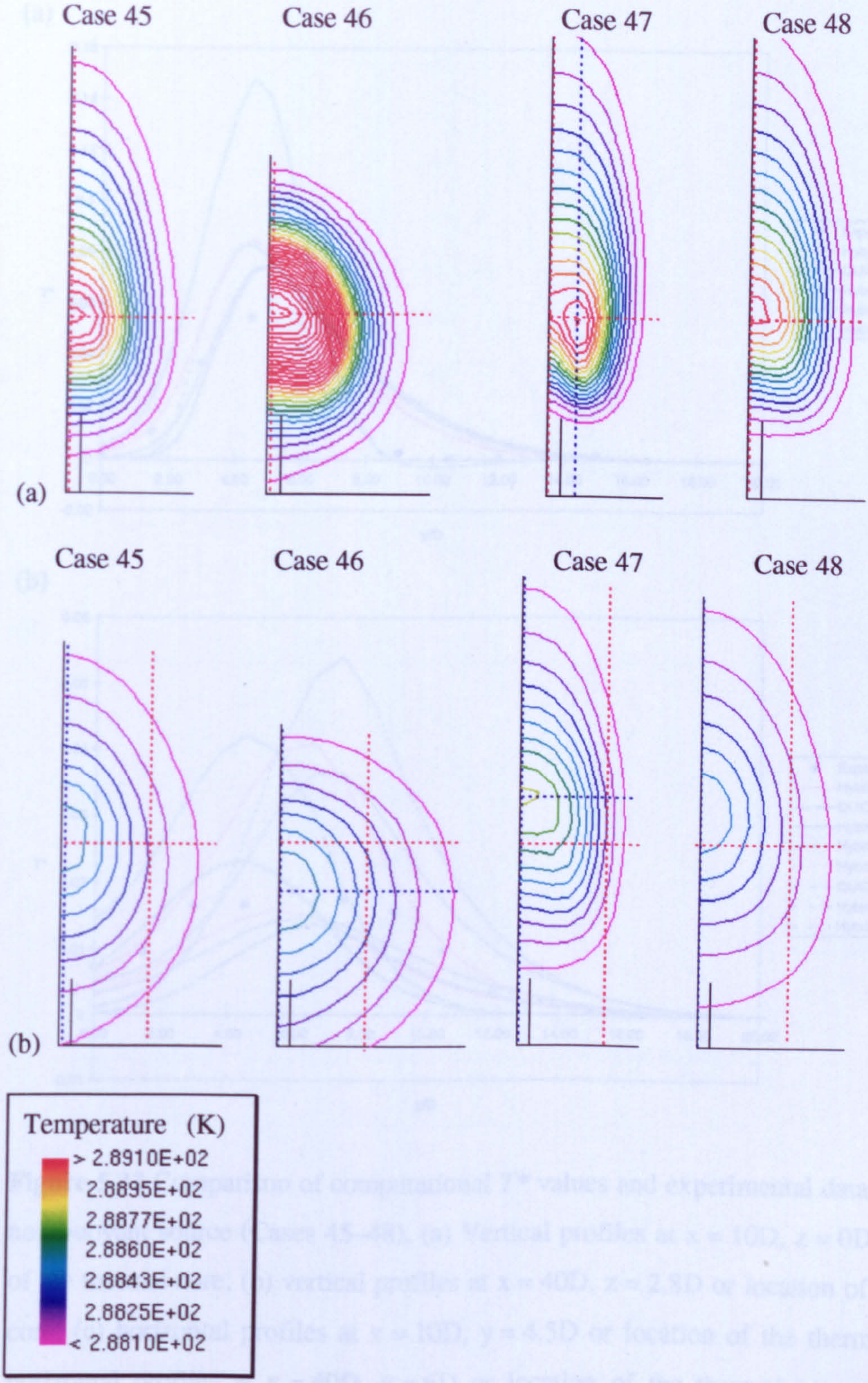

Figure 5.31 Single non-buoyant source (Cases 45–48), temperature contours where (a) refers to x = 10D and (b) to x = 40D. Red dotted lines refer to the location of experimental profiles, blue lines bisect the thermal core. (Original in colour.)

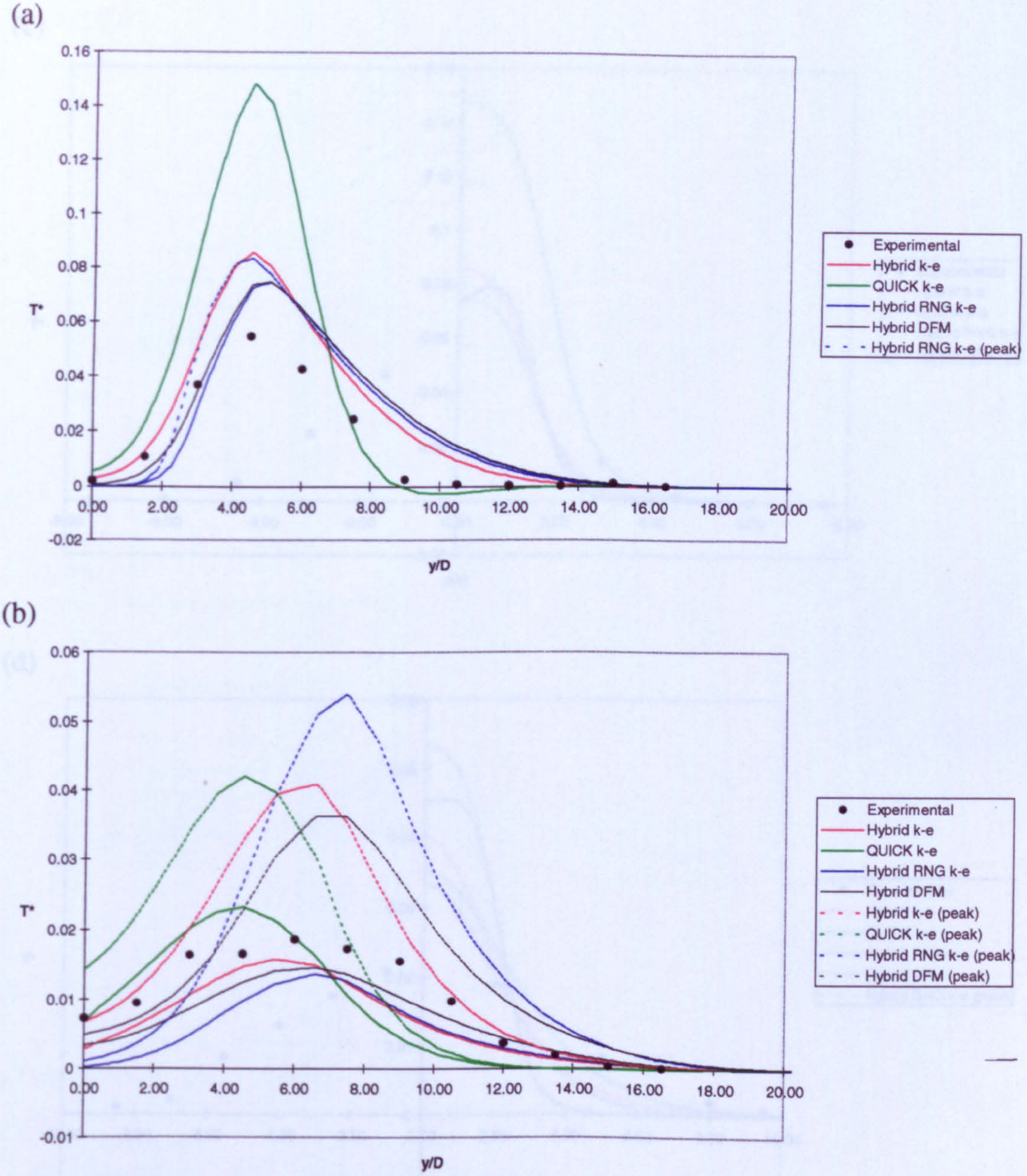

Figure 5.32 Comparison of computational *T** values and experimental data for a single non-buoyant source (Cases 45–48). (a) Vertical profiles at x = 10D, z = 0D or location of the thermal core; (b) vertical profiles at x = 40D, z = 2.8D or location of the thermal core; (c) horizontal profiles at x = 10D, y = 4.5D or location of the thermal core; (d) horizontal profiles at x = 40D, y = 6D or location of the thermal core. (Original in colour.)

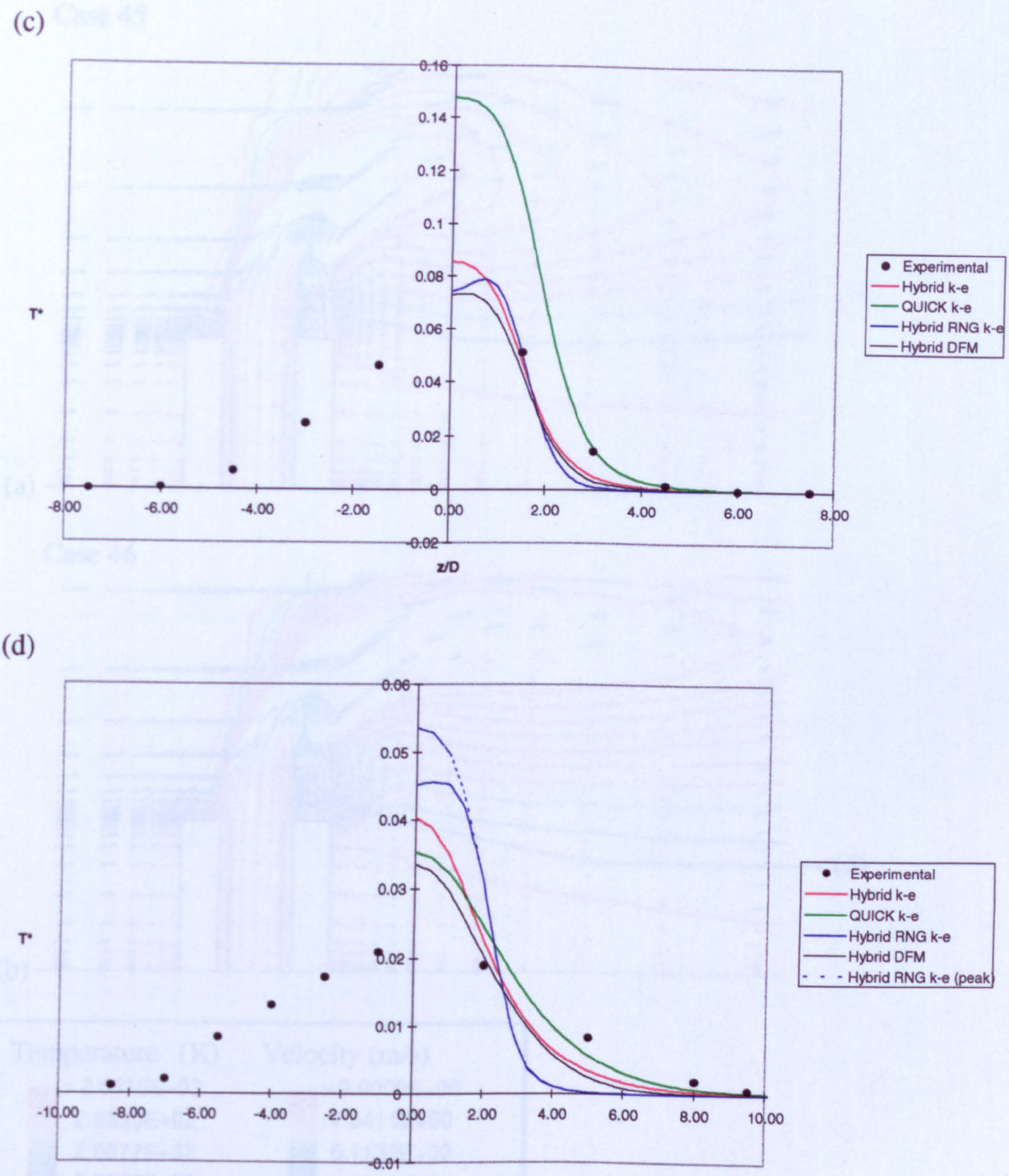

Figure 5.32 *Continued.*

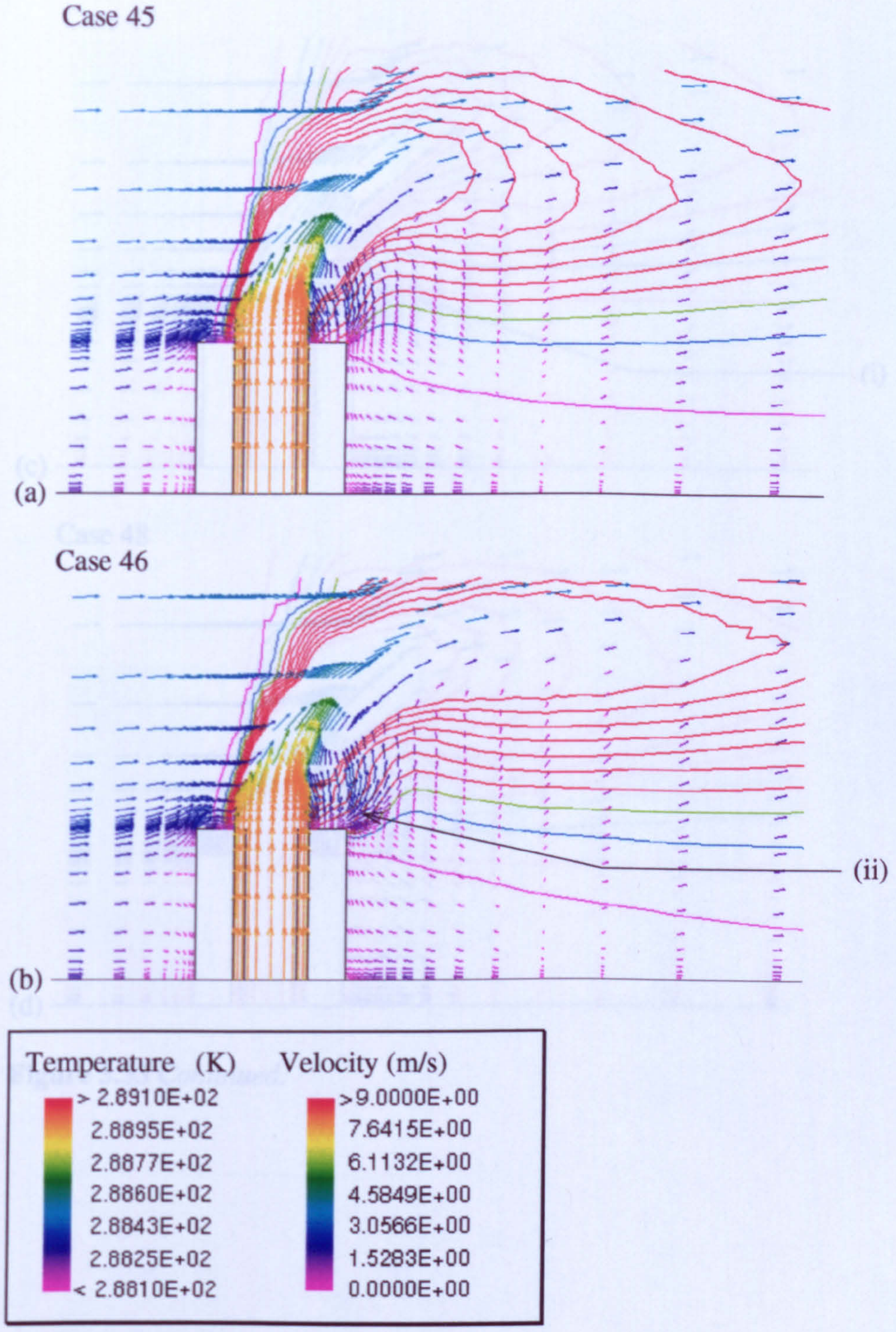

Figure 5.33 Single non-buoyant source (Cases 45–48), velocity vector and temperature contours on the physical symmetry plane. (Original in colour).

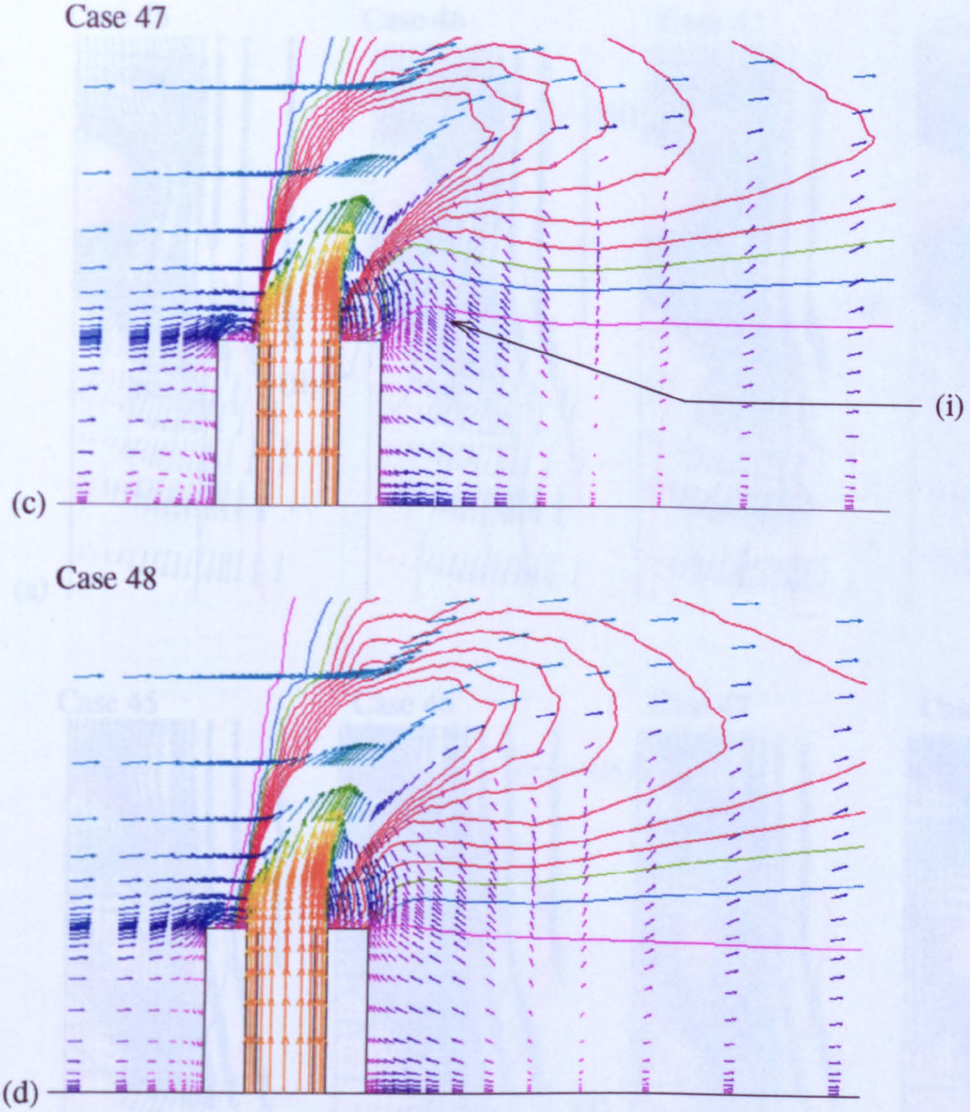

Figure 5.33 *Continued.*

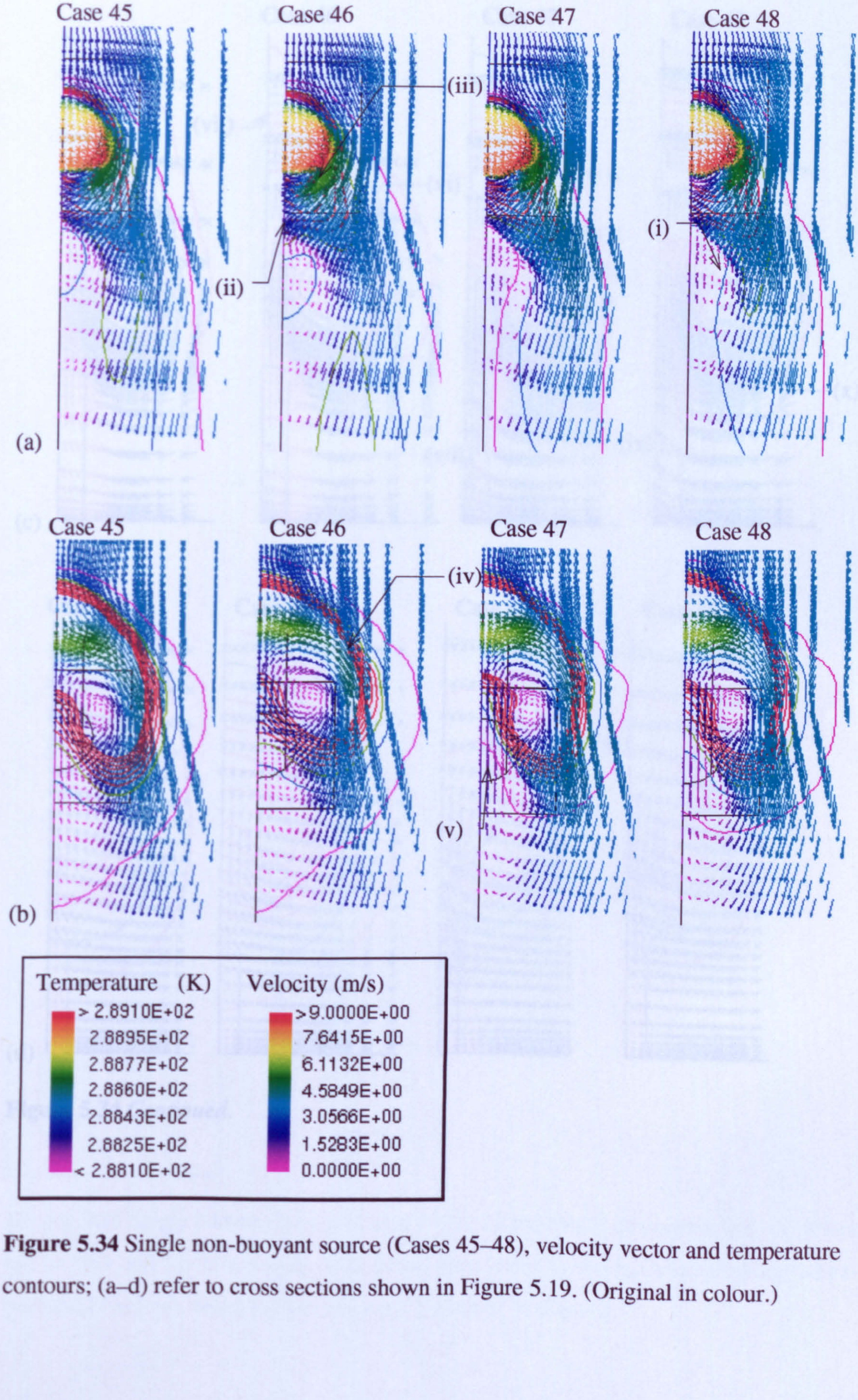

Figure 5.34 Single non-buoyant source (Cases 45–48), velocity vector and temperature contours; (a–d) refer to cross sections shown in Figure 5.19. (Original in colour.)

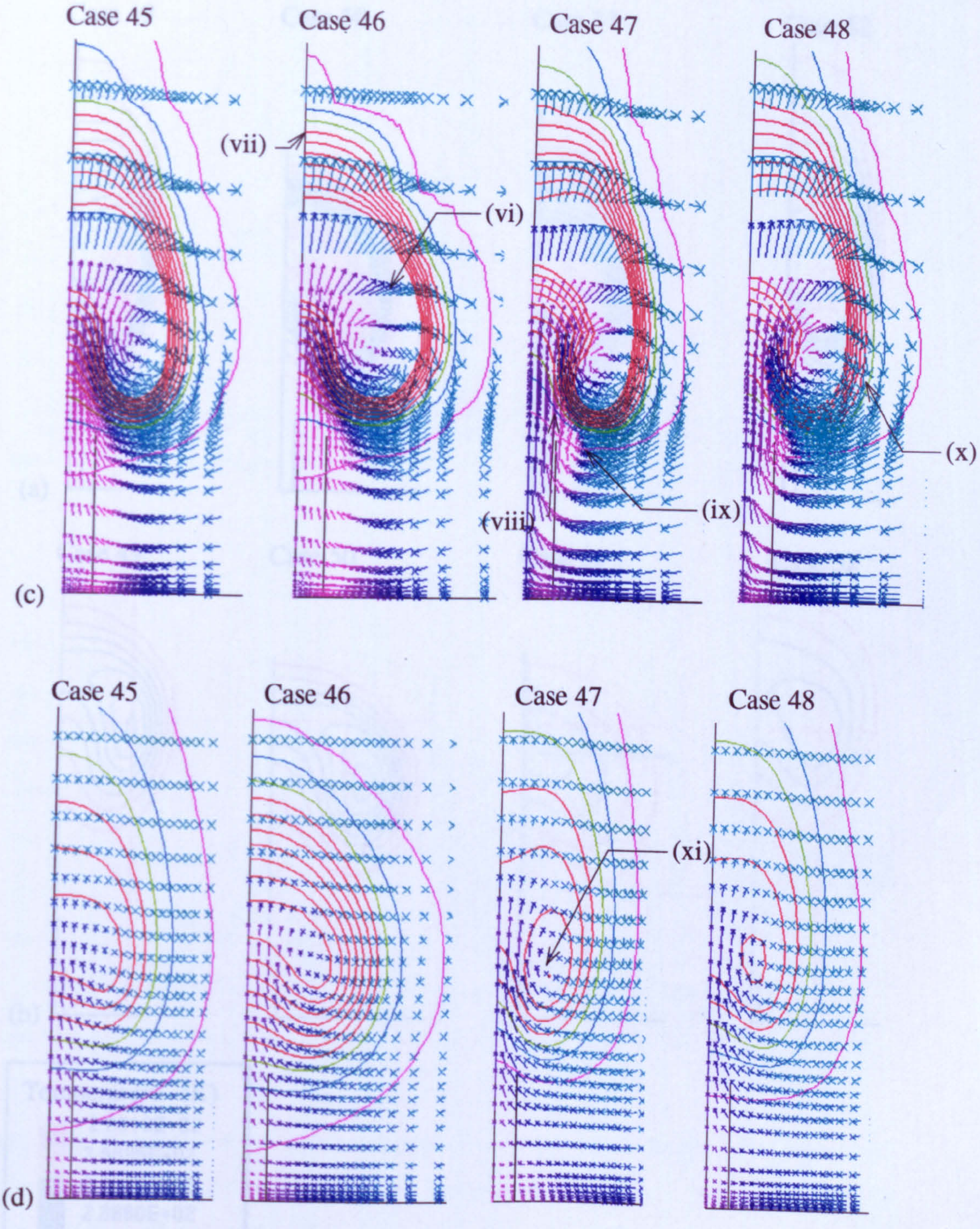

Figure 5.34 *Continued.*

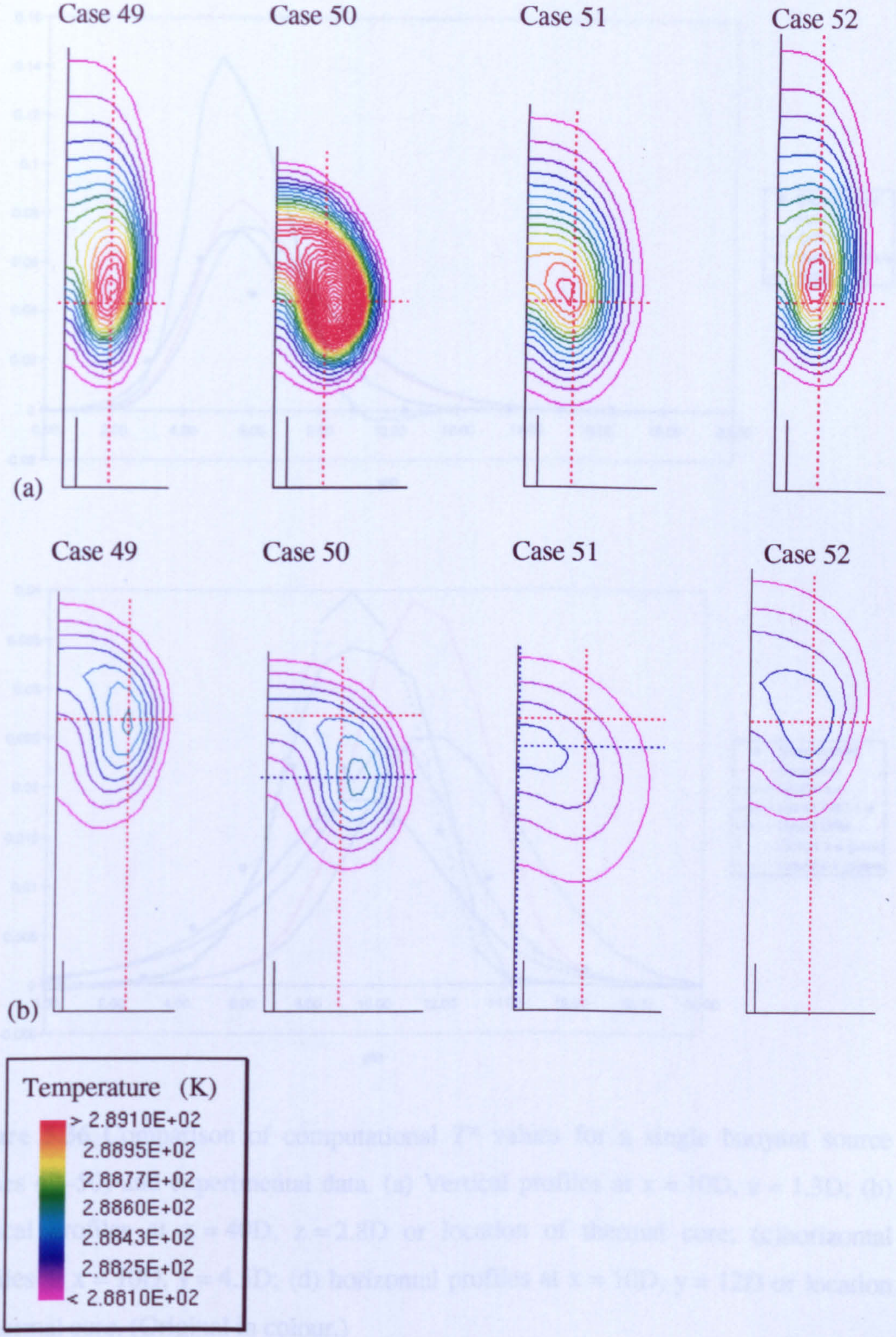

Figure 5.35 Single buoyant source (Cases 49–52), temperature contours where (a) refers to x = 10D and (b) to x = 40D. Red dotted lines refer to the location of experimental profiles, blue lines bisect the thermal core. (Original in colour.)

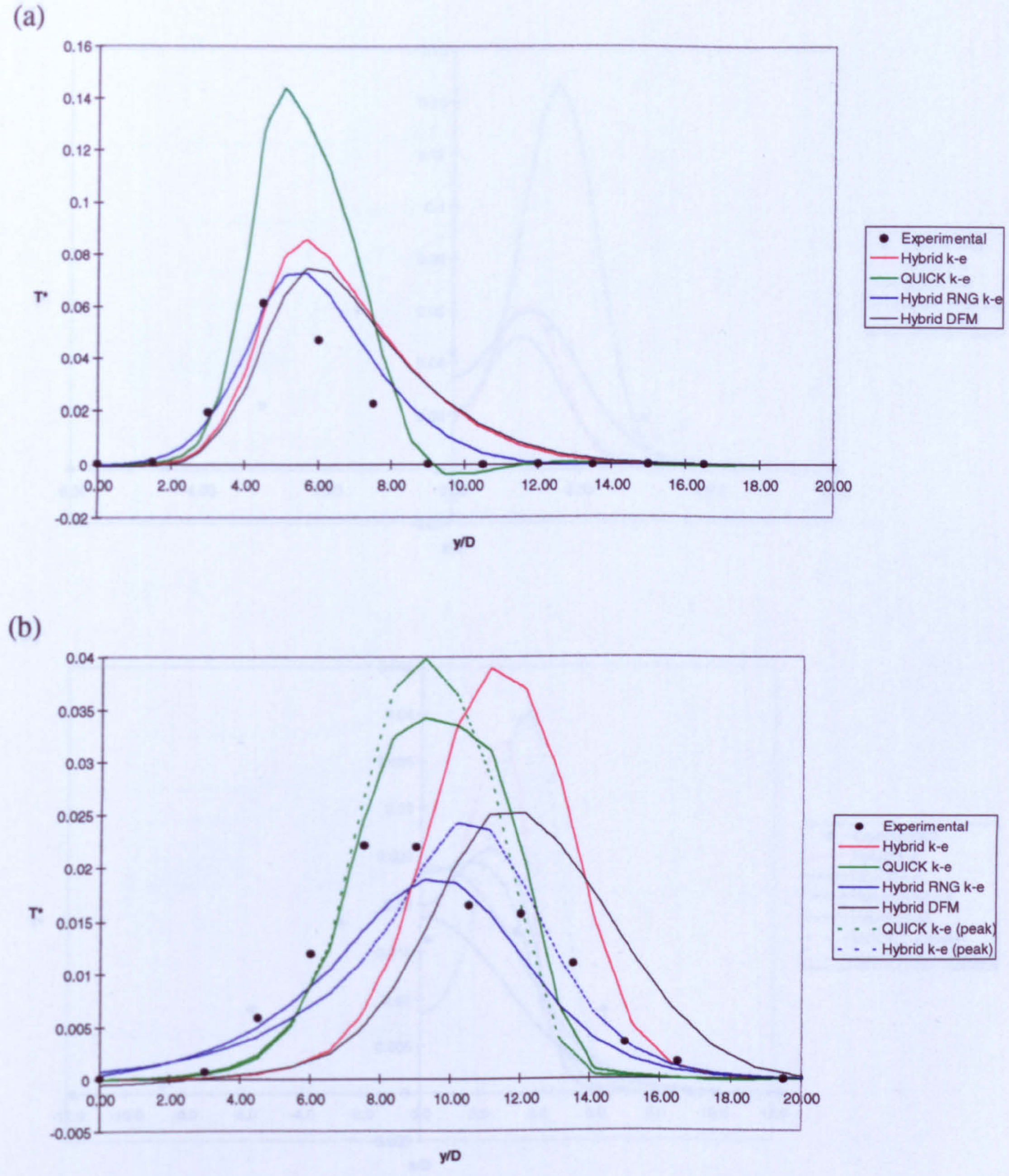

Figure 5.36 Comparison of computational *T** values for a single buoyant source (Cases 47–50) and experimental data. (a) Vertical profiles at x = 10D, z = 1.3D; (b) vertical profiles at x = 40D, z = 2.8D or location of thermal core; (c)horizontal profiles at x = 10D, y = 4.5D; (d) horizontal profiles at x = 10D, y = 12D or location of thermal core. (Original in colour.)

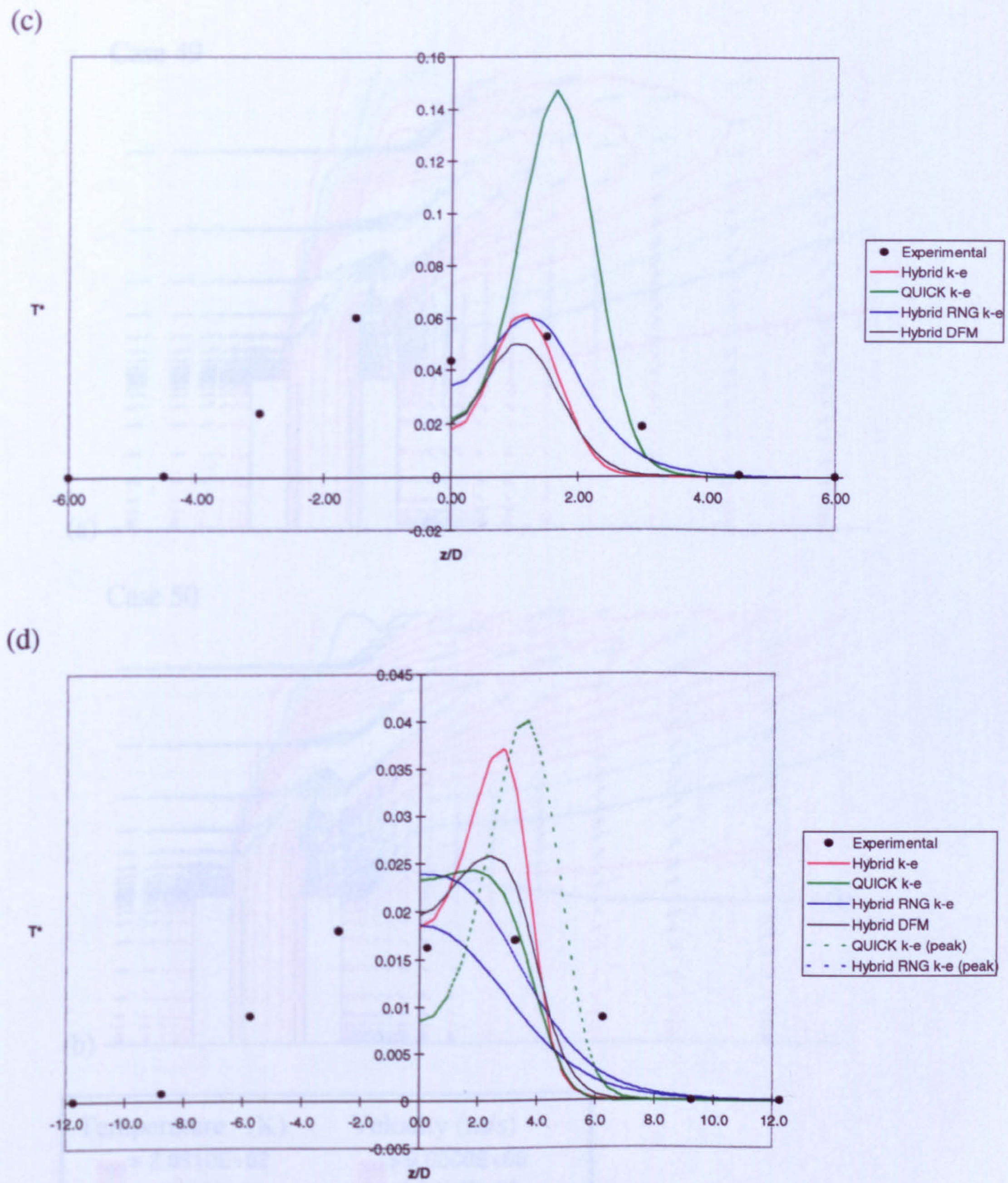

Figure 5.36 *Continued.*

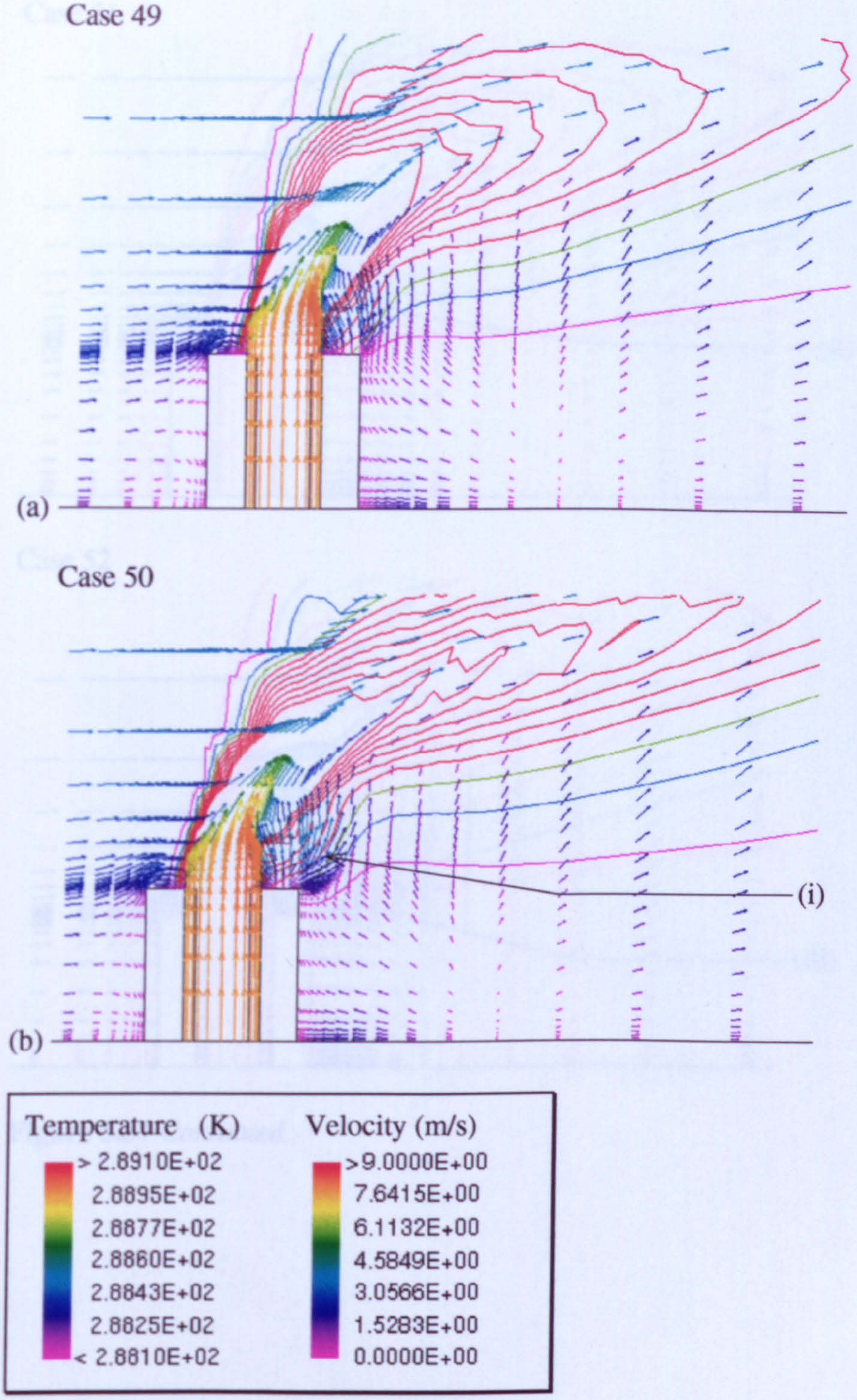

Figure 5.37 Single buoyant source (Cases 49–52), velocity vector and temperature contours on the physical symmetry plane. (Original in colour).

Case 51

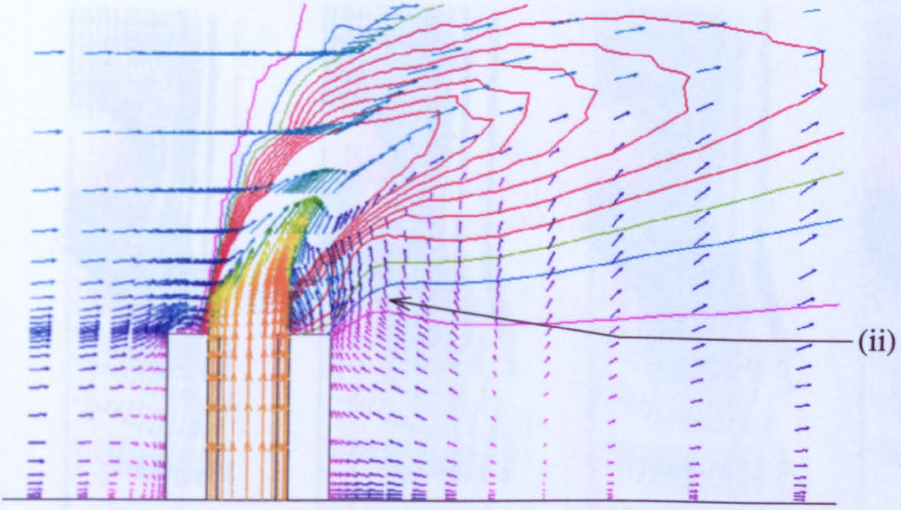

Case 52

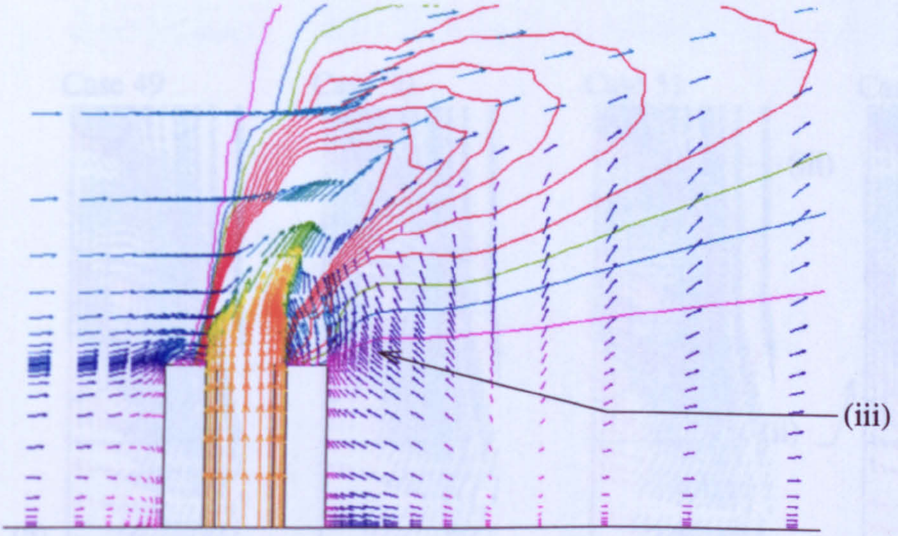

Figure 5.37 *Continued.*

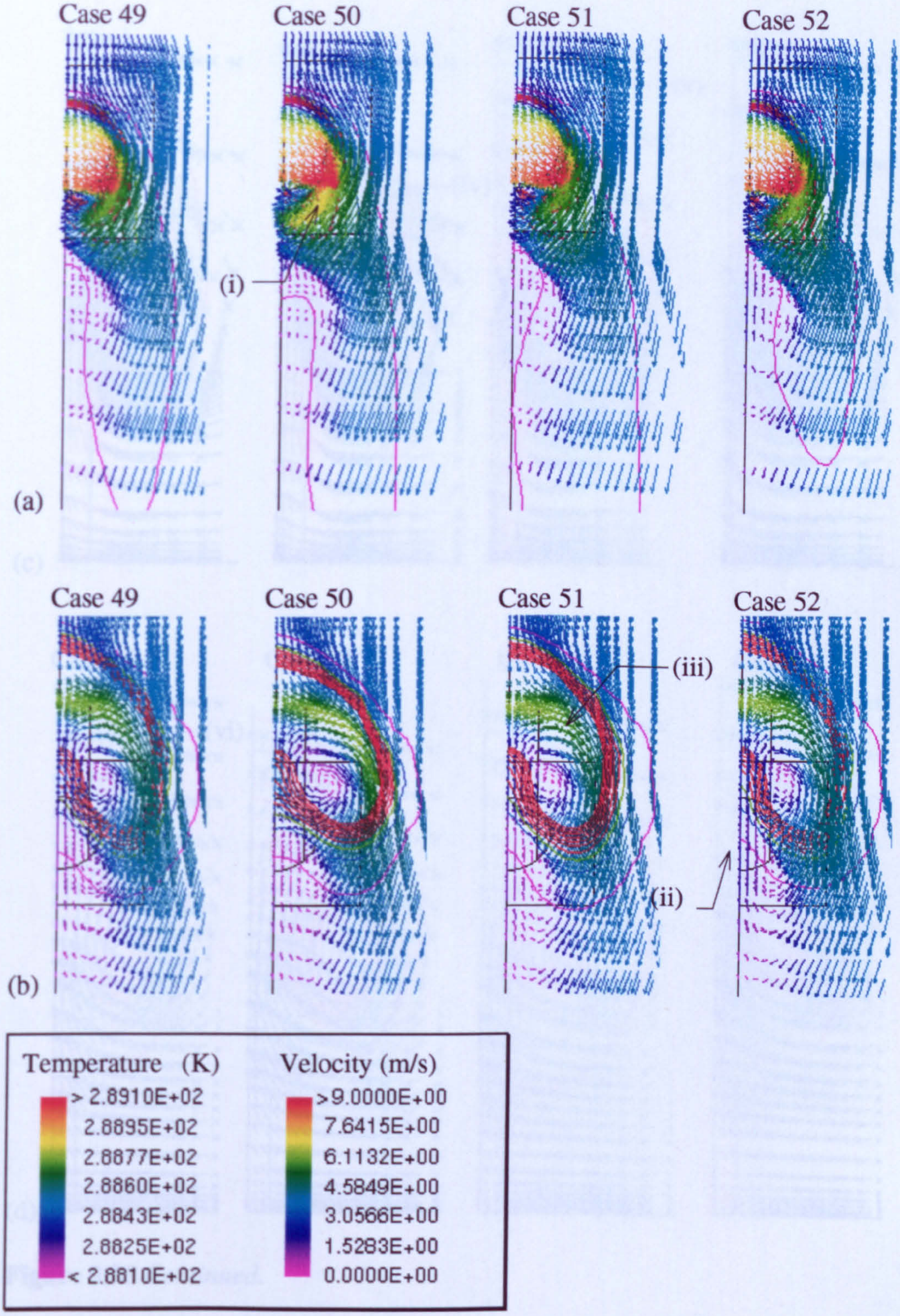

Figure 5.38 Single buoyant source (Cases 49–52), velocity vector and temperature contours; (a–d) refer to cross sections shown in Figure 5.19. (Original in colour.)

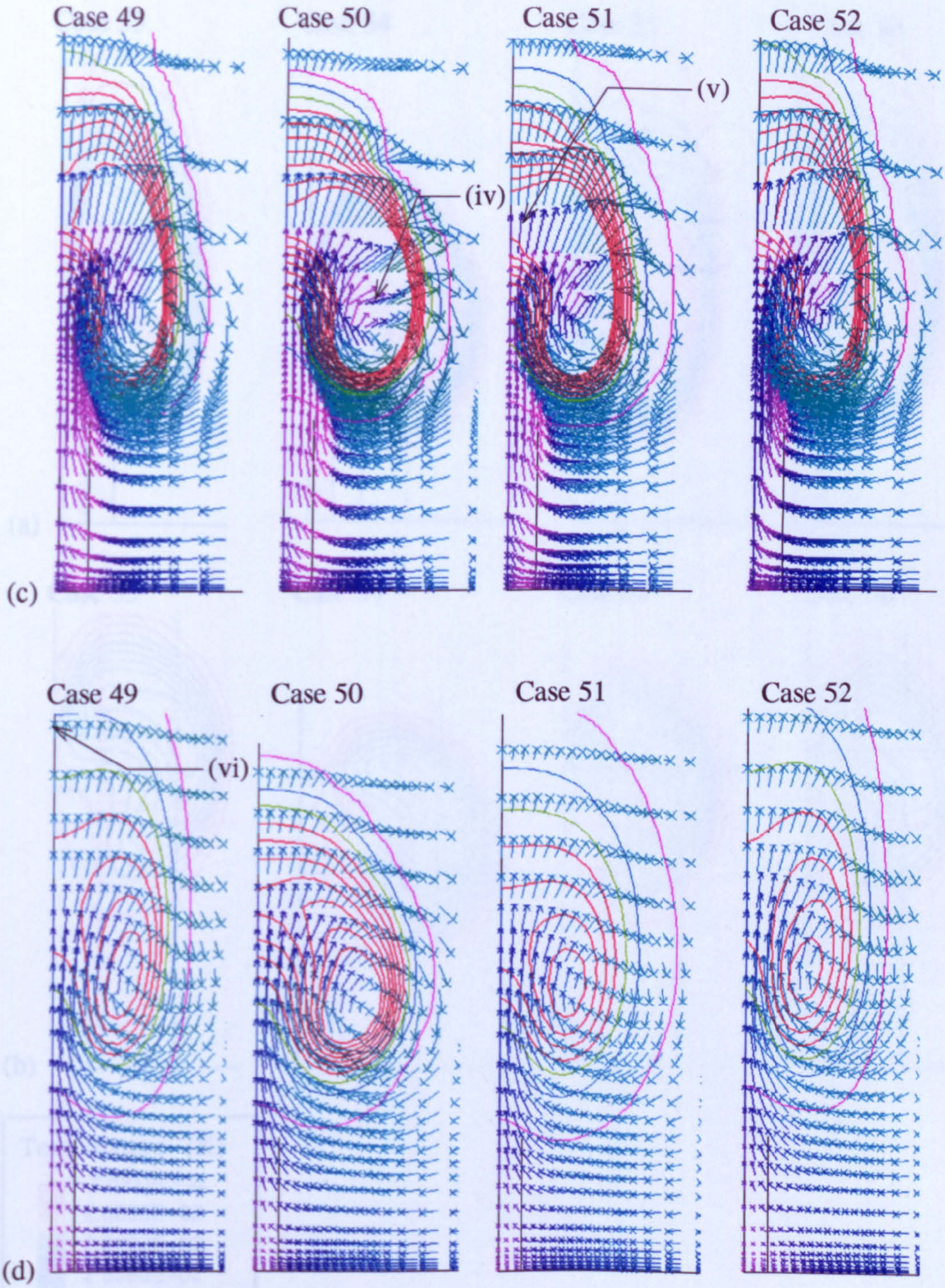

Figure 5.38 *Continued.*

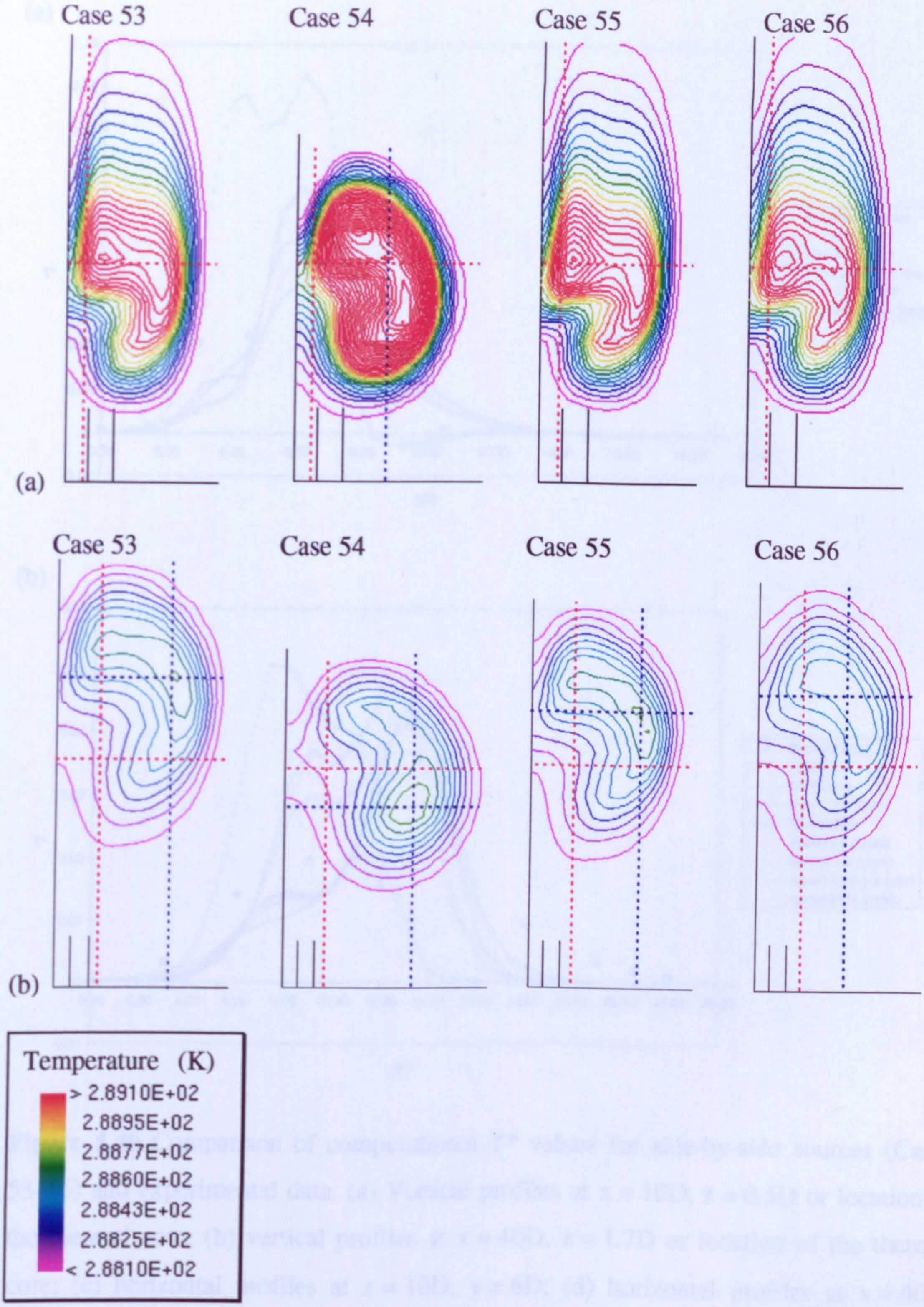

Figure 5.39 Side-by-side sources (Cases 53–56), temperature contours where (a) refers to x = 10D and (b) to x = 40D. Red dotted lines refer to the location of experimental profiles, blue lines bisect the thermal core. (Original in colour.)

(a)

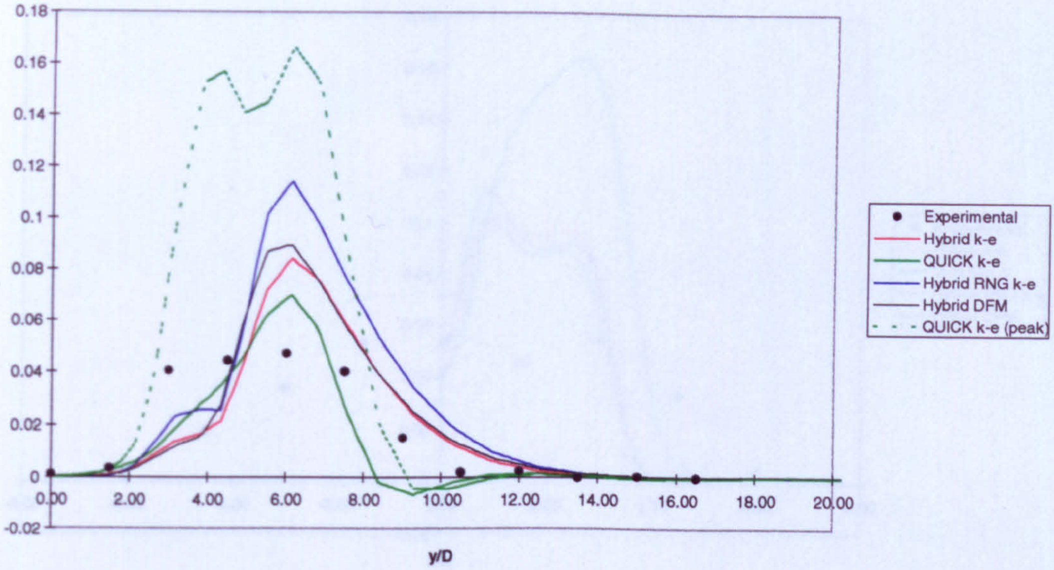

(b)

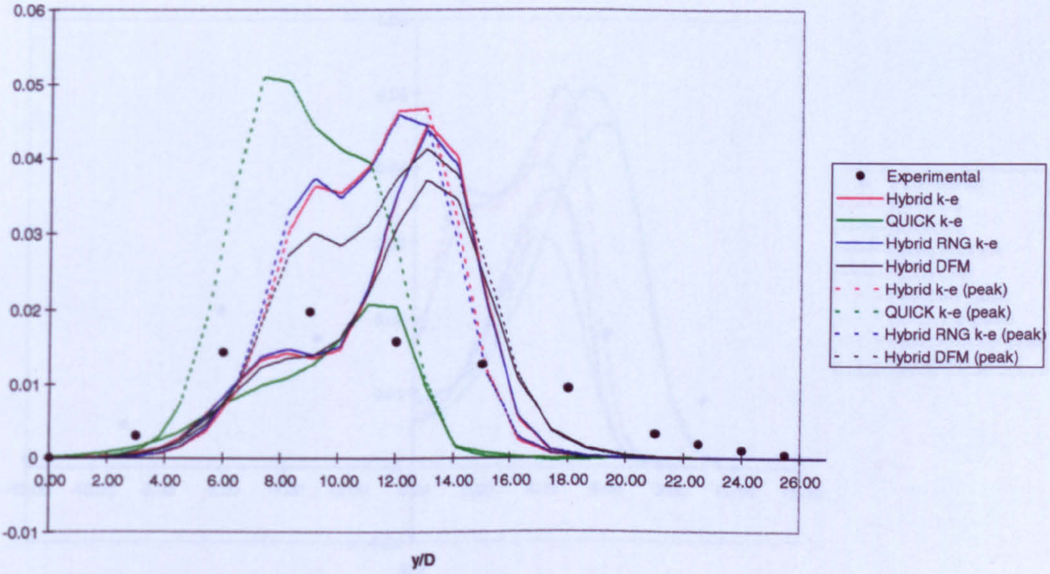

Figure 5.40 Comparison of computational T^* values for side-by-side sources (Cases 53–56) and experimental data. (a) Vertical profiles at x = 10D, z = 0.5D or location of the thermal core; (b) vertical profiles at x = 40D, z = 1.7D or location of the thermal core; (c) horizontal profiles at x = 10D, y = 6D; (d) horizontal profiles at x = 40D, y = 9D or location of the thermal core. (Original in colour.)

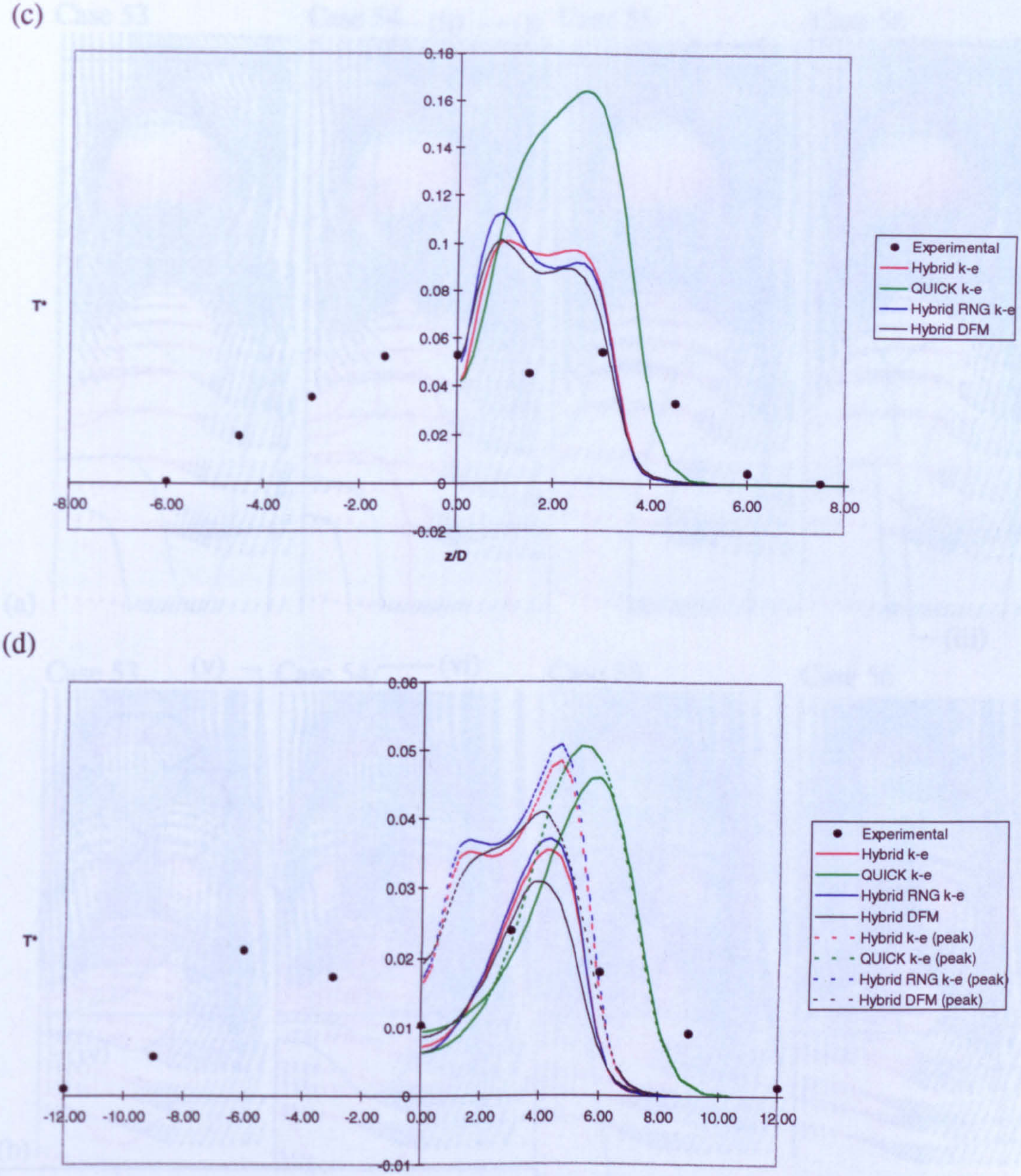

Figure 5.40 *Continued.*

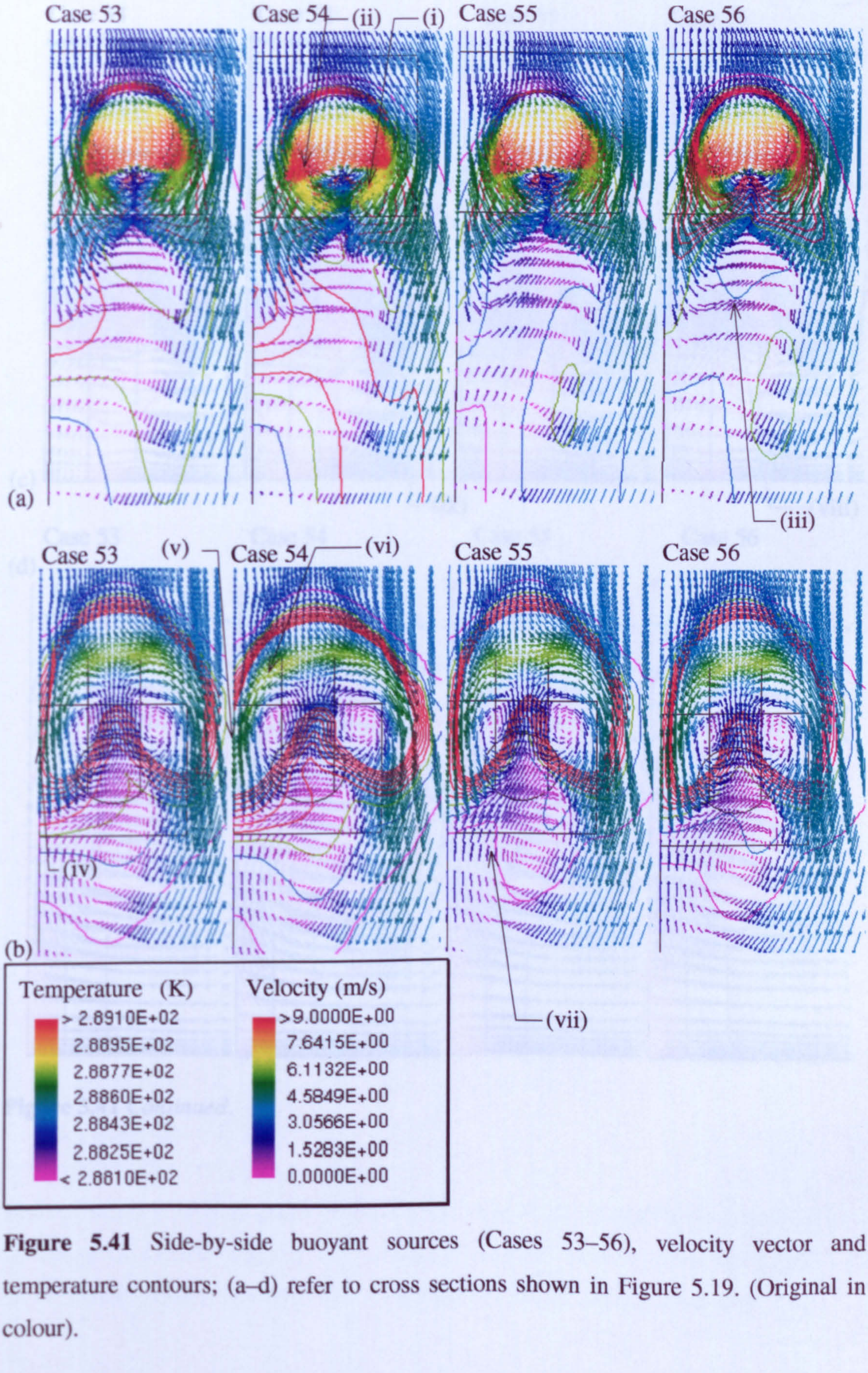

Figure 5.41 Side-by-side buoyant sources (Cases 53–56), velocity vector and temperature contours; (a–d) refer to cross sections shown in Figure 5.19. (Original in colour).

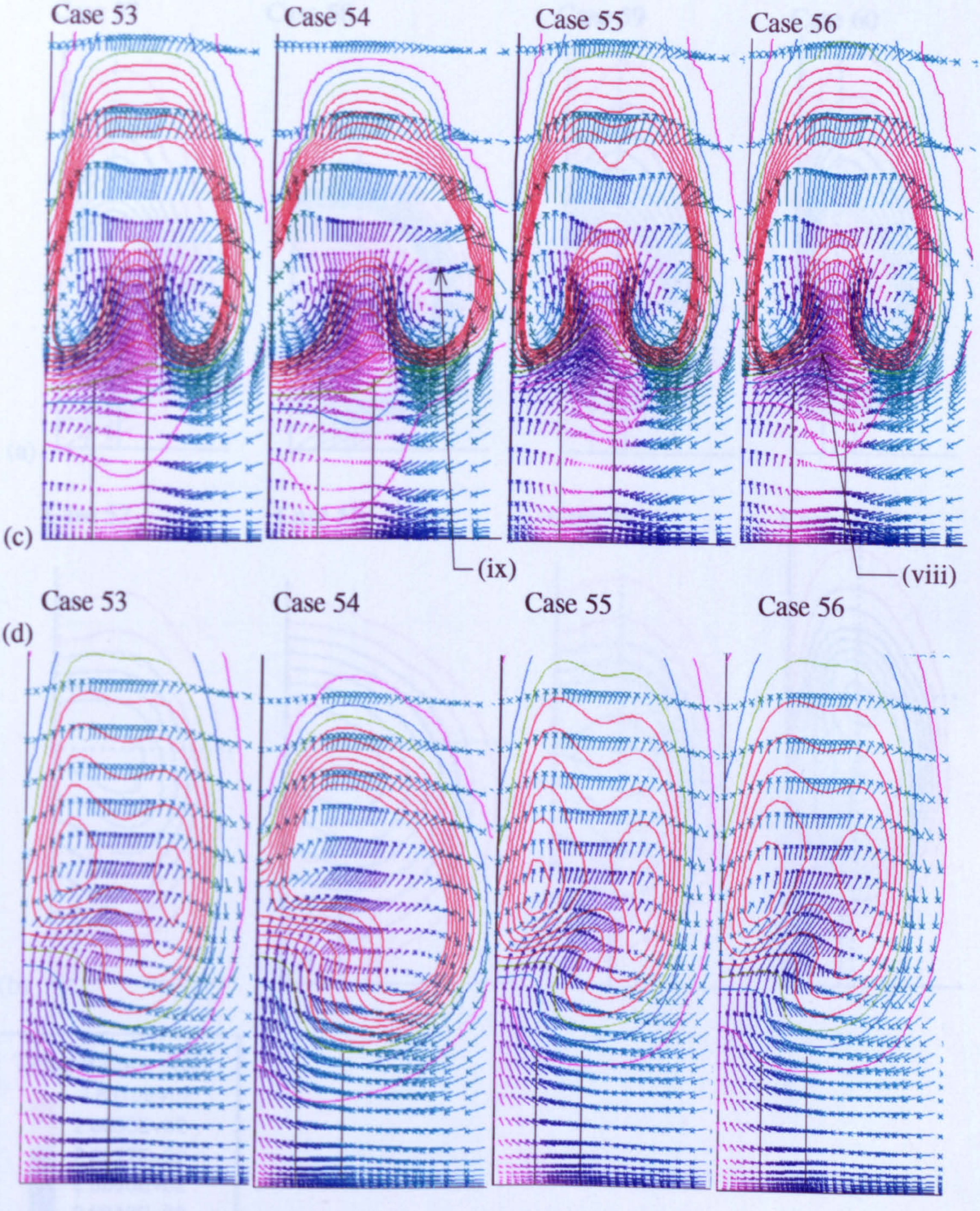

Figure 5.41 *Continued.*

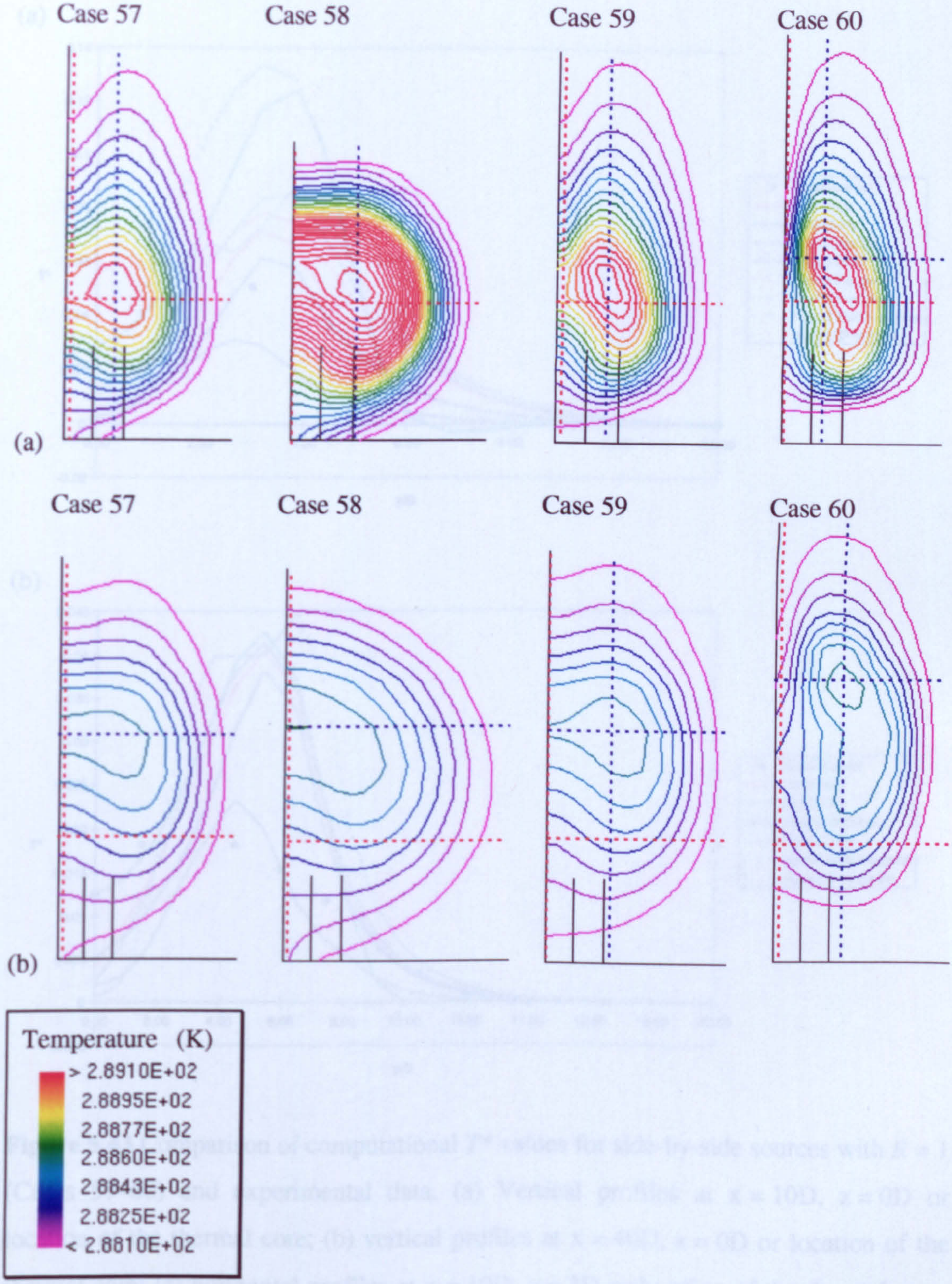

Figure 5.42 Side-by-side sources with $R = 1$ (Cases 57–60), temperature contours where (a) refers to x = 10D and (b) to x = 40D. Red dotted lines refer to the location of experimental profiles, blue lines bisect the thermal core. (Original in colour.)

(a)

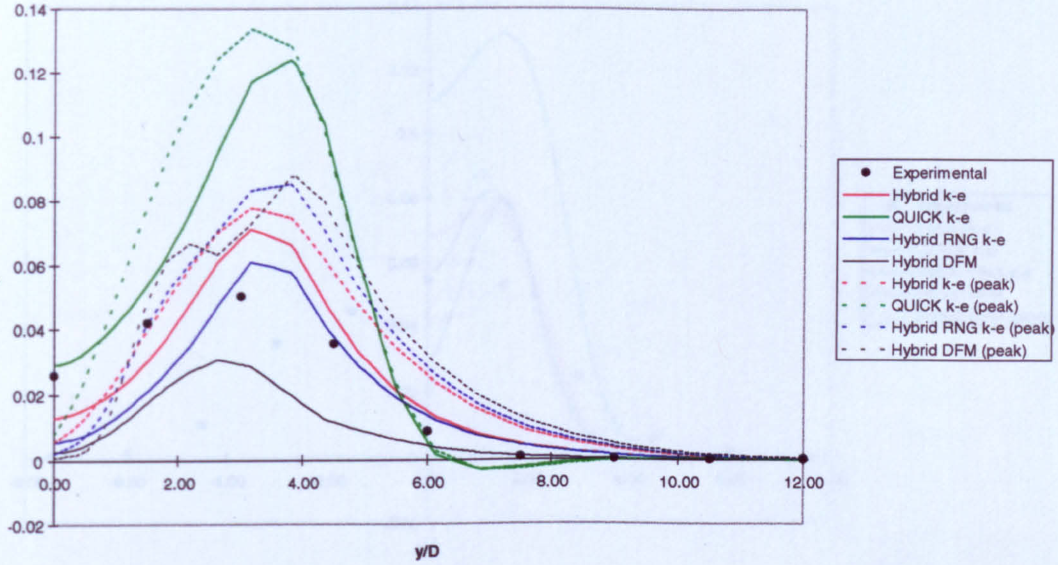

(b)

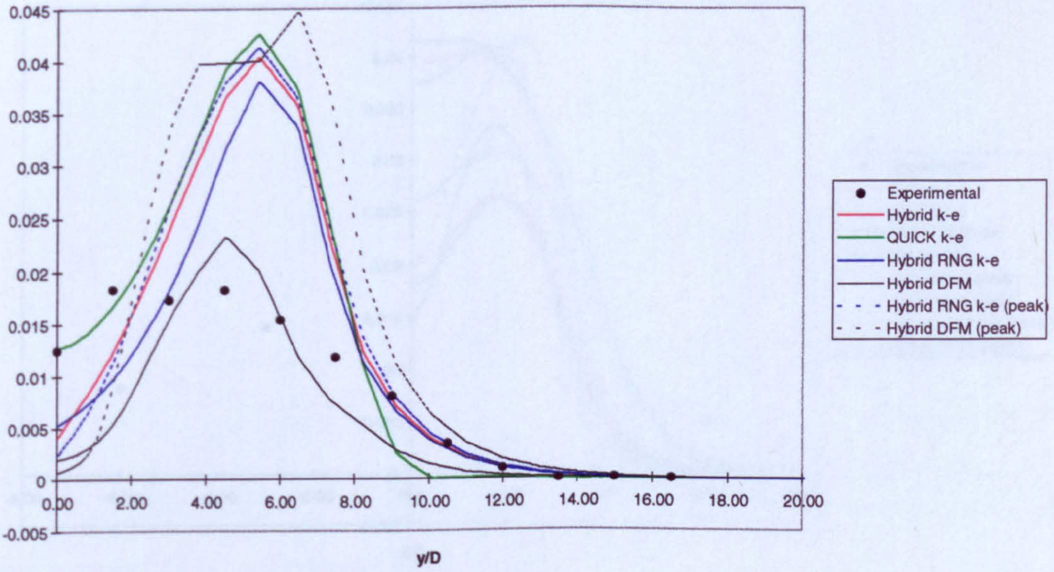

Figure 5.43 Comparison of computational *T** values for side-by-side sources with *R* = 1 (Cases 57–60) and experimental data. (a) Vertical profiles at x = 10D, z = 0D or location of the thermal core; (b) vertical profiles at x = 40D, z = 0D or location of the thermal core; (c) horizontal profiles at x = 10D, y = 3D or location of the thermal core; (d) horizontal profiles at x = 40D, y = 3D or location of the thermal core. (Original in colour.)

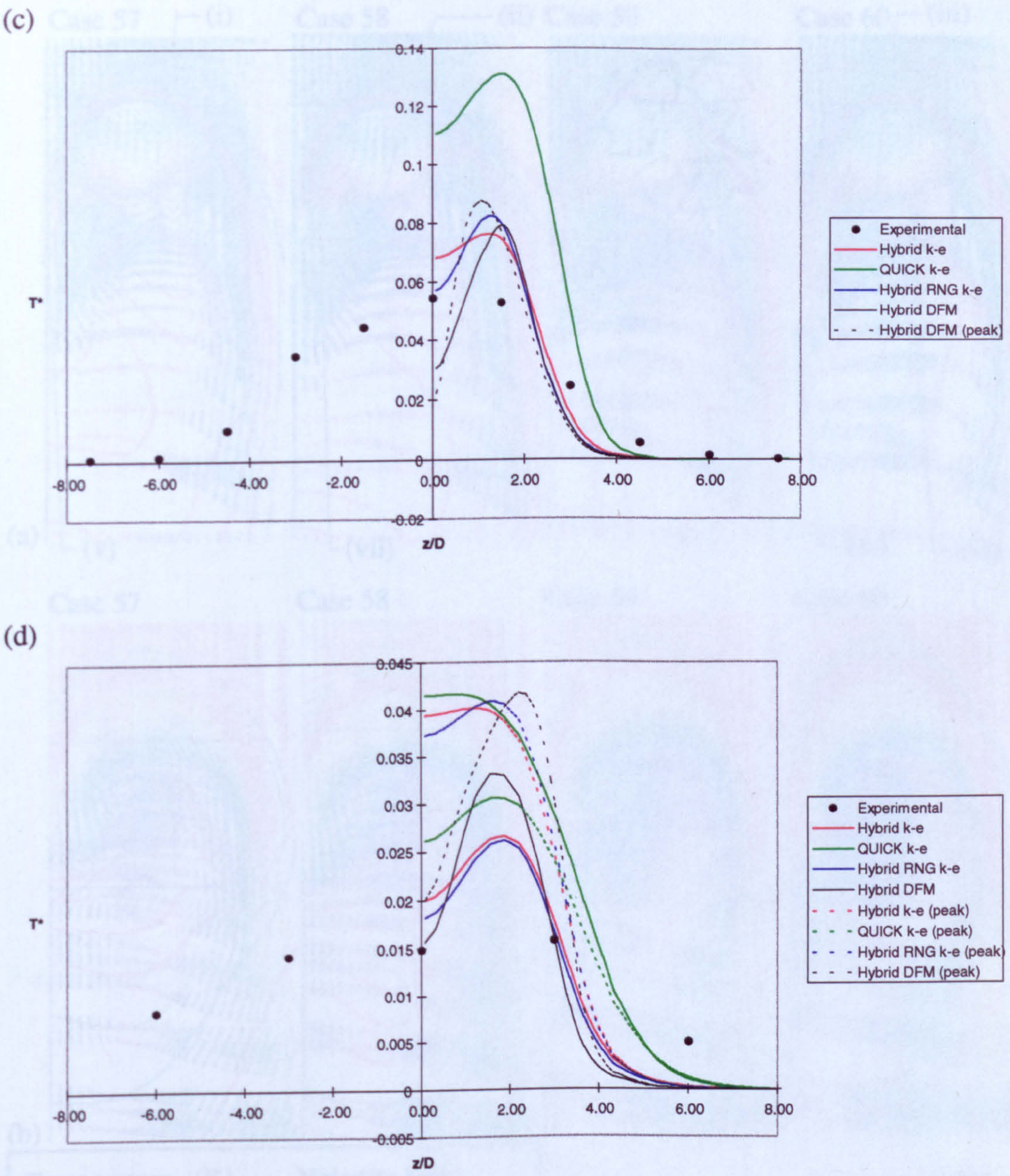

Figure 5.43 *Continued.*

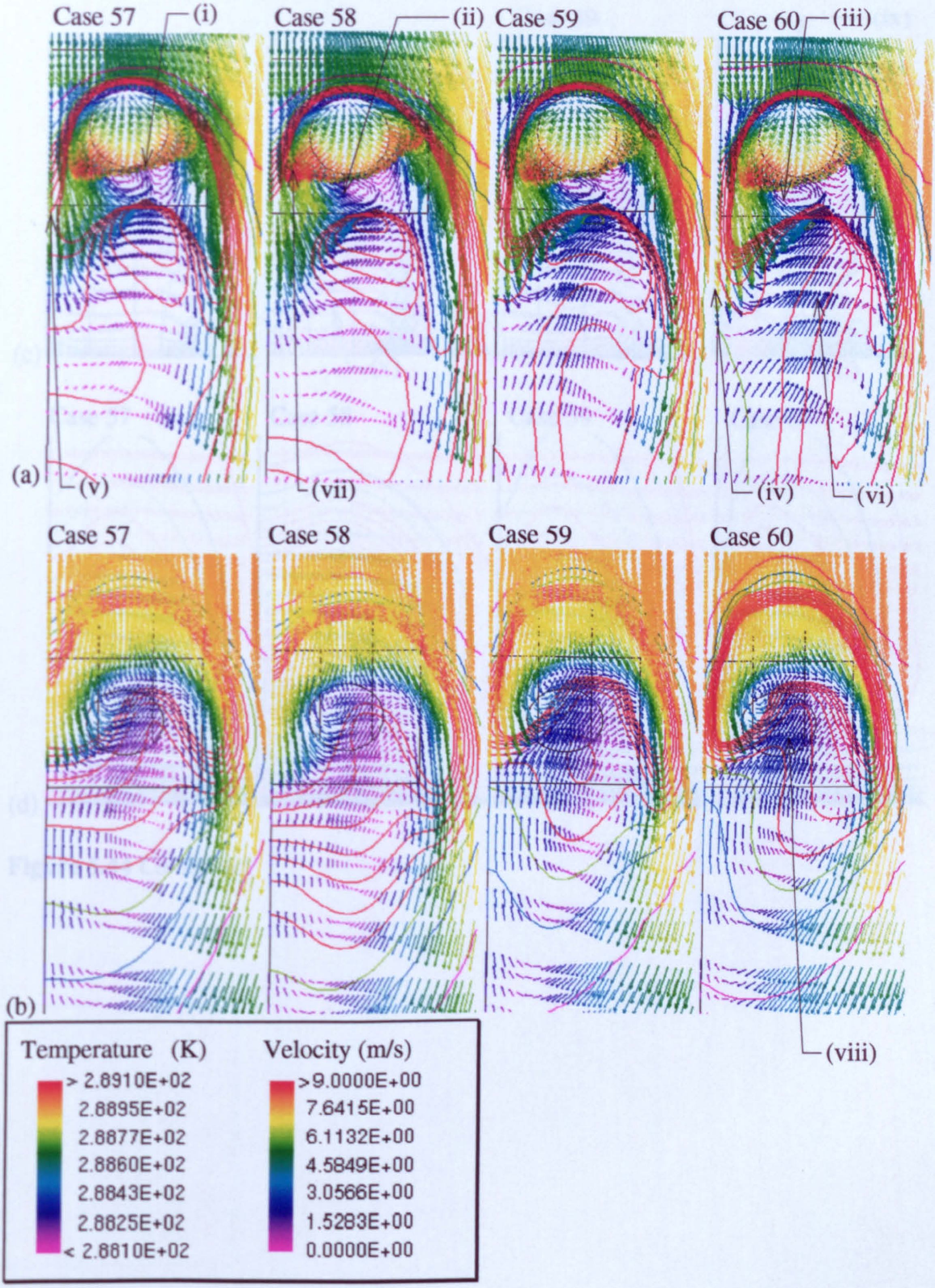

Figure 5.44 Side-by-side buoyant sources, $R = 1.0$ (Cases 57–60), velocity vector and temperature contours; (a–d) refer to cross-sections shown in Figure 5.19. (Original in colour.)

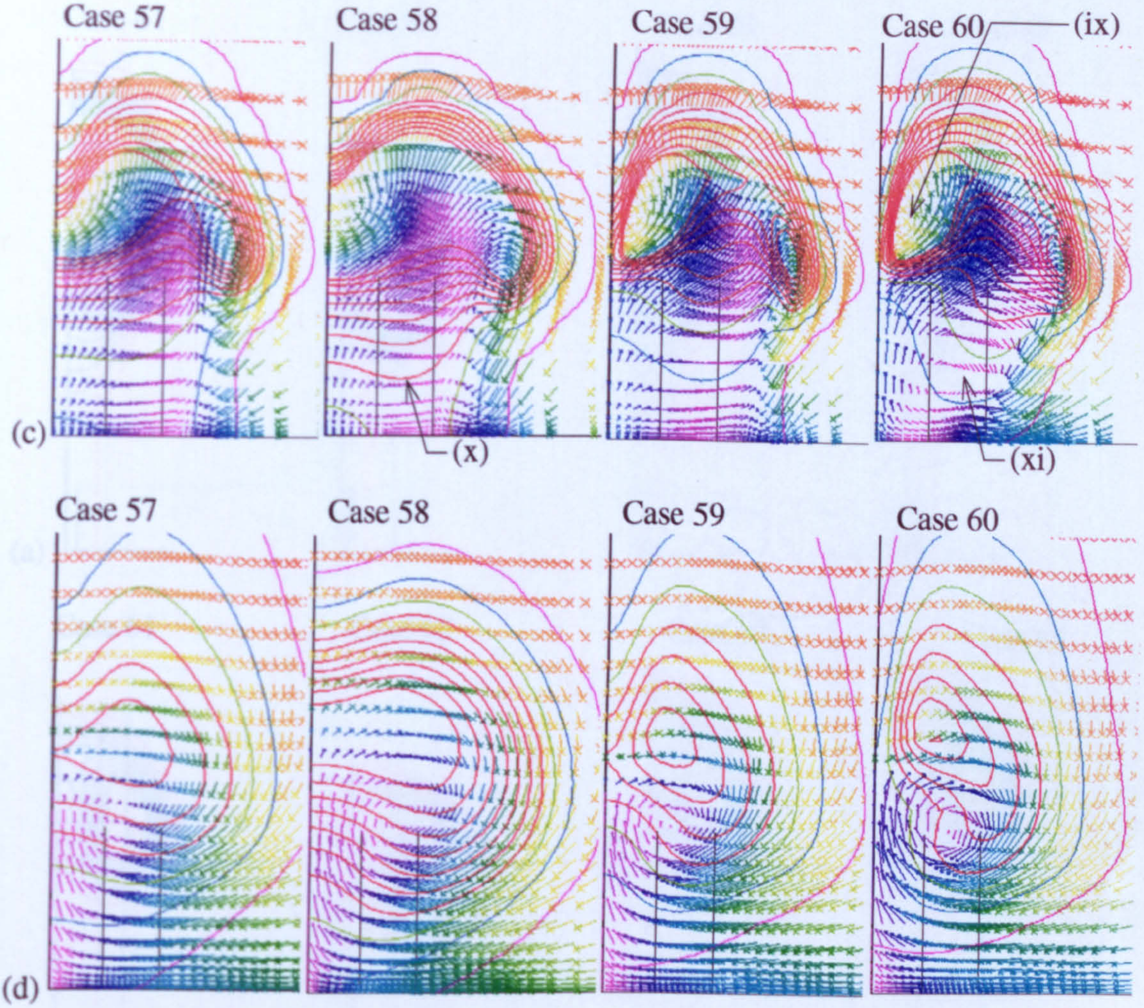

Figure 5.44 *Continued.*

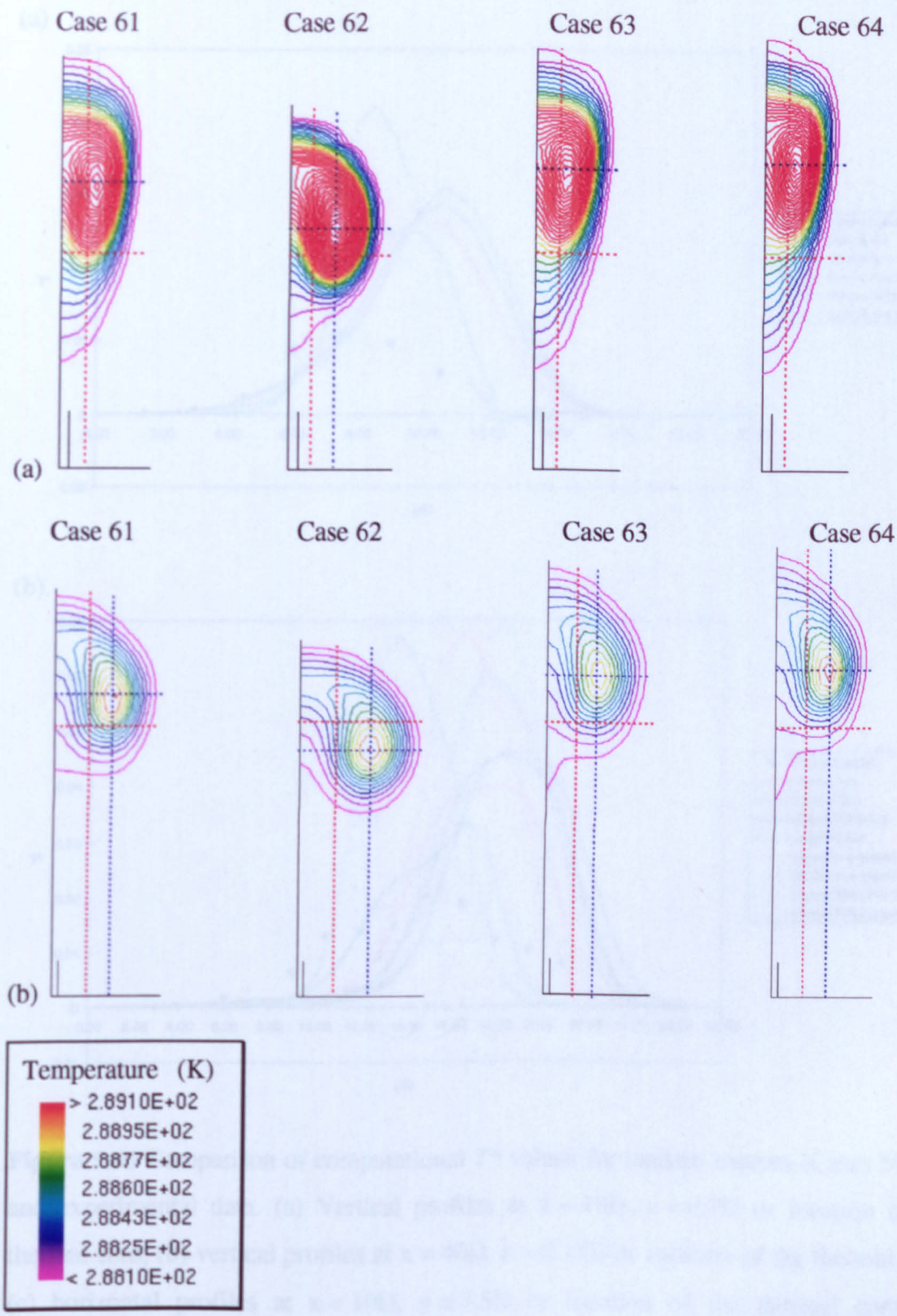

Figure 5.45 Tandem sources (Cases 61–64), temperature contours where (a) refers to x = 10D and (b) to x = 40D. Red dotted lines refer to the location of experimental profiles, blue lines bisect the thermal core. (Original in colour.)

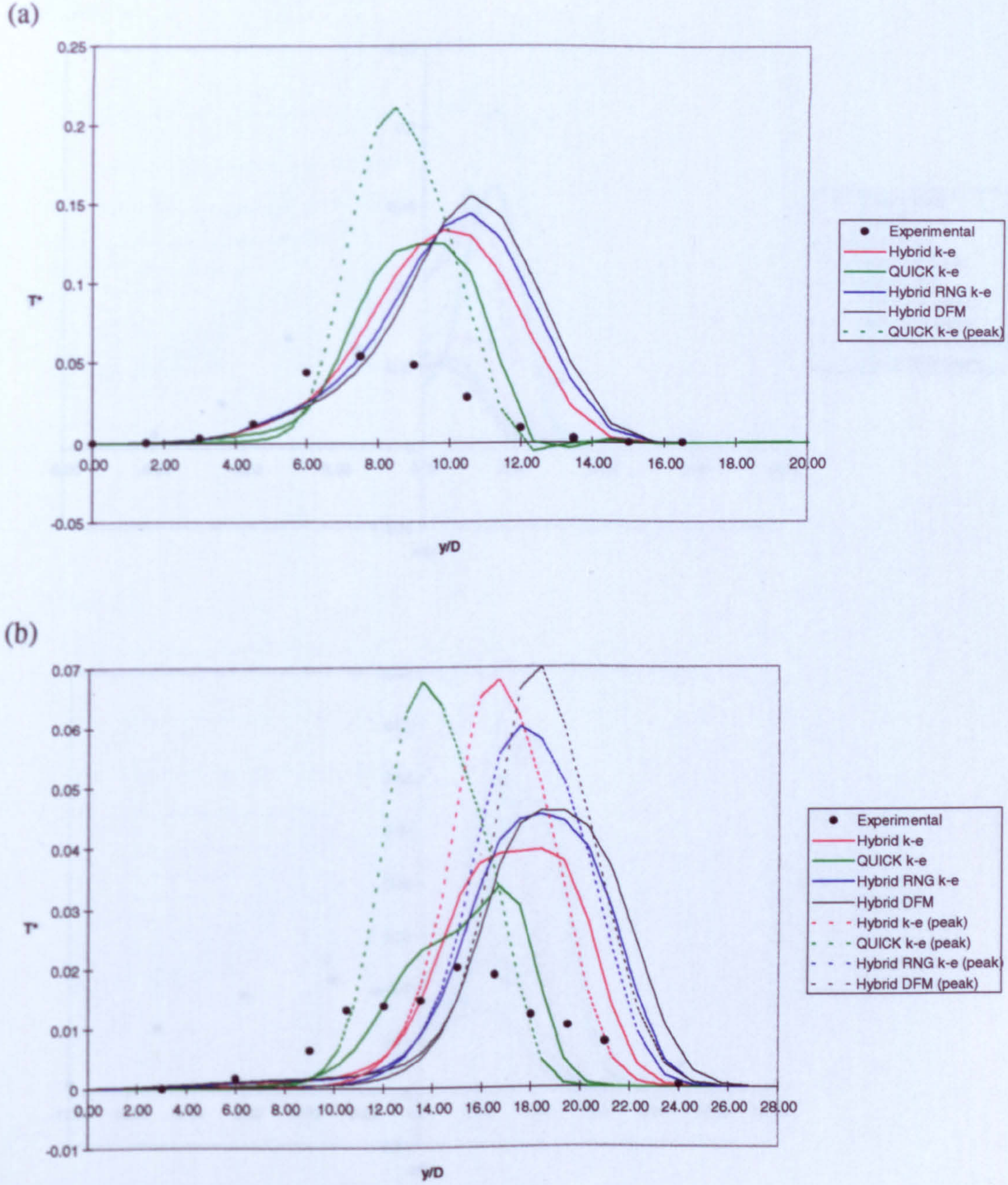

Figure 5.46 Comparison of computational T^* values for tandem sources (Cases 59–62) and experimental data. (a) Vertical profiles at x = 10D, z = 0.7D or location of the thermal core; (b) vertical profiles at x = 40D, z = 0.17D or location of the thermal core; (c) horizontal profiles at x = 10D, y = 7.5D or location of the thermal core; (d) horizontal profiles at x = 40D, y = 15D or location of the thermal core. (Original in colour.)

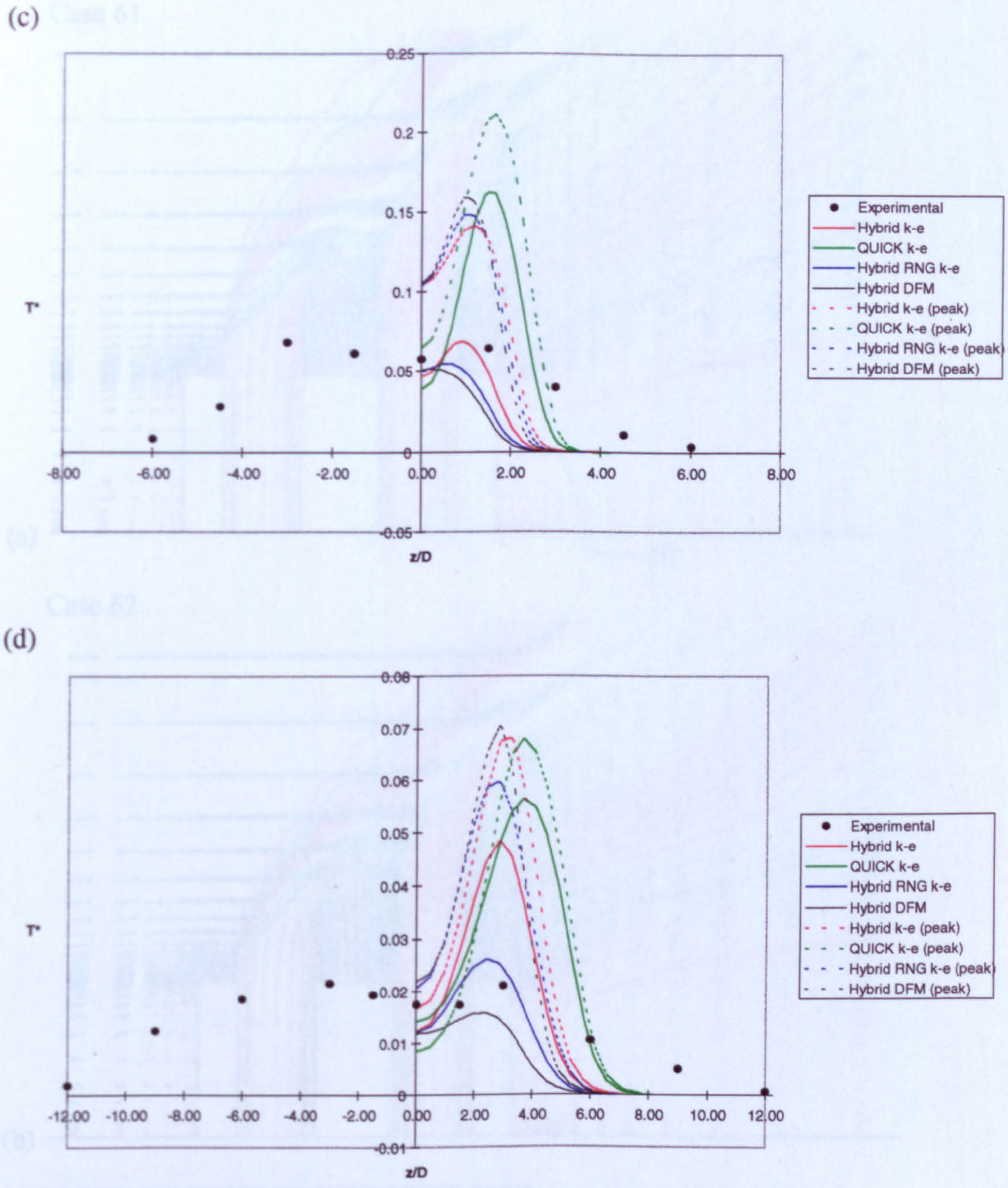

Figure 5.46 *Continued.*

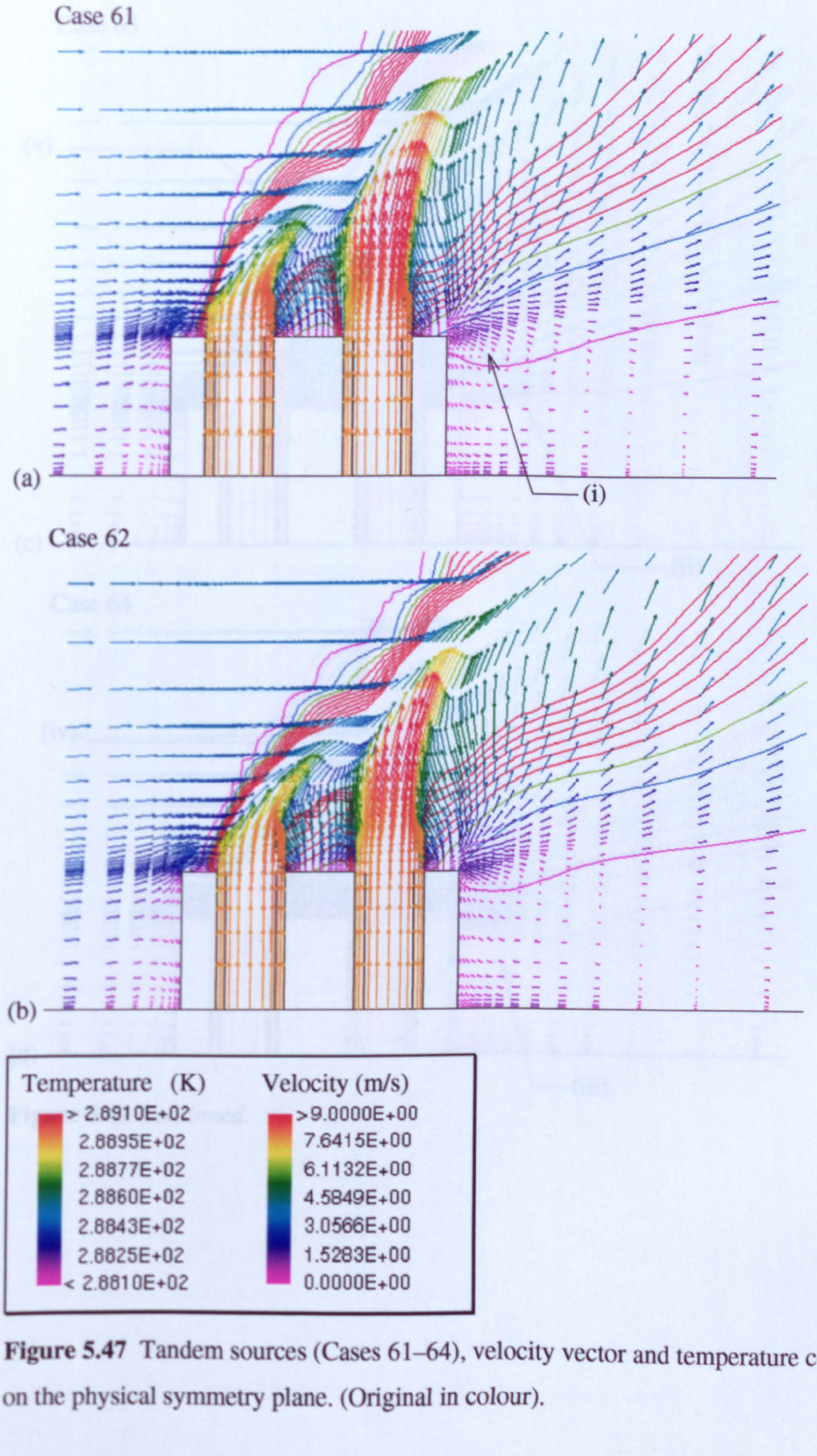

Figure 5.47 Tandem sources (Cases 61–64), velocity vector and temperature contours on the physical symmetry plane. (Original in colour).

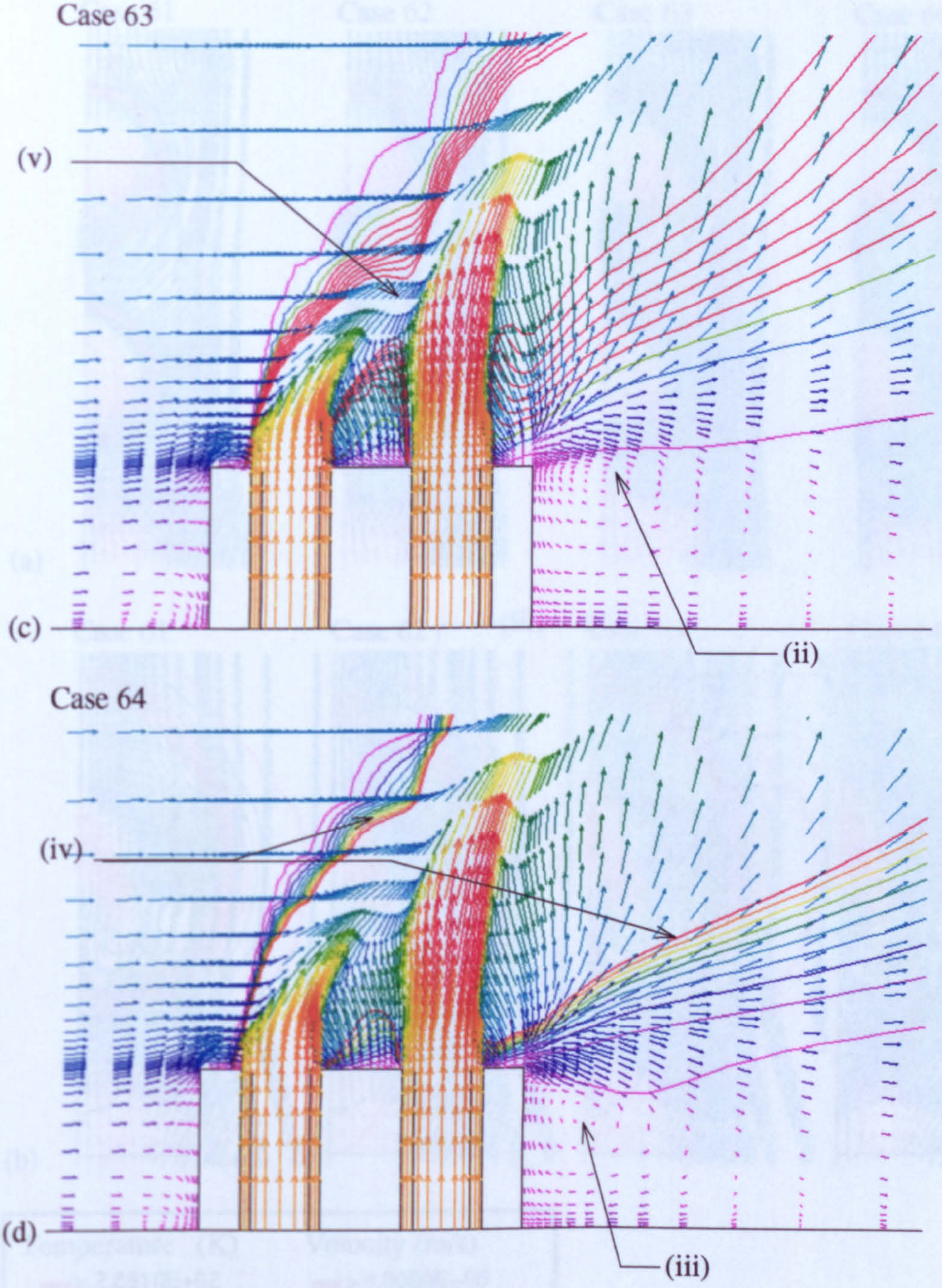

Figure 5.47 *Continued.*

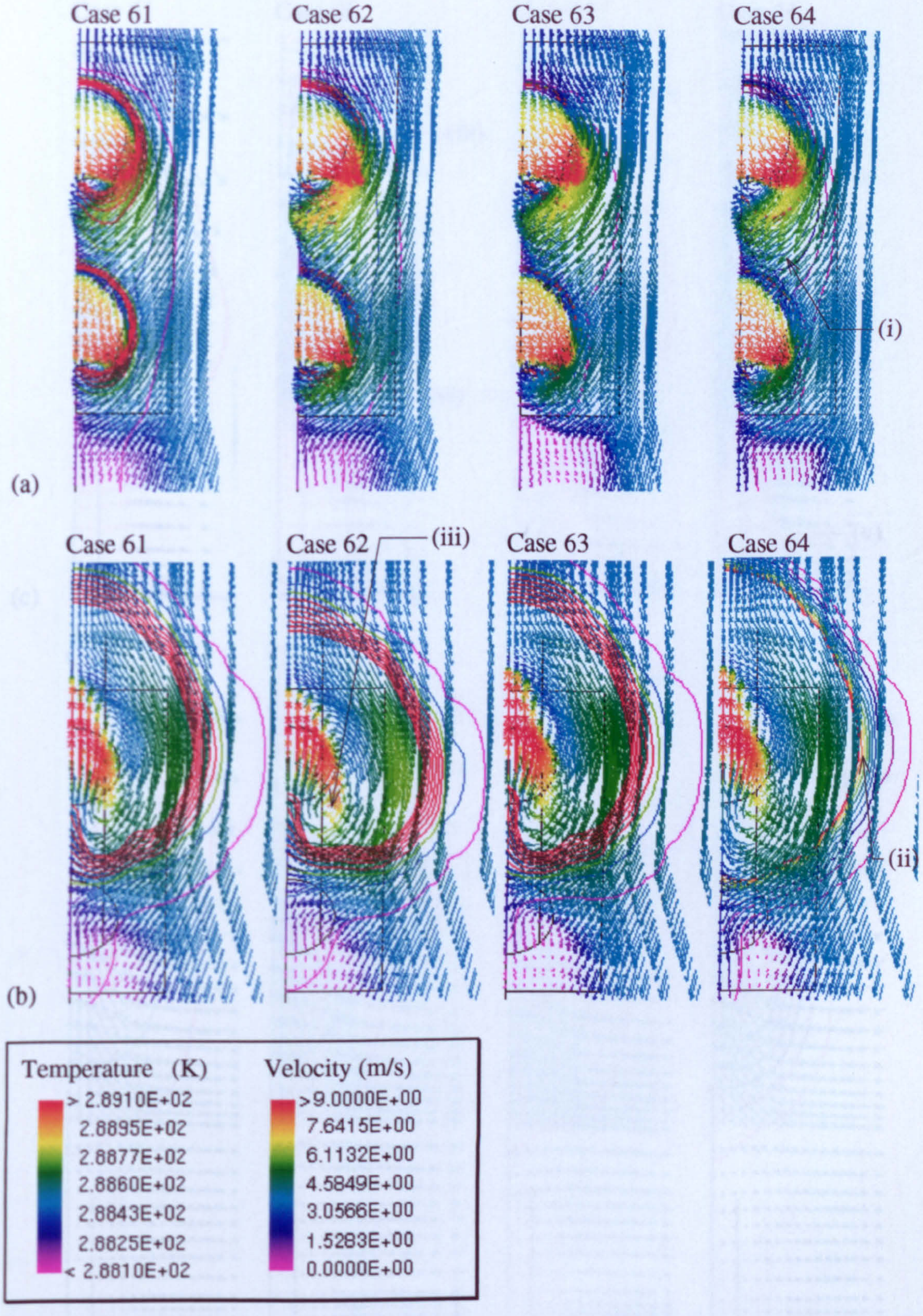

Figure 5.48 Tandem sources (Cases 61–64), velocity vector and temperature contours; (a–d) refer to cross-sections shown in Figure 5.19. (Original in colour.)

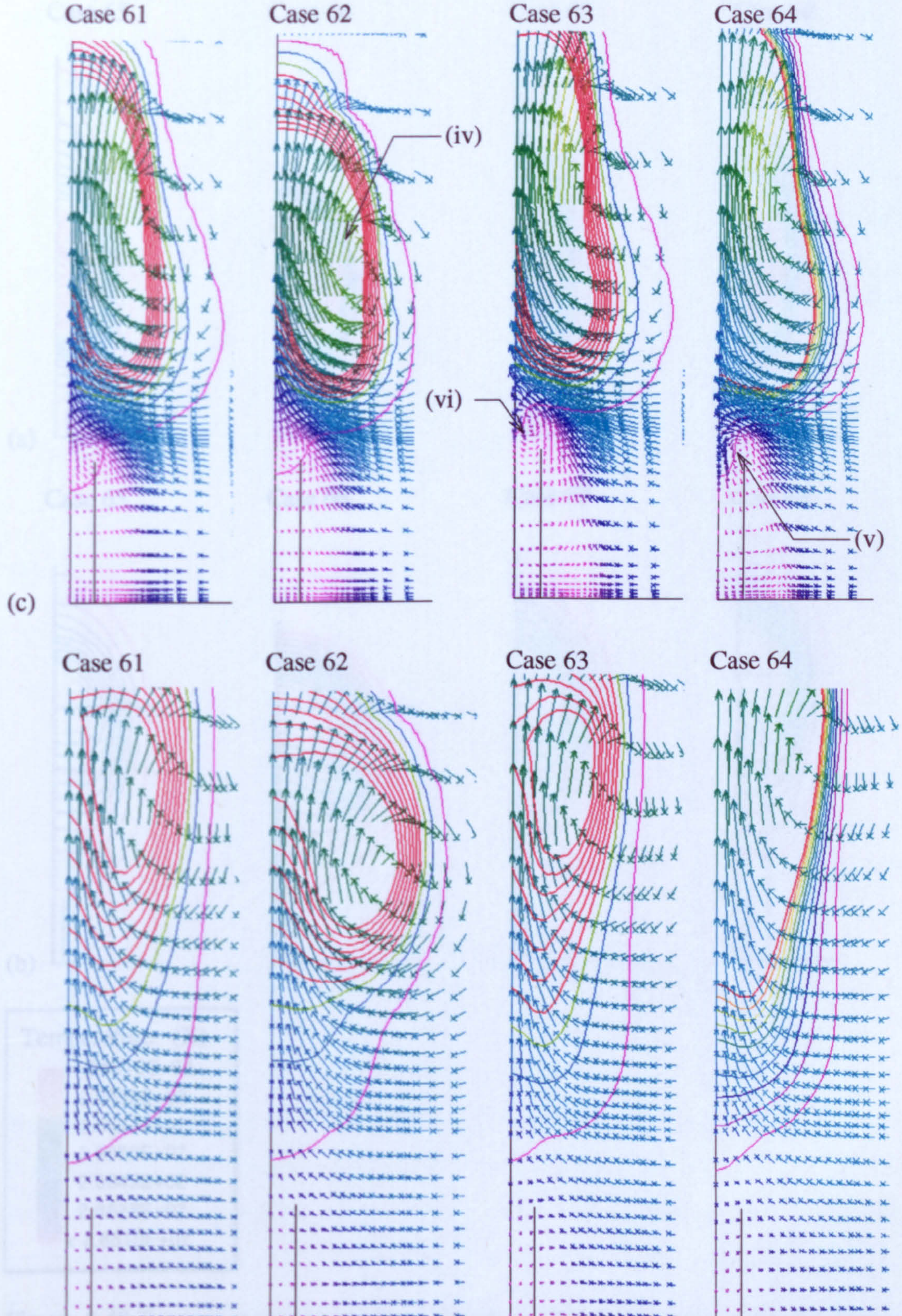

Figure 5.48 *Continued.*

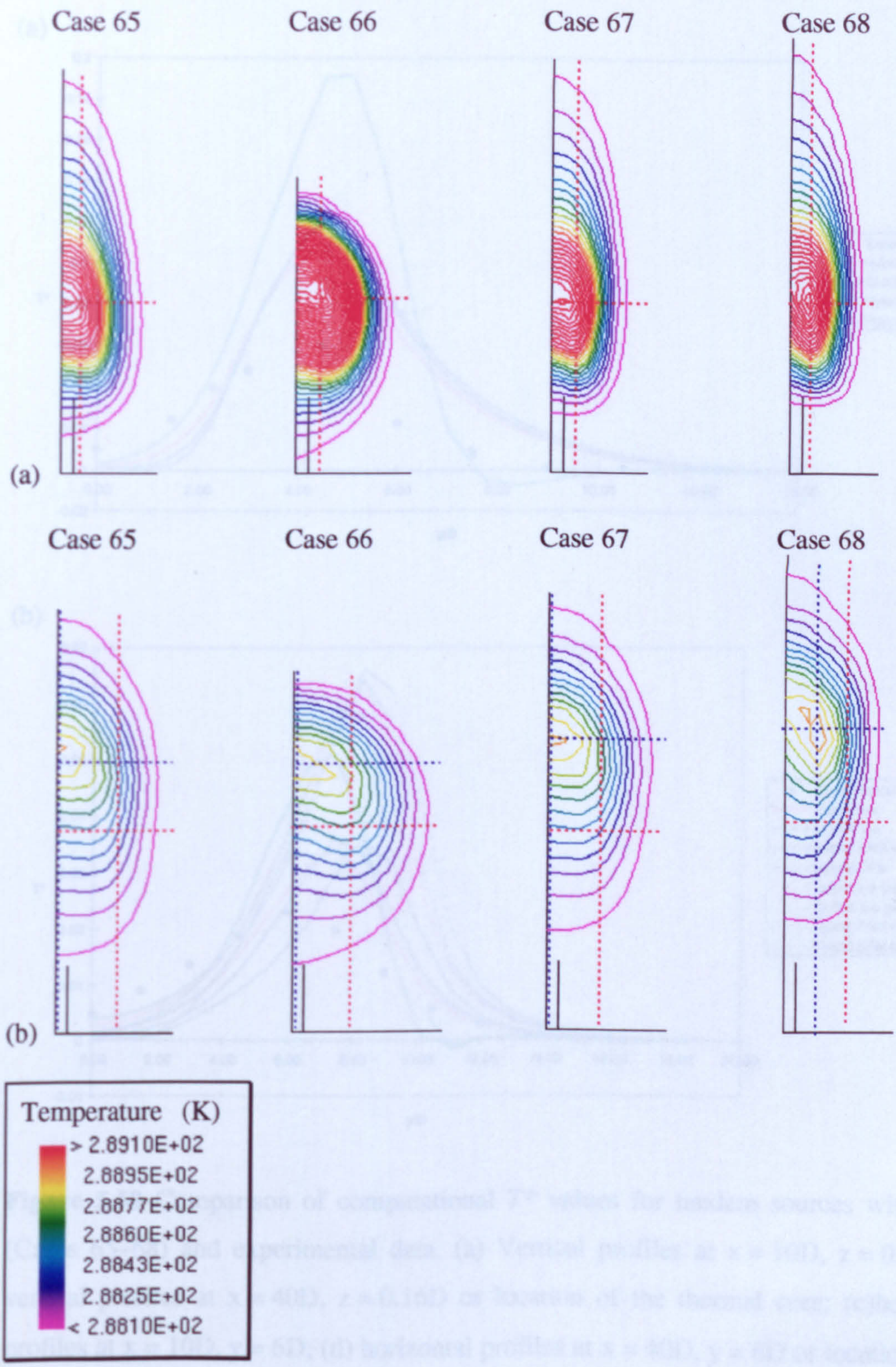

Figure 5.49 Tandem sources with $R = 1$ (Cases 65–68), temperature contours where (a) refers to x = 10D and (b) to x = 40D. Red dotted lines refer to the location of experimental profiles, blue lines bisect the thermal core. (Original in colour.)

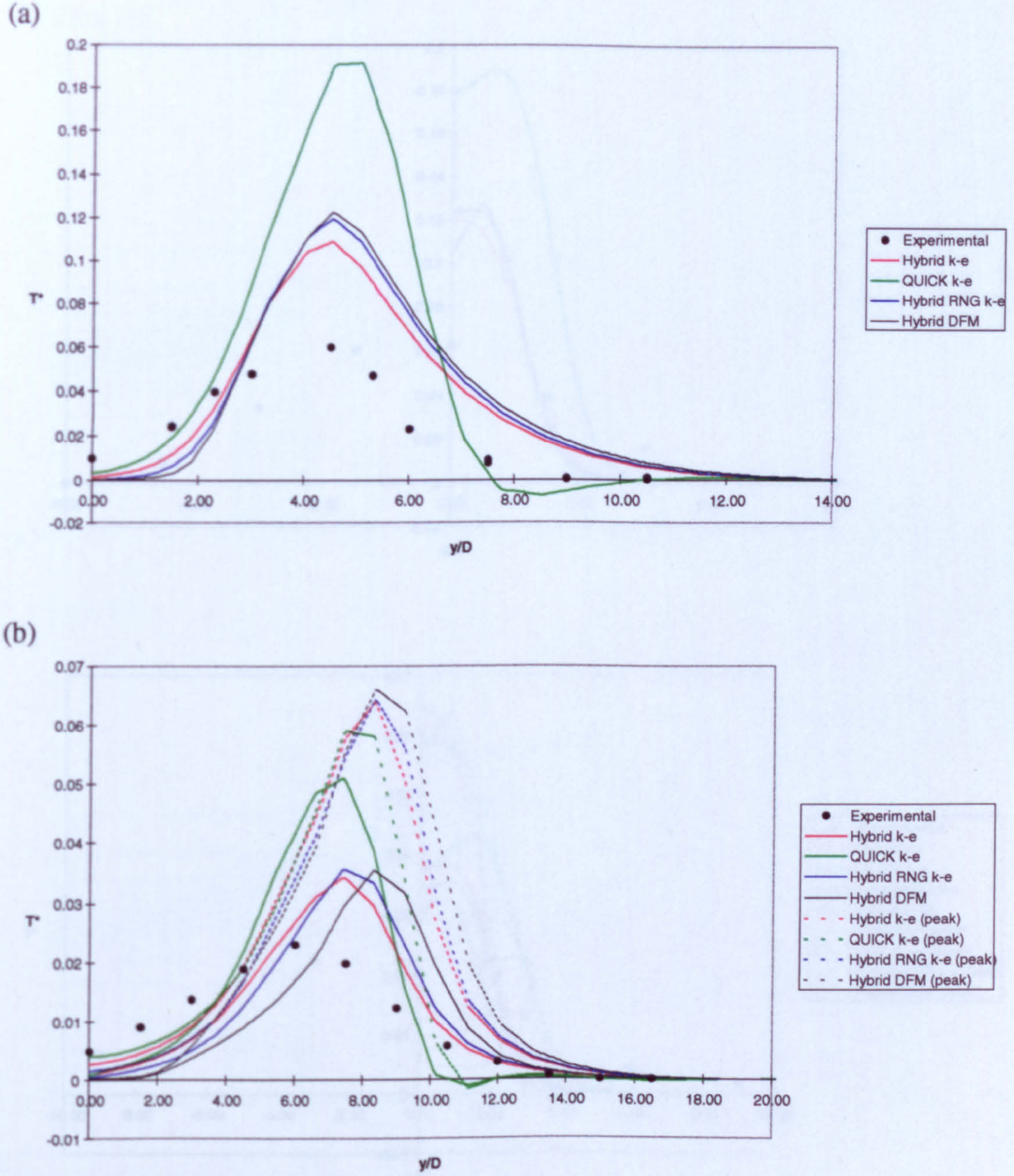

Figure 5.50 Comparison of computational T^* values for tandem sources with $R = 1$ (Cases 65–68) and experimental data. (a) Vertical profiles at x = 10D, z = 0.6D; (b) vertical profiles at x = 40D, z = 0.16D or location of the thermal core; (c)horizontal profiles at x = 10D, y = 6D; (d) horizontal profiles at x = 40D, y = 6D or location of the thermal core. (Original in colour.)

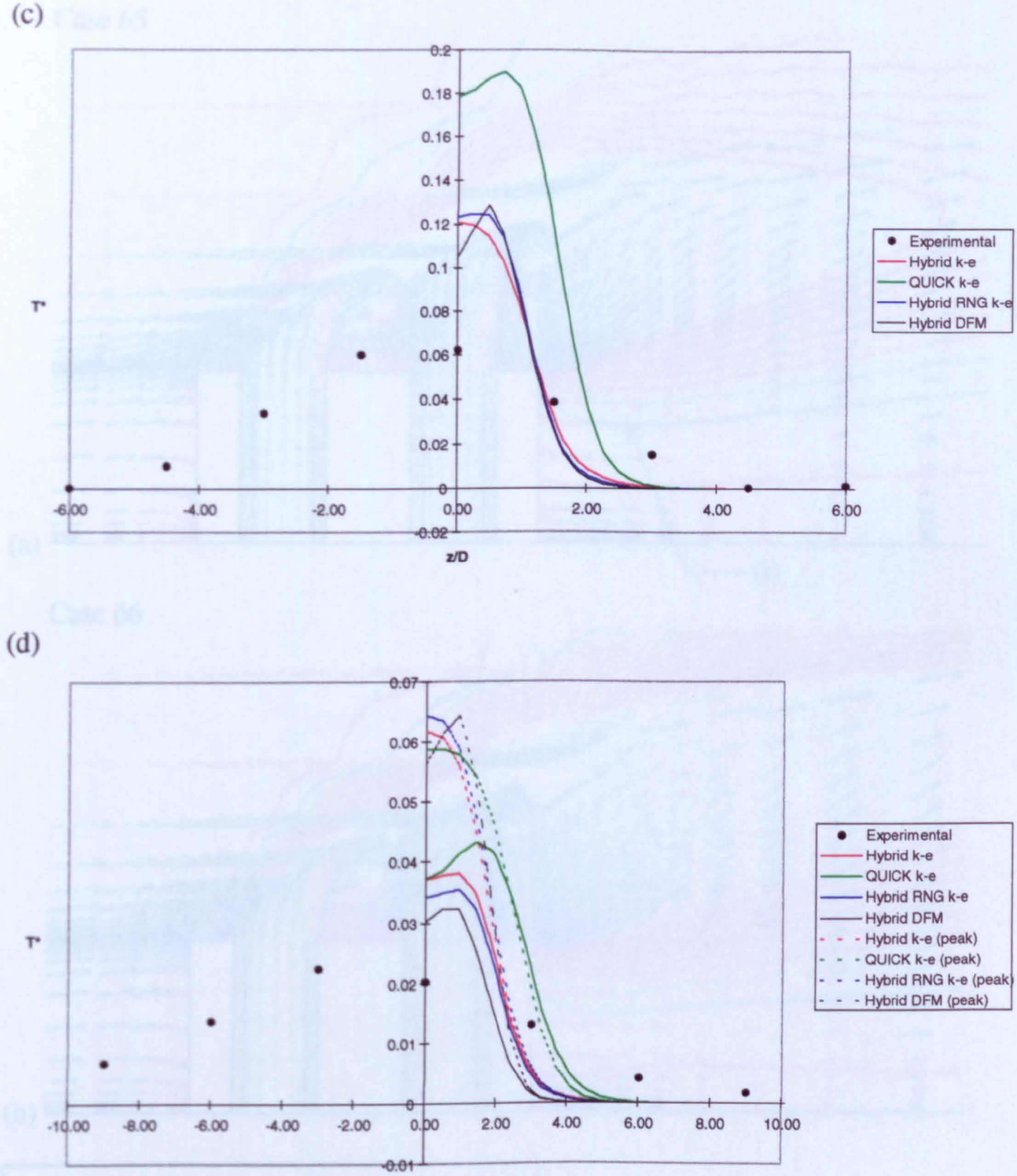

Figure 5.50 *Continued.*

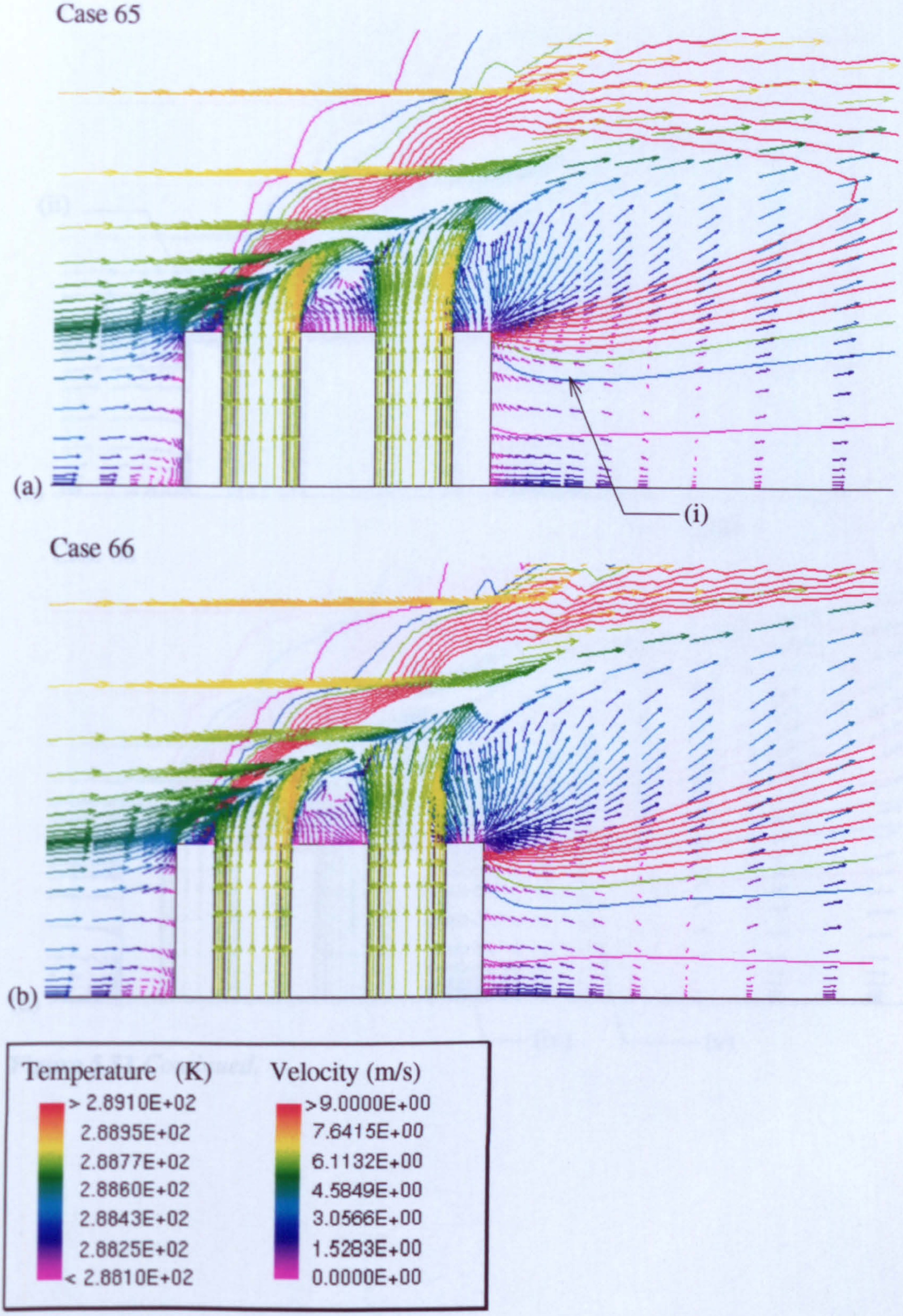

Figure 5.51 Tandem sources with $R = 1$ (Cases 65–68), velocity vector and temperature contours on the physical symmetry plane. (Original in colour).

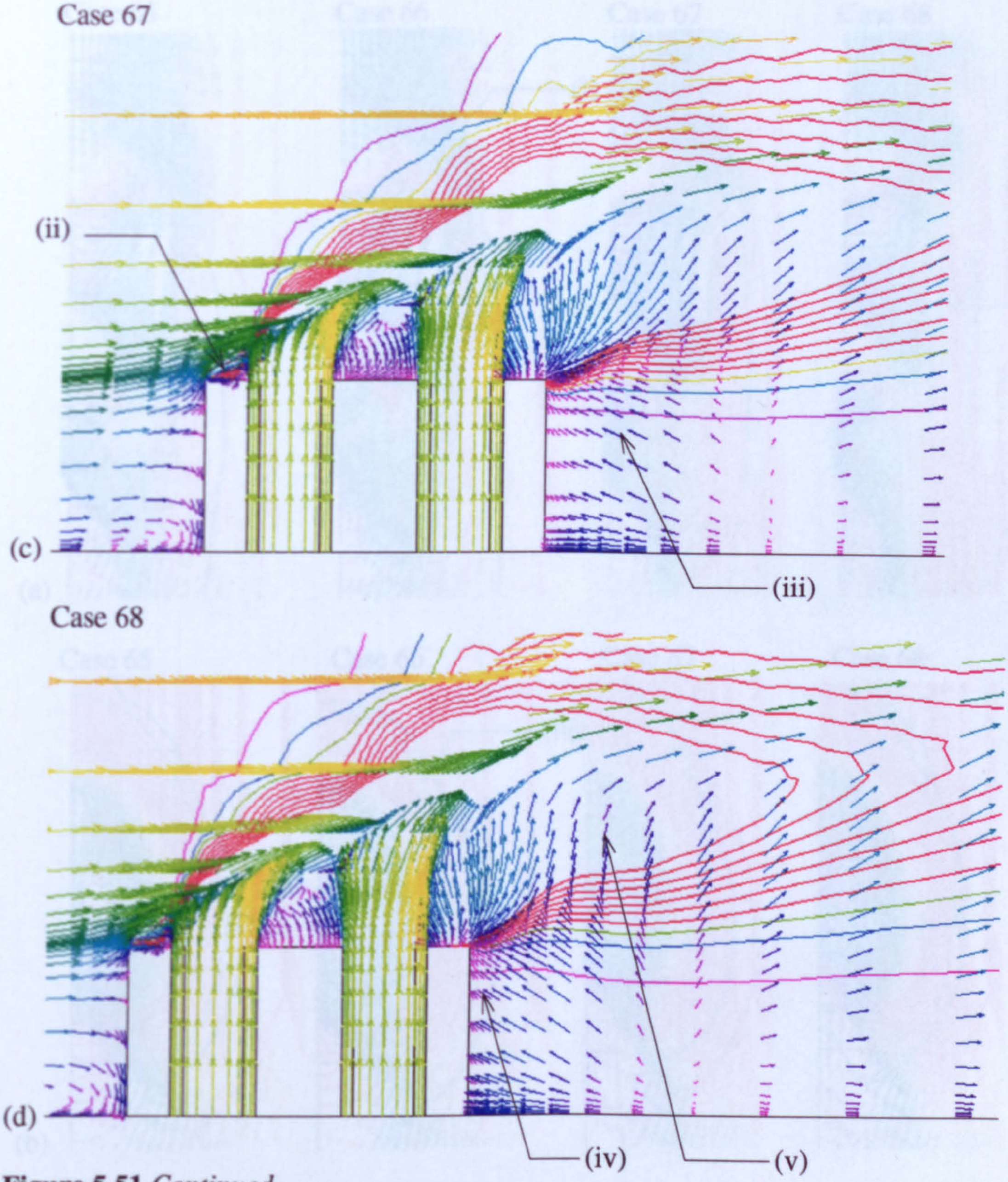

Figure 5.51 *Continued.*

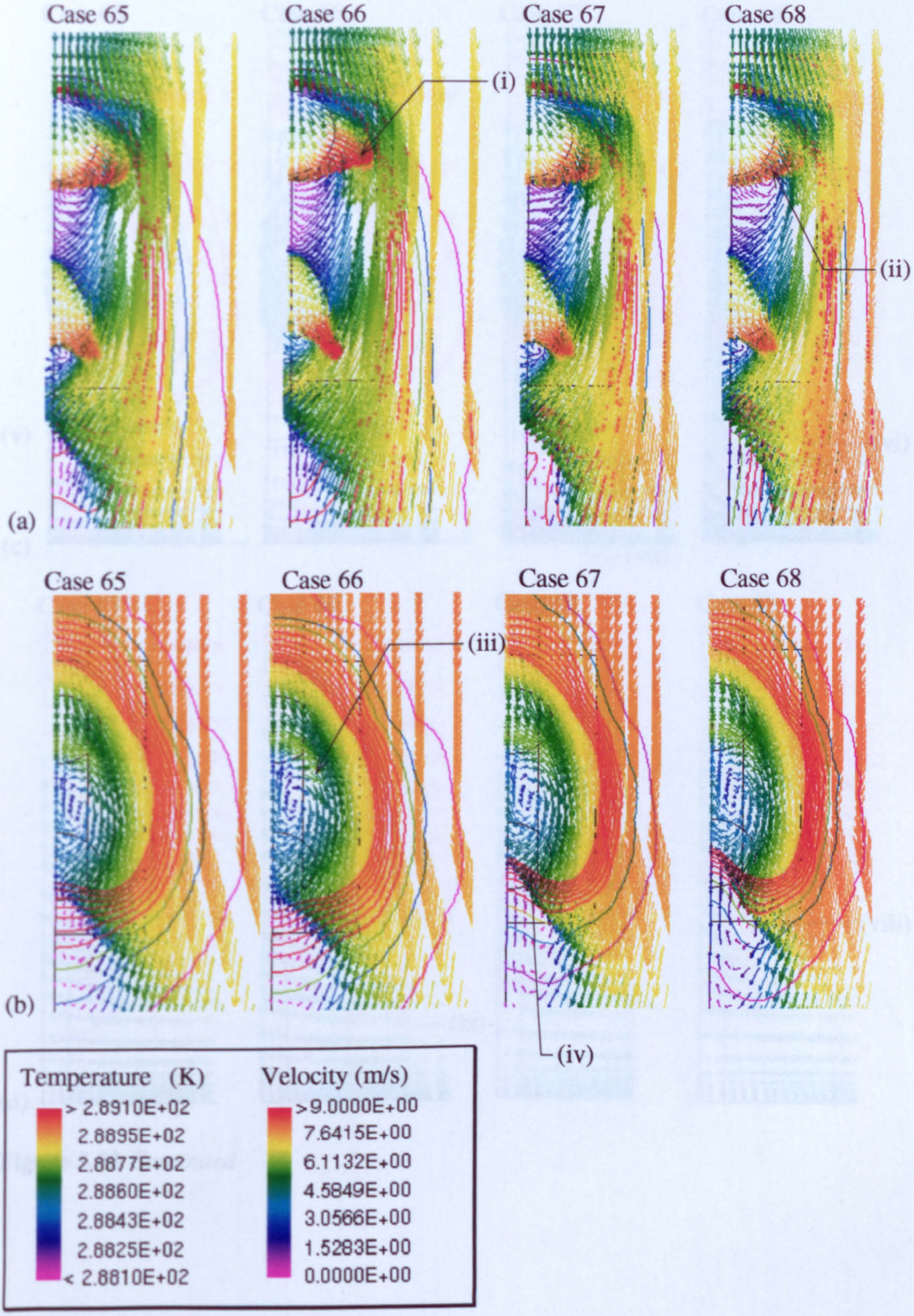

Figure 5.52 Tandem sources with $R = 1$ (Cases 65–68), velocity vector and temperature contours; (a–d) refer to cross sections shown in Figure 5.19. (Original in colour.)

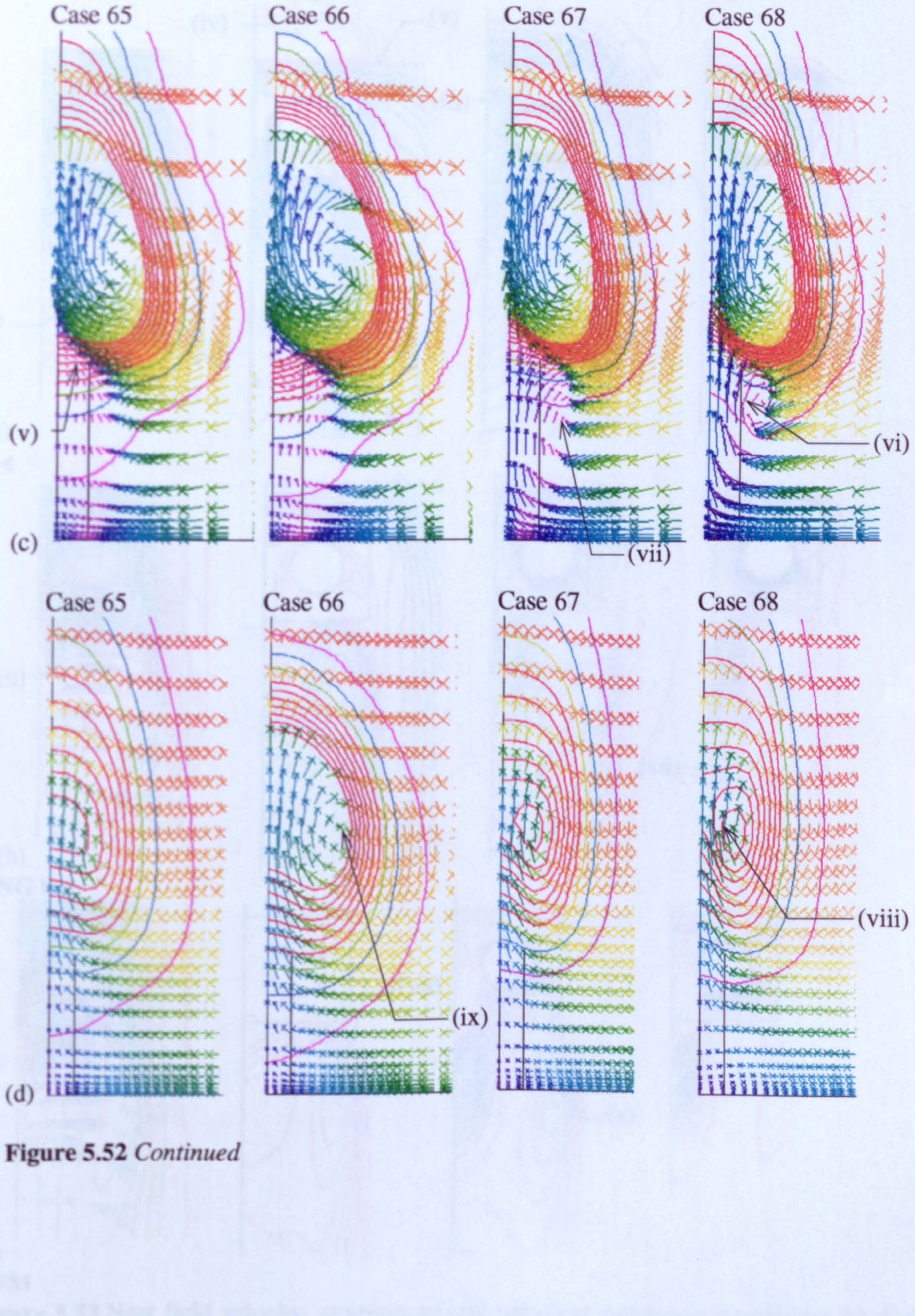

Figure 5.52 *Continued*

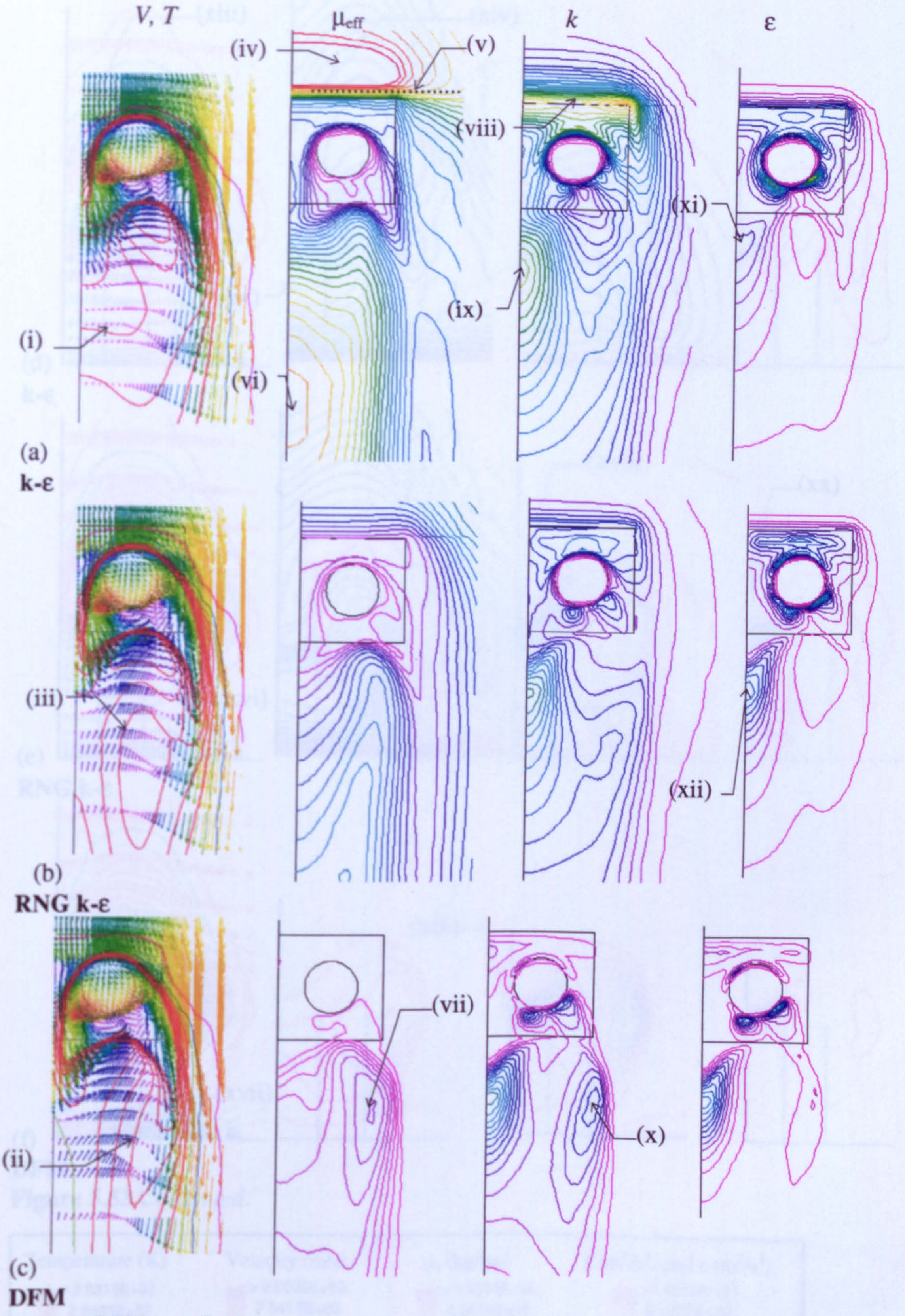

Figure 5.53 Near field velocity, temperature and turbulent parameter distribution for Cases 57, 58 and 60 (*k*-ε, RNG *k*-ε and DFM respectively). Horizontal plane distribution at y = 2.1D (a, b and c) and x = 1D (d, e, f) *Figure caption continued on next page* (Original in Colour)

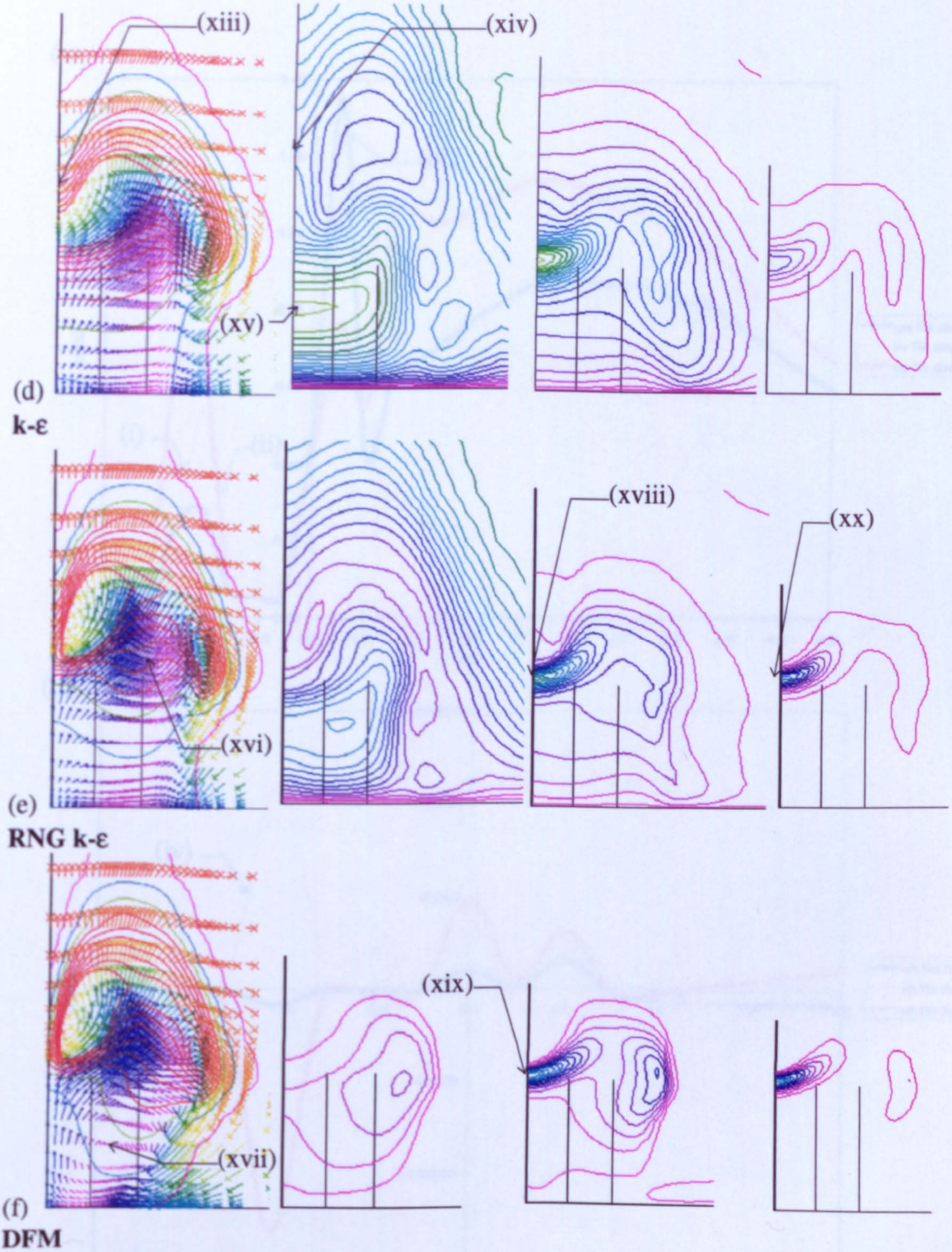

Figure 5.53 C*ontinued*.

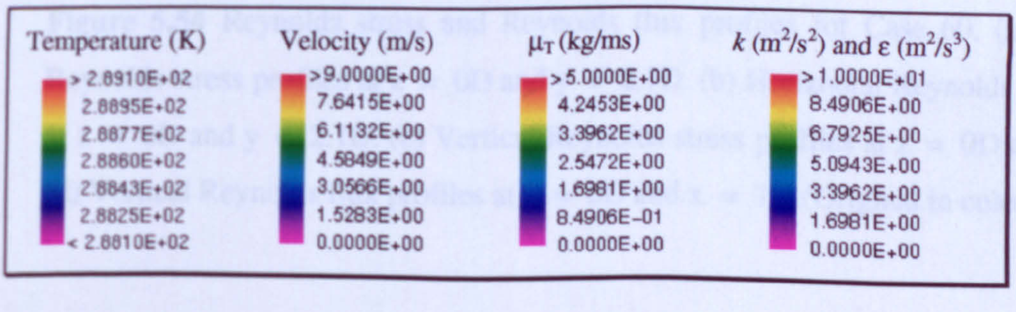

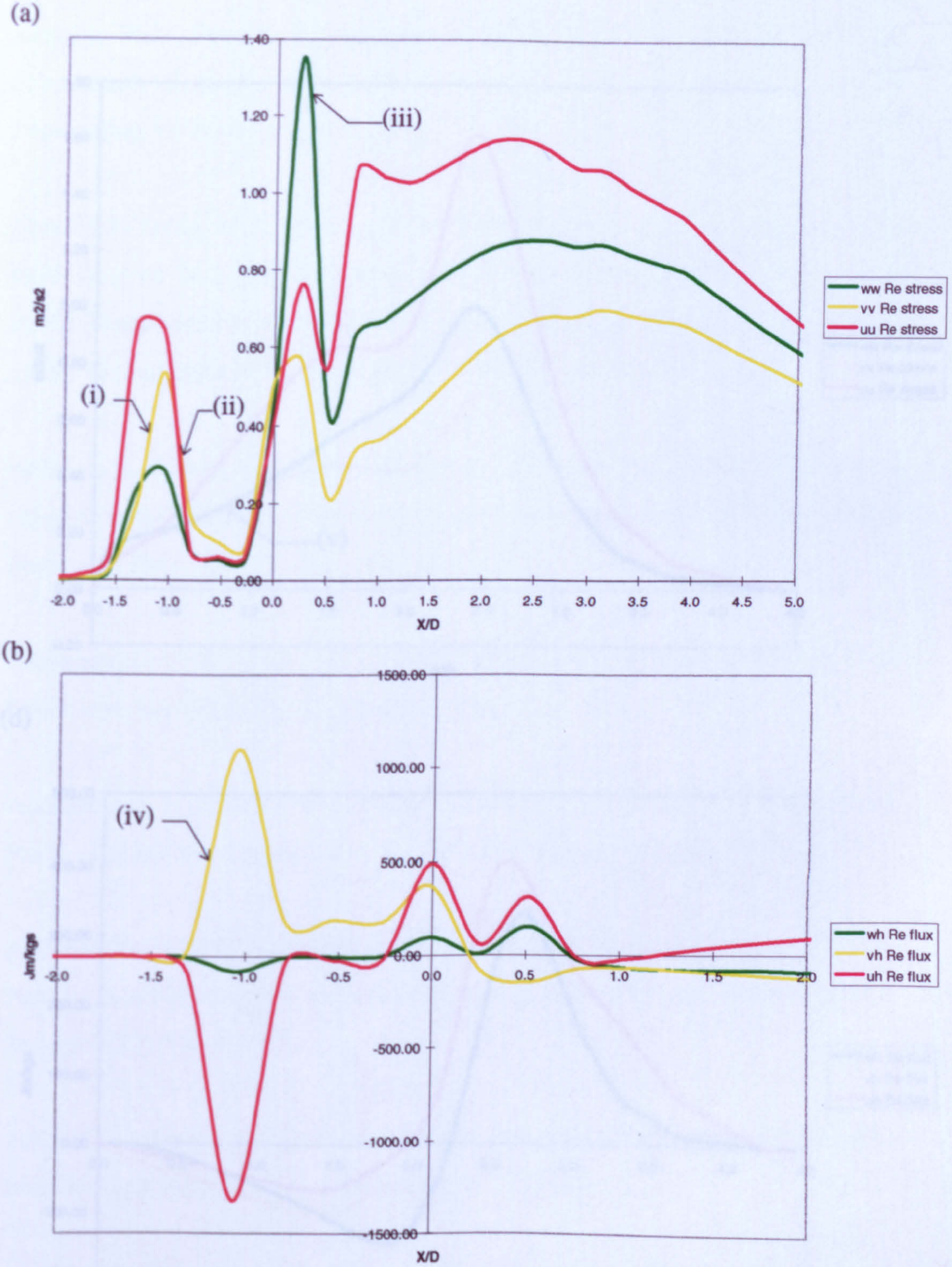

Figure 5.54 Reynolds stress and Reynolds flux profiles for Case 60. (a) Horizontal Reynolds stress profiles at z = 0D and y = 2.1D. (b) Horizontal Reynolds flux profiles at z = 0D and y = 2.1D. (c) Vertical Reynolds stress profiles at z = 0D and x = 1D. (d) Vertical Reynolds flux profiles at z = 0D and x = 1D.(Original in colour.)

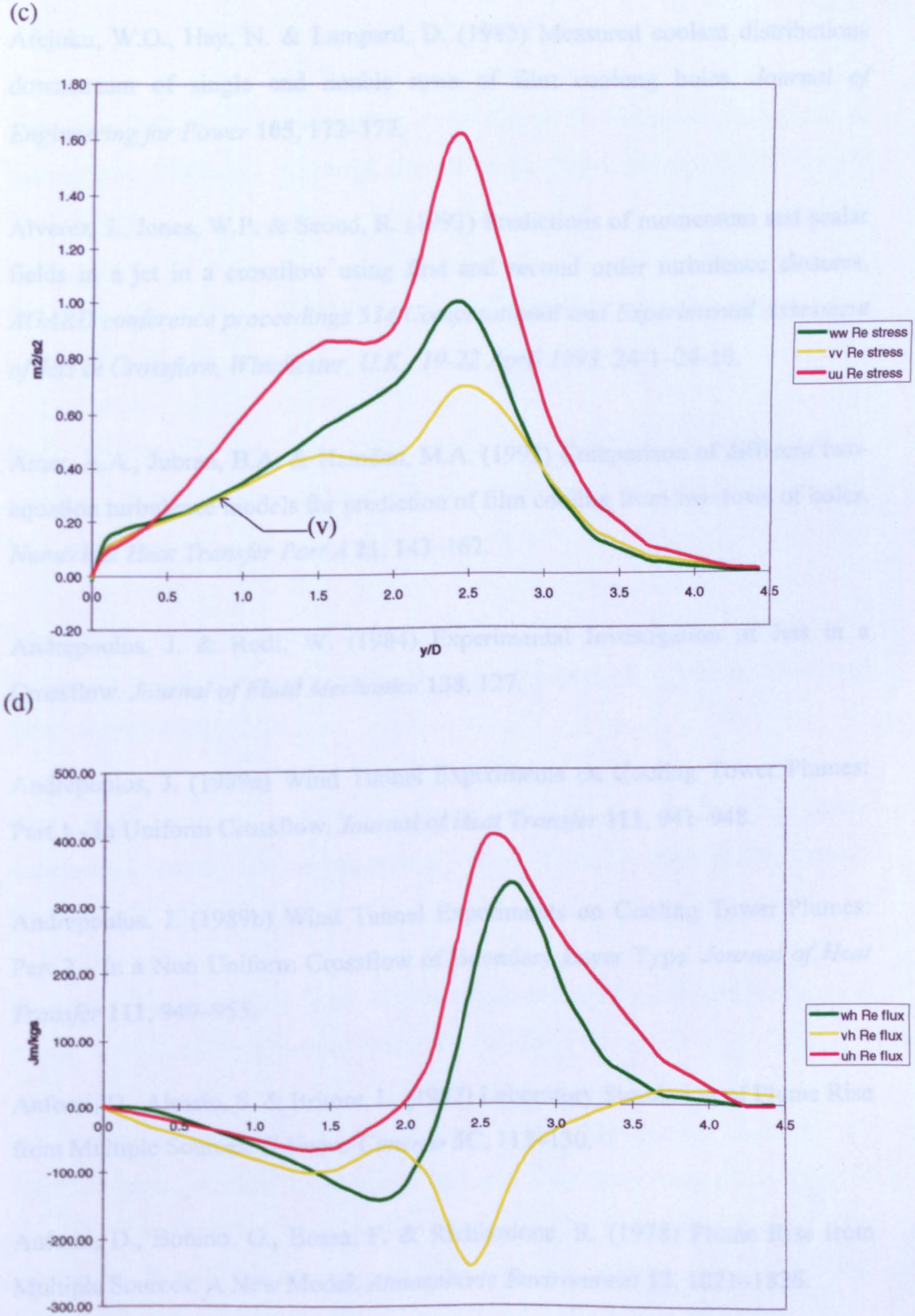

Figure 5.54 *Continued.*

Chapter 6. Conclusions

6.1 OBJECTIVES REALISED BY THESIS

A detailed numerical investigation into both single and adjacent plumes, introduced into a boundary layer type cross-flow, has been conducted.

6.1.1 Sensitivity tests

Grid sensitivity tests have been conducted to minimise grid related false diffusion effects using both the hybrid and QUICK discretisation schemes. No sensitivity to plume rise and dispersion was found in changes to source turbulence intensity or to the inclusion or exclusion of the turbulence model constant C_3. A decrease in the commonly used value of Pr_T (0.9) led to a marked increase in the turbulent diffusion of the thermal plume.

6.1.2 Small-scale model

The small-scale experimental wind tunnel work was computationally modelled for a single source, a side-by-side and a tandem source arrangement. A low Reynolds number turbulence model was used with both hybrid and QUICK discretisation schemes. It was found that horizontal spreading of the plume is underpredicted, compared to the experimental data, whilst dilution and rise of the plume is predicted accurately. Interaction of side-by-side sources was found to be dominated by the prediction of the rotating vortex pair within the bent-over plume. A tandem source arrangement led to early combining of adjacent plume, thus an efficiently enhanced overall rise.

6.1.3 Full-scale model

The full-scale problem was modelled computationally, again for a single source, a side-by-side and a tandem source arrangement. Three turbulence models were used in conjunction with both hybrid and QUICK discretisation schemes. For the single tower both buoyant and non-buoyant sources were considered. The predicted rise of the non-buoyant jet was dominated by the tower wake in the near field. As expected, higher rise heights were predicted for the buoyant source. The QUICK scheme predicted lower rise, compared to the other three models, at 40 source diameters downstream. This is inspite of the core temperature being 75% higher than the other models at 10 source diameters downstream.

For both double source configurations two values of *R* were considered, i.e. 2.33 and 1.0. For the side-by-side towers, at the higher value of *R*, combining of adjacent bent-over plumes took longer compared to the equivalent small-scale case. The QUICK plume once again predicted a lower rise even though the thermal dilution rate was lower near the source compared to all hybrid predictions. At the lower value of *R* merging occurred far more quickly. The DFM predicted lower rise than the other models because of its ability to predict turbulent anisotopic features caused by the complex strain field associated with the tower wake/plume interaction. The tandem tower configuration, when the higher value of *R* was used, resulted in the highest rise. Merging of the two plumes occurred very early compared to the side-by-side plumes. Compared to the experimental results, rise was overpredicted near the source, although this overprediction decreased further downstream. When the lower value of *R* was used, merging occurred even before the plumes were fully bent-over. The shape of the thermal profiles were nearly identical to that of the single source at 10 source diameters downstream.

In general, comparison to the experimental data in both small and full-scales was good when considering plume rise. At 10 source diameters downstream, an average comparative accuracy of between +15% and -5% was achieved for computational plume rise height. At 40 source diameters downstream, the accuracy dropped slightly to between +19% and -10%. These values compare well with the accuracy of empirical predictions using a combined '1/3' and '2/3' law relation (a combination of both pure jet and pure plume trajectory equations). The empirical accuracy for rise heights were between +5% and -11% at 10 source diameters and +15% and -8% at 40 source diameters downstream. Both empirical and CFD results fall well within commonly encountered engineering tolerances.

6.1.4 Turbulence prediction

The turbulence field of the side-by-side sources when $R = 1.0$ (producing a highly complex strain field) has been analysed for the four models used. The standard k–ε model produced very high eddy viscosity levels in regions of stagnation. This results in any recirculating flow features downstream of the stagnation being diffused away (i.e. the plume wake). In comparison, the DFM predicted levels of eddy viscosity up to six times lower, thus allowing the flow to recirculate more readily. The RNG k–ε model, although still an isotropic eddy viscosity model, predicted levels of μ_T more like those of the DFM due to a modified production term in the ε-equation. Therefore, the RNG model also predicted the same recirculating flow features as the DFM. However, there were certain flow features containing additional rates of strain and an anisotropic turbulence field, that the DFM alone could predict. Generally, there is surprisingly little dependence on the choice of turbulence model in the prediction of plume rise height and dilution, although this may in part be due to existing numerical diffusion effects. In this study it has been shown that the correct choice of discretisation scheme is more significant.

6.2 RECOMMENDATIONS FOR FUTURE WORK

This study has concentrated on the two extremes of approach wind direction, 0° and 90° to the tower axis. When the wind approaches from an angle, the interaction between these two limits will produce interaction mechanisms that are a product of the primary mechanisms identified here. A decrease or increase in the spacing between towers would also have a marked effect on plume interaction. A study of both these parameters would be beneficial in obtaining a full range of rise enhancement factors.

Only neutral stratification of the atmospheric boundary layer has been considered here. When there is a high combined plume rise (as in the case of a tandem tower arrangement with high values of R) interaction with an elevated inversion may occur.

The present computational model could readily be extended to include density gradients in the oncoming boundary layer.

To minimise any increase in ground level concentrations, either the point at which the plume is issued into the cross-wind could be raised or the speed of the cross wind could be decreased at the tower top. Both of these could be modelled using the present framework. A plenum on top of the tower could be included, although the increased pressure drop could decrease the volume flow rate of the tower. The 'hand in front of a candle' approach could also be modelled. A solid or semi-permeable barrier is erected just upstream of the tower to divert the cross-wind around the source thus allowing more vertical rise before the plume is bent-over. These are just two design modifications to the existing arrangement. Now that the computational model used in this study has been extensively tested, further designs could be investigated using this CFD framework.

References

Afejuku, W.O., Hay, N. & Lampard, D. (1983) Measured coolant distributions downstream of single and double rows of film coolong holes. *Journal of Engineering for Power* **105**, 172–177.

Alverez, J., Jones, W.P. & Seoud, R. (1993) Predictions of momentum and scalar fields in a jet in a crossflow using first and second order turbulence closures. *AGARD conference proceedings 534 Computational and Experimental Assesment of Jets in Crossflow, Winchester, U.K., 19-22 April 1993,* 24-1–24-10.

Amer, A.A., Jubran, B.A. & Hamdan, M.A. (1992) Comparison of different two-equation turbulence models for prediction of film cooling from two rows of holes. *Numerical Heat Transfer Part A* **21**, 143–162.

Andrepoulos, J. & Rodi, W. (1984) Experimental Investigation of Jets in a Crossflow. *Journal of Fluid Mechanics* **138**, 127.

Andrepoulos, J. (1989a) Wind Tunnel Experiments on Cooling Tower Plumes: Part 1 - In Uniform Crossflow. *Journal of Heat Transfer* **111**, 941–948.

Andrepoulos, J. (1989b) Wind Tunnel Experiments on Cooling Tower Plumes: Part 2 - In a Non Uniform Crossflow of Boundary Layer Type. *Journal of Heat Transfer* **111**, 949–955.

Anfossi, D., Alessio, S. & Britore, L. (1982) Laboratory Simulation of Plume Rise from Multiple Sources. *Il Nuovo Cimento* **5C**, 113–130.

Anfossi, D., Bonino, G., Bossa, F. & Richiardone, R. (1978) Plume Rise from Multiple Sources: A New Model. *Atmospheric Environment* **12**, 1821–1826.

Anfossi, D., Richiardone, R. & Bonino, G. (1979) *Nuovo Cimento* **2**, 488.

Barata, J.M.M., Durao, D.F.G. & Heitor, M.V. (1992) Velocity Charactersitics of Multiple Impinging Jets Through a Crossflow. *Journal of Fluids Engineering* **114**, 231-239.

Batchelor, G.K. (1950) The Application of Similarity Theory of Turbulence to Atmospheric Diffusion. *Quarterly Journal of the Royal Meteorological Society* **76**, 133- 146.

Batchelor, G.K. (1952) Diffusion in a Field of Homogeneous Turbulence. *Proc. Camb. Phil. Soc.* **48**, 345–362.

Batty, K.B. (1976) Sensitivity Tests with a Vapour Plume Model Applied to Cooling Tower Effluents. Master's Thesis, Department of Meteorology, Penn. State University.

Bergeles, G., Gosman, A.D. & Launder, B.E. (1978) The turbulent jet in a cross stream at low injection rates: a three-dimensional numerical treatment. *Numerical Heat Transfer* **1**, 217–242.

Bergeles, G., Gosman, A.D. & Launder, B.E. (1981) The prediction of three-dimensional discrete hole cooling process. Part II. Turbulent flow. *ASME Journal. Heat Transfer* **103**, 141–153.

Bergstrom, D.J. & Stubley, A.B. (1990) Algebraic Stress Model Prediction of a Plume. *Numerical Heat Transfer part A* **18**, 263–281.

Berkowicz, R., Olesen, H.R. & Torp, U. (1986) The Danish Gaussian Air Pollution Model (OML): Description, Test and Sensitivity Analysis in View of Regulatory Applications. *Air Pollution Modelling and Its Applications V*, C. De Wispelaere, F. A. Schiermeier and N. V. Gillani, Eds., Plenum, New York, 453–481.

Bornoff, R. & Mokhtarzadeh, R. (1994) Numerical investigation of the interaction of adjacent cooling tower plumes. *ECCOMAS '94 2nd European Computational Fluid Dynamics Conference, University of Stuttgart, Germany, 5-8 Septemeber.*

Bosanquet, C.H. (1957) The Rise of a Hot Waste Gas Plume. *Journal of the Institution of Fuel* **30**, 322–328.

Briggs, G.A. (1965) A plume rise model compared with observations. *The Journal of Air Pollution Control <mark>Assessment* **15**, 433–438.

Briggs, G.A. (1969) *Plume Rise.* USAEC Critical Review Series, TID-25075, NITS, 81 pp.

Briggs, G.A. (1974) Plume Rise from Multiple Sources. *Proceedings of Cooling Tower Environment* held at University of Maryland, 161–179.

Briggs, G.A. (1975) Plume Rise Predictions. *Lectures on Air Pollution and Environmental Impact Analyses,* D. A. Haugen, Ed., American Meteorological Society, Boston, MA.

Briggs, G.A. (1984) Plume Rise and Buoyancy Effects. *Atmospheric Science and Power Production,* D. Randerson, Ed., U.S. Dept. of Energy **DOE/TIC-27601**.

Calabrese, R.V., Halitsky, J. & Woodard, K. (1974) Prediction of Temperature and Moisture Distributions in Cooling Tower Plumes. In *Symposium on Atmospheric Diffusion and Air Pollution,* 9-13 September 1974. American Meteorological Society, Boston Mass.

Carhart, R.A. & Policastro, A.J. (1991) A Second-Generation Model for Cooling Tower Plume Rise and Dispersion - 1. Single Sources. *Atmospheric Environment* **25A**, 1559–1576.

Carhart, R.A., Policastro, A.J. & Ziemer, S. (1982) Evaluation of Mathematical Models for Natural -Draught Cooling Tower Plume Dispersion. *Atmospheric Environment* **16**, 67–83.

Carpenter, S.B., Thomas, F.W. & Gartrell, F.E. (1968) Full Scale Study of Plume Rise at Large Electric Generating Stations, Tennessee Valley Authority (TVA), Muscle Shoals, Alaska.

Castro, I.P. & Robins, A.G. (1977) The Flow Around Surface-Mounted Cube in Uniform and Turbulent Streams. *Journal of Fluid Mechanics* **79**, 307–335.

CFDS-FLOW3D (1994) Release 3.3 user manual. *Computational Fluid Dynamic Services, Harwell Laboratory, Oxfordshire, OX11 0RA*

Chien, J.C. & Schetz, J.A. (1975) Numerical Solution of the Three-Dimensional Navier-Stokes Equations with Applications to Channel Flows and a Buoyant Jet in a Cross Flow. *Journal of Applied Mechanics* **42**, 575–579.

Chin, S.H. & Roth, K. (1993) A Numerical Investigation of a Subsonic Jet in a Crossflow. *AGARD conference proceedings 534 Computational and Experimental Assesment of Jets in Crossflow, Winchester, U.K., 19-22 April 1993,* 22-1–22-14.

Craig, K.J., Visser, J.A. & der Walt, P.J. (1995) Computational and experimental air pollution simulation - an integrated approach. *Air Pollution Theory and Simulation* 371–380.

Csanady, G.T. (1961) Some observations of smoke plumes. *The International Journal of Air and Water Pollution* **4**, 47–51.

Davis, L.R., Shirazi, M.A. & Slegel, D.L. (1978) Measurement of buoyant jet entrainment from single and multiple sources. *Journal of Heat Transfer* **100**, 442–447.

Demuren, A.O (1983) Numerical calculations of steady three-dimensional turbulent jets in cross flow. *Computational Methods in Applied Mechanical Engineering* 37, 309–328.

Demuren, A.O. & Rodi, W. (1983) Three-dimensional calculation of film coolong by a row of jets. *Proceedings of the fifth GAMM Conference on Numerical Methodsd in Fluid Mechanincs*, Rome, 5–7 October, 49–56.

Demuren, A.O. & Rodi, W. (1987) Three-dimensional numerical calculations of flow and plume spreading past cooling towers. *Journal of Heat Transfer* **109**, 113–119.

Dennis, M.G., Labrie, L.A. & Smith, D.B. (1982) Plume Rise Enhancement: How Good is Briggs' Formulation when Applied to Merged Plumes from Multiple Adjacent Stacks? *Proceedings of the AMS/APCA Third Joint Conference on Application of Air Pollution Meteorology*, 304–307. American Meteorological Society, Boston, MA.

Fay, J.A., Escudier, M. & Hoult, D.P. (1969b) A Correlation of Field Observations of Plume Rise. Fluid Mechanics Laboratory Publication number 69 - 4, Mass. Inst. of Tech.

Frick, W.E. (1975) The Influence of Stratification on Plume Structure. Master's Thesis, Atmospheric Sciences Dept., Oregon State University.

Gangoiti, G., Sancho, J., Ibarra, G. *et al.* (1995) Evaluation of plume rise models from tall stacks in moist atmospheres. *Air Pollution Theory and Simulation* 125–131

Gaffen, D.J., Benocci, C. & Olivari, D. (1987) Numerical modeling of buoyancy dominated dispersal using a Lagrangian approach. *Atmospheric Environment* **21(6)**, 1285–1293.

Gregoric, M., Davis, L.R. & Bushness, D.P. (1982) An Experimental Investigation of Merging Jets in a Cross Flow. *Journal of Heat Transfer* **104**, 236–240.

Haman, K.E. & Malinowski, S.P. (1989) Observations of Cooling Tower and Stack Plumes and their Comparison with Plume Model 'ALINA.' *Atmospheric Environment* **23**, 1223–1234.

Hanna, S.R. (1975) Predicted and Observed Cooling Tower Plume Rise and Visible Plume Length at the John E. Amos Power Plant. *Atmospheric Environment* **10**, 1043–1052.

Hewett, T.A., Fay, J.A. & Hoult, D.P. (1971) Laboratory Experiments of Smokestack Plumes in a Stable Atmosphere. *Atmospheric Environment* **5**, 767–789.

Hensley, J.C. (1985) Cooling Tower Fundamentals. *Published by The Marley Cooling Tower Company.*

Hirst, E.A. (1971) Analysis of Round, Turbulent, Buoyant Jets Discharged to Flowing Stratified Ambients. Oak Ridge National Lab., **ORNL-4685**.

Hölscher, N. & Niemann, H.J. (1987) Some aspects about the flow around a surface-mounted circular cylinder in turbulent shear flows. *Proceedings of the 6th Symposium on Turbulent Shear Flows*, Toulouse, 7–9 September.

Hoult, D.P. & Weil, J.C. (1972) Turbulent Plume in a Laminar Crossflow. *Atmospheric Environment* **6**, 513–531.

Hoult, D.P., Fay, J.A. & Forney, L.J. (1969) A Theory of Plume Rise Compared with Field Observations. *Journal of Air Pollution Control Assessment* **19**, 585–590.

Hunter, G. (1992) The behaviour of plumes form point sources in stratified flows. PhD Thesis.

Ideriah, F.J.K. (1979) A Numerical Procedure for Calculating Partly Elliptic Flows. *Journal of Mechanical Engineering Science* **21**, 373–380.

Ince, N.Z. & Leschinzer, M.A. (1993) Calculation of Single and Multiple Impinging Jets in a Crossflow with and without Impingment Using Reynolds Stress Transport Closure. *AGARD conference proceedings 534 Computational and Experimental Assesment of Jets in Crossflow, Winchester, U.K., 19-22 April 1993,* 23-1–23-14.

Isaac, K.M. & Schetz, J.A. (1982) Analysis of multiple jetts in a cross-flow. *Journal of Fluids Engineering* **104**, 489–492.

Jubran, B. & Brown, A. (1985) Film Cooling of Two Rows of Holes in the Streamwise and Spanwise Directions. *Transactions of the ASME* **107**, 84–91.

Kavsaoglu, M.S. & Akmandor, I.S. (1993) Navier-Stokes Simulation of Two and Three Dimensional Jets in a Crossflow, Effects of Grid and Boundary Conditions. *AGARD conference proceedings 534 Computational and Experimental Assesment of Jets in Crossflow, Winchester, U.K., 19-22 April 1993,* 25-1–25-20.

Keffer, J.F. & Baines, W.D. (1963) The round turbulent jet in a cross wind. *Journal of Fluid Mechanics* **15(4)**, 481–496.

Klimetzek, F. R. (1996) Mesh adaption and error estimation: towards a solver-independent solution. *Basel World CFD Conference Proceedings, May 19-23,* 13.5–13.7.

Kuhlman, J.M. & Chu, L.C. (1983) Reynolds Number Effects on the Nearfield Mean Characteristics of a Laboratory Model Thermal Plume. *Transactions of the ASME* **105**, 34–40.

LaVerne, M.E. (1976) *Oak Ridge Fog and Drift Program (ORFAD) User's Manual,* ORNL/*TM-5021,* Oak Ridge National Laboratory, Oak Ridge, Tenn.

Lee, J.L. (1977) Potential Weather Modification from Cooling Tower Effluents at Conceptual Power Parks. *Atmospheric Environment* **11**, 749–759.

Majumdar, S. & Rodi, W. (1989) Three-Dimensional Computation of Flow Past Cylindrical Structures and Model Cooling Towers. *Atmospheric Environment* **24**, 3–22.

Malin, M.R. & Younis, B.A. (1990) Calculation of turbulent buoyant plumes with a Reynolds stress and heat flux transport closure. *International Journal of Heat and Mass Transfer* **33(10)**, 2247–2264.

Manins, P.C. (1979) Partial Penetration of an Elevated Inversion Layer by Chimney Plumes. *Atmospheric Environment* **13**, 733–741.

Margason, R.J. (1993) Fifty Years of Jet in Crossflow Research. *AGARD conference proceedings 534 Computational and Experimental Assesment of Jets in Crossflow, Winchester, U.K., 19-22 April 1993,* 1-1–1-14.

Mompean, G. (1994) Three-Equation Turbulence Model for Prediction of the Mean Squared Temperature Variance in grid-generated flows and round jets. *International Journal of Heat and Mass Transfer* **37(7)**, 1165-1164.

Montgomery, T.L., Norris, W.B., Thomas, F.W. & Carpenter, S.B. (1973) A Simplified Technique used to Evaluate Atmospheric Dispersion of Emissions from Large Plants. *Journal of Air Pollution Control Assesment* **23**, 388–457.

Moore, R.D. (1977) *The KUMULUS Model for Plume and Drift Calculation for Indian Point Unit No. 2.* Environmental Systems Corporation, Knoxville.

Morton, B.R., Taylor, G.I. & Turner, J.S. (1956) Turbulent Gravitational Convection from Mainland and Instantaneous Sources. *Proceedings of the Royal Society, London,* **A234**, 1–23.

Murphy, B.L. (1975) Plume rise from a row of chimneys. *For presentation at the 68th Annual Meeting of the Air Pollution Control Association,* Boston, Massachusetts, June 15–20.

Nieuwstadt, F.T.M. & De Vlak, J.P.J.M. (1987) A large eddy simulation of buoyant and non-buoyant plume dispersion in the atmospheric boundary layer. *Atmospheric Environment* **21(12)**, 2573–2587.

Ooms & Mahieu (1981) A comparison between a plume path model and a virtual point source model for a stack plume. *Applied Scientific Research,* **36**, 339-356.

Orville, H.D., Hirsch, J.H. & May, L.E. (1975) Application of a Cloud Model to Cooling Tower Plumes and Clouds. *Journal of Applied Meteorology. (in press).*

Overcamp, T.J. & Ku, T. (1986) Effect of a Virtual Origin Correction on Entrainment Coefficients as Determined from Observations of Plume Rise. *Atmospheric Environment* **20**, 293–300.

Overcamp, T.J. & Ku, T. (1988) Plume Rise from Two or More Adjacent Stacks. *Atmospheric Environment* **22**, 625–637.

Overcamp, T.J. (1982) Plume Rise from Two or More Adjacent Stacks. PPRP - 67 (PB83 - 179036), Power Plant Siting Program, State of Maryland.

Patankar, S.V., Basu, D.K. & Alpay, S.A. (1977) Prediction of the Three-Dimensional Velocity Field of a Deflected Turbulent Jet. *Journal of Fluids Engineering*

Patankar, S.V. & Spalding, D.B. (1972) Simulatneous predictions of flow patttern and radiation for three-dimensional flames. *Proceedings of the 14th International Symposium on Combustion*. The Combustion Institute, August.

Papaspyros, J.N.E., Papanicolaou, P.N., Kastrinakis, E.G. *et al.* (1995) Experimental investigation of air pollutant releases. *Air Pollution Theory and Simulation* 185–192.

Perkins, H.C. (1974) *Air Pollution.* McGraw-Hill, New York.

Policastro, A.J., Dunn, W.E. & Carhart, R.A. (1993) A model for seasonal and annual cooling tower impacts. 379–395.

Rhie, C.M. & Chow, W.L. (1983) Numerical study of the turbulent flow past an airfoil with trailing edge seperation. *AIAA* **21**, 1527–1532.

Rodi, W. & Srivatsa, S.K. (1980) A locally elliptic calculation procedure for three-dimensional flows and its application to a jet in a cross flow. *Computer Methods in Applied Mechanics and Engineering* **23**, 67–83.

Rodi, W. (1982) Turbulent Buoyant Jets and Plumes. *Volume 6 of H.M.T. published by Pergamon Press, 57 pp.*

Saame, J. (1971) An Analytical Investigation of the Formation of Dispersion of Fog Plumes from a Natural Draught Water Cooling Tower for Various Meteorological Conditions. Master's Thesis, Department of Mechanical Engineering, University of Pittsburgh.

Sakamoto, H., Moriya, M., Taniguchi, S. & Arie, M. (1982) The Form Drag of Three-Dimensional Bluff Bodies Immersed in Turbulent Boundary Layers. *Journal of Fluids Engineering* **104**, 326–334.

Sandroni, S., Bacci, P. & Anfossi, D. (1981) *Atmospheric Environment* **15**, 95.

Saripalli, K.R. (1987) Laser Doppler Velocity Measurments in 3D Impinging Twin Jet Fountain Type Flows. *Turbulent Shear Flows* **5**, 147-168.

Schatzmann, M. & Policastro, A.J. (1984) An Advanced Integral Model for Cooling Tower Plume Dispersion. *Atmospheric Environment* **18**, 663–674.

Schatzmann, M. & Lohneyer, A. & Ortner, G. (1987) Flue Gas Discharge from Cooling Towers, Wind Tunnel Investigation of Building Downwash Effects on Ground Level Concentrations. *Atmospheric Environment* **21**, 1713-1724.

Schönung, B. & Rodi, W. (1987) Prediction of film cooling by a row of holes with a two-dimensional boundary layer procedure. *ASME Paper* **85-IGT-2**.

Scire, J.S. & Schulman, L.L. (1981) Plume Rise Enhancement from Multiple Sources. *Proc. of the Fifth Symposium on Turbulence, Diffusion and Air Pollution*, 120 -121. American Meteorological Society, Boston, MA.

Sforza, P.M., Steiger, M.H. & Trentacoste, N. (1966) Studies on three-dimensional viscous jets. *AIAA Journal* **4(5)**.

Shayesteh, M.V., Shabaka, I.M.N.A. & Bradshaw, P. (1985) Turbulent Structure of a 3D Impinging Jet in a Crossflow. *AIAA 23rd Aerospace Sciences Meeting, Reno, Nevada, January 14-17.*

Sideridis, G.A., Kastrinkis, E.G. & Nychas, S.G. (1995) Experimental simulation of air pollutant dispersion by atmospheric motions. *Air Pollution Theory and Simulation* 177–184.

Slawson, P.R. & Coleman, J.H. (1977) *Natural-Draught Cooling-Tower Plume Behaviour at Paradise Steam Plant, Waste Heat Management and Utilisation,* Vol 3. Hemisphere Publishing Corporation, Washington D.C.

Slawson, P.R. & Csanady, G.T. (1967) On the Mean Path of Buoyant, Bent-Over Chimney Plumes. *Journal of Fluid Mechanics* **28**, 311–322.

Slawson, P.R. & Csanady, G.T. (1971) The Effect of Atmospheric Conditions on Plume Rise. *Journal of Fluid Mechanics* **47**, 33–49.

Slawson, P.R. & Wigley, P.M. (1975) The Effects of Atmospheric Conditions on the Length of Visible Cooling Tower Plumes. *Atmospheric Environment* **9**, 437–435.

Slawson, P.R. (1981) Some Observations on Modelling the Mechanical-Draft Cooling Tower Plume at Plant Garston. *Atmospheric Environment* **16**, 2089–2094.

Slawson, P.R. & Csanady, G.T. (1966) Section 2.1

Snyder, W.H. & Lawson, R.E. (1990) Fluid modeling simulation of stack-tip downwash. *Atmospheric Environment*. Submitted.

Spillane, K.T. & Elsum, C.C. (1983) Convective Knock-Down of Cooling Tower Plumes. *Atmospheric Environment* **17**, 227–233.

Stephen, D.W. & Moroz, W.J. (1972) Plume Rise from Wet Cooling Towers in Strong Winds. Engineering Research Bulletin B-107, Center for Air Environmental Studies, Penn. State University.

Stern, A.C. (1976) *Air Pollution.* Vol 1, 3rd Edition. Acedemic Press.

Sugiyama, Y. (1979) Experiments on the Flow In and Around Jets Directed Normal to a Crossflow. *Bulletin of the JSME* **22**, 1736–1745.

Tatom, F. B. (1986) Prediction of Stack Plume Downwash. *Journal of Fluids Engineering* **108**, 379–381.

Thorp, J.M. & Orgill, M.M. (1984) Cooling Tower Visible Plume Rise Analyses by Time Integrated Photographs. *Atmospheric Environment* **18**, 675–683.

Tsai, Y.J. & Huang, C.H. (1972) Evaluation of Varying Meteorological Parameters on Cooling Tower Plume Behaviour. In *Symposium on Atmospheric Diffusion and Air Pollution.* American Meteorological Society, Boston Mass, 408–411.

Tennekes, H. (1991) Similarity relations, scaling laws and spectral dynamics. In *Atmospheric Turbulence and Air Pollution Modelling*. D. Reidal Publishing Company, 37–68.

TNO Institute of Environmental and Energy Technology (1995) Cooling Tower plumes; measurement of plume rise and dispersion in a wind tunnel. *Repeat mesurment of cooling tower plume dispersion,* R95-213.

Uthe, E.E. (1984) Cooling Tower Plume Rise Analyses by Airborne Lidar. *Atmospheric Environment* **18**, 107–119.

Vandoormal, J.P. & Raithby, G.D. (1984) Enhancement of the SIMPLE method for predicting incompressible fluid flows. *Numerical Heat Transfer* **7**, 147–163.

Versteeg, H.K. & Malalasekera, W. (1995) Introduction to CFD, the finite volume method. *Longman Scientific and Technical.*

Venter, G.P.N. (1977) A comparison of observed plume trajectories with those predicted by two models. *Atmospheric Environment* **11**, 421–426.

Viollet, P.L. (1977) Etude de Jets dans des Courants Transversiers et dans des Milieux Stratifiés. Dissertation, Université Pieere et Marie Curie, Paris, France.

Weil, J.C. (1982) Source Buoyancy Effects in Boundary Layer Diffusion. *Workshop on the Parameterization of Mixed Layer Diffusion,* Physical Science Laboratory

Weil, J. (1974) The Rise of Moist Buoyant Plumes. *Journal of Applied Meteorology* **13**, 435–443.

Willis, G.E. & Deardorff, J.W. (1983) On Plume Rise Within the Convective Boundary Layer. *Atmospheric Environment* **17**, 2435–2447.

Willis, G.E. & Deardorff, J.W. (1981) A laboratory study of dispersion from a source in the middle of the convectively mixed layer. *Atmospheric Environment* **12**, 1305–1313.

Winiarski, L. & Frick, W. (1978) Cooling Tower Plume Model. USEPA Ecological Research Series, EPA-600/3-76-100, USEPA, Corvallis, Oregon.

Winiarski, L. & Frick, W. (1978) Methods of Improving Plume Models, Cooling Tower Environment - 1978. *Proc. Power Plant Siting Commission, Maryland Department of Natural Resources,* PP5P-CPCTP-22, WRRC Special Report No. 9.

Yavuzkurt, S., Moffat, R.J. & Kays, W.M. (1980) Full-coverage film cooling. Part I. Three-dimensional measurements of turbulence structure. *Journal of Fluid Mechanics* **101(1)**, 129–158.

Yakhot, V. & Orszag, A. (1986) Renormalisation group analysis of turbulence 1. Basic theory. *Journal of Scientific Computing* **1(1)**, 3–47.

Zhang, X. & Ghoniem, A.F. (1994) A computational model for the rise and dispersion of wind-blown, buoyancy-driven plumes—III. Linearly stratified atmosphere. *Atmospheric Environemnt* **28**, 30005–3018.

Zhang, X. & Ghoniem, A.F. (1994b) A computational model for the rise and dispersion of wind-blown, buoyancy-driven plumes—III. Penetration of atmospheric inversion. *Atmospheric Environment* **28**, 3019–3032.

Appendix A

An example of the raw TNO wind tunnel experimental data for a single non-buoyant source is shown. Full-scale and small-scale values of cross-wind speed at the tower top, plume source velocity, density ratio and source exit diameter are given. Measuring locations are given in full-scale distances. x refers to the downstream location, y refers to the lateral offset relative to the centre of the tower array and z is the vertical height. It should be noted that the wind tunnel work uses z to represent the vertical distance whereas y is used in the computational study.

To convert from the absolute concentration quoted in the raw data to the equivalent T^* value it is divided by 0.003 (source concentration = 0.3%)

File: N5T0A000

1x1, no buoyancy, angle 0 deg.

Full-scale model (1:300)

	Full scale	Small scale
Ambient windspeed:	3.00 m/s	0.39 m/s
Exit velocity:	7 m/s	0.91 m/s
Density ratio:	0.95	0.74
Exit diameter:	10 m	33 mm

N^{th}	x m	y m	z m	Conc. m3/m3
1	100.0	-.0	0.0	6.3334E-06
2	100.0	-.0	30.0	1.0976E-04
3	100.0	-.0	60.0	1.2747E-04
4	100.0	-.0	90.0	6.7344E-06
5	100.0	-.0	120.0	8.9638E-07
6	100.0	-.0	150.0	3.4235E-06
7	100.0	-.0	15.0	3.2124E-05
8	100.0	-.0	45.0	1.6307E-04
9	100.0	-.0	75.0	7.2740E-05
10	100.0	-.0	105.0	1.7879E-06
11	100.0	-.0	135.0	1.0658E-06
12	100.0	-.0	165.0	0.0000E+00
13	100.0	-90.0	45.0	0.0000E+00
14	100.0	-60.0	45.0	1.8851E-06
15	100.0	-30.0	45.0	7.3660E-05
16	100.0	-75.0	45.0	0.0000E+00
17	100.0	-45.0	45.0	2.0673E-05
18	100.0	-15.0	45.0	1.3802E-04
19	100.0	15.0	45.0	1.5282E-04
20	100.0	45.0	45.0	5.4425E-06
21	100.0	75.0	45.0	0.0000E+00
22	100.0	30.0	45.0	4.2623E-05
23	100.0	60.0	45.0	0.0000E+00
24	100.0	90.0	45.0	0.0000E+00
25	400.0	-.0	0.0	2.1848E-05
26	400.0	-.0	30.0	4.9298E-05
27	400.0	-.0	60.0	5.5804E-05
28	400.0	-.0	90.0	4.6434E-05
29	400.0	-.0	120.0	1.0892E-05
30	400.0	-.0	150.0	8.4214E-07
31	400.0	-.0	15.0	2.8319E-05
32	400.0	-.0	45.0	4.9975E-05
33	400.0	-.0	75.0	5.1815E-05

y-correction = -1.7m

```
34     400.0   -.0     105.0    2.9205E-05
35     400.0   -.0     135.0    5.8205E-06
36     400.0   -.0     165.0    2.5387E-07
37     400.0   -90.0   60.0     6.2117E-06
38     400.0   -60.0   60.0     3.9407E-05
39     400.0   -30.0   60.0     6.2542E-05
40     400.0   -105.0  60.0     3.5028E-06
41     400.0   -75.0   60.0     2.5024E-05
42     400.0   -45.0   60.0     5.1916E-05
43     400.0   -.0     60.0     5.6884E-05
44     400.0   30.0    60.0     2.4916E-05
45     400.0   60.0    60.0     6.1329E-06
46     400.0   75.0    60.0     2.0409E-06
47     400.0   105.0   60.0     0.0000E+00
48     400.0   135.0   60.0     0.0000E+00
49     800.0   -.0     0.0      2.6493E-05
50     800.0   -.0     30.0     3.1837E-05
51     800.0   -.0     60.0     2.7488E-05
52     800.0   -.0     90.0     3.0290E-05
53     800.0   -.0     120.0    1.6438E-05
54     800.0   -.0     150.0    3.9829E-06
55     800.0   -.0     180.0    0.0000E+00
56     800.0   -.0     210.0    0.0000E+00
57     800.0   -.0     240.0    0.0000E+00
58     800.0   -.0     105.0    2.4149E-05
59     800.0   -.0     135.0    1.3014E-05
60     800.0   -.0     165.0    2.9145E-06
61     800.0   -150.0  90.0     5.6784E-06
62     800.0   -120.0  90.0     1.4115E-05
63     800.0   -90.0   90.0     2.0595E-05
64     800.0   -60.0   90.0     2.4475E-05
65     800.0   -30.0   90.0     2.7138E-05
66     800.0   -.0     90.0     2.2569E-05
67     800.0   30.0    90.0     8.7732E-06
68     800.0   60.0    90.0     5.0696E-06
69     800.0   90.0    90.0     1.0852E-06
70     800.0   -195.0  90.0     2.6928E-06
71     800.0   -165.0  90.0     6.0991E-06
72     800.0   -135.0  90.0     1.0125E-05
73     1200.0  -.0     0.0      2.4591E-05
74     1200.0  -.0     30.0     2.4043E-05
75     1200.0  -.0     60.0     1.8183E-05
76     1200.0  -.0     90.0     2.0643E-05
77     1200.0  -.0     120.0    1.6373E-05
78     1200.0  -.0     150.0    7.1147E-06
79     1200.0  -.0     180.0    1.1489E-06
80     1200.0  -.0     210.0    0.0000E+00
81     1200.0  -.0     240.0    0.0000E+00
82     1200.0  -.0     105.0    1.4274E-05
83     1200.0  -.0     135.0    1.1223E-05
84     1200.0  -.0     165.0    6.9688E-06
85     1200.0  -180.0  90.0     8.5705E-06
86     1200.0  -150.0  90.0     8.8091E-06
87     1200.0  -120.0  90.0     8.3858E-06
88     1200.0  -90.0   90.0     1.3107E-05
89     1200.0  -60.0   90.0     1.6886E-05
90     1200.0  -30.0   90.0     1.8586E-05
91     1200.0  -.0     90.0     1.7730E-05
92     1200.0  30.0    90.0     1.3268E-05
93     1200.0  60.0    90.0     8.4560E-06
94     1200.0  90.0    90.0     6.4047E-06
95     1200.0  120.0   90.0     2.8424E-06
96     1200.0  150.0   90.0     1.4965E-06
```

y-correction = -26.8m

y-correction = -45.1m

y-correction = -28.7m